FLOW MEASUREMENT IN OPEN CHANNELS BY COMBINED USE OF FREE SURFACE PIV AND CFD

A THESIS SUBMITTED TO
THE GRADUATE SCHOOL OF NATURAL AND APPLIED SCIENCES
OF
MIDDLE EAST TECHNICAL UNIVERSITY

BY

SIAMAK GHARAHJEH

IN PARTIAL FULLFILLMENT OF THE REQUIREMENTS
FOR
THE DEGREE OF DOCTOR OF PHILOSOPHY
IN
CIVIL ENGINEERING

AUGUST 2016

Approval of the thesis:

FLOW MEASUREMENT IN OPEN CHANNELS BY COMBINED USE OF FREE SURFACE PIV AND CFD

submitted by **SIAMAK GHARAHJEH** in partial fulfillment of the requirements for the degree of **Doctor of Philosophy in Civil Engineering Department, Middle East Technical University** by**,**

Prof. Dr. Gülbin Dural Ünver

Dean, Graduate School of **Natural and Applied Sciences**

Prof. Dr. İsmail Özgur Yaman

Head of Department, **Civil Engineering**

Prof. Dr. İsmail Aydın

Supervisor, **Civil Engineering Dept., METU**

Examining Committee Members:

Prof. Dr. Lale Balas
Civil Engineering Dept., Gazi University

Prof. Dr. İsmail Aydın
Civil Engineering Dept., METU

Prof. Dr. Serkan Özgen
Aerospace Engineering Dept., METU

Assoc. Prof. Dr. Mete Köken
Civil Engineering Dept., METU

Assoc. Prof. Dr. Yakup Darama
Civil Engineering Dept., Atılım University

Date: 1 August 2016

I hereby declare that all information in this document has been obtained and presented in accordance with academic rules and ethical conduct. I also declare that, as required by these rules and conduct, I have fully cited and referenced all material and results that are not original to this work.

Name, Last name: SIAMAK GHARAHJEH

Signature:

ABSTRACT

FLOW MEASUREMENT IN OPEN CHANNELS BY COMBINED USE OF FREE SURFACE PIV AND CFD

Gharahjeh, Siamak

PhD., Department of Civil Engineering

Supervisor: Prof. Dr. İsmail Aydın

August 2016, 276 pages

Stream discharge measurement in open channels is of great importance in hydraulic engineering. For many years, classical devices such as propellers, current meters and weirs have been used for this purpose. In recent times, non-intrusive methods such as PIV (Particle Image Velocimetry) and PTV (Particle Tracking Velocimetry) have been very popular as they are more practical and convenient to automatically collect water free surface velocity which is further analyzed for discharge measurement. Image processing, or so called PIV as a generic name, has been used in this study with the same aim. Extensive set of experiments are carried out in a tilting channel of both rectangular and compound cross section for discharge measurement with the assistance of measured free surface velocity. Experiments are conducted to measure instantaneous velocities of a number of points on the water free surface across the channel width by PTV application for various flow conditions. Sometimes, entire velocity distribution has also been measured by PIV on the free surface. Technical issues regarding tracer particle size and type, travel distance, lighting, recording speed, camera position, image distortion and state of flow are discussed and useful recommendations are suggested. Experimental measurements are used to validate the mathematical model (numerical model) of the problem. Validation includes the calibration of numerical free surface velocity via employment of experimental measurements. This phase obliges the introduction of a new parameter into the numerical model, named as surface

damping parameter. Last important aspect of the research is the inverse estimation of wall roughness in addition to discharge when free surface velocity, flow cross section and channel bed slope are given inputs.

Keywords: Discharge measurement, Wall roughness, Free surface velocity, Open channel flows.

ÖZ

YÜZEY PIV VE CFD BİRLİKTE KULLANILARAK AÇIK KANALLARDA AKIM ÖLÇÜMÜ

Siamak, Gharahjeh

Doktora, İnşaat Mühendisliği Bölümü

Tez Yöneticisi: Prof. Dr. İsmail Aydın

Ağustos 2016, 276 sayfa

Açık kanallarda akım ölçümü hidrolik mühendisliğinde büyük önem taşır. Uzun yıllar pervaneler ve savaklar gibi klasik ölçüm cihazları bu amaçla kullanılmıştır. Yakın zamanlarda, debi hesabı amacıyla yüzey hızı ölçümü için akımı bozmayan metotlardan olan PIV (Particle Image Velocimetry) ve PTV (Particle Tracking Velocimetry) teknikleri pratik ve otomatik veri toplamaya uygun olduğundan daha çok kullanılmaya başlandı. Görüntü işleme, yaygın adıyla PIV, bu araştırmada aynı amaç için kullanılmıştır. Ölçülen yüzey hızlarından yararlanarak debi hesabı amacıyla değişken eğimli bir kanalda dikdörtgen ve bileşik kesitler için çok sayıda deney yapılmıştır. Deneyler genelde su yüzeyindeki farklı noktalardaki anlık hızları farklı akım durumlarında PTV kullanılarak ölçmek için yapılmıştır. Bazı durumlarda su yüzeyindeki tüm hız dağılımı da PIV kullanılarak ölçülmüştür. Görüntü işleme için takip olunan parçanın boyutu, çeşidi, yolculuk mesafesi, ışık durumu, kayıt hızı, kamera pozisyonu, görüntü çarpıklığı ve akımın durumu gibi teknik konular tartışılmış ve önerilerde bulunulmuştur. Ölçülen hız ve debiler önerilen sayısal modelin doğrulanması için kullanılmıştır. Deneysel ölçümler kullanılarak hesaplanan yüzey hızlarının kalibrasyonu yapılmıştır. Bu aşamada sayısal model içine su yüzünün türbülans sönümlemesini ifade eden bir parametre tanımlanarak kanal geometrisinin fonksiyonu olarak ifade edilmiştir. Son

olarak, yüzey hızı, kesit alanını ve kanal eğimi verildiğinde, debiyle birlikte duvar pürüzlüğünün hesaplanmasına olanak veren ters çözüm yapılmıştır.

Anahtar kelimeler: Debi ölçümü, Cidar pürüzlülüğü, Yüzey hızı, Açık kanal akımı

To my beloved family

ACKNOWLEDGMENT

My sincere gratitude is firstly dedicated to Prof. Dr. İsmail Aydın, my thesis supervisor. He has been of infinite patience and resilience, support and guidance, encouragement and positive energy at all the times, in my all weak and strong performances.

Then I will dedicate my appreciation towards hydraulics lab technicians for constructing the model set up.

I thank the Scientific and Technological Research Council of Turkey (TUBITAK) for supporting this project (numbered as 113M435).

Last but not least, I must extend my gratitude towards my parents, Halimberdi and Naiyer, who have been endorsing me all the way along even when I am far from home.

TABLE OF CONTENTS

ABSTRACT v

ÖZ vii

ACKNOWLEDGMENT x

TABLE OF CONTENTS xi

LIST OF TABLES xv

LIST OF FIGURES xviii

LIST OF SYMBOLS xxxv

CHAPTERS

1. INTRODUCTION 1

1.1 Problem description 1

1.2 Literature survey on video imagery techniques (PIV, PTV and LSPIV) 2

1.2.1 PIV (Particle Image Velocimetry) & PTV (Particle Tracking Velocimetry)- After Adrian (1991) 2

1.2.2 LSPIV (Large-Scale Particle Image Velocimetry) 3

1.2.3 PIV developing history 4

1.2.4 PTV developing history 6

1.3 Literature survey on nonintrusive stream gauging using imaging technique 7

1.4 Literature survey on nonintrusive stream gauging by computational tools 9

1.5 Research objectives and problem overview 10

2. EXPERIMENTS 13

2.1 Experimental set up 13

2.1.1 Flume 13
2.1.2 Roughness geometry 17
2.2 Flow conditions 21
2.2.1 Flow over smooth rectangular channels 21
2.2.2 Flow over rough rectangular channels 25
2.2.3 Flow over smooth compound channels 28
2.2.4 Flow over floodplain rough compound channels 29
2.2.5 Flow over all bed rough compound channels 29
2.3 Experimental procedures 30
2.3.1 Prandtl-Pitot tube 30
2.3.2 Hot-film experiments 31
2.3.3 Image processing 37
2.3.4 PTV tool and components (Algorithm, Seeding, Particle dispenser and Lighting) 38
2.3.5 PIV tool and components (Algorithm, Seeding and Particle dispenser) 41
2.3.6 Camera lens distortion effect removal 44
2.3.7 LSPIV experiment 50
3. NUMERICAL MODEL 55
3.1 Modeling three-dimensional velocity field in open channel flows 55
3.2 Governing equations and turbulence model 56
3.3 Mesh quality determination 61
4. ANALYSIS ON RECTANGULAR CHANNEL EXPERIMENTS 67
4.1 Uniform flow generation in smooth and rough rectangular channels 67
4.2 PTV remarks, experimental observations and error analysis 71
4.3 PIV remarks, experimental observations and post processing 80
4.4 Surface damping parameter in smooth rectangular channels (D^+) 86

4.5 Surface damping parameter in rough rectangular channels 91

4.6 Inverse solutions for roughness and discharge estimation in rectangular channels 97

5. ANALYSIS ON COMPOUND CHANNEL EXPERIMENTS 109

5.1 Inverse discharge determination in GVF in smooth compound channels 109

5.1.1 Failure of Manning uniform depth calculation in compound channels 109

5.1.2 Flow seepage from floodplain into main channel in compound channels 112

5.1.3 Inverse discharge estimation with known surface roughness and unknown energy slope in smooth compound channels 113

5.1.4 Flood plain discharge integration from experimental measurements 120

5.2 Inverse solutions for roughness determination in all bed rough compound channels . 122

5.3 Inverse solutions in floodplain rough compound channels 131

6. CONCLUSIONS AND RECCOMENDATIONS 139

6.1 Conclusions 139

6.2 Recommendations 141

REFERENCES 143

APPENDICES

A. WATER SURFACE PROFILES FOR SMOOTH COMPOUND CHANNEL EXPERIMENTS 151

B. WATER SURFACE PROFILES FOR FLOODPLAIN ROUGH COMPOUND CHANNEL EXPERIMENTS 155

C. WATER SURFACE PROFILES FOR ROUGH COMPOUND CHANNEL EXPERIMENTS 157

D. HOT-FILM MEASUREMENTS 161

E. COMPUTER PROGRAM THAT DOES THE PTV ANALYSIS AND IMAGE RECTIFICATION 167

F. COMPUTER PROGRAM FOR GRADUALLY VARIED SURFACE PROFILE CALCULATIONS 179

G. SURFACE PROFILES FOR THE MANNING ROUGHNESS DETERMINATION IN SMOOTH RECTANGULAR CHANNELS 183

H. EXPERIMENTAL SURFACE VELOCITIES OBTAINED BY PTV FOR SMOOTH RECTANGULAR CHANNEL 187

I. EXPERIMENTAL SURFACE VELOCITIES OBTAINED BY PIV FOR SMOOTH RECTANGULAR CHANNEL 211

J. NUMERICAL AND EXPERIMENTAL SURFACE VELOCITIES IN SURFACE DAMPING FACTOR DETERMINATION PHASE IN SMOOTH RECTANGULAR CHANNELS.....219

K. SURFACE VELOCITIES FOR INVERSE SOLUTIONS IN RECTANGULAR CHANNELS.....227

L. CODE THAT INTEGRATES THE VELOCITY IN FLOOD PLAIN FOR DISCHARGE CALCULATION.....261

M. EXPERIMENTAL VELOCITY MEASUREMENTS BY PITOT TUBE IN FLOOD PLAIN IN SMOOTH COMPOUND CHANNELS.....263

N. EXPERIMENTAL VELOCITY MEASUREMENTS BY PITOT TUBE IN FLOOD PLAIN IN ALL BED ROUGH COMPOUND CHANNELS.....267

O. EXPERIMENTAL VELOCITY MEASUREMENTS BY PITOT TUBE IN FLOOD PLAIN IN FLOODPLAIN ROUGH COMPOUND CHANNELS 271

CURRICULUM VITAE 275

LIST OF TABLES

Table 2-1: Roughness types studied for rectangular channels..... 19

Table 2-2 : Flow conditions of surface profile recordings in smooth rectangular channel ... 21

Table 2-3 : Smooth rectangle channel experiments for bed slope of 0.001 22

Table 2-4 : Smooth rectangle channel experiments for bed slope of 0.002 22

Table 2-5 : Smooth rectangle channel experiments for bed slope of 0.004 22

Table 2-6 : Smooth rectangle channel experiments for bed slope of 0.008 23

Table 2-7 : Smooth rectangle channel experiments for bed slope of 0.015 23

Table 2-8 : Smooth rectangle channel experiments for bed slope of 0.025 23

Table 2-9 : Smooth rectangle channel experiments for bed slope of 0.035 23

Table 2-10 : Smooth rectangle channel experiments for bed slope of 0.045 24

Table 2-11 : Smooth rectangle channel experiments for bed slope of 0.055 24

Table 2-12 : Hot-film experiments in smooth rectangular channel..... 24

Table 2-13 : Flow conditions for roughness type 1 25

Table 2-14 : Flow conditions for roughness type 2 26

Table 2-15 : Flow conditions for roughness type 3 26

Table 2-16 : Flow conditions for roughness type 4 27

Table 2-17 : Flow conditions for roughness type 5 27

Table 2-18 : Flow conditions for roughness type 6 28

Table 2-19 : Flow conditions for smooth compound channels..... 28

Table 2-20 : Flow conditions for floodplain rough compound channels..... 29

Table 2-21 : Flow conditions for all bed rough compound channels 30

Table 2-22 : Data points used for curve fitting in Hot-film calibration 35

Table 3-2 : The surface velocity errors for named cases for mesh determination 63

Table 3-3: Numerical discharge for various mesh sizes compared to experimental discharge 65

Table 4-1 : PTV measurements for a nearly fixed point on the free surface (case 1).....79

Table 4-2 : PTV measurements for a nearly fixed point on the free surface (case 2).....80

Table 4-3 : Measured and computed discharge comparison with the D^+ coming from equation (4.7).....88

Table 4-4 : The result of discharge and roughness estimation (inverse solution) by using a single surface velocity for roughest channel case (k_{s2}) 99

Table 4-5 : The result of discharge and roughness estimation (inverse solution) by using a single surface velocity for smallest roughness case (k_{s6}) 100

Table 4-6 : Result of inverse solution for roughness of k_{s1}.....103

Table 4-7 : Result of inverse solution for roughness of k_{s2}.....104

Table 4-8 : Result of inverse solution for roughness of k_{s3}.....104

Table 4-9 : Result of inverse solution for roughness of k_{s4}.....105

Table 4-10 : Result of inverse solution for roughness of k_{s5}.....105

Table 4-11 : Result of inverse solution for roughness of k_{s6}.....106

Table 5-1 : Uniform depth according to Manning relation for smooth compound channel in two specific flow conditions.....109

Table 5-2 : Inverse solution details for smooth compound channel, Case 1.....114

Table 5-3 : Inverse solution details for smooth compound channel, Case 2.....115

Table 5-4 : Inverse solution details for smooth compound channel, Case 3.....116

Table 5-5 : Inverse solution details for smooth compound channel, Case 4.....117

Table 5-6 : Inverse solution details for smooth compound channel, Case 5.....118

Table 5-7 : Inverse solution details for smooth compound channel, Case 6.....119

Table 5-8 : Numerical and experimental flood plain discharge comparisons for smooth compound channels 122

Table 5-9 : Uniform and GVF flow over all bed rough compound channels..... 123

Table 5-10 : Inverse solution details for all bed rough compound channel, Case 1..... 124

Table 5-11 : Inverse solution details for all bed rough compound channel, Case 2..... 125

Table 5-12 : Inverse solution details for all bed rough compound channel, Case 3..... 126

Table 5-13 : Inverse solution details for all bed rough compound channel, Case 4..... 127

Table 5-14 : Inverse solution details for all bed rough compound channel, Case 5..... 129

Table 5-15 : Inverse solution details for all bed rough compound channel, Case 6..... 130

Table 5-16 : Numerical and experimental flood plain discharge comparisons for all bed rough compound channels 131

Table 5-17 : Inverse solution details for floodplain rough compound channel, Case 1 132

Table 5-18 : Inverse solution details for floodplain rough compound channel, Case 2 133

Table 5-19 : Inverse solution details for floodplain rough compound channel, Case 3 134

Table 5-20 : Inverse solution details for floodplain rough compound channel, Case 4 135

Table 5-21 : Inverse solution details for floodplain rough compound channel, Case 5 136

Table 5-22 : Numerical and experimental flood plain discharge comparisons for all bed rough compound channels……..……...137

LIST OF FIGURES

Figure 2-1: The schematic view of the set-up 13

Figure 2-2 : The jack 14

Figure 2-3 : Camera holder mounted on the canal 15

Figure 2-4 : Dimensions of the box that models the compound channel 16

Figure 2-5 : Magnetic flowmeter.....16

Figure2-6 : Magnetic flowmeter calibration 17

Figure 2-7 : Two different roughness types seen on the channel bed 18

Figure 2-8 : Schematic view of the rib type roughness 18

Figure 2-9 : Floodplain rough (left picture) and all bed rough (right picture) compound channel.....20

Figure 2-10 : Pitot tube with manometer mounted on…….……..30

Figure 2-11 : The liquid grounding of miniCTA 31

Figure 2-12 : Water temperature change with respect to time elapse 32

Figure 2-13 : Monometer (left), Pitot tube and the Hot-film probe in operation 33

Figure 2-14 : Pitot tube (left) and Hot-film probe (right).....33

Figure 2-15 : Best fitting the voltage with respect to velocity for Hot-film calibration 34

Figure 2-16 : Velocity measured by Hot-film and Pitot tube in the vertical center line for the slope of 0.015 and Z_n=11.5 cm.....35

Figure 2-17 : Velocity profiles at the vertical column center of cross section measured and computed for flow condition of S_0=0.055, Q=162.3 l/s and Z_n=8 cm 36

Figure 2-18 : A typical object tracking analysis scheme when image is in gray scale with region of interest displayed 38

Figure 2-19 : A typical object tracking analysis scheme in its final state when image is in black and white scale 39

Figure 2-20 : PVC particles used as seeds for PTV and object tracking analysis (left) and PTV particle dispenser (right) 40

Figure 2-21 : Illumination of the working section 41

Figure 2-22 : Schematic illustration of algorithm employed for detection of tracers' displacement in PIV method 43

Figure 2-23 : Particle dispenser used to seed the flow with sawdust in PIV experiments viewed from two different angles 44

Figure 2-24 : Twelve photos taken of checkerboard at different positions for camera calibration 45

Figure 2-25 : The checkerboard at the water free surface and camera positions estimated by calibrating toolbox 47

Figure 2-26 : Re- projection error for 12 images used in calibration 48

Figure 2-27 : Velocity frequency over a couple of points on free surface for distorted images 49

Figure 2-28 : Velocity frequency over a couple of points on free surface for un-distorted images 50

Figure 2-29 : Image produced from obliquely mounted camera 51

Figure 2-30 : The image after geometrical correction is applied 52

Figure 2-31 : The comparison of PTV and LSPIV analysis for a specific case, flow condition is S_0=0.035, Z_n=0.02 m, Q=17.7 l/s and B/Z_n=30 53

Figure 3-1: Numerical velocities for different mesh sizes with PTV results in case 1 62

Figure 3-2 Numerical velocities for different mesh sizes with PTV results in case 2 62

Figure 3-3: Numerical velocities for different mesh sizes with SPTV results in case 3 63

Figure 4-1: The computed and measured surface profiles for subcritical condition, S_0=0 ... 69

Figure 4-2 : The computed and measured surface profiles for supercritical condition, S_0=0.05 69

Figure 4-3 : Comparing effect of travel distance on PTV results (30 and 120 fps)- a) S_0=0.008, Z_n=0.135, Q=165.4 l/s- b) S_0=0.008, Z_n=0.03, Q=16.25 l/s.....72

Figure 4-4 : Frames associated with 30 and 120 fps speeds for S_0=0.008 and Z_n=13.5 cm ..73

Figure 4-5 : PTV analysis comparison of 30 (a) and 120 (b) fps records for the circled particles in Figure 4-2.....74

Figure 4-6 : The frequency of middle surface velocity for a particle (S_0=0.008, Z_n=0.03 m)74

Figure 4-7 : The mean velocity plotted against the travel distance.....76

Figure 4-8 : Relative PTV error between best fit curve and data for a couple of flow conditions 78

Figure 4-9 : A typical PIV analysis with sawdust and ROI (region of interest) manifested..81

Figure 4-10 : The comparison of slow and rapid free surface velocities obtained by PIV and PTV analysis- a) S_0=0.001, Z_n=0.19 m, Q=95.45 l/s- b) S_0=0.0368, Z_n=0.08 m, Q=162.3 l/s 82

Figure 4-11 : The result of a complete PIV analysis that is used to exploit the free surface velocity. 82

Figure 4-12 : Surface velocities compared for measured and calculated values under rough channel flow condition, S_0=0.035, F_r=1.35, λ/k=20.....84

Figure 4-13 : Selection of velocity range for a typical PIV analysis 85

Figure 4-14 : Surface damping parameter (D^+) versus T^2/A in smooth rectangular channels86

Figure 4-15 : Numerical and experimental surface velocities for case 6 (S_0=0.004, Z_n=0.15 m and Q=0.1363 m^3/s).....89

Figure 4-16 : Numerical velocity counters over the channel cross section for case 6 (S_0=0.004, Z_n=0.15 m and Q=0.1363 m^3/s) 89

Figure 4-17 : Streamlines for secondary currents for case 6 (S_0=0.004, Z_n=0.15 m and Q=0.1363 m^3/s) 90

Figure 4-18 : Numerical and experimental surface velocities for case 3 (S_o=0.008- Z_n=0.135 m- Q=165.4 l/s)..... 90

Figure 4-19 : Numerical velocity counters over the channel cross section for case 3 (S_o=0.008- Z_n=0.135 m- Q=165.4 l/s) 91

Figure 4-20 : Streamlines for secondary currents for case 3 (S_o=0.008- Z_n=0.135 m- Q=165.4 l/s) 91

Figure 4-21 : Roughness plotted against relative roughness with D+ spectrum shown..... 93

Figure 4-22 : D^+ values for smooth and k_{s6} cases plotted against the T^2/A..... 93

Figure 4-23 : D^+ values for k_{s6} case plotted against relative roughness 94

Figure 4-24 : Relative numerical and experimental discharge error when equation (4.9) has been used as the D^+ formula 95

Figure 4-25 : Proposed logarithmic function as being best fit to individual data points for rough case D^+..... 96

Figure 4-26 : Contours of D^+ function plotted with regard to T^2/A for constant relative roughness 97

Figure 4-27 : The upper and lower bound of numerical surface velocity when single reference data point on free surface is employed 98

Figure 4-28 : Surface velocity profiles for inverse solution of rough rectangular channel with S_0=001, Q=0.02055 m^3/s, Z_n=0.0977 m and surface RMSE=4.68..... 107

Figure 5-1 : The water surface profile for smooth compound channel with S_0=0.001 and Q=0.102 m^3/s 110

Figure 5-2 : The water surface profile for smooth compound channel with S_0=0.002 and Q=0.102 m^3/s 111

Figure 5-3 : Manifestation of parallel stream trace on the free surface in smooth compound channel for S_0=0.0005 and Q=0.094 m^3/s (Flow direction is shown with white arrow)..... 112

Figure 5-4 : Numerical and experimental Surface velocity for smooth compound channel for Case 1..... 114

Figure 5-5 : Numerical and experimental Surface velocity for smooth compound channel for Case 2 115

Figure 5-6 : Numerical and experimental Surface velocity for smooth compound channel for Case 3 116

Figure 5-7 : Numerical and experimental Surface velocity for smooth compound channel for Case 4 117

Figure 5-8 : Numerical and experimental Surface velocity for smooth compound channel for Case 5 118

Figure 5-9 : Numerical and experimental Surface velocity for smooth compound channel for Case 6 119

Figure 5-10 : Pitot tube measurement locations in flood plain 121

Figure 5-11: Integration of discharge for internal flood plain area 121

Figure 5-12 : Numerical and experimental Surface velocity for all bed rough compound channel for Case 1 124

Figure 5-13 : Numerical and experimental Surface velocity for all bed rough compound channel for Case 2 125

Figure 5-14 : Numerical and experimental Surface velocity for all bed rough compound channel for Case 3 126

Figure 5-15 : Numerical and experimental Surface velocity for all bed rough compound channel for Case 4 127

Figure 5-16 : Numerical and experimental Surface velocity for all bed rough compound channel for Case 5 129

Figure 5-17 : Numerical and experimental Surface velocity for all bed rough compound channel for Case 5 130

Figure 5-18 : Numerical and experimental Surface velocity for floodplain rough compound channel for Case 1 132

Figure 5-19 : Numerical and experimental Surface velocity for floodplain rough compound channel for Case 2 133

Figure 5-20 : Numerical and experimental Surface velocity for floodplain rough compound channel for Case 3 134

Figure 5-21 : Numerical and experimental Surface velocity for floodplain rough compound channel for Case 4 135

Figure 5-22 : Numerical and experimental Surface velocity for floodplain rough compound channel for Case 5 136

Figure A-1 : Water surface profile of smooth compound channel (S_0=0.0005 & Q=0.094 m^3/s)..... 151

Figure A-2 :Water surface profile of smooth compound channel (S_0=0.001 & Q=0.102 m^3/s) 151

Figure A-3 :Water surface profile of smooth compound channel (S_0=0.002 & Q=0.102 m^3/s) 152

Figure A-4 : Water surface profile of smooth compound channel (S_0=0.01 & Q=0.166 m^3/s) 152

Figure A-5 :Water surface profile of smooth compound channel (S_0=0.015 & Q=0.166 m^3/s) 153

Figure A-6 :Water surface profile of smooth compound channel (S_0=0.02 & Q=0.166 m^3/s) 153

Figure B-1 : Water surface profile of smooth compound channel (S_0=0.002 & Q=0.1 m^3/s) 155

Figure B-2 : Water surface profile of smooth compound channel (S_0=0.004 & Q=0.1 m^3/s) 155

Figure B-3 : Water surface profile of smooth compound channel (S_0=0.008 & Q=0.1 m^3/s) 156

Figure B-4 : Water surface profile of smooth compound channel (S_0=0.02 & Q=0.147 m^3/s) 156

Figure B-5 : Water surface profile of smooth compound channel (S_0=0.025 & Q=0.16 m^3/s) 156

Figure C-1 : Water surface profile of smooth compound channel (S_0=0.002 & Q=0.0505 m^3/s) 157

Figure C-2 : Water surface profile of smooth compound channel (S_0=0.004 & Q=0.0635 m^3/s) 157

Figure C-3 : Water surface profile of smooth compound channel (S_0=0.01 & Q=0.074 m^3/s, Z_n=0.199 m) 158

Figure C-4 : Water surface profile of smooth compound channel (S_0=0.02 & Q=0.1 m^3/s, Z_n=0.2 m).....158

Figure C-5 : Water surface profile of smooth compound channel (S_0=0.03 & Q=0.15 m^3/s, Z_n=0.214 m).....159

Figure C-6 : Water surface profile of smooth compound channel (S_0=0.035 & Q=0.16 m^3/s, Z_n=0.212 m).....159

Figure D-1 : Vertical central line velocity distribution with S_0=0.055, Q=0.162 m^3/s and Z_n=0.8 m 161

Figure D-2 : Vertical central line velocity distribution with S_0=0.035, Q=0.1588 m^3/s and Z_n=0.9 m 162

Figure D-3 : Vertical central line velocity distribution with S_0=0.015, Q=0.1675 m^3/s and Z_n=0.115 m 162

Figure D-4 : Vertical central line velocity distribution with S_0=0.004, Q=0.1632 m^3/s and Z_n=0.17 m 163

Figure D-5 : Vertical central line velocity distribution with S_0=0.001, Q=0.17065 m^3/s and Z_n=0.29 m 163

Figure D-6 : Surface velocity distribution with S_0=0.055, Q=0.1623 m^3/s and Z_n=0.08 m.164

Figure D-7 : Surface velocity distribution with S_0=0.035, Q=0.1588 m^3/s and Z_n=0.09 m.164

Figure D-8 : Surface velocity distribution with S_{0c}=0.015, Q=0.1675 m^3/s and Z_n=0.115 m 165

Figure D-9 : Surface velocity distribution with S_0=0.004, Q=0.1632 m^3/s and Z_n=0.17 m.165

Figure D-10 : Surface velocity distribution with S_0=0.001, Q=0.17064 m^3/s and Z_n=0.29 m 166

Figure G-1 : Surface profile for smooth rectangular channel with S0=0, 0.002 and 0.004 183

Figure G-2 : Surface profile for smooth rectangular channel with S0=0.008, 0.015 and 0.02 184

Figure G-3 : Surface profile for smooth rectangular channel with S0=0.025, 0.03 and 0.035 185

Figure G-4 : Surface profile for smooth rectangular channel with S0=0.04, 0.045 and 0.05 186

Figure H-1 : Surface velocity measured by PTV for S_0=0.001- Z_n=0.05 m- Q=12.9 l/s 187

Figure H-2 : Surface velocity measured by PTV for S_0=0.001- Z_n=0.15 m- Q=68.13 l/s .. 187

Figure H-3 : Surface velocity measured by PTV for S_0=0.001- Z_n=0.19 m- Q=95.45 l/s .. 188

Figure H-4 : Surface velocity measured by PTV for S_0=0.001- Z_n=0.23 m- Q=124.55 l/s 188

Figure H-5 : Surface velocity measured by PTV for S_0=0.001- Z_n=0.26 m- Q=147.28 l/s 189

Figure H-6 : Surface velocity measured by PTV for S_0=0.001- Z_n=0.29 m- Q=170.64 l/s 189

Figure H-7 : Surface velocity measured by PTV for S_0=0.002- Z_n=0.04 m- Q=12.9 l/s 190

Figure H-8 : Surface velocity measured by PTV for S_0=0.002- Z_n=0.07 m- Q=30.85 l/s .. 190

Figure H-9 : Surface velocity measured by PTV for S_0=0.002- Z_n=0.1 m- Q=53.05 l/s 191

Figure H-10 : Surface velocity measured by PTV for S_0=0.002- Z_n=0.14 m- Q=87.2 l/s .. 191

Figure H-11 : Surface velocity measured by PTV for S_0=0.002- Z_n=0.17 m- Q=115.3 l/s 192

Figure H-12 : Surface velocity measured by PTV for S_0=0.002- Z_n=0.22 m- Q=165.7 l/s 192

Figure H-13 : Surface velocity measured by PTV for S_0=0.004- Z_n=0.03 m- Q=11.5 l/s .. 193

Figure H-14 : Surface velocity measured by PTV for S_0=0.004- Z_n=0.06 m- Q=34.4 l/s .. 193

Figure H-15 : Surface velocity measured by PTV for S_0=0.004- Z_n=0.09 m- Q=64 l/s 194

Figure H-16 : Surface velocity measured by PTV for S_0=0.004- Z_n=0.122 m- Q=98.4 l/s 194

Figure H-17 : Surface velocity measured by PTV for S_0=0.004- Z_n=0.15 m- Q=136.3 l/s 195

Figure H-18 : Surface velocity measured by PTV for S_0=0.004- Z_n=0.17 m- Q=163.2 l/s 195

Figure H-19 : Surface velocity measured by PTV for S_0=0.008- Z_n=0.03 m- Q=16.5 l/s ...196

Figure H-20 : Surface velocity measured by PTV for S_0=0.008- Z_n=0.05 m- Q=36.6 l/s ...196

Figure H-21 : Surface velocity measured by PTV for S_0=0.008- Z_n=0.07 m- Q=61.75 l/s .197

Figure H-22 : Surface velocity measured by PTV for S_0=0.008- Z_n=0.09 m- Q=90.5 l/s ...197

Figure H-23 : Surface velocity measured by PTV for S_0=0.008- Z_n=0.115 m- Q=130.65 l/s 198

Figure H-24 : Surface velocity measured by PTV for S_0=0.008- Z_n=0.135 m- Q=165.4 l/s198

Figure H-25 : Surface velocity measured by PTV for S_0=0.015- Z_n=0.03 m- Q=22.2 l/s ...199

Figure H-26 : Surface velocity measured by PTV for S_0=0.015- Z_n=0.05 m- Q=50 l/s 199

Figure H-27 : Surface velocity measured by PTV for S_0=0.015- Z_n=0.065 m- Q=75.3 l/s .200

Figure H-28 : Surface velocity measured by PTV for S_0=0.015- Z_n=0.08 m- Q=103.7 l/s .200

Figure H-28 : Surface velocity measured by PTV for S_0=0.015- Z_n=0.105 m- Q=146 l/s ..201

Figure H-29 : Surface velocity measured by PTV for S_f=0.0131- Z_n=0.115 m- Q=167.5 l/s 201

Figure H-30 : Surface velocity measured by PTV for S_0=0.025- Z_n=0.02 m- Q=15 l/s 202

Figure H-31 : Surface velocity measured by PTV for S_0=0.025- Z_n=0.04 m- Q=45.5 l/s ...202

Figure H-32 : Surface velocity measured by PTV for S_0=0.025- Z_n=0.06 m- Q=86 l/s 203

Figure H-33 : Surface velocity measured by PTV for S_f=0.02058- Z_n=0.08 m- Q=121.35 l/s 203

Figure H-34 : Surface velocity measured by PTV for S_f=0.01716- Z_n=0.102 m- Q=160 l/s 204

Figure H-35 : Surface velocity measured by PTV for S_0=0.035- Z_n=0.02 m- Q=17.7 l/s ..204

Figure H-36 : Surface velocity measured by PTV for S_0=0.035- Z_n=0.04 m- Q=53.7 l/s ...205

Figure H-37 : Surface velocity measured by PTV for S_f=0.02737- Z_n=0.065 m- Q=101.7 l/s 205

Figure H-38 : Surface velocity measured by PTV for S_f=0.0246- Z_n=0.09 m- Q=158.8 l/s206

Figure H-39 : Surface velocity measured by PTV for S_0=0.045- Z_n=0.015 m- Q=12.5 l/s 206

Figure H-40 : Surface velocity measured by PTV for S_0=0.045- Z_n=0.035 m- Q=49.25 l/s207

Figure H-41 : Surface velocity measured by PTV for S_f=0.03973- Z_n=0.0535 m- Q=87 l/s207

Figure H-42 : Surface velocity measured by PTV for S_f=0.02863- Z_n=0.087 m- Q=162.6 l/s 208

Figure H-43 : Surface velocity measured by PTV for S_0=0.055- Z_n=0.0145 m- Q=13.8 l/s208

Figure H-44 : Surface velocity measured by PTV for S_0=0.055- Z_n=0.0345 m- Q=54.4 l/s209

Figure H-45 : Surface velocity measured by PTV for S_f=0.04755- Z_n=0.0525 m- Q=96.1 l/s 209

Figure H-46 : Surface velocity measured by PTV for S_f=0.0368- Z_n=0.08 m- Q=162.3 l/s210

Figure I-1 : Surface velocity measured by PIV for S_0=0.001- Z_n=0.05 m- Q=12.9 l/s 211

Figure I-2 : Surface velocity measured by PIV for S_0=0.001- Z_n=0.15 m- Q=68.13 l/s 211

Figure I-3 : Surface velocity measured by PIV for S_0=0.001- Z_n=0.19 m- Q=95.45 l/s 212

Figure I-4 : Surface velocity measured by PIV for S_0=0.001- Z_n=0.26 m- Q=147.28 l/s ... 212

Figure I-5 : Surface velocity measured by PIV for S_0=0.004- Z_n=0.03 m- Q=11.5 l/s 213

Figure I-6 : Surface velocity measured by PIV for S_0=0.004- Z_n=0.09 m- Q=64 l/s 213

Figure I-7 : Surface velocity measured by PIV for S_0=0.004- Z_n=0.17 m- Q=163.2 l/s 214

Figure I-8 : Surface velocity measured by PIV for S_0=0.015- Z_n=0.05 m- Q=50 l/s 214

Figure I-9 : Surface velocity measured by PIV for S_0=0.015- Z_n=0.08 m- Q=103.7 l/s 215

Figure I-10 : Surface velocity measured by PIV for S_f=0.0131- Z_n=0.115 m- Q=167.5 l/s 215

Figure I-11 : Surface velocity measured by PIV for S_0=0.035- Z_n=0.02 m- Q=17.7 l/s 216

Figure I-12 : Surface velocity measured by PIV for S_0=0.035- Z_n=0.04 m- Q=53.7 l/s 216

Figure I-13 : Surface velocity measured by PIV for S_f=0.0246- Z_n=0.09 m- Q=158.8 l/s . 217

Figure I-14 : Surface velocity measured by PIV for S_0=0.055- Z_n=0.0145 m- Q=13.8 l/s . 217

Figure I-15 : Surface velocity measured by PIV for S_0=0.055- Z_n=0.0345 m- Q=54.4 l/s . 218

Figure I-16 : Surface velocity measured by PIV for S_f=0.0368- Z_n=0.08 m- Q=162.3 l/s ..218

Figure J-1 : Numerical and experimental surface velocities for S_o=0.045 (Sf=0.0286)- Z_n=0.087 m- Q=162.61 l/s.....219

Figure J-2 : Numerical and experimental surface velocities for S_o=0.0131- Z_n=0.115 m- Q=167.5 l/s 219

Figure J-3 : Numerical and experimental surface velocities for S_o=0.008- Z_n=0.135 m- Q=165.4 l/s 220

Figure J-4 : Numerical and experimental surface velocities for S_o=0.008- Z_n=0.09 m- Q=90.5 l/s 220

Figure J-5 : Numerical and experimental surface velocities for S_o=0.004- Z_n=0.17 m- Q=163.2 l/s 221

Figure J-6 : Numerical and experimental surface velocities for S_o=0.004- Z_n=0.15 m- Q=136.3 l/s 221

Figure J-7 : Numerical and experimental surface velocities for S_o=0.004- Z_n=0.09 m- Q=64 l/s 222

Figure J-8 : Numerical and experimental surface velocities for S_o=0.002- Z_n=0.1 m- Q=53.05 l/s 222

Figure J-9 : Numerical and experimental surface velocities for S_o=0.002- Z_n=0.17 m- Q=115.3 l/s 223

Figure J-10 : Numerical and experimental surface velocities for S_o=0.001- Z_n=0.29 m- Q=170.64 l/s 223

Figure J-11 : Numerical and experimental surface velocities for S_o=0.001- Z_n=0.15 m- Q=68.13 l/s 224

Figure J-12 : Numerical and experimental surface velocities for S_o=0.001- Z_n=0.19 m- Q=95.45 l/s 224

Figure J-13 : Numerical and experimental surface velocities for S_o=0.001- Z_n=0.26 m- Q=147.28 l/s 225

Figure K-1 : Measured and computed surface velocity with S_0=0.055, k_{s1}=3.9 cm, RMSE=6.24, Z_n=0.074 m, Q_{exp}=55 l/s 227

Figure K-2 : Measured and computed surface velocity with S_0=0.055, k_{s1}=2.9 cm, RMSE=8.23, Z_n=0.1325 m, Q_{exp}=162.4 l/s 228

Figure K-3 : Measured and computed surface velocity with S_0=0.045, k_{s1}=3.6 cm, RMSE=5.53, Z_n=0.10031 m, Q_{exp}=87 l/s 228

Figure K-4 : Measured and computed surface velocity with S_0=0.045, k_{s1}=3.1 cm, RMSE=5.95, Z_n=0.1426 m, Q_{exp}=87 l/s 229

Figure K-5 : Measured and computed surface velocity with S_0=0.035, k_{s1}=3.35 cm, RMSE=5.95, Z_n=0.1173 m, Q_{exp}=101.8 l/s 229

Figure K-6 : Measured and computed surface velocity with S_0=0.035, k_{s1}=2.85 cm, RMSE=7.98, Z_n=0.15 m, Q_{exp}=159.1 l/s 230

Figure K-7 : Measured and computed surface velocity with S_0=0.025, k_{s1}=3.15 cm, RMSE=7.1, Z_n=0.11561 m, Q_{exp}=86 l/s 230

Figure K-8 : Measured and computed surface velocity with S_0=0.025, k_{s1}=2.75 cm, RMSE=9.55, Z_n=0.1678 m, Q_{exp}=160 l/s 231

Figure K-9 : Measured and computed surface velocity with S_0=0.015, k_{s1}=3.4 cm, RMSE=4.88, Z_n=0.12618 m, Q_{exp}=75.3 l/s 231

Figure K-10 : Measured and computed surface velocity with S_0=0.015, k_{s1}=2.32 cm, RMSE=4.86, Z_n=0.19825 m, Q_{exp}=167.7 l/s 232

Figure K-11 : Measured and computed surface velocity with S_0=0.004, k_{s1}=3.5 cm, RMSE=7.7, Z_n=0.151 m, Q_{exp}=51 l/s 232

Figure K-12 : Measured and computed surface velocity with S_0=0.004, k_{s1}=4.3 cm, RMSE=6.6, Z_n=0.261 m, Q_{exp}=110 l/s 233

Figure K-13 : Measured and computed surface velocity with S_0=0.001, k_{s1}=3.3 cm, RMSE=4.65, Z_n=0.13 m, Q_{exp}=20.55 l/s 233

Figure K-14 : Measured and computed surface velocity with S_0=0.001, k_{s1}=4.25 cm, RMSE=6.43, Z_n=0.261 m, Q_{exp}=55 l/s 234

Figure K-15 : Measured and computed surface velocity with S_0=0.055, k_{s2}=5.4 cm, RMSE=9.52, Z_n=0.0784 m, Q_{exp}=55 l/s 234

Figure K-16 : Measured and computed surface velocity with S_0=0.055, k_{s2}=4.4 cm, RMSE=10.66, Z_n=0.143 m, Q_{exp}=162.4 l/s 235

Figure K-17 : Measured and computed surface velocity with S_0=0.045, k_{s2}=4.8 cm, RMSE=11.1, Z_n=0.1062 m, Q_{exp}=87 l/s 235

Figure K-18 : Measured and computed surface velocity with S_0=0.045, k_{s2}=4.2 cm, RMSE=10.4 , Z_n=0.1507 m, Q_{exp}=162.6 l/s 236

Figure K-19 : Measured and computed surface velocity with S_0=0.025, k_{s2}=4.55 cm, RMSE=7.75 , Z_n=0.1238 m, Q_{exp}=86 l/s 236

Figure K-20 : Measured and computed surface velocity with S_0=0.025, k_{s2}=3.6 cm, RMSE=9.2, Z_n=0.175 m, Q_{exp}=160 l/s 237

Figure K-21 : Measured and computed surface velocity with S_0=0.015, k_{s2}=4.6 cm, RMSE=11.01, Z_n=0.1336 m, Q_{exp}=75 l/s 237

Figure K-22 : Measured and computed surface velocity with S_0=0.015, k_{s2}=3.3 cm, RMSE=8.74, Z_n=0.21 m, Q_{exp}=167.7 l/s 238

Figure K-23 : Measured and computed surface velocity with S_0=0.004, k_{s2}=4.65 cm, RMSE=8.5, Z_n=0.1586 m, Q_{exp}=51 l/s 238

Figure K-24 : Measured and computed surface velocity with S_0=0.004, k_{s2}=5.8 cm, RMSE=11.13, Z_n=0.2763 m, Q_{exp}=110 l/s 239

Figure K-25 : Measured and computed surface velocity with S_0=0.001, k_{s2}=4.3 cm, RMSE=10.83, Z_n=0.1365 m, Q_{exp}=20.55 l/s 239

Figure K-26 : Measured and computed surface velocity with S_0=0.001, k_{s2}=5.8cm, RMSE=12.33, Z_n=0.2763 m, Q_{exp}=55 l/s 240

Figure K-27 : Measured and computed surface velocity with S_0=0.055, k_{s3}=0.44 cm, RMSE=5.15, Z_n=0.0516 m, Q_{exp}=55 l/s 240

Figure K-28 : Measured and computed surface velocity with S_0=0.055, k_{s3}=0.53 cm, RMSE=4.85, Z_n=0.1031 m, Q_{exp}=162.4 l/s 241

Figure K-29 : Measured and computed surface velocity with S_0=0.035, k_{s3}=0.56 cm, RMSE=2.92, Z_n=0.0891 m, Q_{exp}=101.8 l/s 241

Figure K-30 : Measured and computed surface velocity with S_0=0.035, k_{s3}=0.55 cm, RMSE=4.02, Z_n=0.1185 m, Q_{exp}=159.1 l/s 242

Figure K-31 : Measured and computed surface velocity with S_0=0.015, k_{s3}=0.48 cm, RMSE=3.532, Z_n=0.0944 m, Q_{exp}=75.3 l/s 242

Figure K-32 : Measured and computed surface velocity with S_0=0.015, k_{s3}=0.4 cm, RMSE=6.12, Z_n=0.156 m, Q_{exp}=167.7 l/s 243

Figure K-33 : Measured and computed surface velocity with S_0=0.004, k_{s3}=0.5 cm, RMSE=8.1, Z_n=0.113 m, Q_{exp}=51 l/s 243

Figure K-34 : Measured and computed surface velocity with S_0=0.004, k_{s3}=0.57 cm, RMSE=5.54, Z_n=0.192 m, Q_{exp}=110 l/s 244

Figure K-35 : Measured and computed surface velocity with S_0=0.001, k_{s3}=0.49 cm, RMSE=4.68, Z_n=0.0977 m, Q_{exp}=20.55 l/s 244

Figure K-36 : Measured and computed surface velocity with S_0=0.001, k_{s3}=0.5 cm, RMSE=4.81, Z_n=0.192 m, Q_{exp}=55 l/s 245

Figure K-37 : Measured and computed surface velocity with S_0=0.055, k_{s4}=1.07 cm, RMSE=7.31, Z_n=0.1133 m, Q_{exp}=162.4 l/s 245

Figure K-38 : Measured and computed surface velocity with S_0=0.055, k_{s4}=1.25 cm, RMSE=5.166, Z_n=0.0599 m, Q_{exp}=55 l/s 246

Figure K-39 : Measured and computed surface velocity with S_0=0.035, k_{s4}=1.25 cm, RMSE=5.056, Z_n=0.132 m, Q_{exp}=159.1 l/s 246

Figure K-40 : Measured and computed surface velocity with S_0=0.035, k_{s4}=1.32 cm, RMSE=3.53, Z_n=0.1003 m, Q_{exp}=101.8 l/s 247

Figure K-41 : Measured and computed surface velocity with S_0=0.015, k_{s4}=0.9 cm, RMSE=6.51, Z_n=0.1723 m, Q_{exp}=167.7 l/s 247

Figure K-42 : Measured and computed surface velocity with S_0=0.015, k_{s4}=1.1 cm, RMSE=3.33, Z_n=0.1054 m, Q_{exp}=75.3 l/s 248

Figure K-43 : Measured and computed surface velocity with S_0=0.004, k_{s4}=1.5 cm, RMSE=4.17, Z_n=0.2194 m, Q_{exp}=110 l/s 248

Figure K-44 : Measured and computed surface velocity with S_0=0.004, k_{s4}=1.25 cm, RMSE=3.55, Z_n=0.1281 m, Q_{exp}=51 l/s 249

Figure K-45 : Measured and computed surface velocity with S_0=0.001, k_{s4}=1.55 cm, RMSE=4.25, Z_n=0.2194 m, Q_{exp}=55 l/s 249

Figure K-46 : Measured and computed surface velocity with S_0=0.001, k_{s4}=1.2 cm, RMSE=5.99, Z_n=0.1107 m, Q_{exp}=20.55 l/s 250

Figure K-47 : Measured and computed surface velocity with S_0=0.055, k_{s5}=2.1 cm, RMSE=6.7, Z_n=0.1254 m, Q_{exp}=162.4 l/s 250

Figure K-48 : Measured and computed surface velocity with S_0=0.055, k_{s5}=2.7 cm, RMSE=6.7, Z_n=0.067 m, Q_{exp}=55 l/s 251

Figure K-49 : Measured and computed surface velocity with S_0=0.035, k_{s5}=2.4 cm, RMSE=8.2, Z_n=0.1416 m, Q_{exp}=159.1 l/s 251

Figure K-50 : Measured and computed surface velocity with S_0=0.035, k_{s5}=2.15 cm, RMSE=10.25, Z_n=0.1082 m, Q_{exp}=101.8 l/s 252

Figure K-51 : Measured and computed surface velocity with S_0=0.015, k_{s5}=1.5 cm, RMSE=7.55, Z_n=0.1861 m, Q_{exp}=167.7 l/s 252

Figure K-52 : Measured and computed surface velocity with S_0=0.015, k_{s5}=2.2 cm, RMSE=7.55, Z_n=0.1151 m, Q_{exp}=75.3 l/s 253

Figure K-53 : Measured and computed surface velocity with S_0=0.004, k_{s5}=2.8 cm, RMSE=3.55, Z_n=0.2421 m, Q_{exp}=110 l/s 253

Figure K-54 : Measured and computed surface velocity with S_0=0.004, k_{s5}=2.4 cm, RMSE=4.6, Z_n=0.1405 m, Q_{exp}=51 l/s 254

Figure K-55 : Measured and computed surface velocity with S_0=0.001, k_{s5}=2.9 cm, RMSE=5.5, Z_n=0.2421 m, Q_{exp}=55 l/s 254

Figure K-56 : Measured and computed surface velocity with S_0=0.001, k_{s5}=2.2 cm, RMSE=2.1, Z_n=0.1212 m, Q_{exp}=20.55 l/s 255

Figure K-57 : Measured and computed surface velocity with S_0=0.055, k_{s6}=0.2 cm, RMSE=3.45, Z_n=0.0476 m, Q_{exp}=55 l/s 255

Figure K-58 : Measured and computed surface velocity with S_0=0.055, k_{s6}=0.3 cm, RMSE=2.25, Z_n=0.0943 m, Q_{exp}=162.4 l/s 256

Figure K-59 : Measured and computed surface velocity with S_0=0.035, k_{s6}=0.34 cm, RMSE=3.75, Z_n=0.0943 m, Q_{exp}=162.4 l/s 256

Figure K-60 : Measured and computed surface velocity with S_0=0.035, k_{s6}=0.23 cm, RMSE=4.1, Z_n=0.0805 m, Q_{exp}=101.8 l/s 257

Figure K-61 : Measured and computed surface velocity with S_0=0.015, k_{s6}=0.19 cm, RMSE=3.68, Z_n=0.144 m, Q_{exp}=167.7 l/s 257

Figure K-62 : Measured and computed surface velocity with S_0=0.015, k_{s6}=0.16 cm, RMSE=2.5, Z_n=0.084 m, Q_{exp}=75.3 l/s 258

Figure K-63 : Measured and computed surface velocity with S_0=0.004, k_{s6}=0.18 cm, RMSE=3.3, Z_n=0.1756 m, Q_{exp}=110 l/s 258

Figure K-64 : Measured and computed surface velocity with S_0=0.004, k_{s6}=0.16 cm, RMSE=5, Z_n=0.1037 m, Q_{exp}=51 l/s 259

Figure K-65 : Measured and computed surface velocity with S_0=0.001, k_{s6}=0.18 cm, RMSE=2.75, Z_n=0.1755 m, Q_{exp}=55 l/s 259

Figure K-66 : Measured and computed surface velocity with S_0=0.001, k_{s6}=0.18 cm, RMSE=3.9, Z_n=0.0898 m, Q_{exp}=20.55 l/s 260

Figure M-1 : Flood plain Pitot tube measurements in smooth compound channels with Z=0.251m, Q=0.102 m^3/s and S_0=0.001..... 263

Figure M-2 : Flood plain Pitot tube measurements in smooth compound channels with Z=0.238 m, Q=0.102 m^3/s and S_0=0.002..... 264

Figure M-3 : Flood plain Pitot tube measurements in smooth compound channels with Z=0.225 m, Q=0.166 m^3/s and S_0=0.01..... 264

Figure M-4 : Flood plain Pitot tube measurements in smooth compound channels with Z=0.220 m, Q=0.166 m^3/s and S_0=0.015..... 265

Figure M-5 : Flood plain Pitot tube measurements in smooth compound channels with Z=0.193 m, Q=0.166 m^3/s and S_0=0.02 265

Figure N-1 : Flood plain Pitot tube measurements in all bed rough compound channels with Z_n=0.211 m, Q=0.16 m^3/s and S_0=0.035 267

Figure N-2 : Flood plain Pitot tube measurements in all bed rough compound channels with Z_n=0.213 m, Q=0.15 m^3/s and S_0=0.03 267

Figure N-3 : Flood plain Pitot tube measurements in all bed rough compound channels with Z_n=0.199 m, Q=0.1 m^3/s and S_0=0.02 268

Figure N-4 : Flood plain Pitot tube measurements in all bed rough compound channels with Z_n=0.198 m, Q=0.074 m^3/s and S_0=0.01 268

Figure N-5 : Flood plain Pitot tube measurements in all bed rough compound channels with Z=0.222 m, Q=0.0635 m^3/s and S_0=0.004 269

Figure N-6 : Flood plain Pitot tube measurements in all bed rough compound channels with Z=0.209 m, Q=0.0505 m^3/s and S_0=0.002 269

Figure O-1 : Flood plain Pitot tube measurements in all bed rough compound channels with Z=0.197 m, Q=0.16 m^3/s and S_0=0.025 271

Figure O-2 : Flood plain Pitot tube measurements in all bed rough compound channels with Z=0.204 m, Q=0.147 m^3/s and S_0=0.02 271

Figure O-3 : Flood plain Pitot tube measurements in all bed rough compound channels with Z=0.206 m, Q=0.1 m^3/s and S_0=0.008 272

Figure O-4 : Flood plain Pitot tube measurements in all bed rough compound channels with Z=0.235 m, Q=0.1m^3/s and S_0=0.004……..…….272

Figure O-5 : Flood plain Pitot tube measurements in all bed rough rough compound channels with Z=0.245 m, Q=0.1 m^3/s and S_0=0.002…..…….....…273

LIST OF SYMBOLS

f	Friction factor
F_r	Froude number
f_m	Viscous damping function
f_w	Viscous damping function for solid walls
f_s	Viscous damping function for free surface
g	Gravitational attraction
K	Surface velocity index
k	Rib side length
k_s	Absolute roughness height
k_t	Turbulent kinetic energy
l_m	Mixing length
l_v	Volumetric mixing length
L	Travel distance
n	Manning resistance coefficient
Q	Discharge
R	Similarity index
Re	Reynolds number
R_h	Hydraulic radius
S_0	Channel bed slope
$S_{i,j}$	Rate of strain
S_f	Energy slope
t	Time
T	Free surface width
u	Velocity in flow direction
u_τ	Local shear velocity
v	Velocity in transverse direction
V	Average flow velocity
w	Velocity in vertical direction
x	x axis in Cartesian coordinate system
y	y axis in Cartesian coordinate system
z	z axis in Cartesian coordinate system

Z	Flow depth (used in general sense)
z_m	Axis of water depth starting from mean bed
Z_n	Normal depth (uniform depth)
Θ	Angle of channel bed with horizon
Δx	Distance between two sections of different depth in GVF
ν	Kinematic viscosity
$\delta_{i,j}$	Kronecker delta
κ	Karman constant
λ	Rib spacing
ψ	Stream function
τ	Turbulent kinematic stress
ε	Turbulence kinetic energy dissipation rate
ξ	Vorticity

CHAPTER 1

INTRODUCTION

1.1 Problem description

Flow measurement in open channels is of great significance in many engineering applications. For many years classical devices such as propellers, current meters, obstructions, dye injection analysis and sometimes rating curves have been used for discharge measurement. Acoustic Doppler Velocimetry (ADV) has also been successfully tested for flow measurement with complicated flow patterns (Oberg and Schmidt, 1994). The disadvantages of the mentioned techniques are that they are labor intensive, time consuming and contribute to high costs especially in ADV.

In the recent decade, local remote sensing by radar and monitoring of the rivers with visible imaging systems have emerged with the hope of reducing the costs and operation time. Satellite remote sensing offers possibilities in indicating the stage of the large rivers. The data collected by the satellite is later on used together with altimeter information to identify the stream discharge (Koblinsky et al., 1993; Vorosmarty et al., 1996). Other investigations on non-contact radar techniques (Costa et al., 2000; Plant et al., 2005; Melcher et al.,2002; Costa et al., 2006) address the surface velocity measurement through wave propagation on the free-surface that is used to estimate river discharge within a reliable range of accuracy. In general, non-intrusive methods are much more practical and convenient to automatically collect more accurate data.

The present research is mainly about discharge measurement in open channels using a combination of imagery and computational techniques. The free surface velocity in open channels is under special attention in this study. Surface velocity carries valuable

information in terms of providing tools for discharge estimation. Moreover, surface velocity beholds the signature of channel bed roughness.

This research is meant to provide practicalities of discharge measurement by non-contact tools using free surface velocity. This aim needs to be fulfilled by analyzing turbulent open channel flows with emphasis given to free surface velocity. The method of free surface velocity measurement comes from image processing analysis. A major question of the research is to learn whether bed roughness can be estimated in addition to discharge calculation at once. The study seeks an answer to the stated question throughout a set of numerical and experimental attempts.

In this chapter, the previous studies and their historical backgrounds related to image processing techniques and non-contact discharge measurement are presented. Finally, the research objectives are re-stated with simple and further discussion.

1.2 Literature survey on video imagery techniques (PIV, PTV and LSPIV)

1.2.1 PIV (Particle Image Velocimetry) & PTV (Particle Tracking Velocimetry)- After Adrian (1991)

PIV is a technique where the whole flow field is visualized (measured) at a multitude of points by seeding it with suitable tracer particles, illuminating these particles with a proper source of light, obtaining images of these particles on photographic film or a video array detector, transferring these images to a computer, and using suitable computational algorithms and procedures to deduce the velocity field and related information. If the particle images are digitally acquired and stored, using a high-speed digital camera, rather than recorded on conventional photographic film, then this technique is sometimes referred to as digital particle image velocimetry (DPIV) (Willert and Gharib, 1991).

Thus, particle image velocimetry or PIV is an optical and computational method used to determine the instantaneous velocity field of the fluid.

The main purpose of the imaging technique in velocity calculation is to measure the displacement of marked regions of the flow by observing the location of the images of the markers at two or more times. The measurement of marker displacements between two

consecutive images is made on small regions named as interrogation areas (IA), within the imaged area using a statistical approach. The velocity vector for each interrogation area is then determined by dividing the displacement by the time interval between the successive recordings. The final vector field is achieved by repeating the same image analysis for each interrogation area contained in the field of view.

PIV and PTV measure velocities non-intrusively, but a fundamental requirement is that the flow has to be marked (traced) by appropriately selected particles in most of the situations. The particles should be light enough to follow nearly completely the flow features to be measured, and large enough to be resolved by the imaging device of the PIV system.

The selection of the proper algorithm for image processing is decided by tracer concentration in the flow field. When the tracer concentration is low, individual particles dominate the field, therefore, it is feasible to measure the displacement of these particles individually. This low-image-density mode is referred to as particle-tracking velocimetry (PTV). When the flow tracer concentration is high (but not so high that the particles' overlap leads to patterns' disappearance), a more common approach is to measure the displacement of small groups of particles (patterns) restrained inside an interrogation area where a velocity vector is going to be calculated and assigned for. In this case it is assumed that the group of particles does not change their relative position and configuration considerably in the time interval between images. This high-image-density mode is labeled as particle image velocimetry (PIV). In PIV, particle and background images within an interrogation area are equally important, but in PTV method, individual particles are identified first and then velocity vectors are calculated.

1.2.2 LSPIV (Large-Scale Particle Image Velocimetry)

Large-Scale Particle Image Velocimetry (LSPIV) is an extension of same PIV imaging technique but in larger measuring field such as riverine environment (Fujita et al., 1998). While the LSPIV algorithm for estimating velocities are the same with those used in conventional high-density image PIV (Adrian, 1991), special treatment is needed for flow illumination, flow tracing, and removal of the spatial distortion of the recorded images due to lens aberrations and imaging at oblique angles.

LSPIV history is traced back to when an image-based technique was proposed by Fujita and Komura (1994) and Aya et al. (1995) as an alternative method to river flow monitoring. The technique was capable of effectively determining flow quantities in the plane of the water free surface. The technique combined conventional Particle Image Velocimetry (PIV) concepts with pre-processing procedures for eliminating the image distortion generated by the oblique recording angle and correcting them for distortion introduced by camera lens. The technique was firstly applied to field conditions by Fujita et al. (1997) for measuring flood discharge in the Yodo River (Japan). Later on, the technique was labeled large-scale particle image velocimetry (LSPIV) taking into account the large size of the imaged area (Fujita et al., 1998). PIV is frequently used as a generic name for all imaging techniques including PTV and LSPIV.

1.2.3 PIV developing history

PIV scheme for analyzing images must first be defined before giving further definitions. The algorithm for image processing is directly related to illuminating and recording procedures; i.e., single-frame recording, where several exposures are superposed on the same frame, or multiple framing, where each frame contains only one image exposure. The important advantage of the latter procedure is that the direction of flow motion is fully determined, as opposed to the first approach where costly devices are needed to determine flow direction. The most important adjustable variable for the illumination-recording sequence is the time separation between the exposures. It determines the maximum and minimum velocity that can be measured.

The first scheme is single-frame multiple exposures recording which is associated with Young’s fringe analysis method. The method of image analysis initially adopted in speckle and high image density PIV was the one used in speckle metrology. An 'interrogation' region of the double-exposure image (one photo with pair of images) of the flow was illuminated by a low-powered laser beam. The image pairs acted as interfering point sources, with the transmitted light forming Young's fringes. The transparency and the plane on which the fringes were being observed were arranged to be in the principal focal planes of a converging lens, so that the fringe pattern was an accurate Fourier transform of the phase and the amplitude of the transmitted light from the interrogation region (Goodman, J. W.,

1968). Fourier Transform is used to convert images from the spatial domain into the frequency domain. The spatial frequency domain is interesting because: 1) it may make explicit periodic relationships in the spatial domain, and 2) some image processing operators are more efficient or indeed only practical when applied in the frequency domain.

The amplitude and orientation of the fringe spacing was used to infer the image displacements. Linear direction searching methods were, at first, used to determine fringe direction.

The second primary scheme is single exposure multiple frame recording. In multiple framing, where each frame contains only one image exposure, particle displacements are usually determined by statistical means, most often, computing two-dimensional correlation on pairs of images. A significant increase in computational efficiency is gained by calculating the correlation coefficients in the frequency domain by using fast Fourier transforms (Adrian, 1991; Willert and Gharib, 1991).

This scheme which consists of the correlation methods is itself identified by three subcomponents, namely Auto correlation, cross correlation and optical correlation analysis.

Autocorrelation has been traditionally used in high-image-density flow situations. In autocorrelation it is analyzed how similar, or correlated, is a recorded image with an identical copy of itself which has been displaced with an unknown distance. Because the autocorrelation function is symmetrical, the direction of the displacement cannot be obtained from the statistical analysis. Directional ambiguity is resolved by artificially shifting the image position between exposures using software (electronic shifting) or hardware devices (rotating mirror, polygon scanner, birefringent crystal). Further technical details of the method has been documented in Grant. I, (1997).

Cross-correlation is commonly used in low-density-image (PTV) mode where it is easy to match the pair for individual particle images. Cross-correlation is computed between an interrogation area in the first image and interrogation areas within a search region in the second image. The pair of particles showing the maximum cross-correlation coefficient is selected as a candidate vector. Cross-correlation can be also used as an alternative algorithm for high-image-density (PIV) mode (Stevens and Coates, 1994; Utami et al., 1991).

For Optical correlation analysis, related information can be found in Grant. I, 1997 and Adrian, 1991).

1.2.4 PTV developing history

As observed by Adrian (1991), PTV is traced back to flow-visualization techniques such as particle-streak photography and stroboscopic photography (Van Dyke, 1982). In modern PTV, the quantitative results are obtained through using computerized analyses of the seeded images. PTV is known to be effective for examining flows with large velocity gradients, a condition that is reported to pose problems for conventional PIV methods (Huang et al., 1993a and 1993b).

Two well-established PTV algorithms are the four-frame in-line tracking method (Kobayashi et al., 1989; Hassan and Canaan, 1991) that makes use of four consecutive frames of the tracked particles, and the binary image cross-correlation algorithm (Uemura et al., 1989), which uses only two consecutive frames. In the four-frame tracking method, the displacement of the particles is determined frame-by-frame, while evaluating the geometrical consistency of each seed path.

Typically, an iterative scheme is used to decide the best-match particle trajectory, involving extrapolation of the particle displacement and looking for the nearest neighbor. On the other hand, the binary image cross correlation technique is considered as a variation of the standard cross-correlation PIV, in which the correlation functions are computed for each interrogation window centered on the first frame of particles using an adaptive shifting scheme.

Additional two-frame algorithms that employ a particle- cluster matching concept have been suggested (Okamoto et al., 1995, Ishikawa et al., 1997). In this method, particles from the first and second frames are conceived to be creating a cluster with their respective neighboring particles, and the selection of the best match particles is carried out on the basis of a deformation index defined for the relationship between the clusters in the two frames. Another two-frame method is based on the use of a suitable cost function in particle tracking algorithms. An example is the algorithm proposed by Ohyama et al. (1993), in which the best-match particle pairs are identified by using a fitness function that reduces the total sum

of the squares of particle displacements to minimum. The neural network PTV proposed by Labonté (1999) can also be categorized among this set of algorithms. Although time consuming, this algorithm seems more efficient and reliable in identifying and tackling unpaired particles between the consecutive frames.

1.3 Literature survey on nonintrusive stream gauging using imaging technique

Image based water surface velocity measurement and consequently discharge estimation by a suitable method is a potential alternative to stream gauging in open channels. Particle Image Velocimetry (PIV) is a very powerful technique to obtain velocity vector fields in any plane of motion. Technique is based on identifying and describing the motion of tracer particles in digitized video records. The only cost-effective, quick, simple and nonintrusive way of discharge assessment, for certain stream monitoring situations, is digital imaging system in which Particle Image Velocimetry (PIV) is used to make free-surface velocity measurement and make use of this velocity for further analysis. Image-based discharge measurement in gravity driven streams is the act of calculating discharge by measuring surface velocity and analyzing it accordingly.

Ever since the seminal work of Fujita et al. (1998), the application of the Particle Image Velocimetry (PIV) technique to large-scale (LSPIV) parts of the free-surface of flumes and field open-channel flows has been disseminated widely and successfully in the hydraulic research and engineering circle.

The velocity obtained by LSPIV in this approach is then analyzed to yield the discharge. So far, researchers have mostly been calculating discharge through the classical velocity-area concept. In this method, the mentioned free surface velocity is combined with a velocity index (usually K=0.85 by Rantz, 1982) to yield the mean depth averaged velocity which is then integrated over the entire bathymetry and yields the discharge. In this method, for the surveyed bathymetry, velocity distribution is assumed to be either logarithmic or parabolic. The so-called “velocity index” is itself dependent on other variables such as channel geometry, bed roughness and turbulence level and its features are not fully understood and is still a topic to debate among hydraulics’ community.

Fujita et al. (1998), Bradley et al. (2002) and Creutin et al. (2003) furthermore developed and industrialized the Large Scale Particle Image Velocimetry (LSPIV) method to track the motion of either objects or patterns on the water surface to estimate the free-surface velocity. The Large-Scale PIV (LSPIV) involves five steps: illumination, seeding, recording, ortho-rectification and processing (Muste et al., 2009).

Sometimes natural tracers such as foams and turbulent structures on the water surface have been used as tracers (Adam et al., 2012). But often, under normal flow conditions, in devoid of natural tracers (Fujita et al. 1998), artificial tracers (seeding) have been obligatory for PIV analysis (Fujita and Hino 2003; Jodeau et al. 2008; Kim et al. 2008).

Following the LSPIV evolution, experimental systems for real-time discharge estimation were designed to make continuous and fast discharge measurements at the field in the real time (Hauet et al., 2008, Adam et al., 2012).

As already stated, conventional methods and instruments for stream gauging measurement involve deployment in the river with a boat or sensors. The high operational hazards involved in the deployments of boats and equipment during extreme flows limits the practicality of these methods. Remote methods are safer and easier options for measuring flood discharge. An alternative is to record images of the flow free surface from shore or from the air. Also, video recording provides the opportunity for monitoring the lateral extension of the river due to flooding.

In literature, Muste et al. (2011) has explored the extent to which LSPIV can be used to measure discharge in normal and extreme flow conditions. Among few researches on river gauging by PIV under extreme conditions, Jodeau et al. (2008) and Le Coz et al. (2010) have applied LSPIV to measure discharge for dam releases and flash floods, respectively. Findings of their researches have validated the use of LSPIV. In Coz et al.'s (2010) research for example, discharges ranging from 300 to 2500 m^3/s with LSPIV means were proven to be usually in acceptable agreement (<20%) with the rating curves. By contrast, technical challenges and sources of errors have often been reported. Dramais et al. (2011) successfully deployed LSPIV during a reservoir flashing and a flood event with a return period of 10 years. The multiplicative error induced by the velocity coefficient was confirmed to be a major source of error. Muste et al. (2009) made the measurement and mapping of the flow distribution during floods and in the vicinity of hydraulic structures. While the result of their

research was not exhaustive, they intended to illustrate that LSPIV can quickly and safely take measurements in natural-scale streams for providing comprehensive, quantitative flow information over a wide range of flow types (uniform, non-uniform) and measurement conditions (e.g., floods, low, shallow flows) with minimum or no site preparation at all.

The latest reports on LSPIV conduction with similar functions to earlier studies are also described in the following papers: Zang et al., (2013), Tauro et al., (2015) and Hauet et al., (2014).

1.4 Literature survey on nonintrusive stream gauging by computational tools

In spite of numerous studies revolving around stream gauging by free surface velocity measurement, there are few available reports of combined use of computational techniques (or CFD) and non-intrusive methods for the desired purpose. In such cases, simulating dip phenomenon and formulation of flow resistance becomes an important subject.

Total flow resistance may be divided into two components from modeling point of view as boundary resistance and channel resistance. Boundary resistance is the friction acting along the channel wetted surface mainly due to wall roughness elements. Channel resistance is a combination of drag forces on vegetation extending into upper layers of flow and resistance due to non-uniformities as a result of cross-section or alignment changes.

As for the general roughness parameter, beside CFD approach, Manning roughness coefficient is a famous value widely used in hydraulic community for general resistance representation. The coefficient is used in Manning relation for discharge computation. However, its estimation in natural environment is not an easy task as it is dependent on many factors such as height, shape and spacing of surface roughness elements and channel irregularities. Many empirical methods have so far made suggestions on its value estimation (Urquhart, 1975), but usually this coefficient is determined according to characteristic size of the boundary particles and distribution of particle size on the river bed.

On CFD side of debate, some studies in literature have reported the inverse speculation of resistance parameter using CFD methods. Ramesh et al., (2000) has made this attempt possible by embedding an optimization model inside CFD solver in unsteady flow condition. Unsteady condition is most suitable due to availability of data in different gauging stations.

Nevertheless, in this report discharge was an input to the solver. Bradley et al. (2002) has made use of free surface velocity as input to a hydraulic model which solves for conservation of mass equation. As a result, three dimensional velocity in the flow filed is obtained and used to calculate discharge. A non-intrusive discharge measuring technique based on CFD solutions is also introduced by Baud et al. (2005). The water surface is recorded to determine the geometry and the velocity field of the free surface. A commercial finite element program was employed to compute the three-dimensional velocity field using the free surface data as boundary conditions.

The dip phenomenon, on the other hand, is an important factor that controls the surface velocity distribution by pulling the high momentum central areas of flow cross section towards the corners. Although its effect comes into picture only under certain flow conditions (such as in flow inside narrow channels), the earlier mentioned studies have not made attempt to take into consideration the effect of secondary currents as a result of dip existence. Computational approach can be successful if the turbulence structure of the flow field is appropriately described by correctly simulating turbulence driven secondary currents. Such an attempt has been made by using a Non-linear Mixing Length Model (NMLM) (Aydin, 2009). In this research, channel resistance is assumed absent, the quantity of water that can be carried in a channel then is solely determined by boundary resistance acting from the wall against the fluid. For uniform flow conditions in a prismatic channel of known cross-section and bed slope, there is a unique velocity field that can be obtained by solving the governing differential equations combined with an appropriate turbulence closure. Velocity at the free surface is computed at last as a result of general solution which reflects all hydrodynamic characteristics of the solution domain. The velocity integration over the area of cross section is the discharge. The present study has made extensive use of this last paper concept with major modifications to the solver that are to be explained in the next section.

1.5 Research objectives and problem overview

The present research is committed to address several major issues. To improve the understanding of discharge measurement over rough open channels is the primary objective

of this study. In order to reach this ultimate goal, several obstacles are further down on the way that will need to be paid attention.

As the title of the thesis implies, in the first phase, for stream gauging, water free surface velocity is to be measured for a variety of different flow conditions. Among limited alternatives for the desired purpose, digital imaging technique is adopted. While photography is employed for the velocity measurement, certain considerations should be taken into account. The optical distortion introduced into the pictures due to the wide lens of the camera should be checked to see if image un-distorting by camera calibration is necessary. Furthermore, if shooting has to be through an oblique angle to cover more of the flow field- for instance- spatial image correction is to be implemented on the photos. Finally, for the analysis of surface velocities in hand and before making use of them for discharge computation, error investigation will be performed on the data. According to the observations, laboratory experiences and obtained knowledge of the technique, relevant recommendations and remarks will have to be made with regard to several issues. These technical issues can revolve around tracer particle size and type, travel distance of particles, lighting condition of the laboratory, recording speed of the videos, camera position and any possible link between all the named factors.

In the second phase, mathematical model of the flow has to be scrutinized. The mathematical model of this uniform open channel flow in prismatic channels is the numerical solution of governing equations of motion. There are certain problems tied with current version of the numerical model such as uncertainties in obtaining correct surface velocity distribution in addition to locating the position of the maximum velocity underneath surface (or dip phenomenon). Once the free surface velocity distribution is calibrated in this numerical model using experimental data, next step would be to move the focus to rough channels. Generally, when adequate input data is provided for the CFD model, it can be run to integrate the velocity over the cross section of the flow to yield the discharge. Usually, input data that is known a prior is the channel bed slope, cross section information and sometimes wall roughness. In devoid of wall roughness, experimental surface velocity can be used as additional data for the CFD solver instead of wall roughness. The invers solution in which wall roughness estimation can be possible is the application of optimization model to CFD solver in search for wall roughness using surface velocity. Therefore, an

optimization model is considered to perform searches that ultimately finds the true wall roughness beside discharge.

Even though many open channels are approximated as rectangle, the final attempt of the research is to perform same kind of analysis for compound channels. The compound channels are sometimes a good representation of flood time flow situation with a main channel and a flood plain in the side bank.

In second chapter, experimental set up has been manifested. All the flow conditions of the experiments are presented. Moreover, information related to camera calibration and image re-construction are given. In third chapter, numerical model has been demonstrated with down to detail parametric descriptions. The mesh quality has been determined for consistency of simulations. In chapter four and five, the result of analysis on rectangular and compound channels are discussed, respectively. The mainstream analysis are discharge and solid boundary roughness determination.

CHAPTER 2

EXPERIMENTS

2.1 Experimental set up

2.1.1 Flume

The experimental setup consists of a 12 m long tilting channel with a width of 60 cm and a depth of 35 cm. The three surfaces (sides and bottom) are made up of glass. The channel is supported by a steel structure connected to a reservoir in the upstream end. The downstream end of the channel is a free fall where water discharges back into turning channels and from there to underground pool. A variable height weir has been designed at the downstream end of the channel to manipulate the water surface profile at subcritical flow conditions. Water is recirculated via a pump having discharge capacity of around 170 l/s. The schematic figure of the set-up is depicted in Figure 2-1 below.

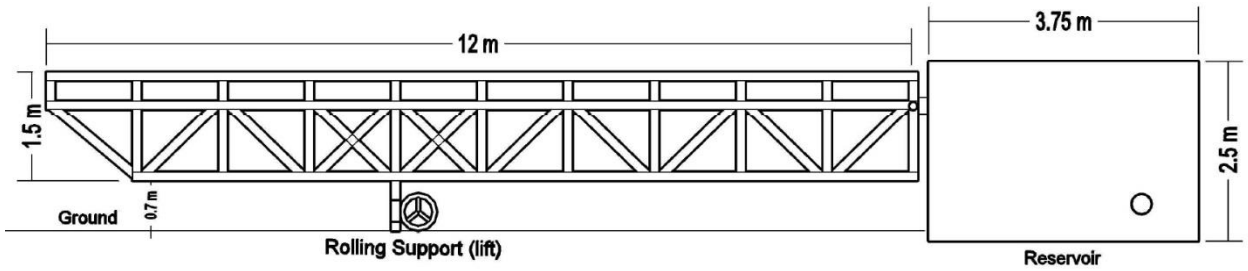

Figure 2-1: The schematic view of the set-up

The channel is supported by a pin at the reservoir side and a jack at 2/3 of the length as shown. At the location of rolling support, there is the lift (shown in Figure 2-2) to adjust the channel slope.

Figure 2-2 : The jack

Height of the channel is determined from a Vernier attached at the end to set for the desired slope. At the inlet to the channel there are several vertical parallel screens arranged to subside the fluctuations generated at the water surface. In addition, a glass plate parallel to water surface is used at the channel entrance to smoothen the surface waves.

A camera holder is constructed as seen in Figure 2-3.

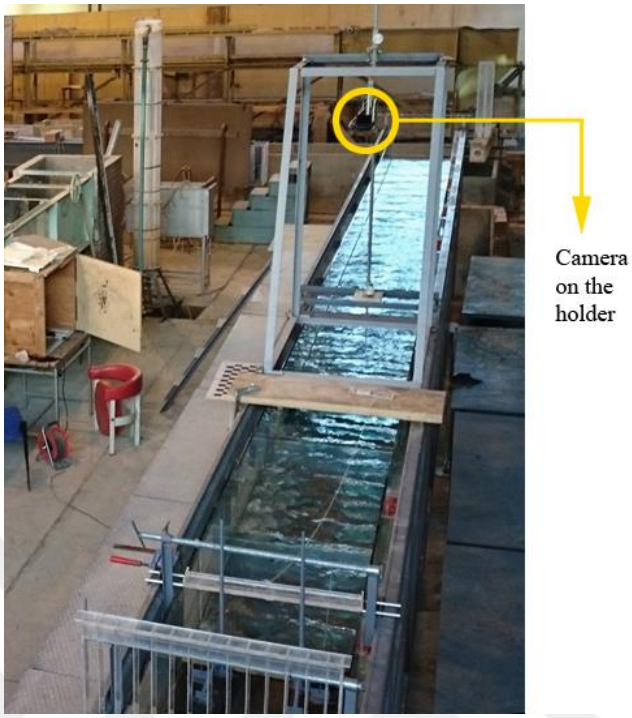

Figure 2-3 : Camera holder mounted on the canal

The holder is designed to roll along the channel to make the recording possible in different working sections. The camera mounted on the frame is about 1.5 m above the free water surface. This height is enough to eliminate the need for image correction due to camera lens distortion introduced into video records (this will be proven in next sections).

The cross section of the channel was initially rectangle (with 60 cm width and 35 cm height). A different section was also constructed to model compound channels by placing a void box inside the main channel. The dimensions of the box are shown in the Figure 2-4.

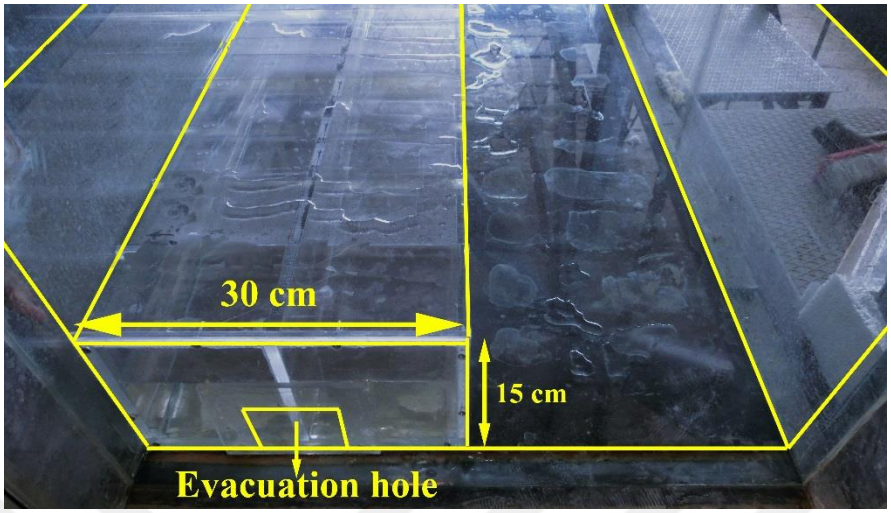

Figure 2-4 : Dimensions of the box that models the compound channel

The box holds an evacuation lid to discharge the excess water to avoid alga formation after the experiments are over.

The discharge is read through a magnetic flowmeter shown in Figure 2-5.

Figure 2-5 : Magnetic flowmeter

The given discharge by magnetic flowmeter was compared to weir discharge just to make sure the machine is correctly calibrated and is measuring the true discharge values. For this purpose, channel downstream plate was raised to form a weir with the channel bed slope adjusted to zero. The result of calibration is shown in Figure 2-6.

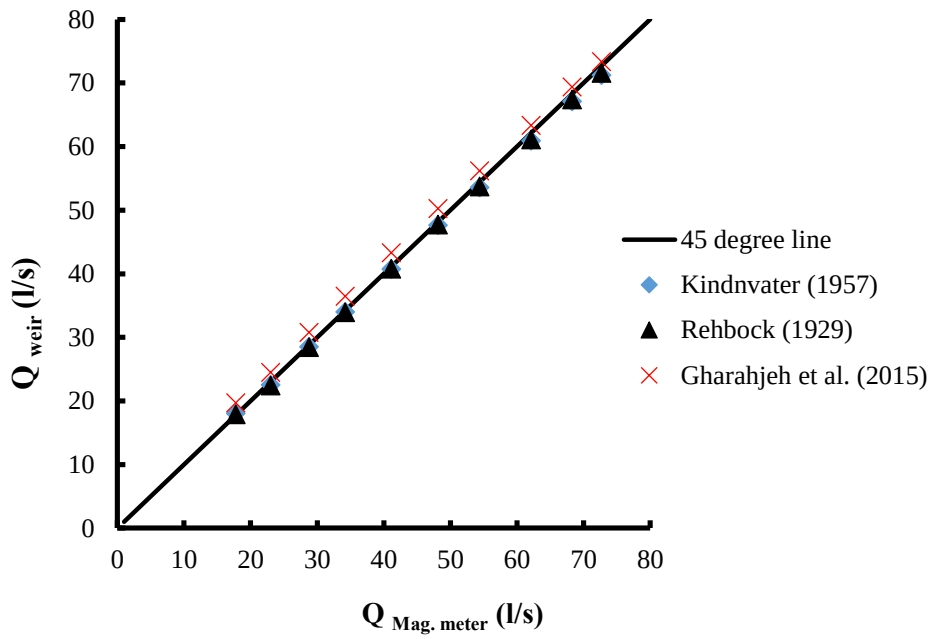

Figure2-6 : Magnetic flowmeter calibration

2.1.2 Roughness geometry

For experimental simulation of rough open channels, roughness elements were placed on the bed of the channel. Two major types of roughness tried were two dimensional regular transverse square bars and bubble wrap seen in Figure 2-7 below.

Figure 2-7 : Two different roughness types seen on the channel bed

The bubble wrap type roughness on the left of the Figure 2-7 is the commercially available sheet used to cover the fragile commodity (this roughness type was tried for rectangular channels only). The square-rib roughness on the right in Figure 2-7, is constructed by placing of consecutive ribs side by side in the stream wise direction. Schematic figure of the rib type roughness is demonstrated in Figure 2-8.

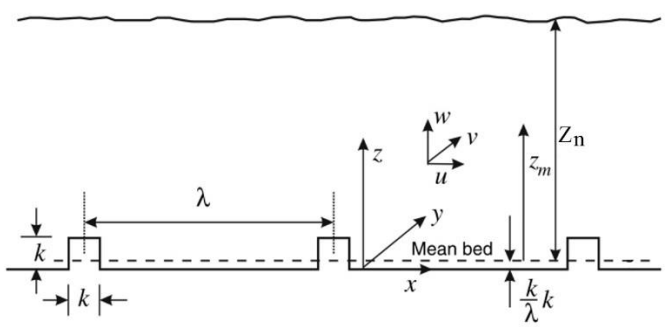

Figure 2-8 : Schematic view of the rib type roughness

In Figure 2-8, k is the rib cross section dimension, λ is the rib spacing, Z_n is uniform water depth and z_m is the water depth axis from mean bed elevation. The velocity components are also defined as u,v and w where u is the stream wise velocity and the other v and w are cross

wise velocity components. Similarly, x will be the axis in the direction of flow, y the axis in transverse direction and z is the vertical axis in opposite direction to the gravity.

It ıs important to note here that in the rest of this piece of writing, Z_n has been used as normal water depth either on smooth or rough channels. Normal water depth is called as such when flow reaches uniformity.

The details of these roughness types are presented in table 2-1.

Table 2-1: Roughness types studied for rectangular channels

Roughness type	Roughness type	Manning coefficient ($s/m^{1/3}$)	Rib spacing (cm)	Rib dimension (cm)	Bubble diameter (cm)	Bubble height (cm)
1	Square ribs (k_{s1})	0.0165	20	1 x 1	-	-
2	Square ribs (k_{s2})	0.0252	10	1 x 1	-	-
3	Square ribs (k_{s3})	0.0159	40	0.6 x 0.6	-	-
4	Square ribs (k_{s4})	0.0190	20	0.6 x 0.6	-	-
5	Square ribs (k_{s5})	0.0218	10	0.6 x 0.6	-	-
6	Bubble warp (k_{s6})	0.0140	-	-	1	0.3

In Table 2-1, k_s is the absolute roughness representative. The Manning coefficient appearing on Table 2-1 has been calculated via using simple Manning relation by consideration of experimental observations (such as flow uniformity, discharge, flow depth and channel bed slope).

$$n=\frac{A\sqrt{S_0}}{Q}R_h^{\frac{2}{3}} \tag{2.1}$$

Equation (2.1) is used for calculation of Manning coefficient. In this equation, A is the area of channel cross section, S_0 is channel bed slope, Q is flow discharge and R_h is the hydraulic radius.

For compound channels, only the square rib roughness type was constructed. The configuration of the roughness for compound channel was similar to roughness type 5 in rectangular channels (0.6 cm in 0.6 cm rib cross section dimension with 10 cm of rib spacing). However, in compound channels roughness was once placed only at the floodplain and another time all over the bed. In Figure 2-9, floodplain rough compound channel is shown on the left and all bed rough case on the right.

Figure 2-9 : Floodplain rough (left picture) and all bed rough (right picture) compound channel

2.2 Flow conditions

The experiments can be divided into five major categories: flow over (a) smooth rectangular channels, (b) flow over rough rectangular channels, (c) flow over smooth compound channels, (d) flow over floodplain rough compound channels and (e) flow over all bed rough compound channels. All experiments have undergone a water surface profile collection. The experiments are mostly for surface velocity measurement by image processing. Moreover, velocity profile at vertical sections has sometimes been collected.

2.2.1 Flow over smooth rectangular channels

The experiments conducted on smooth rectangular channels were used for investigation of multiple aspects. The initial problem dealt with uniform flow generation that calls for conduction of measurements on different flow conditions in order to map the water surface profile. The experiments can be useful in Manning roughness coefficient determination and therefore uniform flow generation. Table 2-2 gives the details of flow conditions for surface profile plotting.

Table 2-2 : Flow conditions of surface profile recordings in smooth rectangular channel

Exp. No.	S_0	Q (m^3/s)	Z_n (m)	$Z_{critical}$ (m)	U (m/s)	F_r
1	0	0.173	...	0.204	-	-
2	0.002	0.172	0.220	0.203	1.30	0.88
3	0.004	0.172	0.170	0.200	1.68	1.30
4	0.008	0.172	0.130	0.200	2.20	1.95
5	0.015	0.172	0.110	0.203	2.61	2.51
6	0.020	0.171	0.100	0.203	2.85	2.88
7	0.025	0.171	0.094	0.202	3.04	3.16
8	0.030	0.171	0.088	0.202	3.24	3.49
9	0.035	0.172	0.084	0.203	3.42	3.77
10	0.040	0.172	0.081	0.203	3.54	3.98
11	0.045	0.172	0.077	0.203	3.73	4.29
12	0.050	0.172	0.075	0.203	3.83	4.47

Major experiments in smooth rectangular channels start with the formation of uniform flow. For several flow conditions shown in Table 2-3 through Table 2-12, conducted experiments have been used for surface velocity measurements by image processing, proposal of PTV remarks in this unique laboratory situation and numerical solution calibration (artificial roughness inclusion to numerical solver for calibrating it according to experimental results).

Table 2-3 : Smooth rectangle channel experiments for bed slope of 0.001

S_0	$Q(m^3/s)$	$Z_n(m)$	F_r
0.001	0.0129	0.05	0.61
0.001	0.0681	0.15	0.62
0.001	0.0954	0.19	0.61
0.001	0.1245	0.23	0.60
0.001	0.1472	0.26	0.59
0.001	0.1706	0.29	0.58

Table 2-4 : Smooth rectangle channel experiments for bed slope of 0.002

S_0	$Q(m^3/s)$	$Z_n(m)$	F_r
0.002	0.0129	0.04	0.85
0.002	0.0308	0.07	0.88
0.002	0.0530	0.10	0.89
0.002	0.0872	0.14	0.88
0.002	0.1153	0.17	0.87
0.002	0.1657	0.22	0.85

Table 2-5 : Smooth rectangle channel experiments for bed slope of 0.004

S_0	$Q(m^3/s)$	$Z_n(m)$	F_r
0.004	0.0115	0.03	1.17
0.004	0.0344	0.06	1.24
0.004	0.0640	0.09	1.26
0.004	0.0984	0.12	1.25
0.004	0.1363	0.15	1.24
0.004	0.1632	0.17	1.23

Table 2-6 : Smooth rectangle channel experiments for bed slope of 0.008

S_0	$Q(m^3/s)$	$Z_n(m)$	F_r
0.008	0.0162	0.030	1.66
0.008	0.0366	0.050	1.73
0.008	0.0617	0.070	1.77
0.008	0.0905	0.090	1.78
0.008	0.1306	0.115	1.78
0.008	0.1654	0.135	1.77

Table 2-7 : Smooth rectangle channel experiments for bed slope of 0.015

S_0	$Q(m^3/s)$	$Z_n(m)$	F_r
0.015	0.022	0.030	2.27
0.015	0.050	0.050	2.38
0.015	0.075	0.065	2.41
0.015	0.103	0.080	2.43
0.015	0.146	0.100	2.28
0.015	0.167	0.110	2.28

Table 2-8 : Smooth rectangle channel experiments for bed slope of 0.025

S_f	S_0	$Q(m^3/s)$	$Z_n(m)$	F_r
-	0.0250	0.015	0.02	2.82
-	0.0250	0.045	0.04	3.01
-	0.0250	0.086	0.06	3.10
0.0205	-	0.121	0.08	2.85
0.0171	-	0.160	0.10	2.69

Table 2-9 : Smooth rectangle channel experiments for bed slope of 0.035

S_f	S_0	$Q(m^3/s)$	$Z_n(m)$	F_r
-	0.0350	0.0177	0.020	3.31
-	0.0350	0.0537	0.040	3.57
0.0273	-	0.1017	0.065	3.26
0.0246	-	0.1588	0.090	3.13

Table 2-10 : Smooth rectangle channel experiments for bed slope of 0.045

S_f	S_0	$Q(m^3/s)$	$Z_n(m)$	F_r
-	0.0450	0.0125	0.015	3.61
-	0.0450	0.0492	0.035	4.00
-	0.0450	0.0870	0.05	3.74
0.0367	-	0.1626	0.087	3.37

Table 2-11 : Smooth rectangle channel experiments for bed slope of 0.055

S_f	S_0	$Q(m^3/s)$	$Z_n(m)$	F_r
-	0.0550	0.0138	0.014	3.99
-	0.0550	0.0544	0.034	4.51
0.0475	-	0.0961	0.052	4.25
0.0368	-	0.1623	0.080	3.81

In some Tables 2-8 through 2-11, there is a different slope instead of bed slope. In such cases, uniform flow generation must have been tricky and therefore energy slope has been used in its substitution. The additional details with regard to experiments themselves are discussed in proper sections.

A few experiments are done for velocity measurement by Hot-film probe in smooth rectangular channel. The flow conditions for these experiments are given in Table 2-12.

Table 2-12 : Hot-film experiments in smooth rectangular channel

S_0	$Q(m^3/s)$	$Z_n(m)$
0.001	0.1706	0.290
0.004	0.1632	0.170
0.013	0.1675	0.115
0.025	0.1588	0.089
0.036	0.1623	0.080

2.2.2 Flow over rough rectangular channels

The flow conditions for experiments in rough rectangular channels have been presented according to roughness type (already given in Table 2-1).

In Tables 2-13 through 2-18, the Manning roughness coefficient has been calculated from Manning discharge relation by observing or enforcing uniform flow in the lab. That is, for every specific roughness, individual Manning roughness values related to a specific flow condition are averaged for all flow conditions (under different slopes and discharges). Friction factor shown for this case on the related tables are of valuable information in upcoming sections and can be calculated via the equation (2.2).

$$f=\frac{8gn^2}{R_h^{1/3}} \tag{2.2}$$

In equation (2.2), g is the gravitational attraction and f is the friction factor.

Table 2-13 : Flow conditions for roughness type 1

Z_n (m)	S_0	Q (m^3/s)	F_r	n	f
0.073	0.055	0.055	1.46	0.028	0.163
0.133	0.055	0.162	1.78	0.023	0.095
0.100	0.045	0.087	1.45	0.026	0.128
0.142	0.045	0.162	1.60	0.023	0.095
0.117	0.035	0.101	1.34	0.024	0.110
0.115	0.025	0.086	1.16	0.024	0.107
0.167	0.025	0.160	1.24	0.022	0.083
0.126	0.015	0.075	0.89	0.024	0.105
0.199	0.015	0.167	1.00	0.021	0.071
0.261	0.004	0.110	0.43	0.024	0.088
0.151	0.004	0.051	0.46	0.024	0.099
0.261	0.001	0.055	0.21	0.024	0.088
0.130	0.001	0.020	0.23	0.024	0.102

Table 2-14 : Flow conditions for roughness type 2

Z_n (m)	S_0	Q (m^3/s)	F_r	n	f
0.143	0.055	0.162	1.59	0.026	0.116
0.078	0.055	0.055	1.33	0.031	0.195
0.150	0.045	0.162	1.47	0.025	0.108
0.106	0.045	0.087	1.33	0.028	0.147
0.157	0.035	0.159	1.35	0.024	0.100
0.123	0.035	0.101	1.24	0.026	0.126
0.123	0.025	0.086	1.05	0.026	0.127
0.175	0.025	0.160	1.16	0.023	0.093
0.133	0.015	0.075	0.82	0.026	0.123
0.210	0.015	0.167	0.92	0.022	0.081
0.276	0.004	0.110	0.40	0.025	0.095
0.158	0.004	0.051	0.42	0.025	0.106
0.276	0.001	0.055	0.20	0.025	0.095
0.136	0.001	0.020	0.21	0.025	0.110

Table 2-15 : Flow conditions for roughness type 3

Z_n (m)	S_0	Q (m^3/s)	F_r	n	f
0.103	0.055	0.162	2.61	0.016	0.048
0.051	0.055	0.055	2.49	0.016	0.060
0.109	0.045	0.162	2.38	0.016	0.046
0.073	0.045	0.087	2.32	0.016	0.053
0.118	0.035	0.159	2.07	0.016	0.046
0.089	0.035	0.101	2.03	0.016	0.052
0.087	0.025	0.086	1.75	0.016	0.049
0.129	0.025	0.160	1.81	0.015	0.041
0.094	0.015	0.075	1.38	0.015	0.047
0.156	0.015	0.167	1.44	0.015	0.037
0.192	0.004	0.110	0.69	0.015	0.040
0.113	0.004	0.051	0.71	0.015	0.045
0.192	0.001	0.055	0.34	0.015	0.040
0.097	0.001	0.020	0.35	0.015	0.047

Table 2-16 : Flow conditions for roughness type 4

Z_n (m)	S_0	Q (m^3/s)	F_r	n	f
0.113	0.055	0.162	2.26	0.018	0.062
0.059	0.055	0.055	1.99	0.020	0.091
0.124	0.045	0.162	1.98	0.019	0.064
0.084	0.045	0.087	1.87	0.020	0.077
0.132	0.035	0.159	1.76	0.018	0.062
0.100	0.035	0.101	1.70	0.019	0.071
0.144	0.025	0.160	1.54	0.018	0.056
0.099	0.025	0.086	1.45	0.019	0.070
0.105	0.015	0.075	1.16	0.018	0.064
0.172	0.015	0.167	1.24	0.017	0.049
0.219	0.004	0.110	0.56	0.019	0.056
0.128	0.004	0.051	0.59	0.019	0.059
0.219	0.001	0.055	0.28	0.019	0.050
0.110	0.001	0.020	0.29	0.019	0.079

Table 2-17 : Flow conditions for roughness type 5

Z_n (m)	S_0	Q (m^3/s)	F_r	n	f
0.125	0.055	0.162	1.94	0.021	0.081
0.067	0.055	0.055	1.68	0.024	0.123
0.141	0.035	0.1591	1.58	0.021	0.075
0.108	0.035	0.101	1.52	0.022	0.088
0.186	0.015	0.167	1.11	0.019	0.060
0.115	0.015	0.075	1.02	0.021	0.082
0.242	0.004	0.110	0.49	0.019	0.055
0.140	0.004	0.051	0.51	0.022	0.082
0.121	0.001	0.020	0.25	0.026	0.119
0.242	0.001	0.055	0.24	0.022	0.074

Table 2-18 : Flow conditions for roughness type 6

Z_n (m)	S_0	Q (m^3/s)	F_r	n	f
0.094	0.055	0.162	2.98	0.014	0.037
0.047	0.055	0.055	2.81	0.014	0.047
0.109	0.035	0.159	2.34	0.014	0.037
0.080	0.035	0.101	2.35	0.014	0.039
0.144	0.015	0.167	1.63	0.013	0.030
0.175	0.004	0.110	0.79	0.013	0.031
0.103	0.004	0.051	0.81	0.013	0.035
0.175	0.001	0.055	0.39	0.013	0.031
0.089	0.001	0.020	0.40	0.013	0.037

2.2.3 Flow over smooth compound channels

Experiments on smooth compound channels are summarized in Table 2-19 under flow conditions label. The uniformity was not achievable in these experiments because of channel short length, therefore, flow depth (Z) in Table 2-19 is the local flow depth (and related F_r number) where experiments are performed. (water surface profiles are attached in Appendix A). The flow is called Gradually Varied Flow (GVF) in such cases.

Table 2-19 : Flow conditions for smooth compound channels

S_0	Z (m)	Q (m^3/s)	F_r
0.0005	0.250	0.094	0.62
0.0010	0.251	0.102	0.67
0.0020	0.238	0.102	0.74
0.0100	0.225	0.166	1.36
0.0150	0.220	0.166	1.42
0.0200	0.193	0.166	1.88

2.2.4 Flow over floodplain rough compound channels

Experiments in floodplain rough compound channels are shown in Table 2-20. (water surface profiles are attached in Appendix B).

Table 2-20 : Flow conditions for floodplain rough compound channels

S_0	Z (m)	Q (m^3/s)	F_r
0.002	0.245	0.100	0.68
0.004	0.235	0.100	0.74
0.008	0.206	0.100	0.99
0.020	0.204	0.147	1.47
0.025	0.197	0.160	1.73

Again, uniform flow was not formed and all the information in Table 2-20 are for local section of a gradually varied flow.

2.2.5 Flow over all bed rough compound channels

The Table 2-21 shows the flow condition for experiments in all bed rough compound channels. For the first two experiments, uniform flow condition has not been satisfied and the related information are associated with local flow situation.

Table 2-21 : Flow conditions for all bed rough compound channels

S_0	Z_n (m)	Q (m^3/s)	F_r	Comment
0.002	0.210	0.050	0.479	GVF
0.004	0.222	0.063	0.533	GVF
0.01	0.199	0.074	0.79	Uniform
0.02	0.200	0.100	1.056	Uniform
0.03	0.214	0.150	1.367	Uniform
0.035	0.212	0.160	1.488	Uniform

In all bed rough compound channel experiments, uniformity was achievable in four out of six experiments (with the following slopes: 0.01, 0.02, 0.03 and 0.035). The surface profile for the first two GVF flows and four remaining uniform flows are given in Appendix C.

2.3 Experimental procedures

2.3.1 Prandtl-Pitot tube

Prandtl-Pitot tube or simply named Pitot tube is a popular flow measurement instrument used for velocity measurement in fluid flow. The Pitot tube is a right angle open ended tube that points in the adverse direction of the flow shown in Figure 2-10.

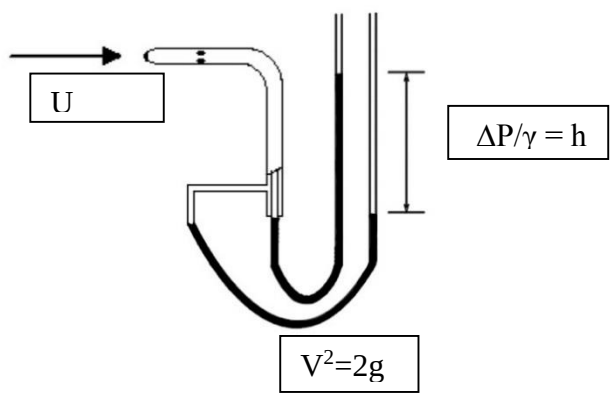

Figure 2-10 : Pitot tube with manometer mounted on

The tube can measure the total pressure (stagnation pressure) by bringing the fluid to rest at the mouth of the tube. Another tube attached alongside the Pitot is placed to measure the static pressure. The difference between two measurements will provide the velocity head that is used for velocity measurement as shown over the schematic Figure 2-10. This device has been widely used throughout this study for versatile purposes such as calibration and velocity profile measurements at different situations.

Another figure is given to show the Pitot tube in operation (see Figure 2-14).

2.3.2 Hot-film experiments

Hot-film is referred to a set up used to conduct velocity and turbulence measurement inside water. Its working principle lies in response of the voltage fed from source in reaction to the cooling rate of the Hot-probe wire when it comes into contact with colder fluid in its proximity. The system components consist of a probe, cables, Constant Temperature Anemometer (CTA), signal conditioners and analog channels. Cabling of the system includes the connection of the Hot-film probe to CTA and that to digitizer and that to computer for data acquisition.

Once the probe is submerged with the electrical charge on, the film can be damaged due to voltage difference between the liquid and the probe wire. This can lead to the breakdown of insulated quartz coating. Therefore water must be grounded to anemometer's signal ground as close to probe as possible shown in Figure 2-11.

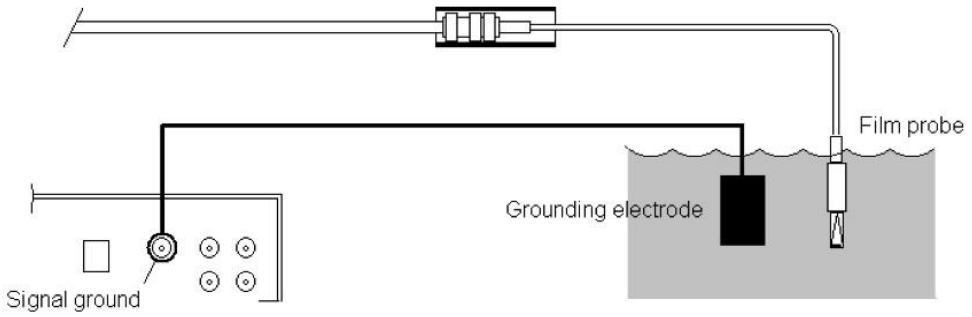

Figure 2-11 : The liquid grounding of miniCTA

It is required that the temperature be kept constant during a record with the knowledge of guaranteeing the CTA adjustment is based on the constant temperature, otherwise further correction to the obtained data will be required.

In this regard, a graph is prepared that relates the ambient (liquid) temperature to time elapsed shown in Figure 2-12. As it can be seen in figure, at least 15 minutes waiting maybe a suitable time to allow a constant ambient temperature to establish. This result is prepared for a low discharge of 18 (l/s) that warranties an even shorter waiting time required for larger flow rates.

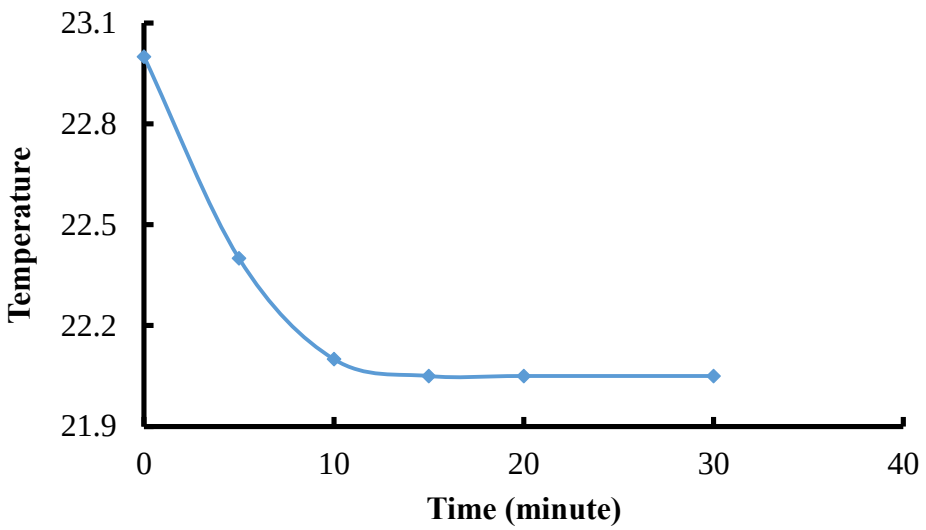

Figure 2-12 : Water temperature change with respect to time elapse

Usually, a velocity calibration is mandatory when working with Hot-film tool. Velocity calibration is the forming of a unique link between acquired voltage from CTA and the actual velocity of the flow. It can be accomplished via exposing the Hot-film probe to a set of known velocities. Usually calibration is performed in probe calibrators such as free jets (for Hot-film used in water) or wind tunnels (for Hot-wire used in air). In the present case, the measured velocities in the various depths of the channel flow by Pitot tube are used as reference values for the Hot-film calibration. The laboratory monometer and the measuring system are shown in Figure 2-13.

Figure 2-13 : Monometer (left), Pitot tube and the Hot-film probe in operation

The Pitot tube and the Hot-film probe are shown in the Figure 2-14 in operation from a closer view. Notice that probe is placed with its wire parallel to channel bed.

Figure 2-14 : Pitot tube (left) and Hot-film probe (right)

The procedure for Hot-film calibration in open channels will be:

- Specify a set of known positions in the flow for both Pitot tube and probe to take measurements. In this case, the center of the channel was chosen for vertical water column profile measurement.
- Record the voltage from CTA output for at least a minute over the exact locations where Pitot tube was used for velocity measurement.
- Consider a minimum of 10 points for accurate calibration.
- Best fit the velocity points against acquired voltages.

Let's take the case of the slope, S_0=0.015. The result of the calibration is given in Figure 2-15.

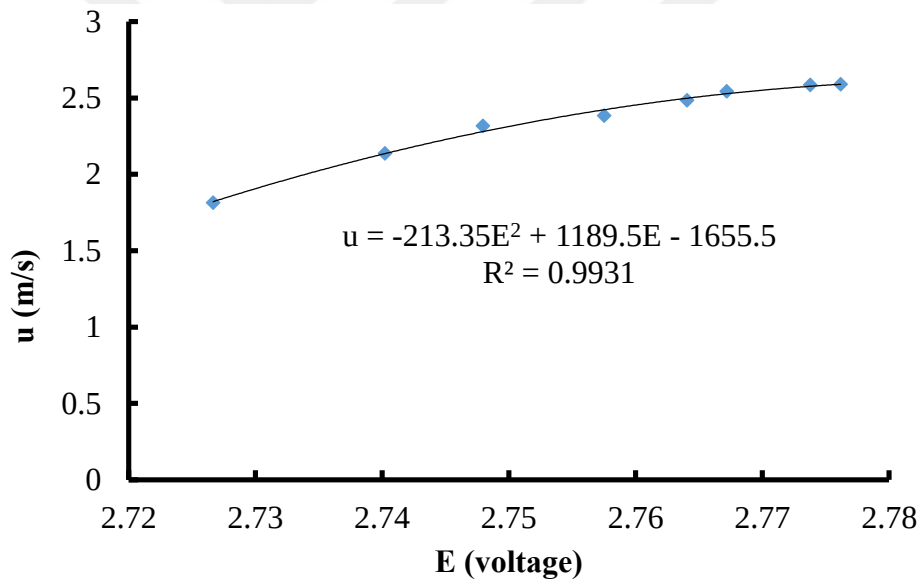

Figure 2-15 : Best fitting the voltage with respect to velocity for Hot-film calibration

Velocities are measured at a deep portion of the flow where measurements are more reliable, in addition, the velocity range is relatively large. Eight data points are used for curve fitting which appear in Table 2-22.

Table 2-22 : Data points used for curve fitting in Hot-film calibration

u (m/s)	z (m)	E (Voltage)	Best fit velocity (m/s)	Relative Error %
1.81	0.004	2.726	1.813	0.000197
2.13	0.014	2.740	2.128	0.003551
2.31	0.024	2.747	2.272	0.086326
2.38	0.034	2.757	2.416	0.043373
2.48	0.044	2.764	2.491	0.002056
2.54	0.054	2.767	2.521	0.018693
2.58	0.064	2.773	2.570	0.008464
2.58	0.074	2.776	2.583	0.001156

The relative error is the error between measured velocities and calculated velocities from best fit function.

The result of the velocity measurement in the center of channel is given in Figure 2-16.

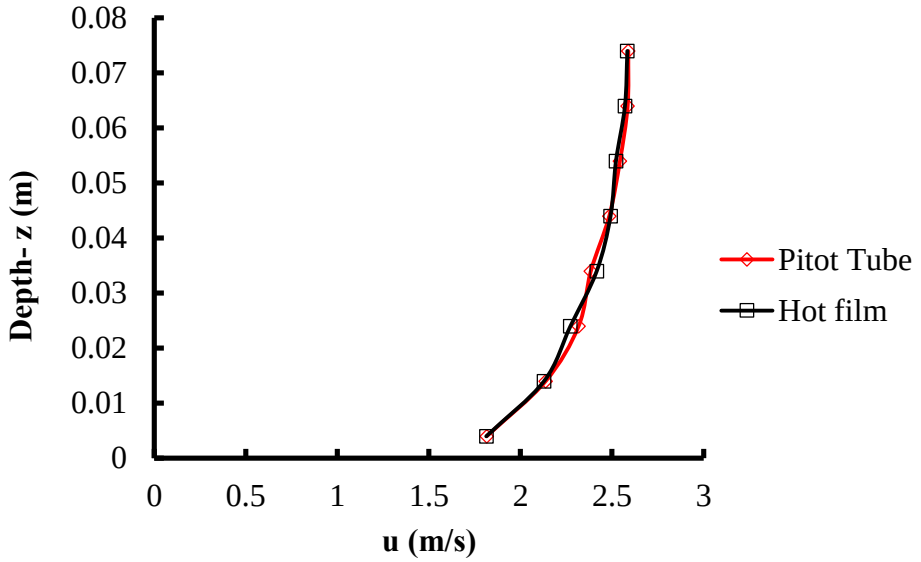

Figure 2-16 : Velocity measured by Hot-film and Pitot tube in the vertical center line for the slope of 0.015 and Z_n=11.5 cm

Hot-film experiments cover five slopes ranging super and subcritical regimes. The velocities are measured in the water column of the cross section in the center of channel with the purpose of observing the dipping phenomenon and near the free surface velocities. In addition to that, aim was to verify to which extend it is possible to collect turbulent data near the free surface of the flow to explore water interaction with air above.

Result of velocity measurement by Pitot tube and Hot-film for one flow condition are shown in the Figures 2-17 and the rest of the figures are supplied in the Appendix D.

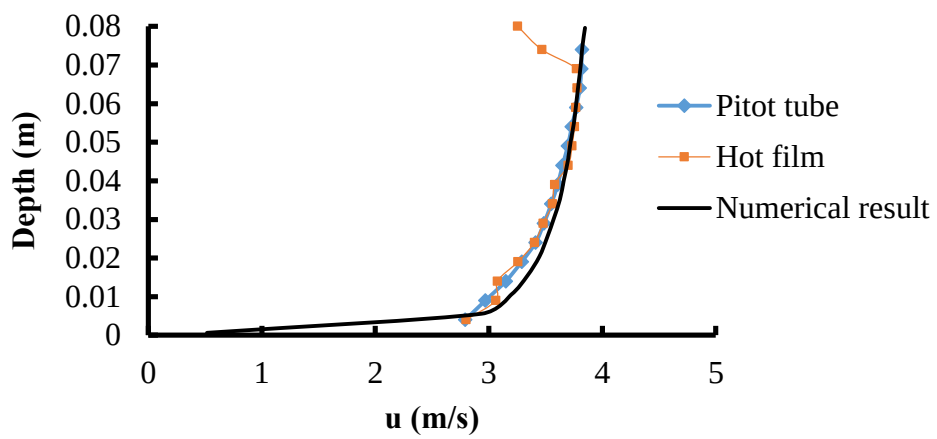

Figure 2-17 : Velocity profiles at the vertical column center of cross section measured and computed for flow condition of S_0=0.055, Q=162.3 l/s and Z_n=8 cm

The manifested figure can be considered as the worst case for the Hot-film measurements. As shown in the figure, there is an acceptable agreement between the Pitot tube measurements and computational velocities in water column. Hot film measurements start to fall apart from other two figures near the free surface for some reasons. Even though this trend is not always the case for the Hot-film measurements, sometimes the opposite has happened. Since very accurate data is favored for the near free surface region, if the Hot-film measurements are not consistently acceptable for all cases then they are not going to be useful at all. It is recommended that all relevant figures be cast a glance in Appendix D.

Because Hot-film measurements are usually accurate and consistent with Pitot tube values in deeper regions of the flow, it is possible that extra heat convection is behind this inaccuracy especially near the free surface which happens more often. Moreover, in relatively high velocity flows, water free surface is quite chaotic and unstable due to eruption of turbulent structures near this region. This can effect on the quality of Hot-film data and can be another reason for its inefficiency.

The repairing of the numerical model was supposed to be accomplished with the assistance of velocity and turbulence measurements coming from this device in certain sections of the flow and on free surface. The aim was to collect the turbulence quantities in air (with Hot-wire) and water (with Hot-film) interface and try to modify the turbulent stresses of numerical model accordingly to take into consideration the air-water interaction. This interaction is believed to introduce excess resistance into the flow and no attempt has been made to investigate this interaction so far and is not reported in the literature.

In either way, the entire Hot-film measurements have been of absolutely no use for analysis due to their unstable outcomes. As a result, instead of Hot-film measurements, Pitot tube was substituted for data collection. Still, it is clear that Pitot tube is incapable of measuring turbulence.

2.3.3 Image processing

The objective of the experiments is to measure the velocity on the free surface of water over specified sections of the channel called working sections where flow is nearly uniform in most of the cases (unless otherwise stated). The tests include the velocity profile measurement for a variety of Froude numbers obtained at different channel slopes. The surface velocity measurement is taken care of by means of imagery. Although there are very limited alternatives for such kind of non-intrusive free surface velocity measurements, the attempt is to make the optimum use of free surface velocity by restraining the measurements to instantaneous velocities of particles at sparse locations by applying PTV (Particle Tracking Velocimetry) method. PTV is the primary strategies that has been employed for the experiments and their further analysis. Yet, sometimes PIV (Particle Image Velocimetry)

has also been practiced for surface full velocity profile distribution for comparison and verification purposes.

2.3.4 PTV tool and components (Algorithm, Seeding, Particle dispenser and Lighting)

A computer code was developed in Matlab to calculate the velocity of particles, the program turns the videos into frames, rectify oblique images whenever needed and analyze them for velocity of particles. The code is supplied in Appendix E. The algorithm for PTV is rather straight forward. The video is initially converted into a set of frames. The area under investigation is specified over the images (Figure 2-18). The images are then binarized by thresholding the background noise. The frames are thus transformed into black and white images where tracer particles (either white or black) are detected by object detecting toolbox in Matlab (Figure 2-19). It is noteworthy that the developed code is treated such as to capture the center of the particle in each frame and the largest particle (regarding the area) is chased by the program for its velocity in case noise is still present in some situations. Plus, time averaged pointwise velocity over the travel distance is computed via this method.

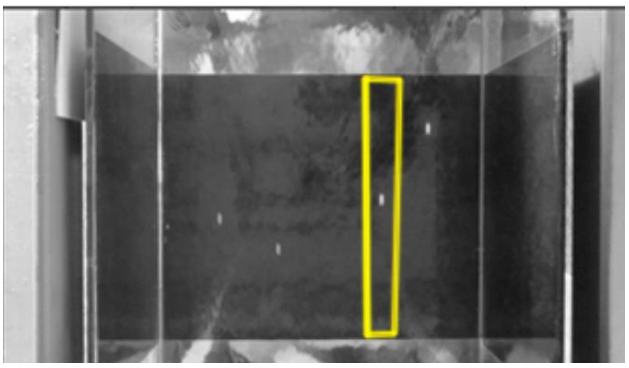

Figure 2-18 : A typical object tracking analysis scheme when image is in gray scale with region of interest displayed

Figure 2-19 : A typical object tracking analysis scheme in its final state when image is in black and white scale

A usual challenge faced in PTV is the unwanted light reflections and shadows on the free surface. The solution for suppressing the background reflection noise is to adopt a high contrast intensity to point the particle out as seen in Figure 2-19. Finally, the distances are calibrated to convert the pixel dimensions over the image into real world distances. The distance of particle moving across the frames is calculated and then divided by time interval separating the two frames.

Proper seed selection for PTV experiments is another problem. There exists many sources of error regarding the seeding issue. One major problem arises from the fact that drag force applied on the particles' submerged volume by water (as the driving force) is distracted by air resistance in the opposite direction. For a particle to follow the free surface perfectly, it should be thin enough to only move on the face of the gas-liquid interface which is practically difficult to achieve. If some volume is in contact with air, the particle will move with a speed less than that of the free surface due to air resistance (especially in high velocities). This problem was closely observed in the experiments. For example, a major portion of polystyrene (with a density of 0.04 gr/m^3) will remain in the air phase. Therefore, in large flow velocities, the effect of air resistance cannot be neglected. Another problem with Polystyrene is the electrical force between the particles that seems to be pulling the particles towards one another until stability is reached. The infeasibility of using confetti (thin paper sheets) was also confirmed. It was observed that the pieces of papers submerged

shortly after coming into contact with water due to turbulent structures on the free surface and particles absorbing water, saturating and plunging. Another factor is the size of the particle. The ideal particle size should be as tiny as possible so that it can follow one single streamline without much spin due to velocity gradients. It is required, on the other hand, that the particles move along the stream lines genuinely and stay on the free surface for sufficiently long distances. In the experiments, nearly 0.5 cm by 0.5 cm square PVC particles with 0.75 gr/cm^3 density are used. Commercially, 0.2 mm thick white PVC sheets are available to be used as cover faces in binding small booklets. An advantage of PVC pieces is that they can stay floating for long distances since they do not absorb water. Many studies in the literature have reported the merits and demerits of using different particles for surface velocity measurement. Some examples of such tests can be found in V. Weitbrecht et al. (2002).

As stated earlier, signature of the free surface can be exploited via the velocity at a single point. This point wise speed was calculated by analyzing the free surface particles at a time, dropping a couple of particles (usually 4 particles over 60 cm wide channel) at various locations from the side wall and computing velocity separately for each particle to obtain multiple test data at a single run.

The PVC particles used in PTV experiments and the particle dispenser are shown in Figure 2-20.

Figure 2-20 : PVC particles used as seeds for PTV and object tracking analysis (left) and PTV particle dispenser (right)

Prior to facilitating the working area with light, tests were conducted under daylight and with available laboratory lighting on the ceiling to verify the illumination requirements. The result of the image analysis proved that there was little or no difference in outcome of the analysis. In spite of this, to stay away from possible unpredicted sources of error, a powerful halogen photographic lamp was placed next to the working section (Figure 2-21).

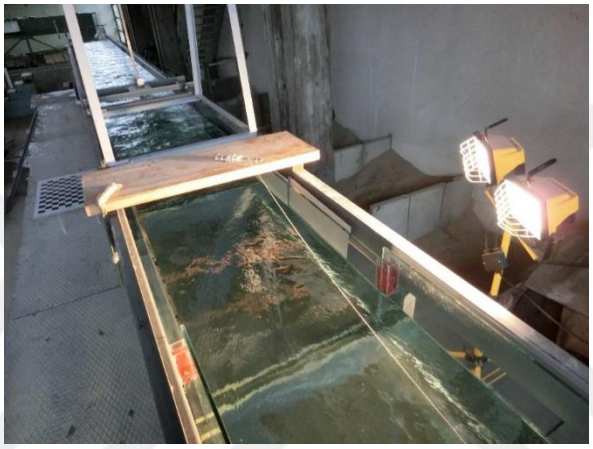

Figure 2-21 : Illumination of the working section

Some tests showed that the color difference between the white particles and the laboratory ground (as seen from the transparent bed of the channel) produced enough contrast for successful image processing. Then again, to stay on the safe side a black card board was attached to the walls of the working section surrounding a portion of the channel bed and side walls to increase the contrast to be as precise as it can be. The same lighting condition was used for PIV experiments.

2.3.5 PIV tool and components (Algorithm, Seeding and Particle dispenser)

The PIV analysis was conducted by the open source code PIVlab (Brevis et al., 2011) in which cross correlation method is practiced. PIVlab is a time-resolved digital particle tracking Velocimetry tool for Matlab developed by MSE. Antoine Patalano- Univ. Nacional de Cordoba and PhD. Brevis Wernher- Univ. of Sheffield.

The program performs particle detection operation initially based on binary correlation. Cross-correlation and relaxation algorithms (Brevis et al., 2011) are then used for solution of temporal matching problem in order to calculate the velocity field. This software aims at the analysis of experimental image velocimetry measurements using a Lagrangian frame of reference, which can offer several benefits compared to the standard Particle Image Velocimetry (PIV) technique. Unlike Eulerian reference frame (PIV method), in Lagrangian reference frame, particles are treated individually that makes it possible for particle labelling and tracking of individual trajectories.

The PIVlab software was used for the whole free surface velocity distribution computation. The image processing method belongs to the so called pattern matching approach that carries out correlation analysis on the gray-level values confined in small regions of the imaged area, called interrogation areas (IA, each corresponding to a unique vector of velocity at the end of an analysis). The cross correlation algorithm used in PIV analysis employs the cross correlation coefficient as a similarity index (Fujita et al., 1998) to match one group of patterns within an IA in image 1 which is most similar to an IA in image 2. Figure 2-22 shows an image pair of two consecutive video frames isolated by a time interval, dt. The IA in the figure is determined by considering the size of the foam pattern tracing the flow, the IA is chosen big enough to form a recognizable pattern inside the IA. The search area (SA) identifies the area that is searched for possible displacements of IA in the image pair, usually the size of the SA is predictable due to an early estimate of the flow velocity magnitude. The arrow from point a_{ij} to point b_{ij} in Figure 2-22 forms the displacement of group of particles.

In fact, the algorithm detects the correlation between the image pattern nested in the IA centered on a point a_{ij} in the image recorded at time t, and the IA centered at point b_{ij} in the image recorded at time t+dt, as demonstrated in Figure 2-22. The correlation coefficient $R(a_{ij}, b_{ij})$ is a similarity index for the groups of pixels contained in the two compared IAs. For more details on correlation coefficient, the article by Fujita et al. (1998) is recommended.

Velocity vectors are derived from displacements being divided by dt, the time between successive frames. The final vector field density relies on the choice of selection of the pitch step which defines the computational grid quality to be analyzed.

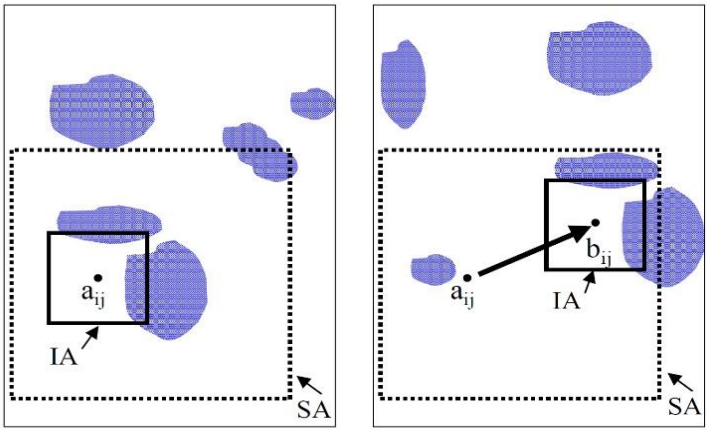

Figure 2-22 : Schematic illustration of algorithm employed for detection of tracers' displacement in PIV method

The seeding for PIV analysis should cover the complete water free surface width for analysis. Sometimes in large scale cases, natural tracers such as foams and turbulent structures on the water surface have been used as tracers (Adam et al., 2012). But often, under normal flow conditions, in devoid of natural tracers, artificial tracers (seeding) have been obligatory for PIV analysis (Fujita and Komura, 1994). The sawdust, as a conventional option, was used in the laboratory for PIV analysis. The fine sawdust can be collected from grinding to sculpt the wood. The bulk density of fine sawdust ranges between 192 to 288 kg/m^3 depending on its compact state. As an overall value, 210 kg/m^3 has been reported in some resources.

The **particle dispenser** for PIV experiments should be a tool needed to seed the flow by sprinkling particles over the flow field (water surface in this study). A PIV particle dispenser (as seen in Figure 2-23) was designed to cast a sheet of thin sawdust that covers nearly the

entire width of the channel. The sawdust is a perfect particle to be used for PIV analysis as it forms unique patterns on the free surface to be tracked by the PIV algorithm.

Figure 2-23 : Particle dispenser used to seed the flow with sawdust in PIV experiments viewed from two different angles

2.3.6 Camera lens distortion effect removal

The camera used in the experiments is a Casio EXILIM EX-ZR1000 model with high speed video footage recording capability (up to 1000 frame per second). A vast majority of video and still cameras available in the market use lenses that produce nearly rectilinear images which eliminates the necessity of correcting the images for their distortion. Despite all this, for a perfectly safe and precise analysis, the minor radial distortion due to wide angle lens was removed by following the procedure explained below. (Note: the wide angle lens might be considered normal lens only under very exceptional conditions)

Camera calibration is the process of finding characteristics internal to a camera and finding the location of the camera with respect to a fixed object. The camera parameters are categorized as intrinsic and extrinsic parameters. The intrinsic parameters (characteristics inside a camera) include the focal length of the lens used, optical center and distortion coefficient. Knowing these parameters facilitates improving the image quality, correct the lens distortion and map real world distances to pixels and vice versa. The camera's location in space is known as its extrinsic parameters. Knowing extrinsic parameters is crucial for

stereo calibration, stereo calibration implies perceiving three dimensional information from visual observation.

A camera calibration toolbox in Matlab was used for calibration purpose. The first step in camera calibration is to have 10 to 20 images taken from a flat chess board (or any board with regular patterns) at different angles and distances for accurate calibration (see Figure 2-24). The next step is specifying the size of squares and extracting the corners of the outer boundary of the board. This step is necessary for finding the mapping between world units and image pixels. The squares of the chessboard are then detected automatically by the application. Lastly, it is the calibrating phase to complete the work flow. There are many different approaches to calculate camera characteristic parameters. Matlab camera calibration toolbox uses a combination of algorithms for different subcomponents. All the relevant references are cited in their website:

http://www.vision.caltech.edu/bouguetj/calib_doc/htmls/ref.html

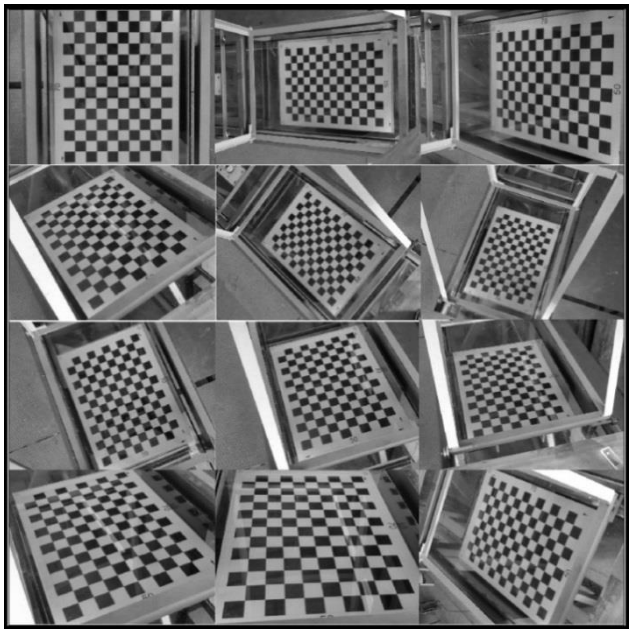

Figure 2-24 : Twelve photos taken of checkerboard at different positions for camera calibration

Once calibration is over, camera's intrinsic and extrinsic parameters are computed and stored. Intrinsic parameters are characteristics inside a camera that include the focal length of the lens used, optical center and distortion coefficient. The camera's location in space is known as its extrinsic parameters. Knowing extrinsic parameters is crucial for stereo calibration, stereo calibration implies perceiving three dimensional information from visual observation. It is worth noting that all 12 photos used in calibration are taken under a constant focal length (set manually to maintain consistency) and a fixed zoom level. Focal length is a distance at which the rays of light converge to form the image behind the lens.

Lens distortion is a common problem and causes the straight lines in the real world appear curved in the image. By applying the intrinsic parameters, this distortion can be removed. Once extrinsic parameters are identified, position of the board (placed at the bed of the channel adjusted to the water free surface level) can be depicted. In the following Figure 2-25, chess board and camera positions are demonstrated. Sometimes, this is useful in deciding if enough pictures are not taken from proper angles more images may be needed to improve the calibration results.

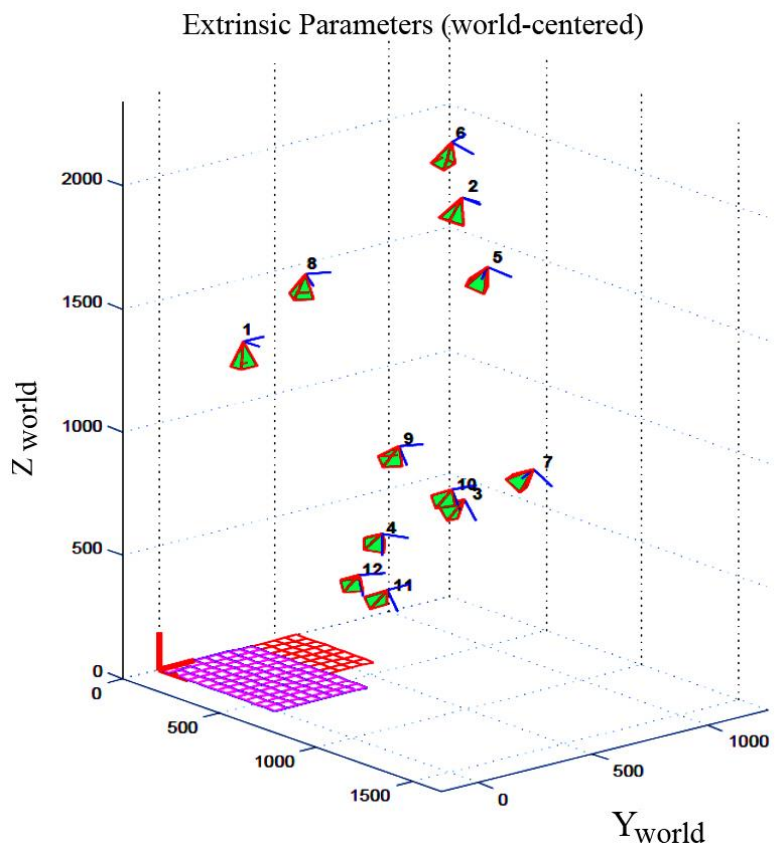

Figure 2-25 : The checkerboard at the water free surface and camera positions estimated by calibrating toolbox

Visualizing the re-projection error is another way of identifying bad images and substituting them for a better result. Re-projection error is a measure of calibration error and it is the difference between binds detected in the image and binds re-projected back onto the image using the calculated intrinsic parameters. The origin of re-projection error arises from extracting the outer edges of a calibration image inaccurately since it is manually entered. The re-projection error results are shown in Figure 2-26 (12 colors for 12 images used) to show all images taken are acceptable because of low error values. The goal of the camera calibration is to identify whether image analysis are influenced by slightly distorted images. In the practice, calibration is a must for LSPIV analysis specially when dealing with natural environment.

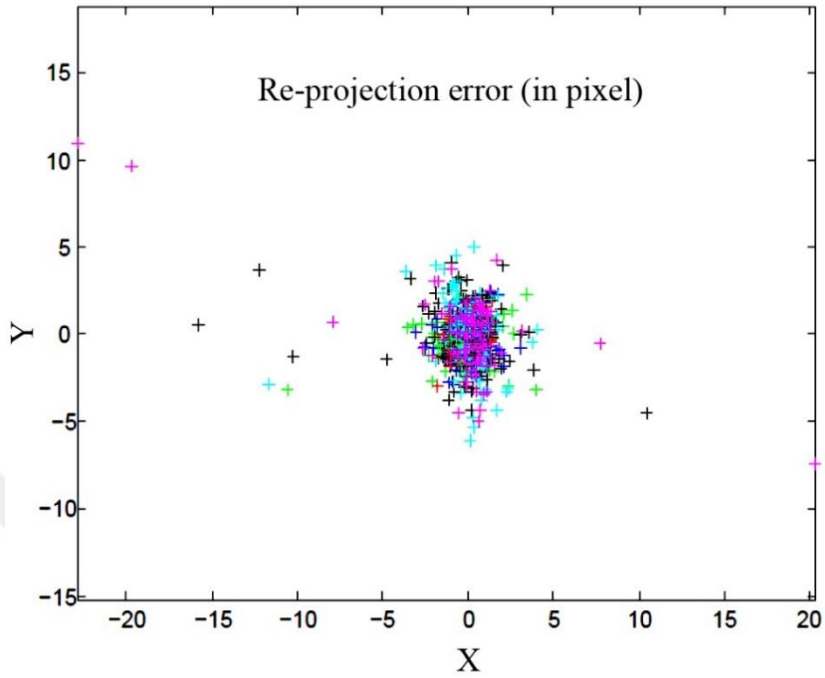

Figure 2-26 : Re- projection error for 12 images used in calibration

Effect of lens distortion on PTV analysis can now be investigated when camera is calibrated (or it is to say the images produced by camera are made distortion free).

The camera calibration parameters were applied on a test case to verify whether or not there is an effect on the PTV analysis from distorted images. For this purpose, two separate analysis were performed on two same set of photos- once with and other time without the lens distortion taken into account (for same flow conditions, obviously). The results of the analysis are shown in Figure 2-27 and Figure 2-28 in terms of velocity frequency. Figure 2-27 shows the frequency of velocity distribution over the free surface in a couple of points when photos are not yet corrected for distortion. Figure 2-28 shows the same quantity for the un-distorted set of photos. The two figures demonstrated the frequency of unidirectional velocity magnitude on the free surface of water for nearly 100 set of velocities for a discharge of 140 l/s at bed slope of 0.0005. The mean velocity for distorted case is computed as 0.796 m/s whereas same quantity is computed as 0.7936 m/s for un-distorted set of same images. The relative error between the two mean values is 0.3 percent which is indeed

negligible. This is a technical indication that lens distortion can introduce quite an unimportant amount of distortion into analysis if focal length and zooming level are kept identical to this case for any other test to be conducted. It should be noted that under such closely manipulated laboratory conditions, where camera can be placed in a favorable height and positioned normal to flow plane, lens distortion and image rectification will be unnecessary. Throughout this study, almost same optical condition was held to assure the data obtained from PTV experiments are error free and useable. Besides, the same assumption was extended to PIV analysis.

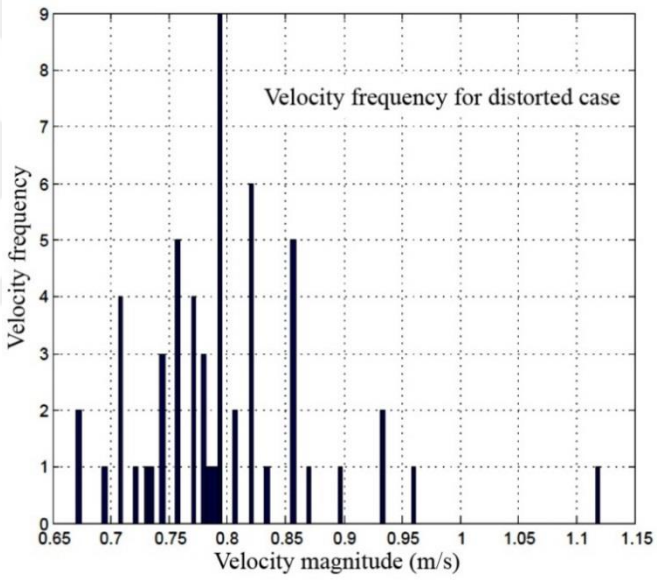

Figure 2-27 : Velocity frequency over a couple of points on free surface for distorted images

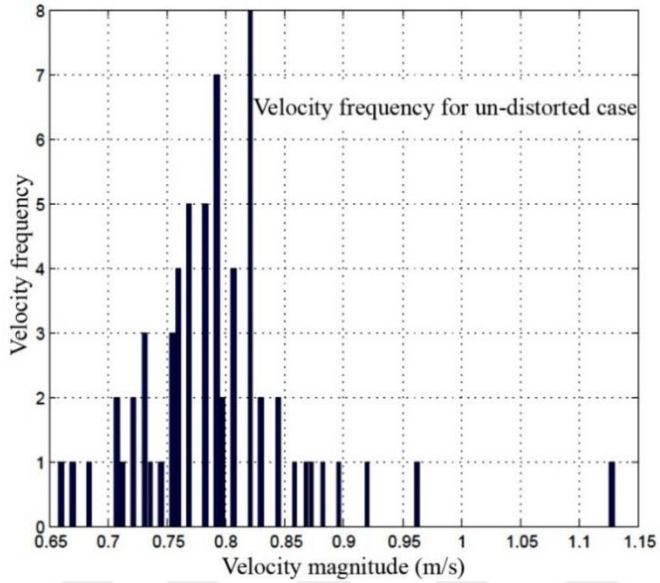

Figure 2-28 : Velocity frequency over a couple of points on free surface for un-distorted images

2.3.7 LSPIV experiment

Detailed information on LSPIV literature study is presented in the literature survey section. To define the term in brief here, LSPIV is an extension of PIV technique which is more often practiced in larger fields of flow such as riverine environment. Since functionality of the method is suitable for larger areas of interest, most of the times, it is required that the video footages undergo a lens distortion removal phase as well as rectification of the video which inevitably is taken from an oblique angle to the flow. The LSPIV is not particularly a must for the laboratory conditions while camera can be placed at any vantage point with relative ease.

In nature, sometimes recording vantage point is different than normal to the free surface position for good reasons, either it is impossible to mount the camera as desired or more of the flow field has to be included in the analysis. Photos shot from an oblique angle must be first re-constructed (transformed into a state of being normal to the free surface) for analysis. In order to benefit an experiment with LSPIV before extending the technique to the field, one test was conducted in the laboratory to verify its result is successful. The camera was

intentionally placed at an angled position to the flow and the produced image is demonstrated in Figure 2-29. The distorted frames were transformed geometrically (seen in Figure 2-30) to reconstruct the view of the flow from top. A linear transformation was employed to map the coordinates of the image into physical space coordinates. This image rectification can be accomplished with having at least four ground control points (GCPs) parallel to water surface. Physical coordinates of the GCPs should be known a priori. In this test, the checker board has been used for obtaining the desired information from GCPs as seen in Figure 2-30, yet any set of other points can work positively as well. The result of the LSPIV with shooting rate of 120 fps (frame per second) has been given in Figure 2-31. As it can be seen in the figure an acceptable agreement exists between regular PTV and LSPIV analysis.

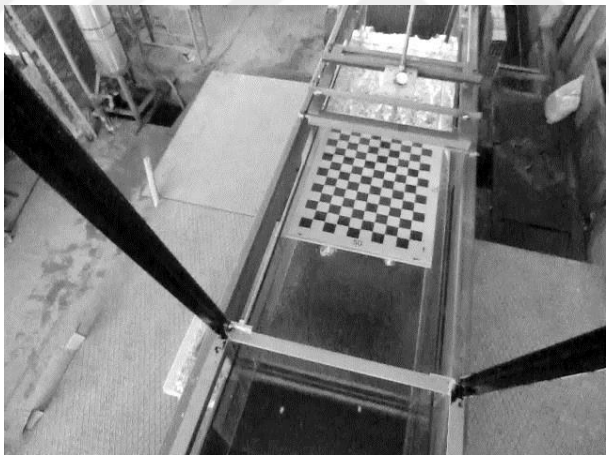

Figure 2-29 : Image produced from obliquely mounted camera

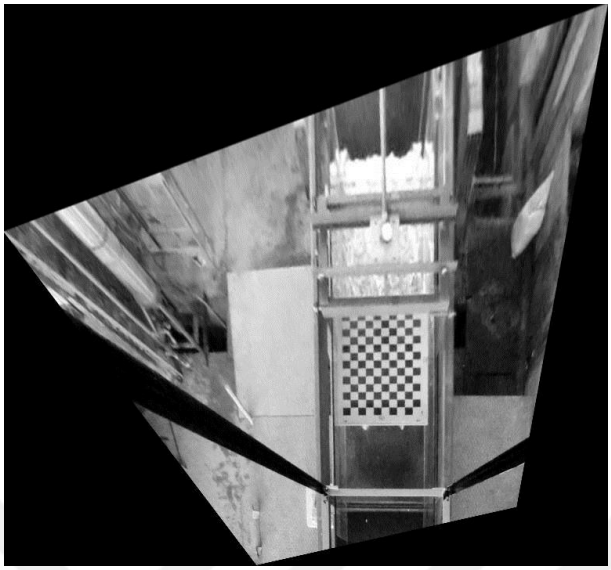

Figure 2-30 : The image after geometrical correction is applied

For LSPIV Artificial seeding is mandatory in the laboratory. In nature, natural seeding might exist which makes the attempt easier. For LSPIV analysis, natural foam or other kind of patterns generated by large-scale turbulent structures breaking up at the free surface may be used. Sometimes natural debris can be used in PTV analysis or floating tree trunk in object tracking. Here however, since same PVC particles are used combined with PTV analysis, the term LSPIV can be replaced with LSPTV as seen on Figure 2-31.

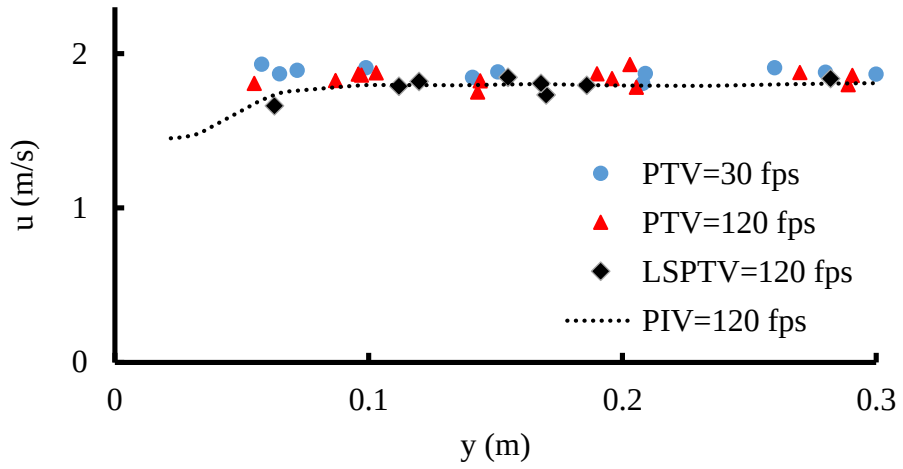

Figure 2-31 : The comparison of PTV and LSPIV analysis for a specific case, flow condition is S_0=0.035, Z_n=0.02 m, Q=17.7 l/s and B/Z_n=30

In Figure 2-31, S_0 is the channel bed slope, Z_n is the normal depth of flow, B is the rectangular channel width equal to 60 cm, Q is the discharge, vertical axis is the velocity in the flow direction and horizontal axis is the distance from channel side wall (half of the field is under attention due to symmetry).

Same procedure will be mandatory in the field where shooting at an angle perpendicular to the stream free surface is difficult. The overwhelming outcome of the laboratory LSPTV analysis guarantees a sound field LSPIV provided that minimal four ground control points with known distances and elevations are considered. However, the developed computer code in this study can handle the image rectification without the need for knowledge of elevations or coordinates (or physical distances) of the GCPs, if ground control points are known to be nearly parallel to water surface, that is horizontal, and GCPs fall on the edges of a square regardless of physical dimensions.

In some figures and relations proposed later in this piece of writing, fps keeps appearing frequently which was implied as frames per second (or simply put, speed of video

recording). It is to say that the fps has the information on time step within itself. For example if fps is 30, it is easy to realize that time step (dt) will be 1/30 seconds.

CHAPTER 3

NUMERICAL MODEL

3.1 Modeling three-dimensional velocity field in open channel flows

The computation of three dimensional velocity field in open channels are done by solving Reynolds-averaged Navier-Stockes equations closed by a turbulence model. Sometimes equations are simplified and downsized to depth integrated style such as one dimensional shallow water equations and other times equations are solved in all directions. There are many turbulence models proposed in the literature as well. The models also vary from very complex to less complex ones. However, most of them are made up of two equations or so called two equation models. One of the most applied and practiced turbulence models is k_t- ε model. This model consists of two equations which are generally referred to as the transport equations for the turbulence kinetic energy (k_t) and its dissipation rate (ε). The standard k_t - ε model is based on isotropic eddy viscosity assumption. This assumption dictates that turbulence has an identical behavior in every direction. Or more technically said, in every point inside of the domain, eddy viscosity is the same for all the Reynolds stress components. Nevertheless, turbulence is anisotropic by nature. In many situations, failing to satisfy this assumption is not much of an importance such as in wide open channels where shear stress is a more dominant factor. However, in an open channel with secondary currents, turbulence anisotropy must be taken into account. Secondary currents effect on the whole mean flow field and prompt the generation of three dimensional structures. Surface velocity gets influenced by these circulating currents too. Gerard (1987) has figured that mechanism of secondary flows is the main reason for creation of vorticity in the flow. This mechanism can be very well explained by solving the longitudinal vorticity transport

equation. Selecting the vorticity transport equation which is solved alongside the Poison stream function equation instead of continuity equation together has some advantages over the other primitive variable formulation. Although advantages of adopting vorticity transport equation is an advantage as long as uniform flows are under investigation, but elimination of solution for pressure field and solving less number of equations for the same three dimensional velocity field can be considered as plus points in this specific problem.

Beside the two equation turbulence model, there are many reports on other turbulence models that simulate the transvers exchange of momentum (the primary reason of secondary currents creation) in open channels, but this is not our aim to describe them here. To minimize the computation complexity in this study, a two dimensional approach with zero-equation nonlinear turbulence model is used. The turbulence model is called nonlinear mixing length (Aydin, 2009). The constitutive equations of this model are presented in terms of a mixing length and it has eliminated the need for turbulent kinetic energy and thereby its dissipation rate. The turbulence model and the governing equations are all defined in this chapter.

3.2 Governing equations and turbulence model

Mathematical model of three dimensional flows in uniform prismatic open channels consists of a set of differential equations that can be solved for the velocity field of the flow. Uniform flow assumption in prismatic channels or in straight river reaches is usually believed to yield quick and acceptable calculation of discharge. For a fully developed, uniform channel flow, velocity distribution over the cross section including the free surface is a reflection of force balance in the flow direction. Channel flows are bounded by the bed and side walls which are solid boundaries with no-slip conditions on the walls. The water surface however, can be assumed to be free when the interaction with air above the surface is considered as negligible.

Regarding the governing equations of flow, mainly, the streamwise velocity component is sufficient to describe the flow field, but turbulence driven secondary flows affect the final velocity distribution by drawing the high speed fluid from the central free surface towards

the slower corners. For the solution of flow field explained as such, the governing equations of motion ought to be solved using an appropriate method. These equations are as follows:

1-The momentum balance in the flow direction.

Reynolds averaged momentum equation for fully developed, steady incompressible, turbulent uniform flow is written:

$$\frac{\partial u}{\partial t}+\frac{\partial (uv)}{\partial y}+\frac{\partial (uw)}{\partial z}=g\sin\theta+\nu\left(\frac{\partial^2 u}{\partial y^2}+\frac{\partial^2 u}{\partial z^2}\right)+\frac{\partial \tau_{yx}}{\partial y}+\frac{\partial \tau_{zx}}{\partial z} \tag{3.1}$$

Where u, v, w, are the mean velocity components in x, y, z directions, respectively, in which *x* is the streamwise direction of the flow; t is time; g is gravitational attraction; θ is the angle of channel bed with horizon; ν is kinematic viscosity and τ is turbulent kinematic stresses.

2- The streamwise vorticity transport equation is written in the flow section:

$$\frac{\partial \xi}{\partial t}+\frac{\partial (v\xi)}{\partial y}+\frac{\partial (w\xi)}{\partial z}=\nu\left(\frac{\partial^2 \xi}{\partial y^2}+\frac{\partial^2 \xi}{\partial z^2}\right)+\frac{\partial^2(\tau_{zz}-\tau_{yy})}{\partial y\partial z}+\frac{\partial^2 \tau_{yz}}{\partial y^2}-\frac{\partial^2 \tau_{yz}}{\partial z^2} \tag{3.2}$$

Equation (3.2) is streamwise vorticity transport equation. In which, ξ is the vorticity in the flow section (y-z plane) and is defined as:

$$\xi=\frac{\partial w}{\partial y}-\frac{\partial v}{\partial z} \tag{3.3}$$

3- Poison equation for stream function (ψ) is used to imply continuity:

$$\frac{\partial^2 \psi}{\partial y^2}+\frac{\partial^2 \psi}{\partial z^2}=-\xi \tag{3.4}$$

In addition to momentum and vorticity transport equations, equation (3.1) and equation (3.2) respectively, Poisson equation has to be solved for the stream function. Stream wise velocity is computed directly from the momentum solution, velocity components normal to stream wise direction are obtained from the stream function solution.

$$v = \frac{\partial \psi}{\partial z} \tag{3.5}$$

$$w = -\frac{\partial \psi}{\partial y} \tag{3.6}$$

The governing equations are solved numerically (via finite volume method) over a staggered grid using a two dimensional approach to uniform channel flow with the zero-equation nonlinear turbulence model. The model tends to capture the secondary flow structures with minimum complexity in modeling.

Computational approach can be successful if the turbulence structure of the flow field is appropriately described by a suitable model to be combined with the so called equations of flow. Such an attempt has been made by using a Non-linear Mixing Length Model (NMLM) (Aydin, 2009). Turbulence anisotropy was taken into account using nonlinear correlations of the strain rates in describing the turbulent stresses. The constitutive equations of the model are expressed in terms of a mixing length, eliminating the need for turbulent kinetic energy, dissipation rate and turbulence viscosity. Model uses a volumetric mixing length to measure the weighted distance from the solid boundaries which is directly obtained from an integral expression. Model is robust since it requires no additional differential equations. The model aims to capture the secondary flow structures in detail by computing the 3D velocity field of uniform channel flow with minimum complexity of modeling and thus requiring less computational effort for the solution.

Based on the NMLM, the turbulent stresses are defined as

$$\tau_{ij} = -\overline{u_i' u_j'} = l_m^2 \begin{bmatrix} |\Omega| S_{ij} - \frac{2}{3} k_t \delta_{ij} \\ - C_1 (S_{ik} S_{jk} - \frac{1}{3} S_{kl} S_{kl} \delta_{ij}) \\ - C_2 (S_{ik} \Omega_{jk} + S_{jk} \Omega_{ik}) \\ - C_3 (\Omega_{ik} \Omega_{jk} - \frac{1}{3} \Omega_{kl} \Omega_{kl} \delta_{ij}) \end{bmatrix} \tag{3.7}$$

In which $S_{i,j}$ (equation (3.8)) is the rate of strain, Ω (equation(3.9)) is vorticity and $|\Omega|$ (equation (3.10)) is the magnitude of vorticity vector.

$$S_{ij} = \frac{\partial u_i}{\partial x_j} + \frac{\partial u_j}{\partial x_i} \tag{3.8}$$

$$\Omega_{ij} = \frac{\partial u_i}{\partial x_j} - \frac{\partial u_j}{\partial x_i} \tag{3.9}$$

$$|\Omega| = \sqrt{\Omega_{12}^2 + \Omega_{13}^2 + \Omega_{23}^2} \tag{3.10}$$

In equation (3.7), k_t is turbulent kinetic energy, $\delta_{i,j}$ is Kronecker delta, C_1, C_2 and C_3 are constants adjusted experimentally and l_m is the turbulent mixing length. The mixing length used can be described in terms of distance from boundaries and is defined as:

$$l_m = \kappa l_v f_\mu \tag{3.11}$$

In which $\kappa = 0.41$ is Karman constant, l_v is volumetric mixing length and f_μ is a damping function given by:

$$f_\mu = \min (f_s, f_w) \tag{3.12}$$

Where f_w is the damping effect received from solid wall boundary and f_s is the same effect coming from free surface boundary. Minimal damping value between f_s and f_w was used to be restrictive in terms of speculating the local turbulence magnitudes in the flow domain. For instance, if the computation is happening in the wall proximity, the smaller f_w value is counted as there is indeed less turbulence beside the wall. The volumetric length scale can be obtained according to the suggestion made by Aydın (2003):

$$l_v = \frac{\pi}{\int_w \frac{dA_r}{r^3} + \lambda \int_s \frac{dA_r}{r^3}} \tag{3.13}$$

The damping function is expressed in terms of new dimensionless length scales and the local shear velocity. The details of wall and free surface damping functions and their components are demonstrated in equations (3.14), (3.15), (3.16) and (3.17).

$$f_w = 1 - \exp(-l_{xv}^+ / A^+) \tag{3.14}$$

$$l_{xv}^+ = l_v u_\tau / \nu \tag{3.15}$$

$$f_s = 1 - \exp(-D^+ l_{zv}^+ / l_{xv}^+) \tag{3.16}$$

$$l_{zv}^+ = d u_\tau / \nu \tag{3.17}$$

l_{xv}^+ and l_{zv}^+ are dimensionless distances in which d is the vertical distance from the free surface, D^+ is a parameter that controls the damping rate and subsequently has an effect on the free surface velocity distribution, A^+=26 is a dimension-less constant and u_τ is local shear velocity. Local shear velocity can be computed from

$$u_\tau = \sqrt{\left|\nu \frac{\partial u}{\partial y} + \tau_{yx}\right| + \left|\nu \frac{\partial u}{\partial z} + \tau_{zx}\right|} \tag{3.18}$$

Determination of D^+ has been extensively explained in the next chapter. In order to find its value, measured free surface velocity is used. In fact, the D^+ has been adjusted in such a way that numerical model re-creates the close to reality surface velocities. The judgment for this comparison has been possible by collecting experimental measurements.

3.3 Mesh quality determination

To find the most optimum mesh quality for the solution domain, it is necessary that number of nodes are minimized to an optimum value. In addition, the solution result in that optimum state should be acceptable and has to receive no more improvement by refining the mesh.

Achieving this purpose is important because in further analysis, results of any findings through analysis ought not to be subject to change by changing mesh characteristics.

To fulfill this purpose, three various scenarios of which there is an experimental data available for comparison have been investigated. The cases include the rectangular channel aspect ratios of 2.066, 3.52 and 5.21 when channel bottom width is 0.6 meters. Aspect ratio for a rectangular channel is defined as the width of the channel divided by flow depth. More information on flow cases is given in Table 3-1.

Table 3-1: Flow cases used in mesh determination phase

Case	Aspect ratio	S_0	Z_n (m)	Discharge (m^3/s)
1	2.066	0.001	0.29	0.170
2	3.530	0.002	0.17	0.115
3	5.210	0.015	0.115	0.167

To decide on mesh size and number, it was firstly assumed that cells may remain approximately square at all times. This will make for an easier way of dealing with and referring to each case. The tested mesh sizes are like 0.75, 1, 1.5, 2, 2.5 and 3 cells per one centimeters in each primary direction, making for physical distances of 1.33, 1, 0.66, 0.5, 0.4 and 0.33 centimeters for each cell, respectively. For each case, solution results were examined for changes with refining the mesh. The so called solution priority, by the order of importance, is free surface velocity across the channel and discharge.

Although it was difficult to find standard common grounds between all the cases to decide on a unique mesh size, but in the first glance at all cases, what appears prominent is the nearly same solution results for the mentioned mesh sizes. In Figures 3-1, 3-2 and 3-3, numerical solutions of free surface velocity for mentioned mesh qualities are plotted alongside experimentally measured surface velocities obtained by PTV (Particle Tracking Velocimetry).

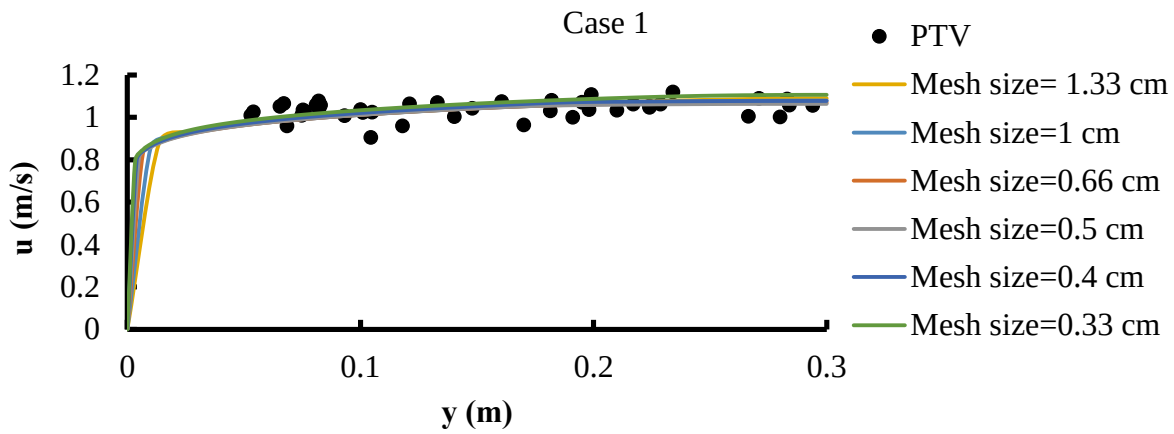

Figure 3-1: Numerical velocities for different mesh sizes with PTV results in case 1

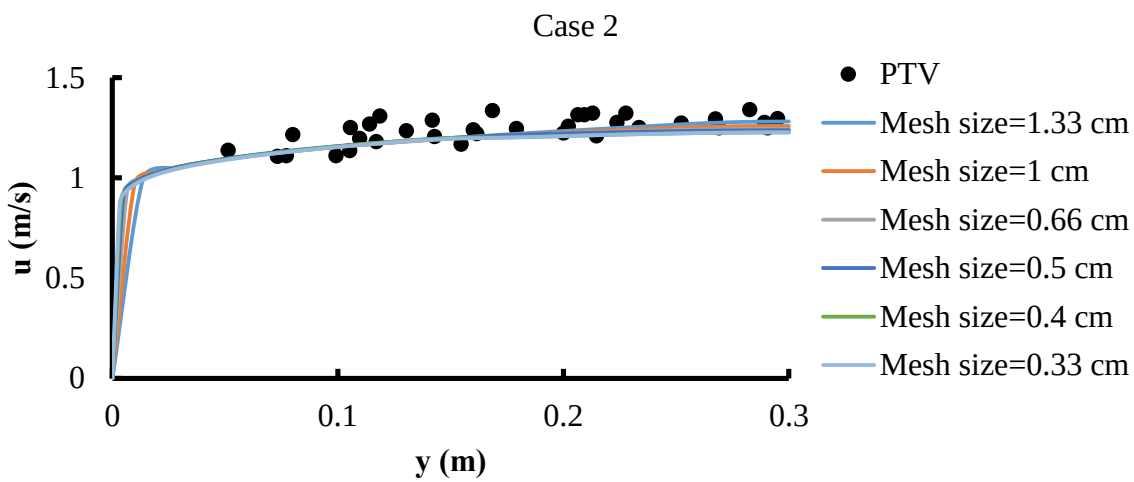

Figure 3-2 Numerical velocities for different mesh sizes with PTV results in case 2

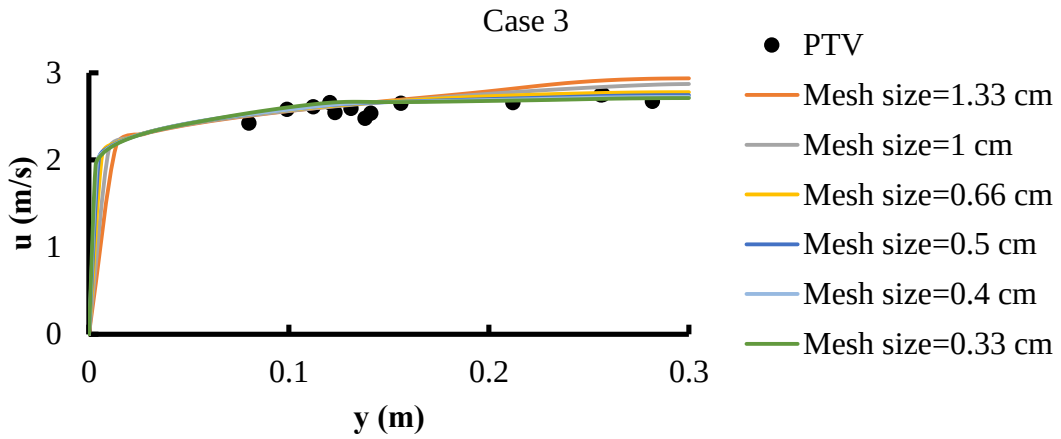

Figure 3-3: Numerical velocities for different mesh sizes with SPTV results in case 3

With a closer look at the results and comparing experimental and numerical values, the following table can be presented.

Table 3-2 : The surface velocity errors for named cases for mesh determination

Case1-Aspect ratio=2.066		Case 2-Aspect ratio=3.53		Case 3- Aspect ratio=5.21	
Mesh size (cm)	Surface velocity % error	Mesh size (cm)	Surface velocity % error	Mesh size (cm)	Surface velocity % error
1.33	0.979	1.33	2.494	1.33	4.540
1.00	0.500	1.00	3.247	1.00	3.267
0.66	0.307	0.66	3.418	0.66	2.482
0.50	0.032	0.50	3.598	0.50	1.737
0.40	1.210	0.40	4.067	0.40	1.534
0.33	2.826	0.33	4.270	0.33	1.423

In the Table 3-2, mesh size and surface velocity errors are presented. Surface velocity error is a rough estimate of difference existing between numerical and experimental velocities. To calculate the error, measured velocities from PTV which are fallen within the range of 5 to 30 cm away from side wall were averaged (considering half of the channel width due to

symmetry). Same mean value was computed for the numerical result in the same distance as the velocity remains nearly uniform in this reach. Then, the difference between these two values were cast into error display. It is noteworthy that since PTV velocities are not uniformly distributed across the free surface, the computed error cannot be a real index of what is usually referred to as error. Still, for the same calculation is compared in every case makes the comparison meaningful.

According to Table 3-2, error has a general trend of decreasing with increasing the mesh density up to 0.5 cm mesh size in case 1 implying that no further mesh improvement is needed. In case 2, error value is oscillatory up to 0.5 cm mesh size for which it increases after that, giving credit to the same conclusion found in case 1. In case 3, however, error appears to be continuously decreasing which is no less felt by visual recognition. A final decision on mesh size according to this error value is impossible unless other parameters are looked closer at. The important point to learn from these error values are that this index is large with course mesh and small with fine mesh, still the magnitude of error is not much of big difference to debate on.

When mesh size is finer than 0.66 cm, computation time increases significantly. Besides, with coarser mesh, first node by the side wall is insufficiently distant from wall as seen from all figures associated with cases of interest. Surface velocity distribution in Case 3 can provide an answer for mesh determination quest. That is, a minimum of 0.66 cm mesh size is obligatory and otherwise the free surface velocity distribution would be wavy.

Above all, the discharge gets minimal influence from mesh size which can be seen in Table 3-3. With considering all the facts and experiences behind the computer, mesh size of 0.66 cm was decided as the optimal mesh quality with a knowledge to a fair and square trade off.

Table 3-3: Numerical discharge for various mesh sizes compared to experimental discharge

Case 1	Exp. Q = 0.1706 m^3/s		Case 2	Exp. Q = 0.1153 m^3/s		Case 3	Exp. Q = 0.1675 m^3/s	
Mesh size (cm)	Num. Q (m^3/s)	Discharge % error	Mesh size (cm)	Num. Q (m^3/s)	Discharge % error	Mesh size (cm)	Num. Q (m^3/s)	Discharge % error
1.33	0.165	3.094	1.33	0.113	1.908	1.33	0.170	1.594
1.00	0.165	3.164	1.00	0.112	2.107	1.00	0.169	1.235
0.66	0.165	3.217	0.66	0.112	2.246	0.66	0.169	0.907
0.50	0.165	3.246	0.50	0.112	2.307	0.50	0.168	0.543
0.40	0.165	3.293	0.40	0.112	2.862	0.40	0.168	0.417
0.33	0.164	3.393	0.33	0.111	3.026	0.33	0.168	0.382

CHAPTER 4

ANALYSIS ON RECTANGULAR CHANNEL EXPERIMENTS

4.1 Uniform flow generation in smooth and rough rectangular channels

Uniform flow is a state at which flow depth, velocity and discharge at every section of the channel reach are constants. In such a condition, water surface slope, energy slope and channel bottom slope are all parallel. On the other hand, it is necessary that flow is fully developed to be so-called uniform. This can be possible if the velocity distribution across the channel cross section is unaltered in the reach. Such a stable pattern can be formed if the boundary layer is fully developed starting from a more uniform mean velocity over the cross section in the upstream towards a developed velocity distribution at the cross section once long enough distance has been elapsed heading towards downstream.

In the experiments conducted, for the glass channel of zero absolute roughness height, the Manning roughness was observed to be n=0.009 by optimization technique (while value of 0.009 to 0.01is usually suggested for glass in the literature) after surface profiles were closely investigated. To identify the laboratory glass Manning coefficient, experimental and computational surface profiles for the experimental working range (given in Table 2-2) were tried to be overlapped. This attempt can be actualized by minimizing the difference between computational and measured surface profiles while continuously shifting the value of Manning coefficient in search for optimal n value (this is called optimization method). The computation of surface profiles was assisted through gradually varied flow (GVF) analysis and a computer program was developed to look after this task (this computer code is supplied in Appendix F). From among several different methods of GVF analysis, direct

step method (DSM) was deployed. In direct step method, distances between computational nodes are calculated from assumed water depths using the energy relationship.

$$\Delta x = \frac{(E_2 - E_1)}{(S_0 - \bar{S}_f)} \tag{4.1}$$

In equation (4.1), Δx is the distance between two consecutive sections of different depths. E is the specific energy ($y+V^2/2g$, where V is average velocity) associated with a section. S_0 is the channel bed slope and $\bar{S}_f$ is the mean friction slope of two adjacent sections. The energy slope (S_f) is calculated using the Manning's equation.

$$S_f = \frac{V^2 n^2}{R_h^{\frac{4}{3}}} \tag{4.2}$$

In equation (4.2) R_h is hydraulic radius (four times area of cross section divided by wetted perimeter).

For the working set up in the laboratory, either S_2 or M_2 profiles were possibly generated for supercritical and subcritical flows, respectively. In supercritical flows (as for S_2 profile), the flow depth changes between critical depth and 1.01 times the normal flow depth. Therefore, for as many sections as there are nominated for the desired reach, computations were carried out from critical depth in upstream towards downstream normal depth. On the other hand, for subcritical M_2 profile, depth varies between 0.99 times normal depth and critical depth, nonetheless the calculations are done the opposite direction in regard to supercritical procedure, from downstream towards upstream.

Two symbolic results of the computations already explained are presented and compared to experimental surface profile records for two sub and super critical flow regimes in Figure 4-1 and Figure 4-2.

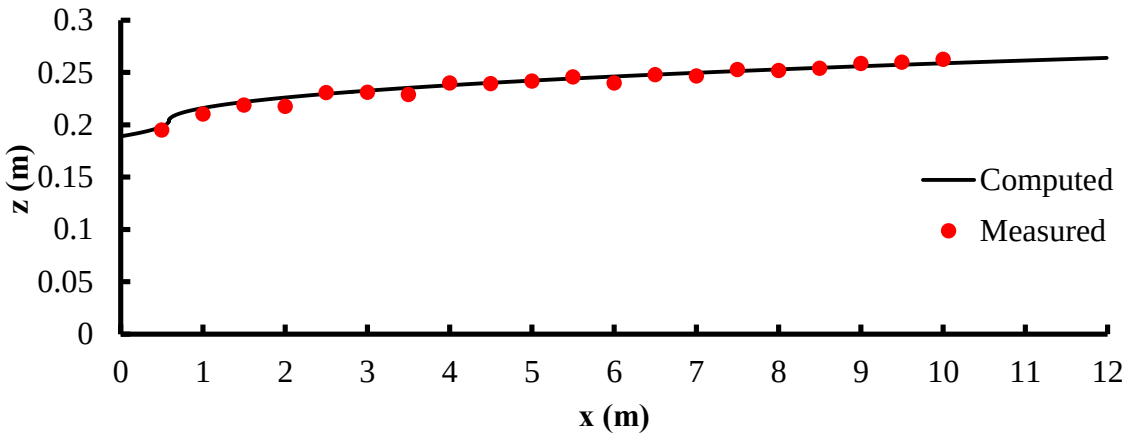

Figure 4-1: The computed and measured surface profiles for subcritical condition, S_0=0

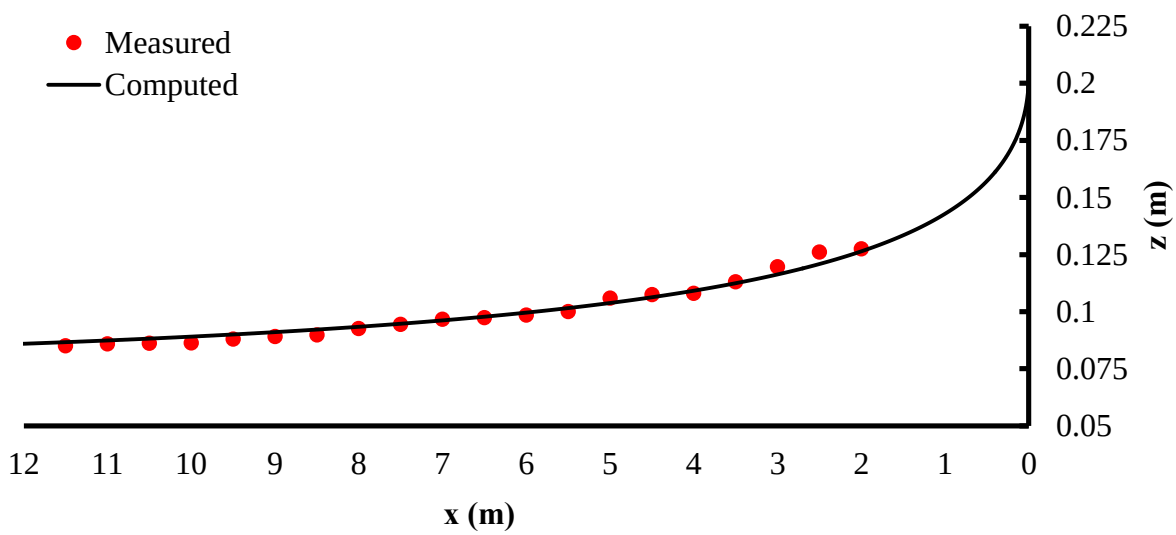

Figure 4-2 : The computed and measured surface profiles for supercritical condition, S_0=0.05

As seen in Figure 4-1 and Figure 4-2, the optimum Manning roughness value for matching computational and measured profiles is determined as 0.009. The surface profile for the rest of the experiments is supplied in Appendix G.

(Surface profiles for rough channels are not given in appendix because flow is uniform at most of the times.)

Determination of Manning coefficient is important because at times when uniformity is difficult to reach due to short length of laboratory channel, Manning relation can be used to find a uniform depth. This uniform depth can be enforced by either upstream or downstream plate or weir, respectively, to form uniformity.

It is worth to emphasize that uniformity establishment is especially hard to achieve in subcritical cases. In other words, GVF profiles in subcritical situations are far longer than their supercritical counterparts.

For the rough channels case, precisely identical approach is adopted. The only difference is that in very rough flow conditions, flow reaches uniformity quickly making the job easier to handle. The Manning roughness coefficient was already given in Table 2-1 as average values. The individual Manning roughness coefficients are also given in Tables 2-13 through 2-18.

One other issue in rough channels case is the correct bed elevation selection for uniform depth computation. Since there are roughness geometries on the bed of the channel, a mean bed elevation needs to be indicated for correct uniform depth value in the Manning relation.

According to a paper written by Pokrajac et al. (2007), the mean bed elevation for transvers square rib type roughness is calculated like:

$$Z_{mean}=Z_n- k^2/\lambda \tag{4.3}$$

In equation (4.3), Z_{mean} is the mean bed elevation, Z_n is the total water depth (from lower bed), k is dimension of side of the square and λ is the distance of ribs.

For bubble wrap type roughness a different sort of calculation is needed. The second type of roughness type used was bubble wrap attached to the bed of the channel (as already shown on Figure 2-7). The bubble warp sheet is a commercially abundant material used in the wrapping of fragile cargo very commonly. It consists of nearly cylindrical air bags that are placed tightly next to each other.

The procedure of finding a mean bed elevation for this roughness type is a simple one. Every cylindrical air bag is 3 mm high and has a diameter of 1 cm. In every 10 cm in 10 cm square area of this bubble wrap there are 81 air bags. Therefore, with subtracting the average air volume off the total bulk volume (air and water), imaginary average water thickness can be found. It is obvious that the bulk volume is the volume of a cuboid whose thickness is equal to that of air bag height (3 mm) and the air volume is the volume of air confined within 81 cylinders of 3 mm height and 1 cm diameter.

The result of the foregoing explanations yields the thickness of 1.9 mm for average air thickness and 1.1 mm for water. Thus, every time this type of experiments are conducted, the measured water depth (from lower bed bottom) must be subtracted by average fictitious air thickness which is 1.9 mm.

4.2 PTV remarks, experimental observations and error analysis

There are several general observations made in experiments and PTV image analysis. During the PTV analysis, a number of challenges were faced that provides room for establishing a set of do's and don'ts. The importance of such notes lays in that for the very unique purpose of discharge computation where only a few instantaneous surface velocities are going to be used, deviating from suggested remarks might endanger the accuracy of the calculations. The notes based on experimental observations are as follow:

a) The location where particle is dropped is a weighty issue. The laboratory particle dispenser is placed 1.7 meters upstream of the video recording section. Larger distances were shown to be unnecessary or even problematic by conducting tests. The particles seem to be amalgamating when they are to travel a large distance before arriving at the

recording station. This problem is certainly inevitable in large discharges as surface waves and turbulence distract the particles in random directions.

b) Another experimental observation marked was that the particles used to escape away the side walls in high velocities if they were dropped near the wall in the first place. On the other hand, it is known that velocity distribution over the free surface of water has a large gradient next to the wall due to larger vorticity in wall vicinity. Thus, it should be noted that surface velocity calculation by means of PTV is difficult in the high velocity gradient regions. Besides, mistaking the point wise velocity magnitude or its location near the wall will result in large errors in numerical discharge calculation.

c) Another issue revolves around camera distance to the water surface. In the camera calibration section, camera calibration proved that 1.5 m perpendicular distance from channel is sufficient to avoid distortion removal of the images. Even a shorter altitude has been reported by Polatel (2006) with no lens distortion effect on frames. Larger distance from the channel allows for more of the field (or particle travel distance) to be included in the analysis. This problem seems to be especially important when dealing with large velocities. For large velocities, either longer travel distance or higher recording speeds (larger fps) with shorter travel distances may be needed to obtain more dependable point wise velocities. This parameter was investigated for a couple of cases and the result shows that no outstanding effect can be seen on the analysis result as seen in Figure 4-3.

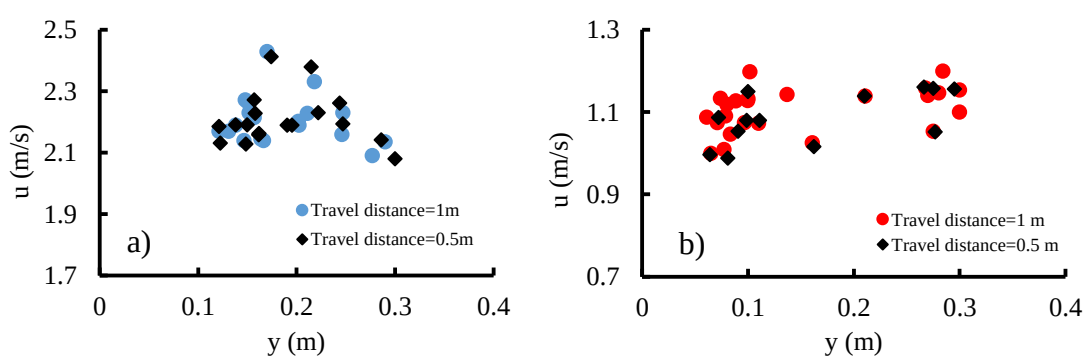

Figure 4-3 : Comparing effect of travel distance on PTV results (30 and 120 fps)- a) S_0=0.008, Z_n=0.135, Q=165.4 l/s- b) S_0=0.008, Z_n=0.03, Q=16.25 l/s

d) The most important remark made was determining a limitation on flow and recording speed in PTV. The free surface velocity and recording speed are inseparable icons of image processing. On a broader scale, the whole process is affected by several other factors as for particle size, camera distance to free surface, lighting condition (improves particle detection in high velocities), foams forming on the free surface (specific to high velocities), surface waves, light reflections, travel distance and the like. Particle size factor can be neglected as it cannot be taken any smaller than 0.5 cm square PVC pieces. The closer the camera gets into the recording flow field, particle size may be allowed to be taken smaller but then again images will be distorted. At the end of the day, the entire set of data was image processed using the nearly constant particle size. For the constant camera elevation of approximately 1.5 m and travel distance of nearly 0.5 m for the major portion of the free surface velocity analysis, a rough link was identified between recording speed (named as frame per second-fps) and free surface velocity. For identification of the so called fps relation with free surface velocity, take the case of S_0=0.008 and Z_n=13.5 cm for instance. The average free surface velocity near the center of the channel (0.1 m <y < 0.5 m for rectangular channel of 0.6 m width) is measured as 2.207 m/s via image processing. A typical frame of this case has been shown for the recording speeds of 30 and 120 fps in the Figure 4-4. The result of analysis for the circled particle (in Figure 4-4) has been shown in the Figure 4-5.

Figure 4-4 : Frames associated with 30 and 120 fps speeds for S_0=0.008 and Z_n=13.5 cm

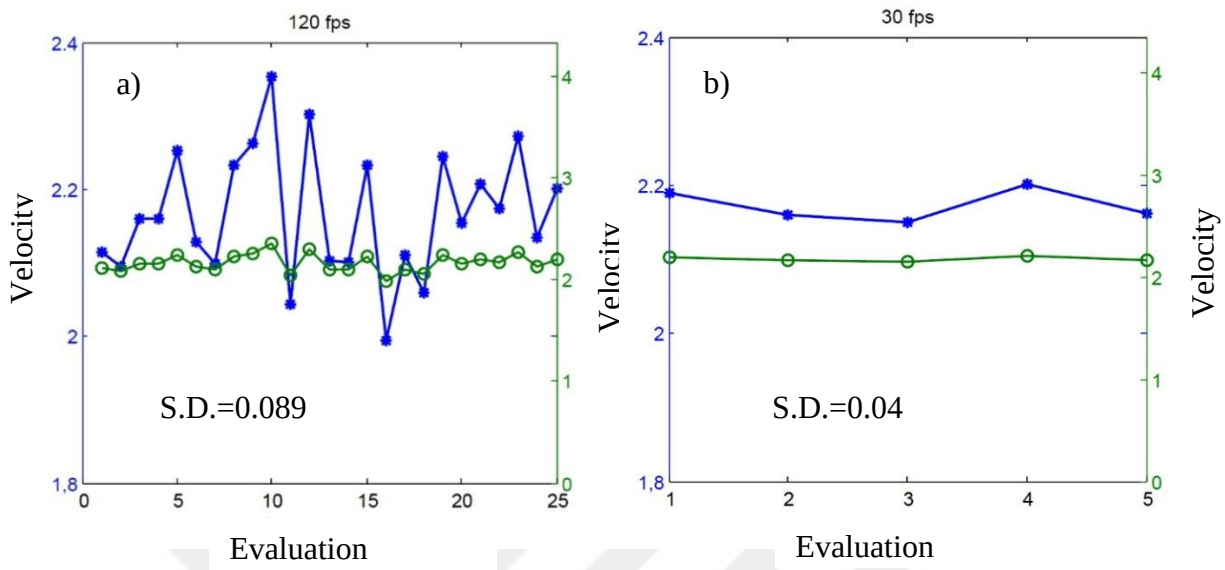

Figure 4-5 : PTV analysis comparison of 120 (a) and 30 (b) fps records for the circled particles in Figure 4-2

The time-averaged point wise velocity was calculated as 2.18 m/s for the particle at y=0.20 m in 30 fps footage and 2.16 m/s at y=0.225 m in 120 fps case. From the analysis of 120 fps footage, it is clearly distinguished that instantaneous velocity is highly oscillatory and only a time-averaged value can represent the true magnitude of particle velocity and therefore travel distance should be long enough. On the other hand, it was observed in the laboratory and presented in Figure 4-4 that in general for velocity magnitudes of larger than 2 m/s new challenges arise when dealing with 30 fps shooting. The air mixing on the free surface forming foams and particles that appear stretched and blending with the background images makes the particle detection phase rather tedious. Although under the condition of excess lighting and additional background contrast, boundary of 2 m/s might be pushed slightly upward, but for conventional working circumstances with ease, an estimate suggestion can be made.

L.fps/u=8 (lower limit recording speed) (4.4)

In equation (4.4), L is the travel distance (L=0.5 m) and u is the time-averaged point velocity that is 2 m/s here. In fact, 8 is the minimum number of frames to be analyzed for a footage. That is, at least 4 instantaneous velocities are to be averaged.

In search of upper limit of L.fps/u, maximum fps of 480 was adopted and a relatively small velocity of 1 m/s was used to come up with a rational ratio (performing analysis on 1000 fps footages requires additional lighting or either a closer camera position to the particle or a larger particle size and therefore is dismissed).

Take the case of S_0=0.008, Z_n=0.03 m and Q=16.25 l/s. The free surface velocity at the middle of the channel was measured as 1.18 (m/s). For the 0.5 m travel distance the velocity fluctuation is presented in the Figure 4-6.

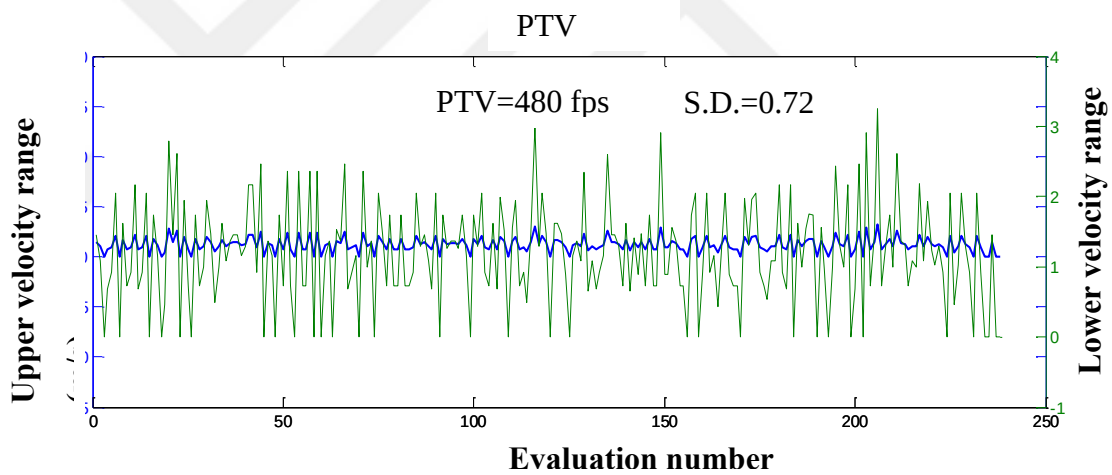

Figure 4-6 : The frequency of middle surface velocity for a particle (S_0=0.008, Z_n=0.03 m)

By examination of effect of travel distance on the mean velocity, the optimal travel distance and thereby optimal L.fps/u ratio will be calculated. The change of mean velocity of the particle as a function of travel distance is shown in Figure 4-7.

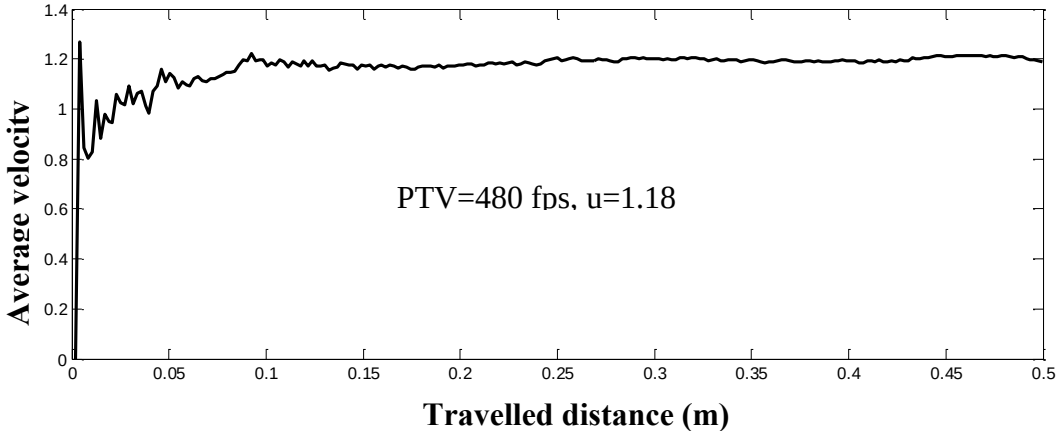

Figure 4-7 : The mean velocity plotted against the travel distance

Scrutinizing Figure 4-7 reveals that mean velocity of the middle surface particle goes independent of the travel distance when it has traveled long enough towards downstream. At around 20 cm, mean velocity is nearly constant. To stay on the safe side, 25 cm is used to calculate the desired ratio.

$$L.fps/u=120 \text{ (upper limit recording speed)} \tag{4.5}$$

In equation (4.5), L=0.25 m, fps=480 and u=1 m/s (rounded to a lower value, from 1.05 to 1). The mean velocity of particle half way down the path is calculated as 1.045 m/s which is only slightly different from 1.05 m/s as the mean velocity while all travel distance is covered. With the given explanations, an approximate range can be recommended to relate the velocity to be measured and the recording speed.

$$8 < L.fps/u < 120 \tag{4.6}$$

Equation (4.6) shows this range. The drawbacks mentioned earlier regarding the lighting condition, particle size and camera distance, background contrast and etc. should be

considered before making use of the suggested ratio. In other words, the suggested ratio can be used as a fair rule of thumb especially when laboratory working conditions are chosen, otherwise the boundaries of the mentioned ratio are open to change under various situations.

Another issue that will have to be dealt with is the error analysis for the mentioned analysis. For conducting an error analysis on the PTV results, usually another experimental free surface measurement is required such as Laser Doppler Velocimetry (LDV) or hot-film measurements for comparison. Hot film measurements were made and it was concluded and reported that the velocities measured via this method were valid in the depth but not near the free surface and therefore were dismissed.

As it was once explained in the seeding section, PVC particles are believed to receive minimum drag effect from air above and inter-particle attraction due to sparse load of seeding that can be assumed as negligible. On the other hand, in Polatel (2006), by assuming zero air resistance on confetti pieces, LDV measurements were conducted to compare LSPIV results of both Styropor (expandable polystyrene) and confetti to calculate an average percentage difference between the two measured velocities to correct the free surface velocity of Styropor which then the difference would account for the air resistance. They used Styropor after calibrating its surface velocity using confetti because of its practicality under extreme flow conditions. Confetti is very similar to PVC particles in thickness and density and it moves right on the air-water interface. Therefore, this is a credit to selection of PVC particles in the present study to make sure that the measurements are as close to true values as possible and otherwise, there may be need for fairly sophisticated technology for conduction of accuracy study because of need for a different measurement.

In this part, a relative error and a precision analysis can be offered for different velocities and recording speeds. Precision is usually associated with the consistency of results with the incline of repetition. For a given flow condition, a set of recordings with various shooting rates were carried out. The PTV results of each case (in a certain flow regime) were best fit into a logarithmic curve and the relative error was presented by calculating the difference between the function and the experimental data. The results are shown in Figure 4-8. The independency of free surface velocity on recording rate can be seen in the figure. Yet, remarks regarding the limitations on particle travel distance and speed mentioned earlier hold valid.

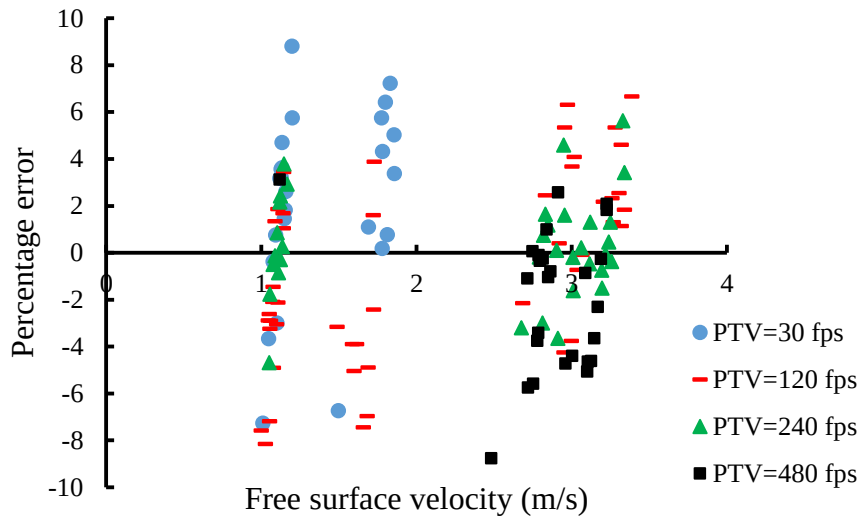

Figure 4-8 : Relative PTV error between best fit curve and data for a couple of flow conditions

Now that the independency of free surface velocity on recording rate has been demonstrated, it is feasible to conduct a more statistical error discussion named as precision analysis. Let us consider the cases for two typical velocities of nearly 1 and 3 m/s.

Case 1- low speed- (S_0= 0.008, Z_n= 0.03 m, $u_{average}$ =1.103 m/s and y= 0.093 m (distance from side wall on the free surface))

For analyzing the precision existing in the point wise velocities, a couple of recordings were made at a nearly fixed location for two cases. Table 4-1 shows the whole experimentally measured free surface at nearly 0.093 m away from wall. Observing a non-oscillatory pointwise velocity is impossible due to some reasons explained in the PTV remarks. Maintaining a particle on a fixed location is hard to achieve as well. Therefore, all measurements recorded between 0.08 and 0.1 m (in a channel of 60 cm width) away from channel wall are assumed acceptable and considered for a point wise velocity analysis. The average velocity of the complete PTV results is 1.10345 m/s for the particle that is located at an average distance of 0.093 m off the channel wall. The relative error of the velocities with respect to defined mean velocity is also shown in the Table 4-1.

Table 4-1 : PTV measurements for a nearly fixed point on the free surface (case 1)

Evaluation number	Distance from wall (m)	Velocity (m/s)	Relative % Error
1	0.083	1.046	-5.42
2	0.088	1.127	2.13
3	0.099	1.128	2.18
4	0.079	1.119	1.38
5	0.101	1.198	7.89
6	0.096	1.075	-2.64
7	0.096	1.060	-4.09
8	0.084	1.105	0.22
9	0.093	1.055	-4.59
10	0.108	1.119	1.38
11	0.101	1.101	-0.15
12	0.096	1.089	-1.32
13	0.083	1.120	1.47
Averages	0.093	1.103	

It is worth mentioning that there are no additional errors taking place in the whole process other than the ones nested in calibration phase in which image distances are converted into real world distances. This error –nevertheless too small- can occur when points over the image (indicating the distance) are picked manually in order to calibrate the image. Thus, no other measurement errors exist in the given analysis. For the thirteen set of PTV measurements, the average velocity is 1.103 m/s and the variance is calculated as 0.00149. Variance is an index of data spread around the mean value. Standard deviation (S.D.) is also computed as 0.03859 m/s. S.D. shows how the data is dispersed. As a rule of thumb it is accepted in statistical sciences that a data falling outside the range of '*mean +/- three times S.D.*' is an obvious outlier and can be eliminated from data set.

Variance = 0.00149

Standard deviation (S.D.) = 0.03859 m/s

u (mean) +/- 3 S.D. =1.219 – 0.987 m/s (none out of 13 data is located outside this range)

Case 2- high speed- (S_0 = 0.025, Z_n = 0.08 m, $u_{average}$ = 2.873 m/s and y = 0.292 m (distance from side wall on the free surface)) In Table 4-2, same quantities explained in case 1 are shown for case 2. None out of 7 data is found as outlier.

Table 4-2 : PTV measurements for a nearly fixed point on the free surface (case 2)

Evaluation number	Distance from wall (m)	Velocity (m/s)	Relative % error
1	0.288	2.874	0.007
2	0.295	2.796	-2.782
3	0.288	2.993	3.999
4	0.291	2.821	-1.871
5	0.292	2.936	2.119
6	0.297	2.825	-1.726
7	0.296	2.871	-0.097
	Average distance = 0.292	Average velocity = 2.873	

Variance = 0.0042

Standard deviation (S.D.)= 0.0648 m/s

u (mean) +/- 3 S.D. =2.678 – 3.067 m/s (none out of 7 data is located outside this range)

u (numerical)=2.88 (m/s)

The experiments with which the mentioned remarks are made and the related flow conditions are given in Tables 2-3 to 2-11, are attached in Appendix H. This Appendix, include the data base for surface velocity measured by PTV. Only half of the free surface (0 < y < 0.3 m) is shown due to symmetry.

4.3 PIV remarks, experimental observations and post processing

PIV image processing procedures consist of the following steps: selection of region of interest, mask creation to leave out void areas, background treatment for providing necessary contrast, running the cross correlation analysis, error detection and erroneous vectors' removal or post processing.

In Figure 4-9 the region of interest has been shown with yellow dashed rectangle for a typical PIV analysis. While the free surface is only enclosed to the yellow parallel lines, the analysis near the channel wall faces difficulties if no additional free board is considered on either sides. In addition, near wall analysis are sometimes confronting shortcomings in a number of conditions due to existence of vortical motions happening under sharp velocity gradient in the vicinity of wall. For the same phenomenon, the particles near the channel wall seem to escape away towards the center making the image analysis difficult near this zone.

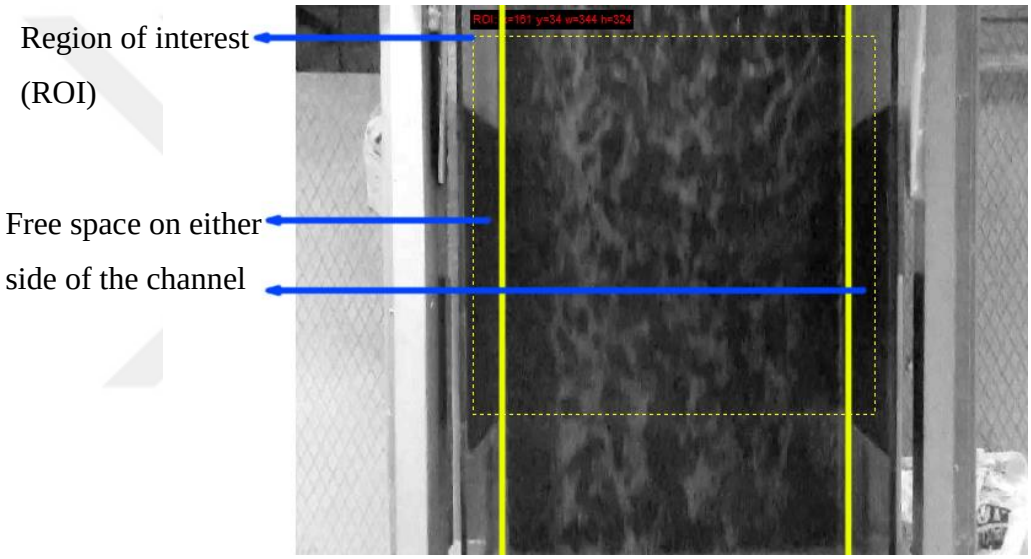

Figure 4-9 : A typical PIV analysis with sawdust and ROI (region of interest) manifested

In relatively larger velocities, due to velocity gradient getting pushed closer to wall, the entire free surface velocity computation seems achievable as compared in Figure 4-10, or otherwise longer footages has to be taken and analyzed to get the entire velocity distribution.

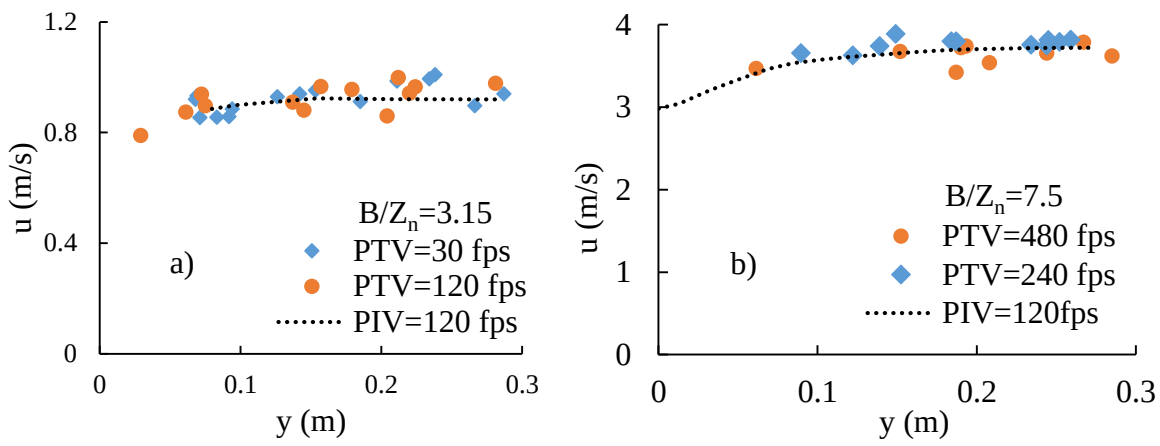

Figure 4-10 : The comparison of slow and rapid free surface velocities obtained by PIV and PTV analysis- a) S_0=0.001, Z_n=0.19 m, Q=95.45 l/s- b) S_0=0.0368, Z_n=0.08 m, Q=162.3 l/s

Figure 4-11 demonstrates the result of PIV analysis for the high velocity case shown in Figure 4-10 with the vector field shown. The vector field is then averaged alongside the channel (in flow direction) due to the assumption of flow uniformity.

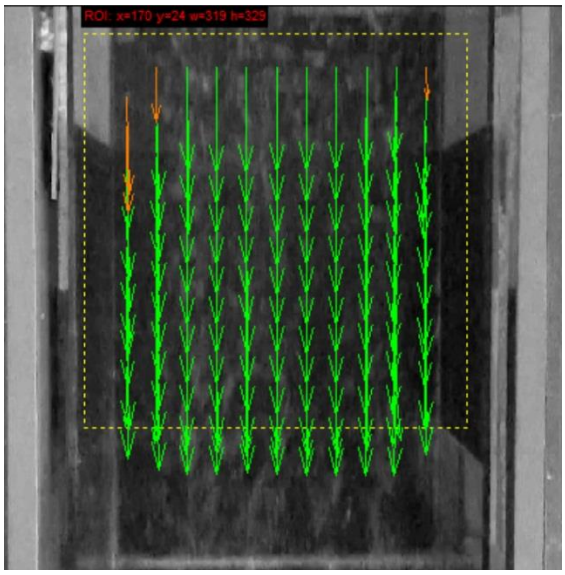

Figure 4-11 : The result of a complete PIV analysis that is used to exploit the free surface velocity.

Another observation made was PIV method failure in rough open channels in certain flow conditions. PIV technique was deployed over rough channel as well. The roughness elements were provided via a series of square ribs set along the channel in transvers direction to the flow. As a result, uniform flow depth naturally increases due to increased turbulence and resistance to flow. According to Roussinova and Balachandar (2011), turbulence intensities are found to be significantly enhanced in presence of roughness. Near the crest of the ribs where shear layer develops, highest turbulence intensities and Reynolds shear stresses are obtained. While turbulence increases, the surface receives effects, subsequently. The existence of structures of various kinds prompts the free surface to appear chaotic. A closer observation of the free surface- when seeded- reveals that particles seem to move towards random directions even in a simple uniform flow that is probably the primary reason for inaccurate results obtained by PIV analysis. It is noteworthy that the conventional cross correlation algorithm used in PIV analysis suffers a number of drawbacks for which an avid reader can find additional information in articles mentioned in related sections of Chapter 1. Among the drawbacks of cross correlation PIV, the presence of velocity gradient in chaotic surface structures can be associated with inaccurate PIV results in rough channels. Based on the present study, PIV analysis was only useful for the smooth channels. Moreover, a more detailed investigation has been reported by Roussinova and Balachandar (2011) regarding the effect of roughness elements and flow depth on turbulence structures.

In Figure 4-12, the foregoing statement has been articulated in visualizing the low velocities computed through PIV when compared to larger Pitot tube and PTV surface velocity measurements for just a typical case. Pitot tube measurements were made at a location of nearly 1.5 cm under the free surface. In Figure 4-12, flow depth is 11.73 cm, making the aspect ratio 5.11 meaning that dip effect will be negligible on the surface velocity and that Pitot measurements maybe a trustable option for making comparisons.

In Figure 4-12, λ is the distance of the ribs, k is the side of the square rib (see Chapter 2, section 2.1.2 for roughness geometries), S_0 is the channel slope and F_r is Froude number.

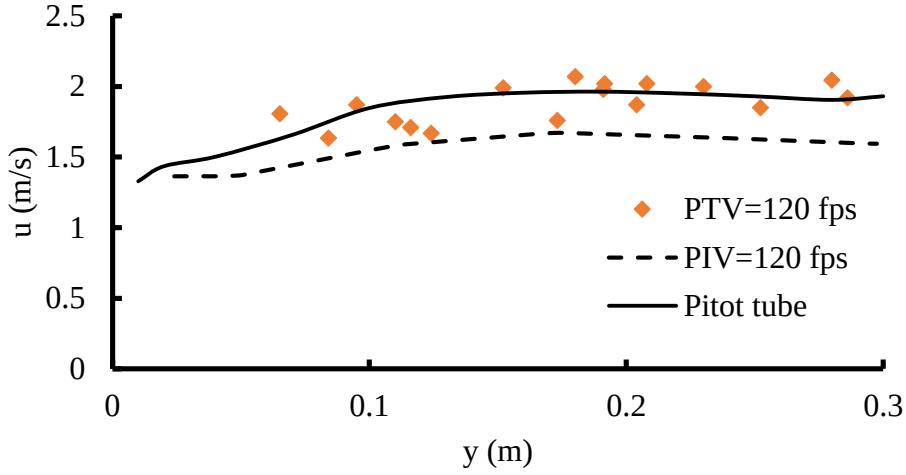

Figure 4-12 : Surface velocities compared for measured and calculated values under rough channel flow condition, S_0=0.035, F_r=1.35, λ/k=20

Under present study, for low relative roughness and small Froude numbers, where flow would appear calm and free of surface structures, PIV was found to give acceptable results regardless of rib existence.

Another issue is to identify a border for which PIV starts to fall off the accuracy. From literature point of view, it was already stated that PIV lacks accuracy in high velocity gradient regions. When flow occurs in rough rectangular channels and when it is supercritical, the images of the sawdust proves the existence of such velocity gradients almost all across the free surface. This maybe the reason behind its relative failure. Identifying a region such as a Reynolds number range to specify a border for either avoidance or conduction of PIV is a difficult question to answer and is beyond the objectives of this research. But it can be claimed with ease that PTV works absolutely better than PIV when free surface is very turbulent and chaotic to the vision based on experimental observations.

Post-processing of the PIV analysis- erroneous vector removal- in PIV analysis is also a weighty subject. Given the statistical means used to calculate the displacements and the

imperfections (noise) of the recorded images, it is possible to get false velocity vectors out. Numerous post processing routines are reported to detect such vectors by Raffel et al. (1998). In the present study, post-processing consisted zone of accuracy for the PIV analysis. Because of image noises that is mostly due to light reflections, some of the analysis pertaining to a certain frame and location on the frames yield obviously wrong velocity magnitudes. These outliers are meant to stand out from the crowd in a velocity range acquisition shown in Figure 4-13. Selection of the velocity range as shown in blue rectangle (in Figure 4-13) eliminates the inaccurate vectors. The velocity range restraining is a constructive tool to maintain the accuracy of analysis especially when flow field is as simple as that of a uniform flow in rectangular prismatic channel. In Figure 4-13, every dot is simply the velocity magnitude computed on any interrogation area for the whole recording length and entire flow field.

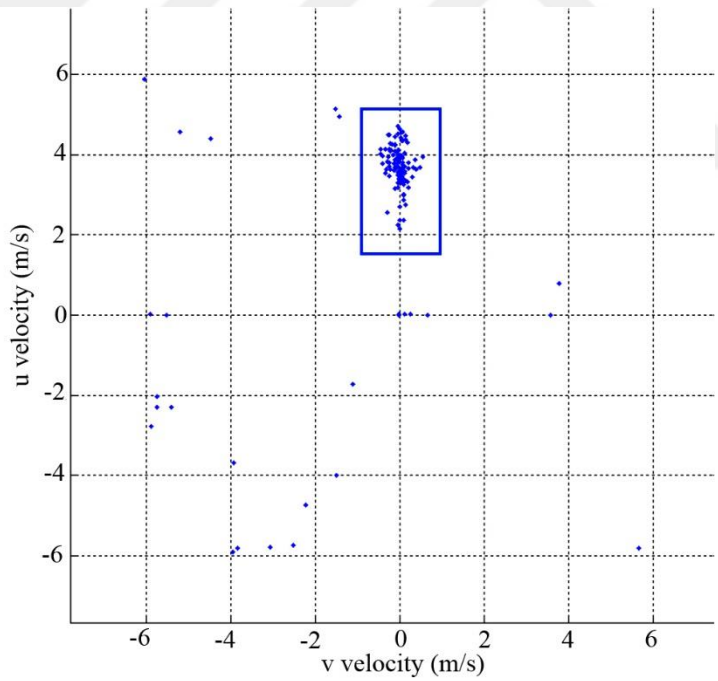

Figure 4-13 : Selection of velocity range for a typical PIV analysis

As a final step, the vectors computed across so many frames are averaged throughout time to yield a single velocity distribution. The longer the duration of recordings, the more precise the results. As a rule of thumb, the recording time was set as minimum 5 to maximum 10 seconds. (The result of PIV measurements are provided in Appendix I).

4.4 Surface damping parameter in smooth rectangular channels (D^+)

In chapter 3, the damping functions (f_w and f_s) and their contribution in the numerical model were shown. For surface damping function (f_s), initially a similar function to wall damping function (f_w) was tried where the only difference was in substitution of volumetric mixing length with vertical distance from surface. The result was the failure of dipping phenomena identification on the computations part. Dipping phenomenon is the shifting down of the location of maximum velocity in the plain of the channel cross section due to existence of secondary currents, whereby typically associated with appearing of maximum velocity near under the central free surface.

Finally, after trying a number of configurations for surface damping parameters, a more whole-domain-representative relation was adopted to capture dipping in addition to correct surface velocity (equation (3.16)). The D^+ parameter is observed to have the desired influence on the mentioned fact. Finding the D^+ relation is dependent on experimental data in order to match the numerical solution to the experimental conditions. This parameter affects on velocity distribution, free surface velocity and to a less extended degree on the discharge.

The procedure of finding the D^+ is explained in a series of steps as follows:

1- Experimental data for a variety of flow conditions (Aspect ratios, more specifically) were provided.
2- D^+ was searched for its optimum value to best match numerical solution with experimental observations (Free surface velocity and discharge, were respectively the important values of interest to carry out the comparing and matching phase).
3- Individually found D^+ values for every case were plotted against many different parameters to find the possible correlation between them.
4- D^+ was seen to be correlated with aspect ratio (B/Z_n) in rectangular sections. In which B is channel width and Z_n is normal flow depth. Later it was assumed that a similar value like T^2/A can be replaced with aspect ratio for a non-rectangular section, where T is free surface width and A is flow area. In any case, for rectangular section both vales are identical.
5- The individual D^+ values when plotted against T^2/A were best fit into a second degree polynomial.

6- The obtained function (2nd degree polynomial) was used to repeat each computational run and the result of comparisons between the numerical solutions and experiments are presented here.

Based on the steps explained, Figure 4-14 shows the individual D^+ values with respect to T^2/A and the best fit function forming the desired relation between them.

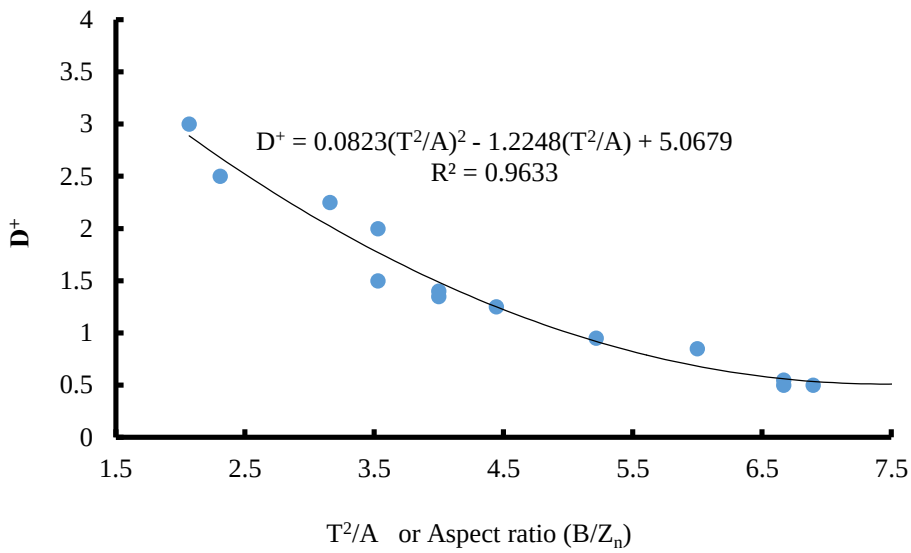

Figure 4-14 : Surface damping parameter (D^+) versus T^2/A in smooth rectangular channels

Equation appearing within Figure 4-14 is a 2nd order polynomial and is relating D^+ values to a geometrical factor (T^2/A).

$$D^+ = 0.0823(T^2/A)^2 - 1.2248(T^2/A) + 5.0679 \quad (4.7)$$

For all the computational runs, same mesh quality (explained in chapter 3, section 3.3) and same termination criteria was imposed.

In the Table 4-3, a couple of different flow conditions and aspect ratios were considered with regard to foregoing D^+ discussion. The values of D^+ have been computed via equation (4.7).

Table 4-3 : Measured and computed discharge comparison with the D^+ coming from equation (4.7)

Case	Slope	D^+	Z_n (m)	Aspect ratio	F_r	$Q_{exp.}$ (m^3/s)	$Q_{num.}$ (m^3/s)	% Error in Q
1	0.045	0.53	0.087	6.89	3.37	0.162	0.168	3.214
2	0.013	0.91	0.115	5.21	2.28	0.167	0.168	0.711
3	0.008	1.25	0.135	4.44	1.77	0.165	0.165	0.253
4	0.008	0.56	0.090	6.66	1.78	0.090	0.092	2.478
5	0.004	1.77	0.170	3.52	1.23	0.163	0.161	1.215
6	0.004	1.48	0.150	4.00	1.24	0.136	0.135	0.925
7	0.004	0.56	0.090	6.66	1.26	0.064	0.064	0.713
8	0.002	0.68	0.100	6.00	0.89	0.053	0.051	2.072
9	0.002	1.77	0.170	3.52	0.87	0.115	0.112	2.643
10	0.001	2.88	0.290	2.06	0.58	0.170	0.165	3.372
11	0.001	1.48	0.150	4.00	0.62	0.068	0.064	5.529
12	0.001	2.02	0.190	3.15	0.61	0.095	0.090	5.248
13	0.001	2.67	0.260	2.30	0.59	0.147	0.140	4.885

In Table 4-3, the numerical and measured discharges are compared using the best fit function for D^+ generation. It can be seen from percentage error difference that both discharges are matching close. The more important issue here is the matching surface velocities because discharge is to be computed using that surface velocity. For the 13 cases shown in Table 4-3, numerical surface velocities, as expected, were close enough to the experimental velocities. It should be reminded that individual D^+ values were come up with, with favoring the closeness of numerically computed surface velocities to experimental values in the first place.

As typical examples, two of the cases (3 & 6) from among 13 cases of Table 4-3 are discussed further leaving the rest to the Appendix J. In Figure 4-15, numerical surface velocity is compared to experimental point-wise measured velocities for half of the domain due to symmetry pertaining to case 6. The velocity distribution for the same case (6) has been demonstrated in Figure 4-16 also for cross section of the channel. Dimensionless velocity distribution for the half of the domain is displayed because of symmetry. Following

these two figures, streamlines for secondary currents are shown in Figure 4-17, too. The secondary currents are the main reason of dipping that seems to be pulling the maximum velocity below the water surface.

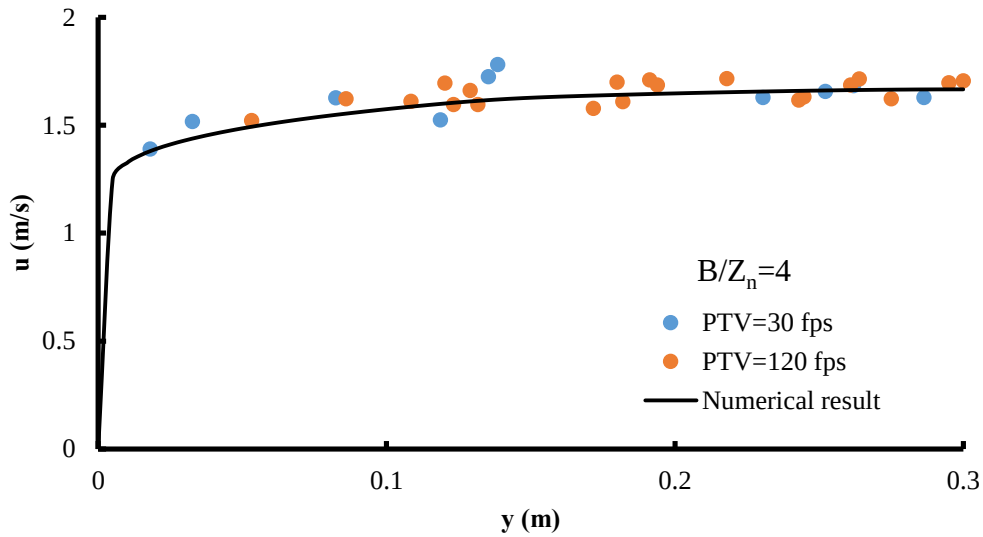

Figure 4-15 : Numerical and experimental surface velocities for case 6 (S_0=0.004, Z_n=0.15 m and Q=0.1363 m^3/s)

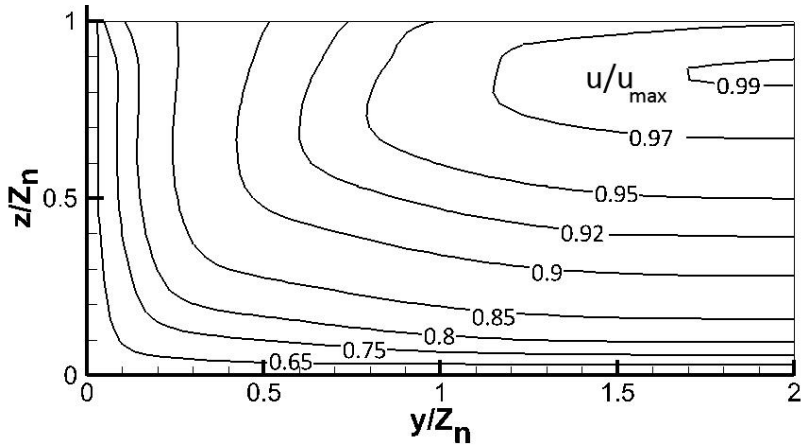

Figure 4-16 : Numerical velocity counters over the channel cross section for case 6 (S_0=0.004, Z_n=0.15 m and Q=0.1363 m^3/s)

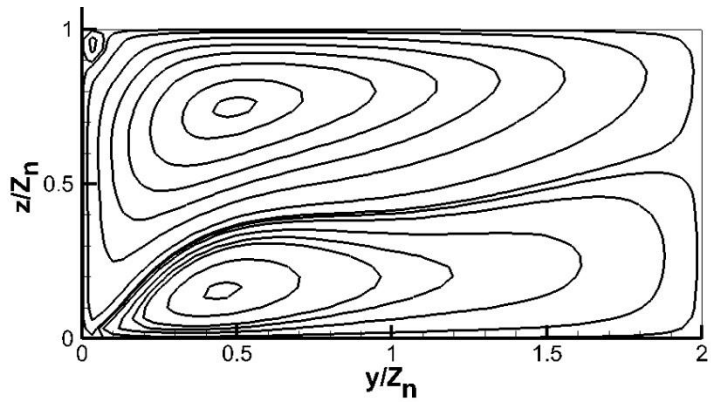

Figure 4-17 : Streamlines for secondary currents for case 6 (S_0=0.004, Z_n=0.15 m and Q=0.1363 m^3/s)

The same set of information for case 3 are demonstrated in Figures 4-18 through 4-20.

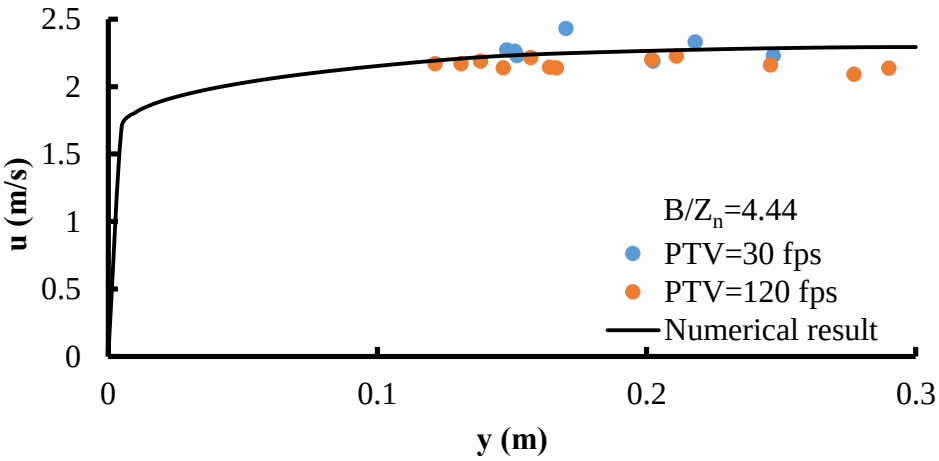

Figure 4-18 : Numerical and experimental surface velocities for case 3 (S_o=0.008- Z_n=0.135 m- Q=165.4 l/s)

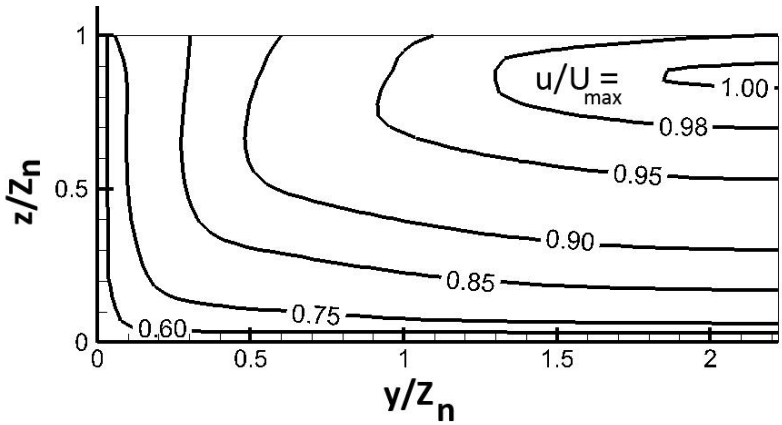

Figure 4-19 : Numerical velocity counters over the channel cross section for case 3 (S_o=0.008- Z_n=0.135 m- Q=165.4 l/s)

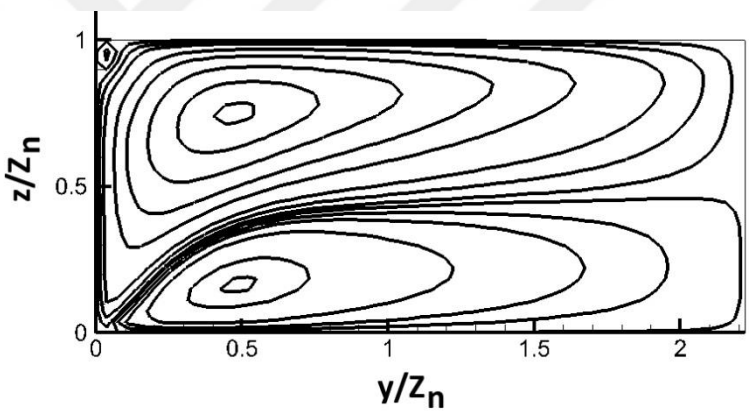

Figure 4-20 : Streamlines for secondary currents for case 3 (S_o=0.008- Z_n=0.135 m- Q=165.4 l/s)

4.5 Surface damping parameter in rough rectangular channels

For determining the value of D^+ (the parameter that controls the free surface damping and thus velocity distribution) in rough rectangular channels, it is necessary that absolute roughness (k_s) value be known first. In other words, it is impossible to complete the numerical solution with two unknowns (k_s and D^+) at once.

For computing the k_s values, the Colebrook equation was used

$$\frac{1}{\sqrt{f}} = -2 \text{ Log} \left(\frac{k_s}{3.7D_h} + \frac{2.51}{Re\sqrt{f}} \right) \tag{4.8}$$

In equation (4.8) f is the friction factor and is already discussed in Chapter 2, section 2.2.2 (Plus, values of absolute roughness will be given in section 4.6).

By contrast to smooth channel case, in rough channels there are two parameters effecting the surface damping term. One already known was geometrical term (T^2/A, where T is free surface top width and A is the cross sectional area) and the other parameter influencing the D^+ is absolute roughness (k_s). In order to remain as general as possible, usually it is better to work with dimensionless parameters, therefore k_s/D_h or relative roughness where D_h is hydraulic diameter has been used in analysis.

In smooth channels, it was demonstrated that the D^+ value was merely a function of flow section geometry. It is noteworthy that in both smooth and rough cases, the important criteria for determining the D^+ value should be the correct surface velocity and the accurate discharge.

Initial investigations on the behavior of the D^+ in rough channels reveals that it is dependent on both relative roughness and geometry of the flow section. However closer interrogations show that as the relative roughness increases, the D^+ value is almost constant and independent of geometry. In Figure 4-21, roughness has been plotted against the relative roughness value for all rough channels that were studied. For the nearly constant relative roughness, D^+ was searched separately to make sure that the value of D^+ is indeed independent of section information and is a constant value. This claim has been shown on Figure 4-21 using up-straight vertical lines.

(Note that finding individual D^+ values, similar to doing so in smooth channels, is the act of adjusting the numerical and experimental free surface velocities for every available experimental data by shifting the D^+ value with a pre-speculation of absolute roughness).

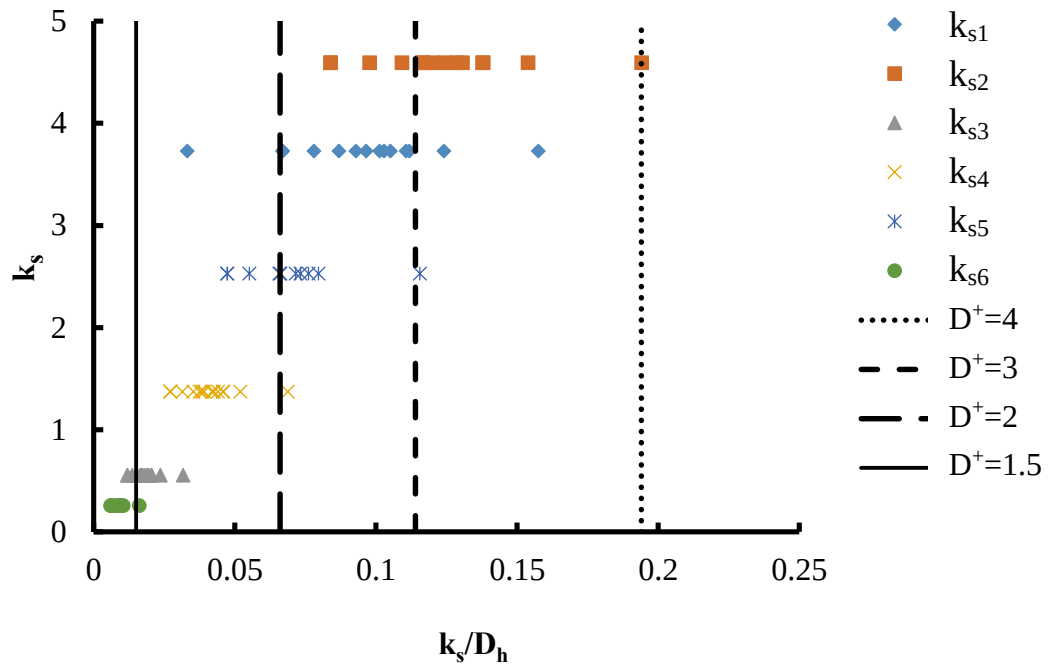

Figure 4-21 : Roughness plotted against relative roughness with D^+ spectrum shown

On the other hand, for the smallest absolute roughness of k_{s6} the individual D^+ are drawn next to smooth surface D^+ curve in Figure 4-22.

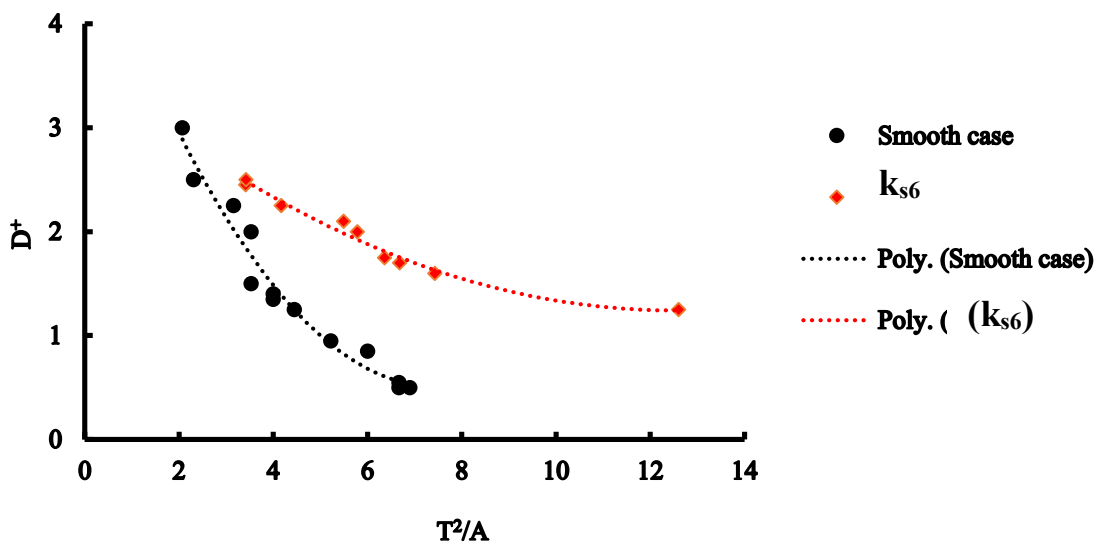

Figure 4-22 : D^+ values for smooth and k_{s6} cases plotted against the T^2/A

As seen from Figure 4-23, value of D^+ gets larger as the roughness increases approaching to constant values. The same trend was later observed with even larger relative roughness where flatter curves are seen.

In Figure 4-23, where D^+ for k_{s6} (smallest absolute roughness) has been shown, it is clearly seen that D^+ in this roughness type receives influence from both flow section geometry and relative roughness.

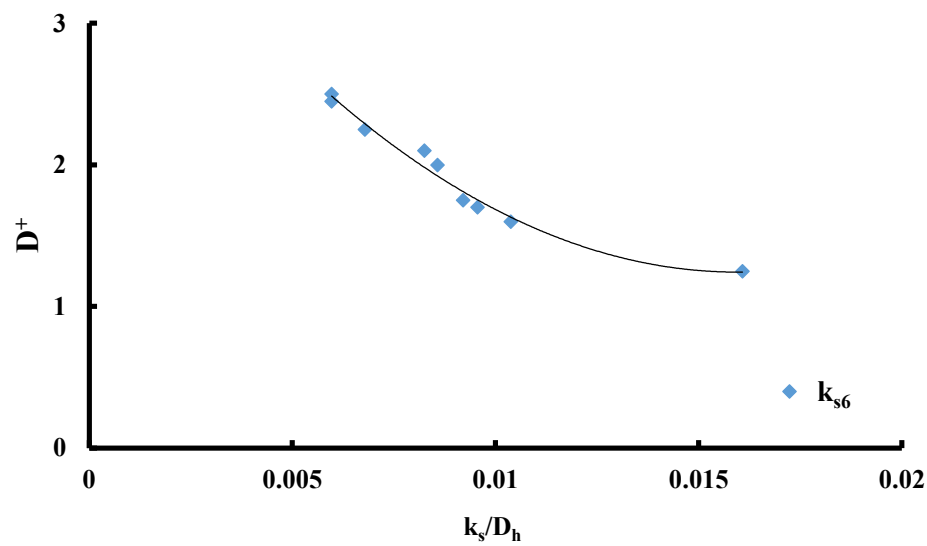

Figure 4-23 : D^+ values for k_{s6} case plotted against relative roughness

To the contrary, this pattern doesn't exist for all the other larger roughness types. That is, as the relative roughness increases, D^+ becomes less dependent on geometry of the flow but rather more dependent on the relative roughness.

All the observations marked so far remind that there could be a universal function to house all the D^+ values. This function was assumed one similar to Colebrook function due to the similarity of natures of the concepts and will be verified later.

The proposed function used to best fit all the individually found D^+ values for all roughness types is recommended as:

$$D^+ = -a \, \mathrm{Log}\left(\frac{k_s}{b\, D_h} + \frac{A\, c}{T^2}\right)^{-d} \qquad (4.9)$$

In equation (4.9) a, b, c and d are constant values to be determined after best fitting the data to the function. The constants are found as follows after best fitting the function to the individually determined D^+ values.

A=-0.35, b=6, c=0.035, d=2

The practicality of the function was verified in comparing the numerically computed discharge and free surface velocities to the experimental measurements. The error between the numerical and experimental discharge for the available data set are shown in Figure 4-24. Still it should be noted that since only an average Colebrook absolute roughness has been used for every roughness type, it is expected that the error is well affected by that rough estimation in addition to many other possible sources of error such as experimental shortcomings.

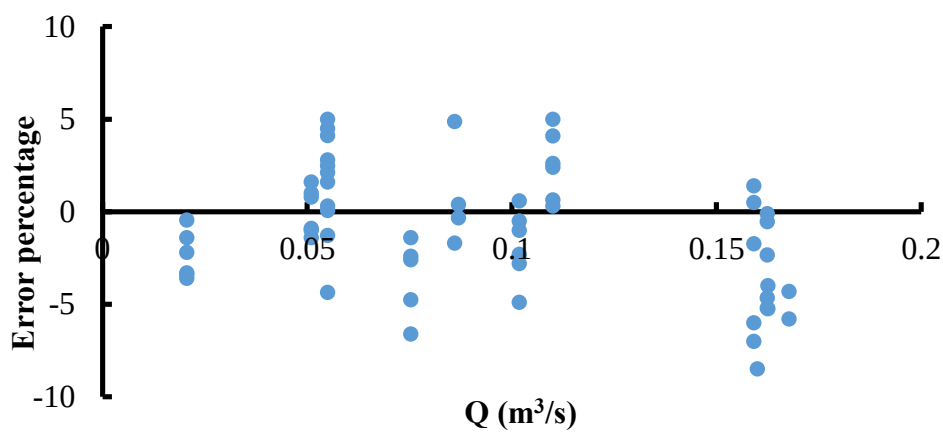

Figure 4-24 : Relative numerical and experimental discharge error when equation (4.9) has been used as the D^+ formula

(Note: Sometimes the discharge error was greater than 10 percent, those data sent are excluded from analysis and from Figure 4-24.)

It is necessary to emphasize that the given absolute roughness values to the numerical solution as an input -which is an average of all flow cases for any specific roughness type- in the D^+ search phase is a major source of discharge error. This is because the absolute roughness value is not a fixed value in the case of open channel flows, unlike pipe flows for instance. The absolute roughness value in open channels can change according to the

magnitude of relative roughness and hydraulic diameter. To more clearly state it, in a certain roughness geometry, for every flow condition there could be a unique absolute roughness associated with specific hydraulic diameter (and in numerical sense it can be determined inversely to minimize the discharge error as small as possible.)

The proposed function (equation (4.9)) and the data points (individual D^+ values) are plotted in Figure 4-25.

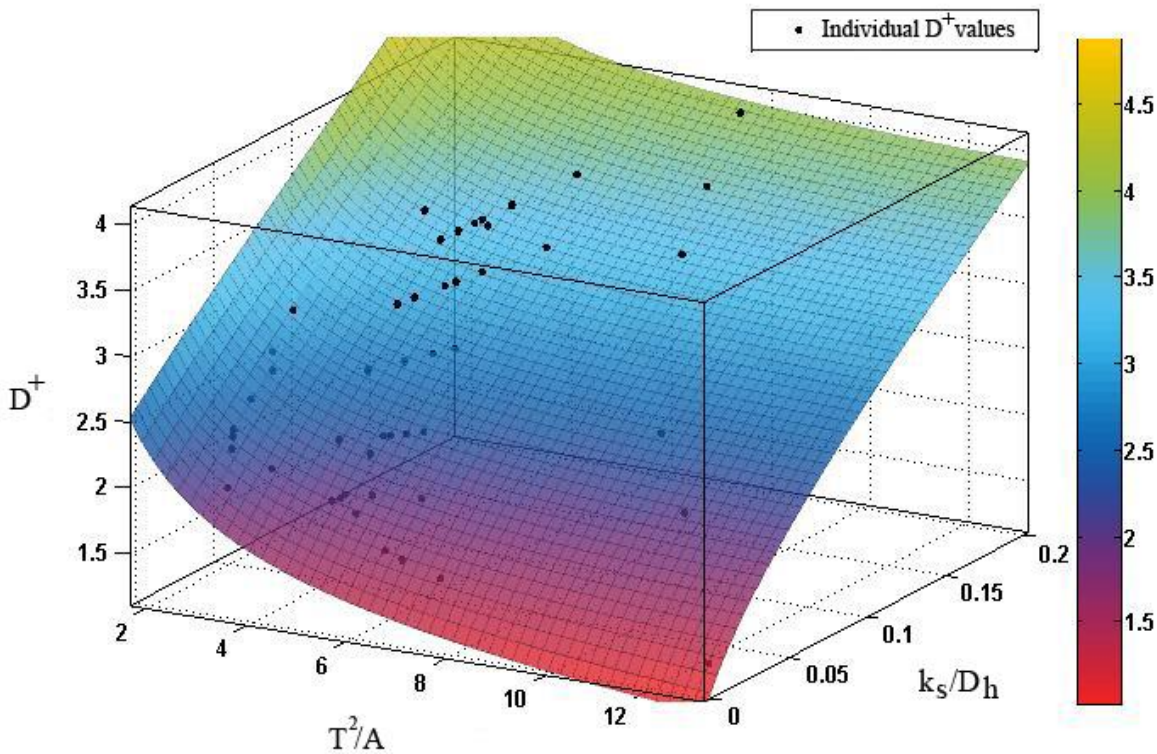

Figure 4-25 : Proposed logarithmic function as being best fit to individual data points for rough case D^+

A different view is presented in Figure 4-26. The figure shows clearly that D^+ is getting less and less influenced from geometry as aspect ratio grows. The curves are plotted for a few cases in which relative roughness is kept constant. This behavior is a similar one to Moody chart curves.

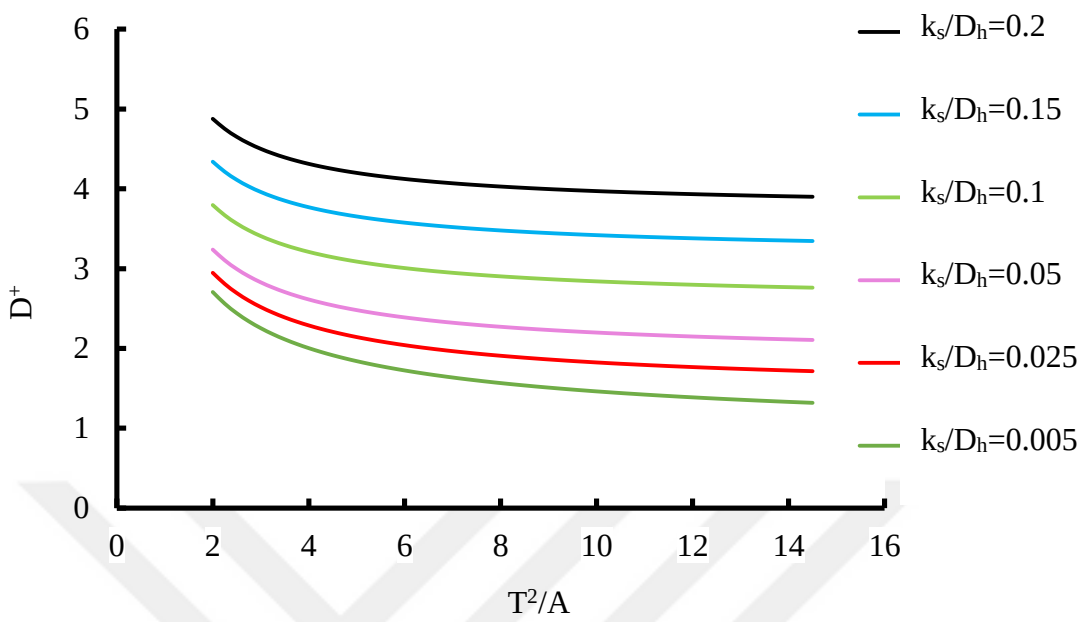

Figure 4-26 : Contours of D^+ function plotted with regard to T^2/A for constant relative roughness

4.6 Inverse solutions for roughness and discharge estimation in rectangular channels

The definition of inverse solution here can be described as in backward search of some kind in which roughness and discharge are computed at once.

It was explained earlier that the main objective of the present study is to make use of free surface velocity in order to make this inverse problem soluble. To be more specific, it is to say that there is a unique roughness (to be determined inversely) for which experimental surface velocity is going to match its numerical counterpart (numerical surface velocity is a result of solution which yields the discharge as well).

The research objective in the first place was to investigate to which extend it is possible to minimize the need for measured surface velocity. For roughness and discharge determination, as a first attempt, it was decided that merely an instantaneous experimental velocity data for a specific point on the free surface would be used (It is named instantaneous because recording lasts a short while just long enough for a particle to enter and exit the view zone of the camera).

However, the analysis shows that pinning the hope on only one measurement that is very much not average-representative, does not contribute to accurate roughness and therefore discharge estimation. The result of this try has been shown on Table 4-4 and Table 4-5 for the largest and smallest roughness cases, respectively. It is obvious that the findings of these extreme cases are mostly likely applicable to any other case in between.

In these tables, y and u demonstrate the distance from channel wall and free surface velocity, respectively. For every specific flow condition, the largest and smallest PTV data (velocity) are used for inverse solution. In order to clarify the practicality of the concept of a single point employment, only the upper or lower most surface velocity was considered to obtain maximum and minimum discharge estimations.

As an example, once the largest free surface velocity data has been used for inverse solution, maximum discharge and the least probable roughness values have been estimated inversely. This has been named on Figure 4-27 as upper bound range. In the same manner, if smallest surface velocity point is used for inverse solution, maximum roughness and least discharge value have been computed. The reason behind this kind of approach is to make sure that there is going to be no larger error percentage than what is given on these two Tables (4-4 and 4-5).

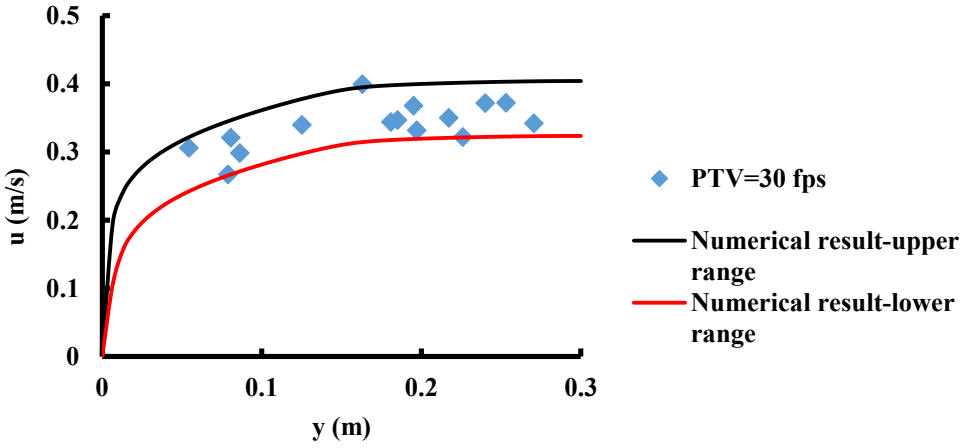

Figure 4-27 : The upper and lower bound of numerical surface velocity when single reference data point on free surface is employed

Table 4-4 : The result of discharge and roughness estimation (inverse solution) by using a single surface velocity for roughest channel case (k_{s2})

k_{s2}=4.82 cm							
Shooting rate (fps)	**y (m)**	**u (m/s)**	**Q invers** (m^3/s)	**invers k_s (cm)**	**% Error in Q**	**%Error in k_s**	**S_0**
	Q_{exp}=	0.020 (m^3/s)					
30 fps	0.226	0.322	0.018	5.8	9.00	-20.33	0.001
30 fps	0.163	0.399	0.025	2.1	-22.14	56.431	0.001
	Q_{exp}=	0.055					
30 fps	0.250	0.385	0.047	9.2	12.96	-90.87	0.001
30 fps	0.241	0.478	0.062	3.6	-14.00	25.31	0.001
	Q_{exp}=	0.051					
30 fps	0.110	0.611	0.056	3.2	-9.80	33.60	0.004
30 fps	0.055	0.456	0.042	8.0	16.27	-65.97	0.004
	Q_{exp}=	0.110					
30 fps	0.246	0.765	0.094	9.7	14.52	-101.24	0.004
30 fps	0.123	0.890	0.131	3.0	-19.16	37.75	0.004
	Q_{exp}=	0.075					
30 fps	0.241	1.125	0.062	8.0	17.51	-65.97	0.015
30 fps	0.049	1.147	0.088	2.6	-18.15	46.05	0.015
	Q_{exp}=	0.167					
120 fps	0.181	1.800	0.182	2.3	-8.94	52.28	0.015
120 fps	0.270	1.483	0.129	8.0	23.07	-65.97	0.015
	Q_{exp}=	0.086					
120 fps	0.103	1.630	0.097	3.0	-13.44	37.75	0.025
120 fps	0.271	1.430	0.073	7.2	14.63	-49.37	0.025
	Q_{exp}=	0.160					
120 fps	0.237	1.677	0.123	8.3	22.83	-72.19	0.025
120 fps	0.050	1.706	0.179	2.3	-12.37	52.28	0.025
	Q_{exp}=	0.101					
120 fps	0.276	1.703	0.088	6.8	13.22	-41.07	0.035
120 fps	0.049	1.599	0.112	3.0	-10.53	37.75	0.035
	Q_{exp}=	0.159					
120 fps	0.024	1.767	0.185	2.1	-16.80	56.43	0.035
120 fps	0.265	1.966	0.129	7.2	18.32	-49.37	0.035
	Q_{exp}=	0.087					
120 fps	0.300	1.744	0.076	7.0	12.14	-45.22	0.045
120 fps	0.057	1.680	0.097	3.5	-12.06	27.38	0.045
	Q_{exp}=	0.162					
120 fps	0.056	2.146	0.188	2.5	-15.65	48.13	0.045
120 fps	0.208	2.160	0.136		15.89	100.00	0.045
	Q_{exp}=	0.055					
120 fps	0.042	1.200	0.051	6.4	6.82	-32.78	0.055
120 fps	0.155	1.720	0.060	4.3	-9.09	10.78	0.055
	Q_{exp}=	0.162					
120 fps	0.172	2.138	0.131	8.3	19.07	-72.19	0.055
120 fps	0.062	2.399	0.191	2.5	-17.89	48.13	0.055

Table 4-5 : The result of discharge and roughness estimation (inverse solution) by using a single surface velocity for smallest roughness case (k_{s6})

k_{s6}=0.264 cm							
Shooting rate (fps)	**y(m)**	**u (m/s)**	**Q invers** (m^3/s)	**invers k_s (cm)**	**% Error in Q**	**% Error in k_s**	**S_0**
	Q exp=	0.020					
30 fps	0.098	0.413	0.019	0.35	6.62	-32.57	0.001
30 fps	0.273	0.539	0.023	0.12	-13.43	54.54	0.001
	Q exp=	0.055					
30 fps	0.213	0.672	0.061	0.13	-11.45	50.75	0.001
30 fps	0.086	0.494	0.049	0.49	9.78	-85.60	0.001
	Q exp=	0.11					
30 fps	0.180	1.370	0.126	0.10	-15.03	62.12	0.004
30 fps	0.164	1.170	0.107	0.30	2.00	-13.63	0.004
	Q exp=	0.051					
30 fps	0.235	1.160	0.059	0.09	-16.76	65.90	0.004
30 fps	0.107	0.846	0.045	0.44	9.92	-67.045	0.004
	Q exp=	0.167					
120 fps	0.118	1.950	0.152	0.35	9.36	-32.57	0.015
120 fps	0.138	2.330	0.182	0.11	-8.52	58.33	0.015
	Q exp=	0.075					
120 fps	0.164	1.952	0.080	0.12	-6.88	54.54	0.015
120 fps	0.101	1.569	0.069	0.28	7.14	-6.06	0.015
	Q exp=	0.159					
120 fps	0.271	3.177	0.168	0.20	-5.93	24.24	0.035
120 fps	0.293	2.841	0.147	0.43	7.16	-62.87	0.035
	Q exp=	0.101					
120 fps	0.083	2.215	0.096	0.34	5.14	-28.78	0.035
120 fps	0.161	2.830	0.112	0.14	-10.51	46.96	0.035
	Q exp=	0.055					
120 fps	0.042	1.200	0.051	6.40	6.82	-32.78	0.055
120 fps	0.155	1.720	0.060	4.30	-9.09	10.78	0.055
	Q exp=	0.162					
120 fps	0.172	2.138	0.131	8.30	19.07	-72.19	0.055
120 fps	0.062	2.399	0.191	2.50	-17.89	48.13	0.055

Inverse solution in this case means the act of adjusting the numerical free surface to the reference individual data point by selecting the proper roughness value. Later, same optimal roughness value is called inverse roughness on these tables.

The most extreme case here maybe associated with largest absolute roughness (k_{s2}). It is claimed to be extreme because according to earlier investigations, PTV analysis for surface velocity appears to be quite scattered. It is obvious that scattered distribution of PTV data as seen on Figure 4-24, which is attributed to rough flows and for roughest channel in this case, can not be a useful data for inverse solution (Of course as long as one data point is to be used). Therefore, the error appearing on Table 4-4 maybe the maximum of all other rough cases.

As expected, discharge estimation for the smallest roughness (k_{s6}) given on Table 4-5 is better than the one for roughest case (k_{s2}) given on Table 4-4. That is discharge is estimated with a smaller percentage of error. For the rest of the roughness cases, it is expected that the discharge would be estimated with an error range that falls between these two cases. Although the large discharge errors occur in small discharges, usually it is not acceptable to estimate the discharge with an error that is larger than 10 percent. Overall, this approach was observed to be not giving very promising results and therefore a different approach was adopted that is explained in the next section.

The single particle method poor results bring into picture another technique in which more than just a single point will be used to inversely solve the problem. This time, absolute roughness value will be calculated beside discharge when channel slope, flow cross section and a few (and not just one) point wise velocities on free surface are given. An **optimization** model has to be planted into the computer solver that searches through different roughness values until measured surface velocities are matching computed surface velocity in the best possible way.

Optimization procedure is based on minimization of difference between the numerical and experimentally measured surface velocities corresponding to estimation of optimal boundary roughness at the end of the run. The objective function of optimization model is tried to be equated to zero. The objective function is relative sum of values of the differences between the measured and computed surface velocities.

$$\sum\left(\frac{u_{computed}-u_{measured}}{u_{computed}}\right) \tag{4.10}$$

In equation (4.10), u is the water surface velocity at various locations.

Initially, a good initial guess on roughness value will contribute to the quick convergence of the solution. Once the solution has converged, objective function enters a control section. If the value of this function is less than zero, the initial roughness needs to be reduced and or increased if otherwise. A certain step is assumed for the roughness increment step. Every time roughness is increased or decreased, next roughness value will be divided by the number of step to approach the optimal value iteratively. Finally, a termination criteria is introduced so that the search will cease after a while. If the objective function, or in other words overall surface velocity error, is less than five percent, the iterations stop. Beside error minimization for optimization model, another error has been defined as Root Mean Square Error (RMSE) for surface velocity itself. The aim is to show how experimental surface velocity measurements are diffused around the numerical velocity profile.

$$\text{Error}= \frac{\mathbf{u_{computed}-u_{measured}}}{\mathbf{u_{computed}}} \times 100 \tag{4.11}$$

Equation (4.11) is the error between numerical and experimental values for every individual experimental surface velocity coming from PTV.

$$\text{RMSE} = \sqrt{\frac{\text{Error}_1^2+\text{Error}_2^2+\text{Error}_3^2+\ldots+\text{Error}_i^2}{\mathbf{N}}} \tag{4.12}$$

In equation (4.12), RMSE has been shown in which N is the number of total experimental measurements, in other words, number of PTV data.

As the RMSE decreases, it shows that the experimental surface velocity measurements coming from image analysis are closely placed around the numerical velocity profile. By contrast, when the RMSE is large- which usually happens in rough channels due to chaotic surface state- measured surface velocities are sparsely distributed around the numerical surface velocity profile.

The result of invers solutions for the six rough channels are shown in the Table 4-6 though Table 4-11. In all these tables, absolute roughness calculated from moody relation is given to make a comparison with numerically estimated roughness. In inverse solution results, Manning coefficient has been inversely computed using the Manning equation (2.1).

Table 4-6 : Result of inverse solution for roughness of k_{s1}

S_0	Z_n (m)	$Q_{exp.}$ (m^3/s)	k_{s1} opt (cm)	$Q_{num.}$ (m^3/s)	$Q_{error\ \%}$	n
0.055	0.074	0.055	3.32	0.058	6.87	0.0288
0.055	0.132	0.162	2.91	0.163	0.55	0.0233
0.045	0.100	0.087	3.74	0.086	-0.12	0.0260
0.045	0.142	0.162	3.32	0.159	-1.57	0.0235
0.035	0.117	0.101	3.52	0.101	-0.54	0.0250
0.035	0.150	0.159	2.98	0.157	-1.06	0.0250
0.025	0.115	0.086	3.52	0.083	-2.70	0.0242
0.025	0.167	0.160	2.47	0.165	3.36	0.0224
0.015	0.126	0.075	3.52	0.074	-0.77	0.0246
0.015	0.198	0.167	2.26	0.169	0.79	0.0211
0.004	0.151	0.051	2.77	0.054	7.70	0.0243
0.004	0.261	0.110	3.57	0.116	5.57	0.0242
0.001	0.130	0.020	3.00	0.021	4.65	0.0249
0.001	0.261	0.055	3.71	0.057	4.67	0.0242
		k_{s1} average=	3.18	k_{s1} moody=	3.72	n average=0.024

Table 4-7 : Result of inverse solution for roughness of k_{s2}

S_0	Z_n (m)	Q $_{exp.}$ (m^3/s)	k_{s2} opt (cm)	Q $_{num.}$ (m^3/s)	Q $_{error}$ %	n
0.055	0.143	0.162	5.50	0.152	-6.30	0.0262
0.055	0.078	0.055	5.25	0.055	0.40	0.0312
0.045	0.150	0.162	4.25	0.162	0.16	0.0254
0.045	0.106	0.087	5.25	0.085	-2.13	0.0284
0.035	0.157	0.159	3.75	0.159	0.29	0.0244
0.035	0.123	0.101	4.75	0.100	-1.66	0.0269
0.025	0.175	0.160	4.00	0.155	-2.75	0.0239
0.025	0.123	0.086	4.50	0.086	0.54	0.0267
0.015	0.210	0.167	3.25	0.167	0	0.0229
0.015	0.133	0.075	5.00	0.073	-2.58	0.0266
0.004	0.276	0.110	5.50	0.111	1.80	0.0261
0.004	0.158	0.051	5.00	0.049	-2.00	0.0259
0.001	0.276	0.055	6.50	0.053	-2.90	0.0261
0.001	0.136	0.020	4.00	0.021	2.40	0.0266
		k_{s2} average=	4.75	k_{s2} moody=	4.82	n average=0.026

Table 4-8 : Result of inverse solution for roughness of k_{s3}

S_0	Z_n (m)	Q $_{exp.}$ (m^3/s)	k_{s3} opt (cm)	Q $_{num.}$ (m^3/s)	Q $_{error}$ %	n
0.055	0.103	0.162	0.62	0.158	-2.67	0.0161
0.055	0.051	0.055	0.53	0.053	-2.70	0.0162
0.035	0.118	0.159	0.67	0.154	-3.04	0.0161
0.035	0.089	0.101	0.65	0.099	-2.53	0.0166
0.015	0.156	0.167	0.50	0.161	-3.6	0.0150
0.015	0.094	0.075	0.45	0.075	-0.18	0.0159
0.004	0.192	0.108	0.63	0.106	-1.60	0.0161
0.004	0.113	0.051	0.46	0.052	2.06	0.0159
0.001	0.192	0.055	0.59	0.054	-0.56	0.0159
0.001	0.097	0.020	0.52	0.020	-0.92	0.0161
		k_{s3} average=	0.56	k_{s3} moody=	0.55	n average=0.016

Table 4-9 : Result of inverse solution for roughness of k_{s4}

S_0	Z_n (m)	Q $_{exp.}$ (m^3/s)	k_{s4} opt (cm)	Q $_{num.}$ (m^3/s)	Q $_{error\ \%}$	n
0.055	0.113	0.162	1.32	0.155	-4.13	0.0185
0.055	0.059	0.055	1.45	0.053	-3.13	0.0203
0.035	0.132	0.159	1.21	0.160	1.11	0.0189
0.035	0.100	0.101	1.40	0.100	-0.87	0.0198
0.015	0.172	0.167	0.81	0.170	1.79	0.0173
0.015	0.105	0.075	1.34	0.072	-3.90	0.0187
0.004	0.219	0.110	1.31	0.114	3.68	0.0190
0.001	0.219	0.055	1.68	0.054	-1.67	0.0190
0.001	0.110	0.020	1.16	0.020	1.66	0.0195
		k_{s4} average=	1.29	k_{s4} moody=	1.37	n average=0.019

Table 4-10 : Result of inverse solution for roughness of k_{s5}

S_0	Z_n (m)	Q $_{exp.}$ (m^3/s)	k_{s5} opt (cm)	Q $_{num.}$ (m^3/s)	Q $_{error\ \%}$	n
0.055	0.067	0.055	2.00	0.058	6.40	0.0247
0.055	0.125	0.162	2.00	0.164	1.50	0.0215
0.035	0.141	0.159	2.00	0.159	0	0.0209
0.035	0.108	0.101	2.30	0.100	-1.66	0.0222
0.015	0.186	0.167	1.50	0.168	0.40	0.0193
0.015	0.115	0.075	2.20	0.073	-2.65	0.0215
0.004	0.242	0.110	2.50	0.113	3.25	0.0219
0.004	0.140	0.051	2.00	0.053	4.25	0.0218
0.001	0.242	0.055	2.24	0.058	5.82	0.0219
0.001	0.121	0.020	1.69	0.021	6.99	0.0224
		k_{s5} average=	2.04	k_{s5} moody=	2.53	n average=0.0218

Table 4-11 : Result of inverse solution for roughness of k_{s6}

S_0	Z_n (m)	$Q_{exp.}$ (m^3/s)	k_{s6} opt (cm)	$Q_{num.}$ (m^3/s)	$Q_{error\ \%}$	n
0.055	0.094	0.162	0.30	0.157	-2.98	0.0141
0.055	0.047	0.055	0.20	0.057	5.12	0.0142
0.035	0.109	0.159	0.23	0.154	-3.08	0.0143
0.035	0.080	0.101	0.23	0.103	1.73	0.0141
0.015	0.084	0.075	0.16	0.076	1.67	0.0134
0.015	0.144	0.167	0.19	0.167	0.13	0.0134
0.004	0.175	0.110	0.18	0.116	5.96	0.0139
0.004	0.103	0.051	0.16	0.054	7.06	0.0138
0.001	0.175	0.055	0.18	0.057	5.40	0.0139
0.001	0.089	0.020	0.18	0.021	4.90	0.0142
		k_{s6} average=	0.20	k_{s6} moody=	0.26	n average=0.014

In Table 4-6 through Table 4-11, the result of invers solutions are given. For a set of different flow conditions such as flow on different bed slopes and different discharges, free surface velocity (for a number of points) has been employed to calculate the mean bed roughness and the discharge at the same time. The roughness are averaged and presented at the bottom of each table to compare them with that of roughness value calculated via Moody chart diagram. It is seen that the computed discharges and the bed roughness are quite acceptable when the difference error for the invers and experimental discharge values are small. Although the obtained roughness values are not always matching the one coming from Moody diagram which itself is a questionable quantity, it is important that discharges are estimated with reasonable accuracy.

Figure 4-28, as an example, manifests that numerical surface velocity distribution is going to pass through the middle of PTV data once optimization technique is used (The remaining figures pertaining to all flow conditions presented in Table 4-6 through Table 4-11 are attached in Appendix K).

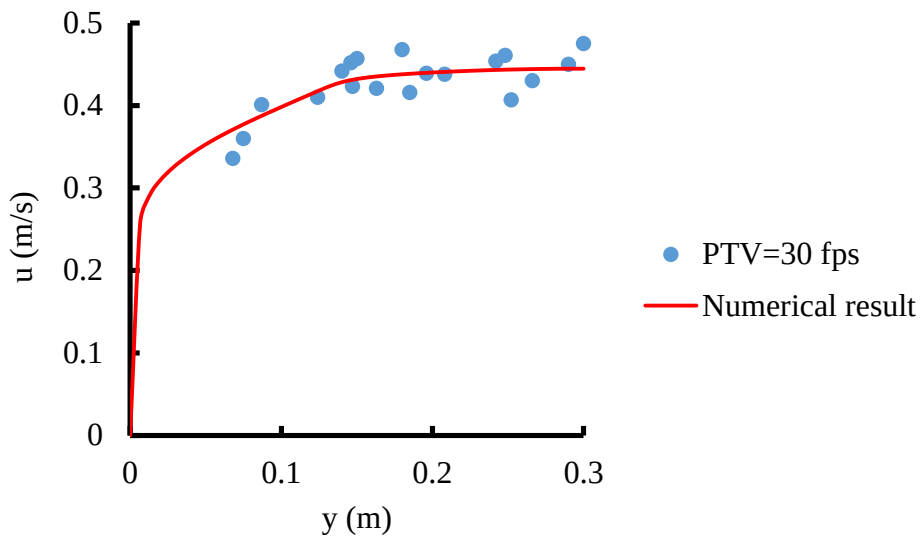

Figure 4-28 : Surface velocity profiles for inverse solution of rough rectangular channel with S_0=001, Q=0.02055 m^3/s, Z_n=0.0977 m and surface RMSE=4.68

CHAPTER 5

ANALYSIS ON COMPOUND CHANNEL EXPERIMENTS

5.1 Inverse discharge determination in GVF in smooth compound channels

5.1.1 Failure of Manning uniform depth calculation in compound channels

Before presenting the discharge estimation results, it is best to point out that Manning relation has clearly failed to approximate the uniform flow depth in compound channels. In other words, experimental observations contradict the Manning formulation calculations so clearly. As seen in Table 5-1, for two different flow conditions, Manning formula gives faulty uniform depth and the data on the table is very self-explanatory.

Table 5-1 : Uniform depth according to Manning relation for smooth compound channel in two specific flow conditions

S_0	n	Manning uniform depth (m)	F_r	Experimental depth range (m)
0.001	0.009	0.231	0.80	0.210-0.255
0.001	0.010	0.244	0.70	0.210-0.255
0.002	0.009	0.187	1.24	0.205-0.238
0.002	0.010	0.198	1.09	0.205-0.238

It is known that Manning resistance coefficient for glass ranges between 0.01 and 0.009. On Table 5-1, uniform depths are calculated based on these two values.

In one of the cases in Table 5-1, for bed slope of 0.001, the flow is subcritical and therefore gradually varied flow depth will start increasing from downstream towards upstream as seen in Figure 5-1.

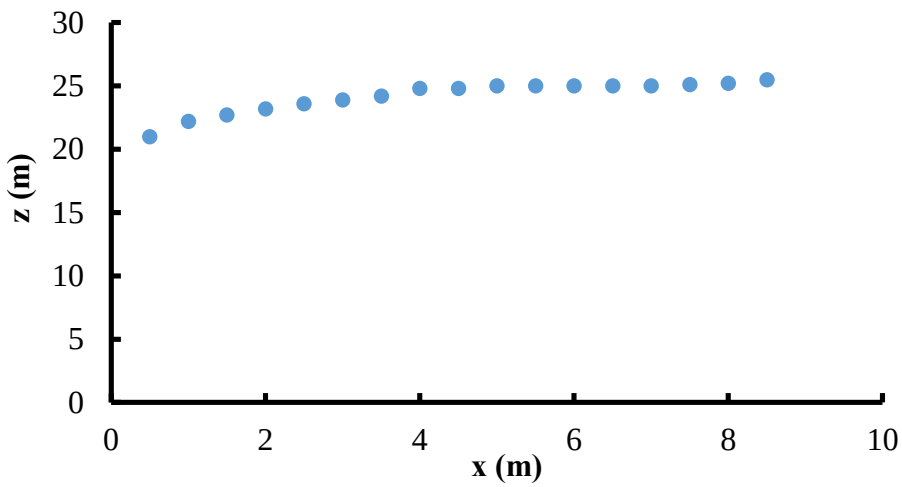

Figure 5-1 : The water surface profile for smooth compound channel with S_0=0.001 and Q=0.102 m^3/s

Since flow depth is yet to increase towards upstream according to lab measurement (because there is no sign of uniformity), it is impossible that a uniform depth can be smaller than the gradually varied depth in such a subcritical flow and thus Manning uniform depth is wrong and not matching the experimental observation. In other words, the largest possible uniform depth given by Manning relation is still smaller than the largest GVF depth and it is a paradox.

In the second case where channel bed slope is 0.002, same thing is happening too. According to Manning calculations flow is nearly critical, however, experimental records disprove this again. In Figure 5-2, the water surface profile for this case has been shown.

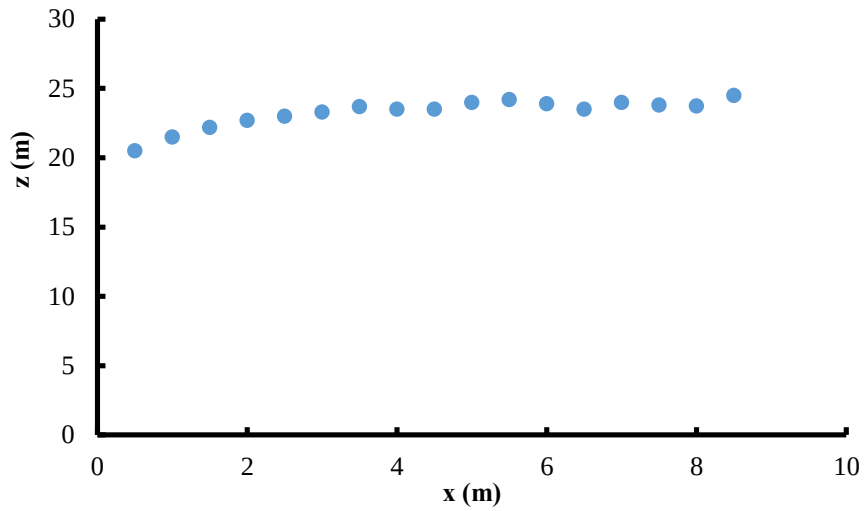

Figure 5-2 : The water surface profile for smooth compound channel with S_0=0.002 and Q=0.102 m^3/s

Since flow appears subcritical, flow depth increases gradually towards the upstream. While the Manning formula computes a uniform depth that is smaller than experimental observation, this makes the use of this relation un-trustable. Finally, it is concluded that Manning formula may not be very useful for smooth compound channels for it obviously is in contradiction to the experimental data.

Since uniform flow generation would be a tough task to cover in compound channels, it was concluded that calculations will be carried out in gradually varied flows. Based on the experiments, it was observed that flow was not uniform almost at all times. From now on, the water depth, corresponding surface velocities and discharge estimations will be performed on certain sections of the channel, called working sections. It is easy to understand that working section is a small portion of gradually varied flow. Nonetheless, this working section can be assumed locally uniform meaning that not much can change in half a meter distance of working section.

5.1.2 Flow seepage from floodplain into main channel in compound channels

Another issue that should be addressed in compound channels is prevention of seepage from flood plain into main channel due to higher velocity in the main channel. This is an indication of flow being partially developed.

To deal with the problem, surface streamlines were traced to confirm negligible flow of such kind. For this purpose, for a number of flow conditions, stream tracers have been shown in Figure 5-3.

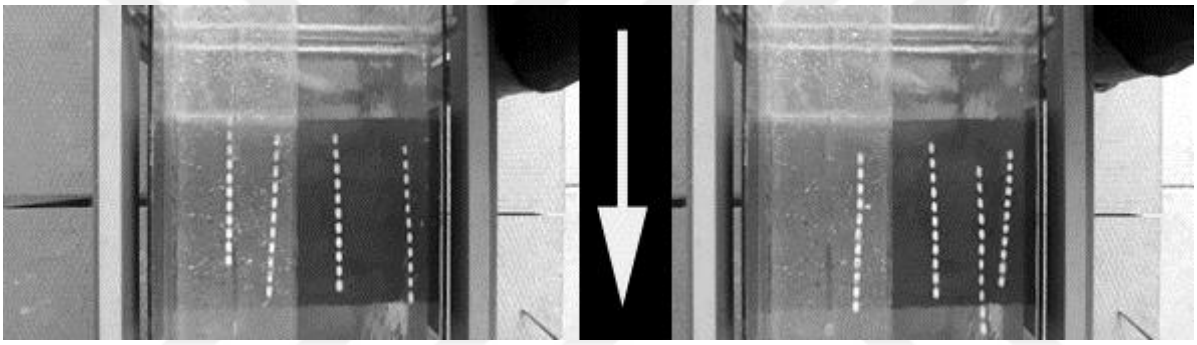

Figure 5-3 : Manifestation of parallel stream trace on the free surface in smooth compound channel for S_0=0.0005 and Q=0.094 m^3/s (Flow direction is shown with white arrow)

In Figure 5-3, stream trace for a few points on the free surface has been shown by several dots. Based on the figure, streamlines may be assumed roughly parallel since oscillations and deviations are very random in many other cases not shown in here. Overall, discharge seepage from the bank into the channel will be ignored with regard to the given explanation. In all other experimental cases, this effect was considered before finalizing the decision for a working section.

5.1.3 Inverse discharge estimation with known surface roughness and unknown energy slope in smooth compound channels

When the flow is not uniform Manning's equation is invalid. However, for gradually varied flow, streamlines may be assumed to be nearly parallel and Manning's equation can be assumed valid locally to predict local flow parameters. In such cases, the bed slope in Manning's equation is changed to energy slope. The purpose of inverse computation in this case is to use free surface velocity in order to estimate the energy slope and discharge inversely for smooth surfaces. That is, since the channel is smooth, bed resistance is known. The only unknown to be found by numerical optimization is energy slope. Finally, with known flow geometry, bed roughness and free surface velocity (at a number of points), energy slope and the discharge will be calculated correctly. In order to find the optimal energy slope, same linear optimization model has been used to predict this value. The optimization model and its components are explained in Chapter 4.

The result of inverse solutions have been shown case by case here in Table 5-2 through Table 5-7: The Z inside these tables is the local flow depth, S_0 is the channel bed slope, S_f is the inversely computed energy slope.

Table 5-2 : Inverse solution details for smooth compound channel, Case 1

Case	1
Z (m)	0.25
S_0	0.0005
S_f	0.0015
$Q_{Experimental}$ (m^3/s)	0.094
$Q_{Numerical}$(m^3/s)	0.097
% Error in Q	3.34
F_r	0.62
Surface RMSE=	8.46

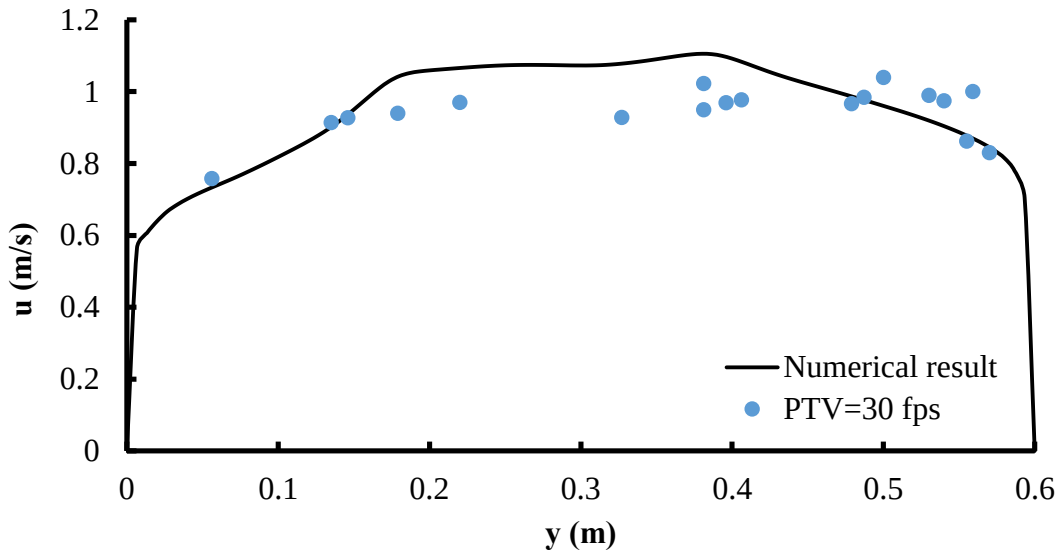

Figure 5-4 : Numerical and experimental Surface velocity for smooth compound channel for Case 1

The RMSE was defined earlier. In here, surface RMSE which is the percentage error between numerical and experimental values indicates how diffused the measurements are around the numerical velocity profile.

Table 5-3 : Inverse solution details for smooth compound channel, Case 2

Case	2
Z (m)	0.251
S_0	0.001
S_f	0.0017
$Q_{Experimental}$ (m^3/s)	0.102
$Q_{Numerical}$ (m^3/s)	0.104
% Error in Q	2.27
F_r	0.67
Surface RMSE=	8.27

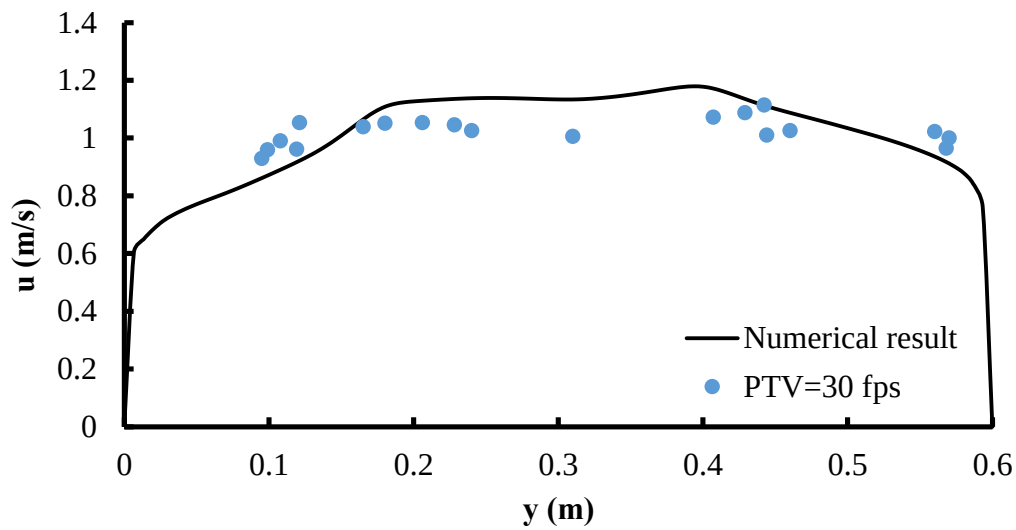

Figure 5-5 : Numerical and experimental Surface velocity for smooth compound channel for Case 2

Table 5-4 : Inverse solution details for smooth compound channel, Case 3

Case	3
Z (m)	0.238
S_0	0.002
S_f	0.00214
$Q_{Experimental}$ (m^3/s)	0.102
$Q_{Numerical}$(m^3/s)	0.105
% Error in Q	3.16
F_r	0.74
Surface RMSE=	8.53

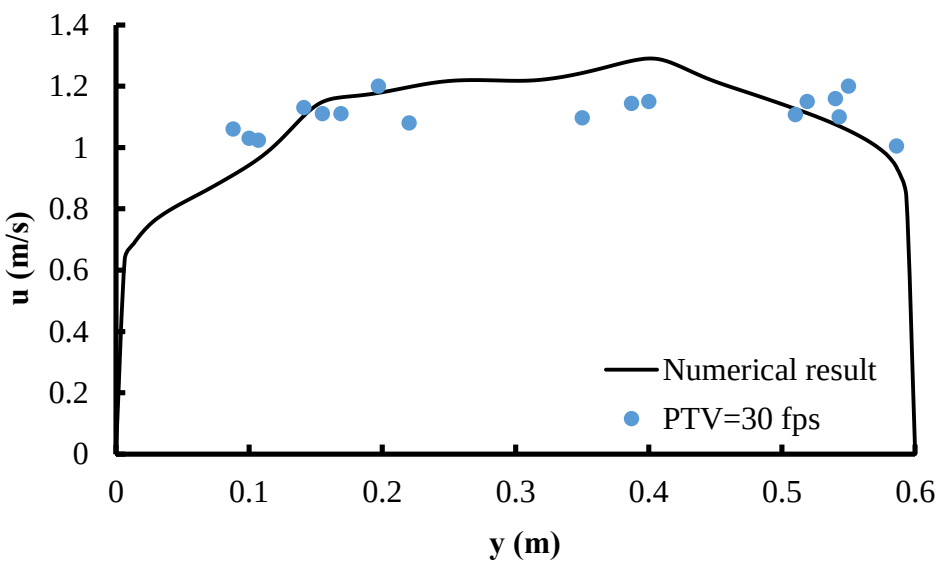

Figure 5-6 : Numerical and experimental Surface velocity for smooth compound channel for Case 3

Table 5-5 : Inverse solution details for smooth compound channel, Case 4

Case	4
Z (m)	0.225
S_0	0.01
S_f	0.0056
$Q_{Experimental}$ (m^3/s)	0.166
$Q_{Numerical}$(m^3/s)	0.158
% Error in Q	-4.22
F_r	1.36
Surface RMSE=	10.11

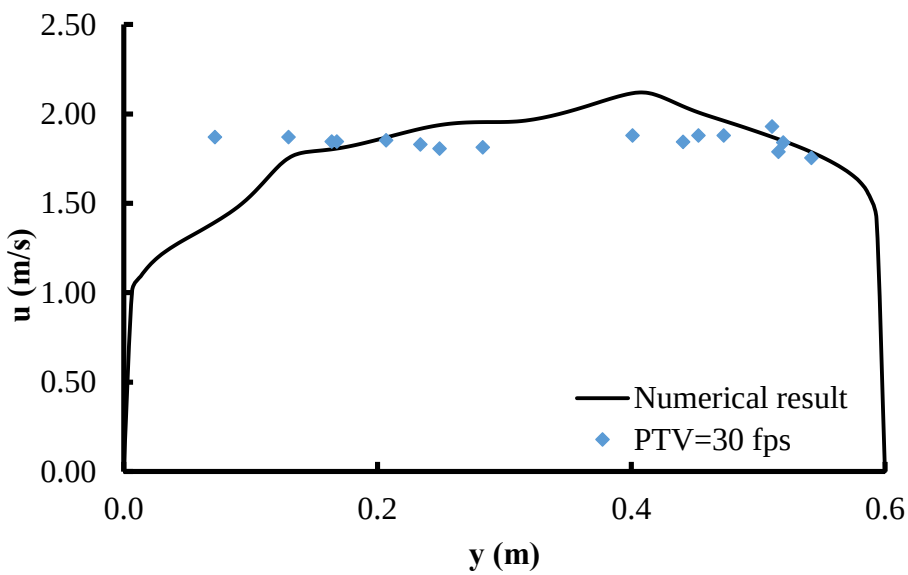

Figure 5-7 : Numerical and experimental Surface velocity for smooth compound channel for Case 4

Table 5-6 : Inverse solution details for smooth compound channel, Case 5

Case	5
Z (m)	0.22
S_0	0.015
S_f	0.0071
$Q_{Experimental}$ (m^3/s)	0.166
$Q_{Numerical}$ (m^3/s)	0.176
% Error in Q	6.06
F_r	1.42
Surface RMSE=	5.97

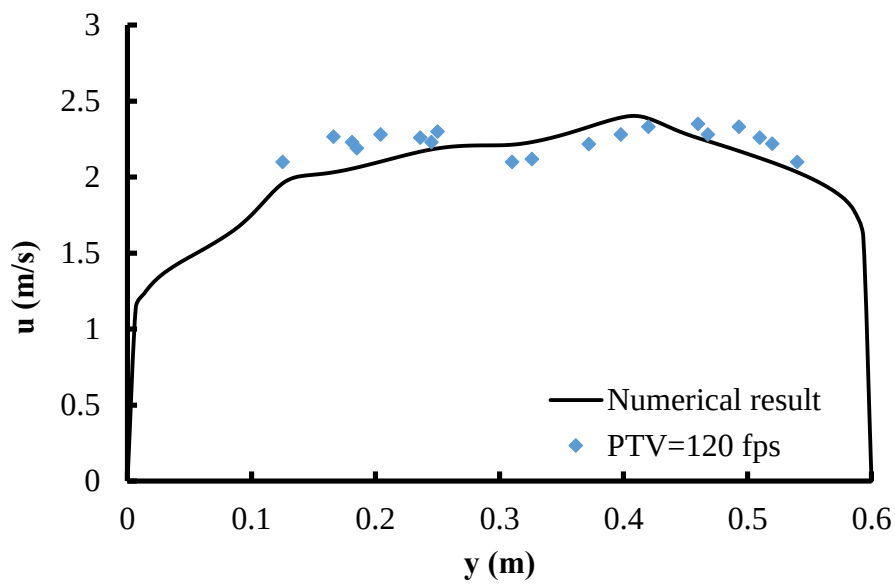

Figure 5-8 : Numerical and experimental Surface velocity for smooth compound channel for Case 5

Table 5-7 : Inverse solution details for smooth compound channel, Case 6

Case	6
Z (m)	0.193
S_0	0.02
S_f	0.0112
$Q_{Experimental}$ (m^3/s)	0.166
$Q_{Numerical}$ (m^3/s)	0.172
% Error in Q	4.08
F_r	1.88
Surface RMSE=	12.62

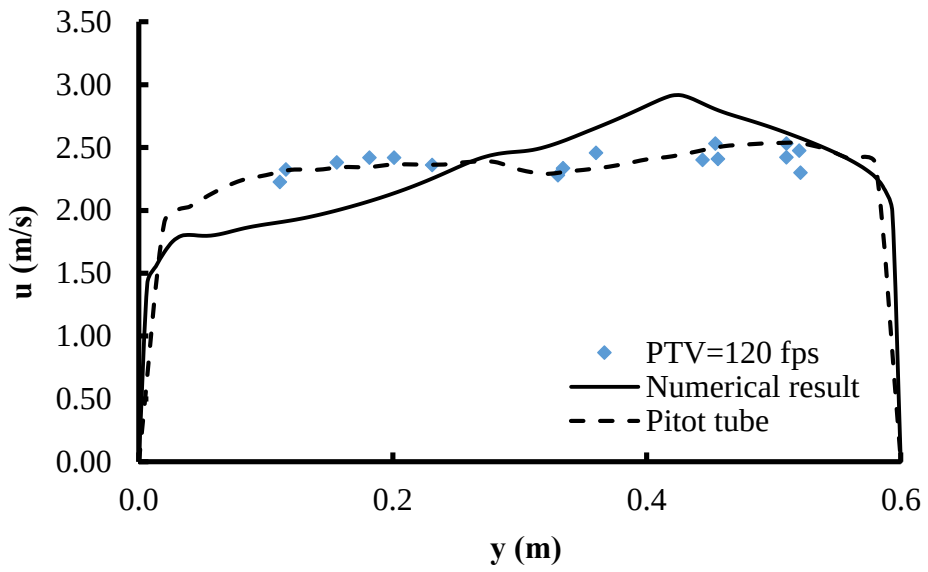

Figure 5-9 : Numerical and experimental Surface velocity for smooth compound channel for Case 6

In Figure 5-9, and also anywhere else where free surface velocity has been measured by Pitot tube device, the measurements are done underneath the free surface by a small distance of usually 1 to 1.5 cm depending on the state of the flow.

The result of inverse solutions presented already yields acceptable discharge estimation with relatively low error percentage in smooth compound channels. A closer look at the results reveals that the state of flow can be estimated from comparing the bed slope and energy

slope. Whenever flow is subcritical, the inversely computed energy slope is always larger than the bed slope. Likewise, the energy slope is smaller than the bed slope when the flow is supercritical.

It is noticeable on these figures that numerical and experimental velocity trends are not perfectly matching. Apparently the judgment on the correctness should be credited to experimental measurements, especially on Figure 5-9 where PTV and Pitot tube measurements are very close and at the same time very different from numerical velocity distribution. Even with the relatively inaccurate numerical surface velocity distribution, the optimization model is robust to predict the discharge rather accurately. The reason of numerical result deviation was inspected by a number of different attempts such as grid, surface damping parameter and termination criteria modifications, but there was no improvement observed. It is suspected that the set of equations and the turbulence model may need a significant mend to re-construct the numerical surface velocity.

5.1.4 Flood plain discharge integration from experimental measurements

Numerical validation could be again testified by comparing numerical and experimental discharges in the flood plain. Before progressing with computations, it was already shown that since streamlines are parallel on the free surface of the flow, therefore it is assumed that no flow is taking place from flood plain into main channel or vice versa. With these considerations in mind, Pitot tube measurements were carried out in the flood plain over the points demonstrated in Figure 5-10.

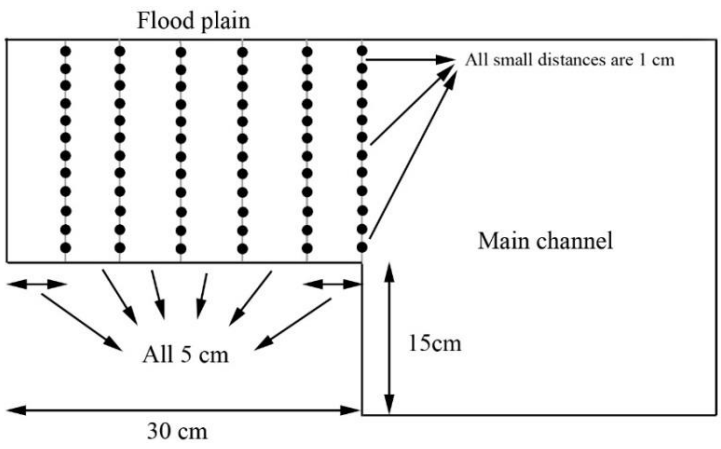

Figure 5-10 : Pitot tube measurement locations in flood plain

The discharge in the flood plain was computed by integrating the velocity over the area, or simply put, by velocity area concept. For the areas beside the wall, best fit power velocity profile was assumed. For the internal points, due to nearly uniform velocity distribution, velocities were averaged over four points to be multiplied by the covering area surrounded by these four points as seen in Figure 5-11.

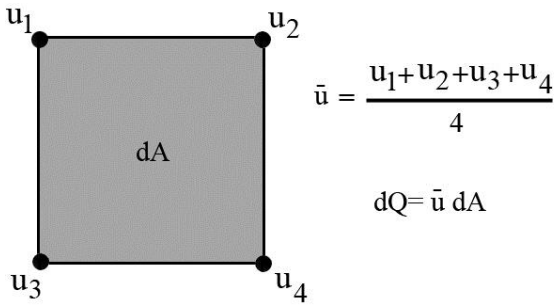

Figure 5-11: Integration of discharge for internal flood plain area

For the near wall regions, the experimental velocity measurements were used to best fit a power function and use it to integrate the discharge on this region. Since the work needed so many repeated calculations, a Matlab code was written that takes care of this task for all the

data in hand (code added in Appendix L). The result of the integration was compared to numerical flood plain discharge and given in Table 5-8.

Table 5-8 : Numerical and experimental flood plain discharge comparisons for smooth compound channels

Case	Numerical flood plain discharge (m^3/s)	Experimental flood plain discharge (m^3/s)	% Error
1	-	-	-
2	0.0289	0.0274	-5.11
3	0.0267	0.0247	-7.37
4	0.0361	0.0353	-2.10
5	0.0399	0.0393	-1.60
6	0.0270	0.0251	-7.03

For the case 1, because of relatively low velocities, Pitot tube measurements were impossible.

The data associated with the Pitot tube measurements in flood plain for smooth compound case are also presented in the Appendix M.

Closeness of the numerical and experimental discharges in the flood plain is another indication of numerical accuracy.

5.2 Inverse solutions for roughness determination in all bed rough compound channels

Inverse solution in all bed rough compound channels is nothing different than the identical procedure applied to its rectangular counterparts. In Chapter two, flow conditions section, it was mentioned that uniformity was reached in a majority of situations and the related surface profiles were attached. By contrast to smooth compound channel case, because flow is uniform this time, bed slope will be an input to the solver and roughness will be an output. Or the task of this section is to present the result of discharge and bed roughness values that are inversely computed. In Table 5-9, uniform and non-uniform flow over all bed rough compound channels are presented.

Table 5-9 : Uniform and GVF flow over all bed rough compound channels

Case	1	2	3	4	5	6
Z_n (m)	0.211	0.213	0.199	0.198	0.22214	0.209
S_0	0.035	0.03	0.02	0.01	0.004	0.002
$Q_{Experimental}$ (m^3/s)	0.160	0.150	0.100	0.074	0.063	0.050
Comment	Uniform	Uniform	Uniform	Uniform	GVF	GVF

The result of inverse solutions are presented in Table 5-10 through Table 5-13. These results are obtained when surface velocity has been used as boundary condition.

Table 5-10 : Inverse solution details for all bed rough compound channel, Case 1

Case	1
Z_n (m)	0.211
S_0	0.035
k_s (cm)	5.02
$Q_{Experimental}$ (m^3/s)	0.160
$Q_{Numerical}$ (m^3/s)	0.148
% Error in Q	-7.23
n	0.0177
Surface RMSE=	7.80

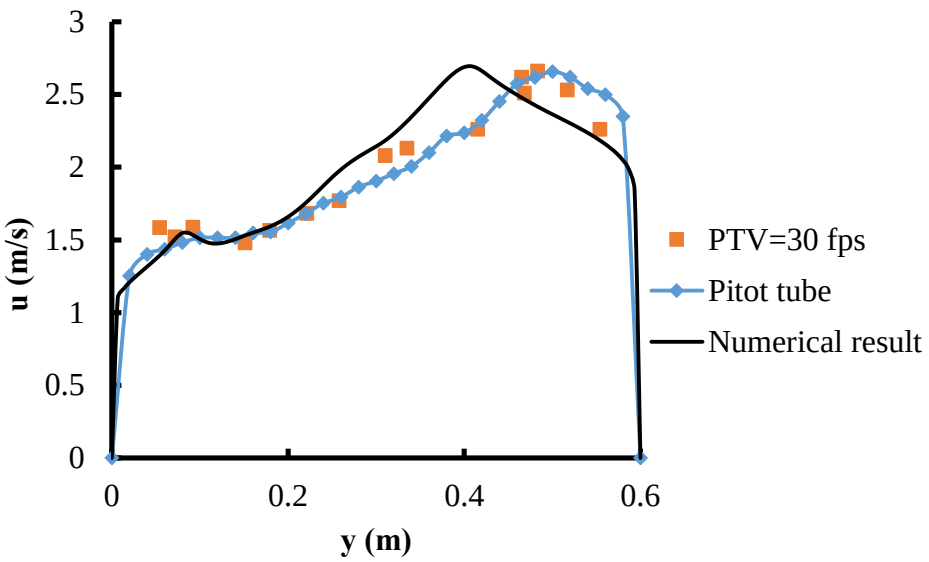

Figure 5-12 : Numerical and experimental Surface velocity for all bed rough compound channel for Case 1

Table 5-11 : Inverse solution details for all bed rough compound channel, Case 2

Case	1
Z_n (m)	0. 213
S_0	0.03
k_s (cm)	4.65
$Q_{Experimental}$ (m^3/s)	0.150
$Q_{Numerical}$ (m^3/s)	0.141
% Error in Q_{Error}	-5.60
n	0.0179
Surface RMSE=	9.09

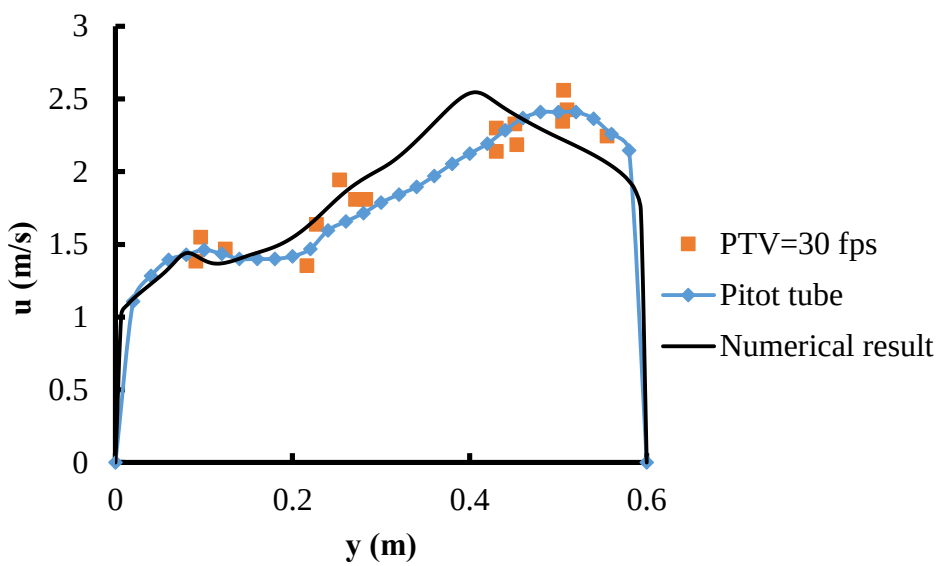

Figure 5-13 : Numerical and experimental Surface velocity for all bed rough compound channel for Case 2

Table 5-12 : Inverse solution details for all bed rough compound channel, Case 3

Case	3
Z_n (m)	0.1996
S_0	0.02
k_s (cm)	5.14
Q $_{Experimental}$ (m^3/s)	0.1
Q $_{Numerical}$ (m^3/s)	.097
% Error in Q	-2.94
n	0.0188
Surface RMSE=	12.98

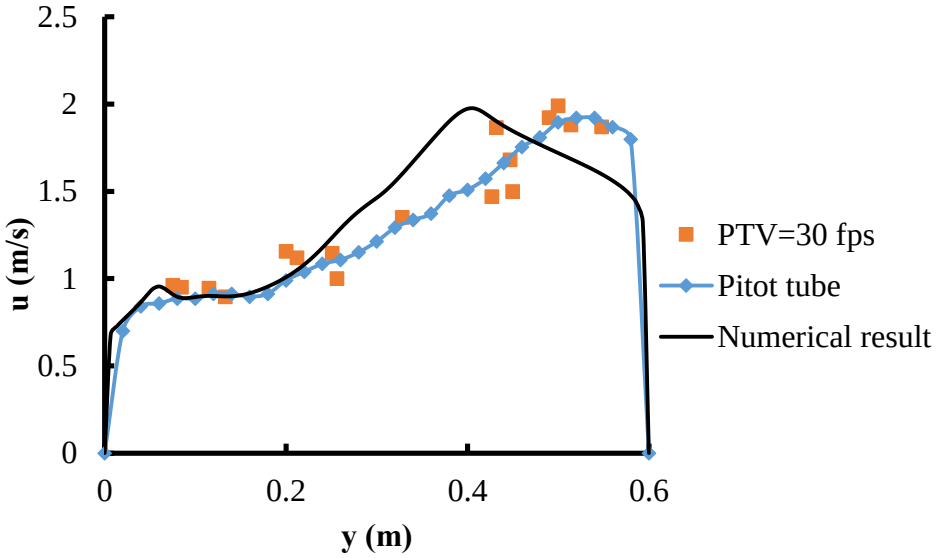

Figure 5-14 : Numerical and experimental Surface velocity for all bed rough compound channel for Case 3

Table 5-13 : Inverse solution details for all bed rough compound channel, Case 4

Case	4
Z_n (m)	0.198
S_0	0.01
k_s (cm)	3.85
$Q_{Experimental}$ (m^3/s)	0.074
$Q_{Numerical}$(m^3/s)	0.073
Q_{Error}	-0.51
n	0.0176
Surface RMSE=	13.28

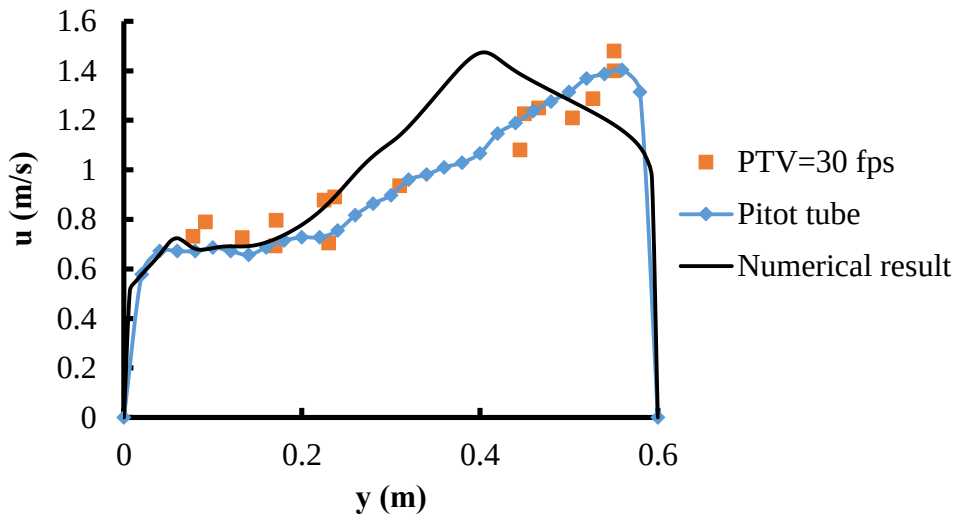

Figure 5-15 : Numerical and experimental Surface velocity for all bed rough compound channel for Case 4

Similar to smooth compound channels, the discharge has been again estimated with an acceptable range of inaccuracy. But the numerical surface velocity distribution is nowhere near accurate for the reason explained earlier in smooth compound channels section. It is suspected that invers roughness found can be biased by un-matching numerical and experimental surface velocities. Therefore, another approach is adopted to find the roughness just to make sure that true roughness value is used later. Finding of true

roughness value is important because it is going to be used for a case where flow is gradually varied over all bed rough channel. The average bed roughness found from matching the numerical and experimental surface velocities in four presented cases earlier is 4.66 cm (averaging 5.02, 4.65, 5.14 and 3.85 given in Table 5-10 through Table 5-13, respectively).

The second approach is to equate the experimental and numerical discharges in search for optimal bed roughness. For this purpose, the only change in optimization model is to minimize the difference error between numerical and experimental discharges rather than surface velocities. Doing so yields the computed inverse bed roughness as 3.85, 3.75, 4.64 and 3.76 for Cases 1 through 4 in Table 5-9, respectively. The average bed roughness will now be 4 cm. This value, or average k_s for rough bed compound channel, is used in GVF over all bed rough and GVF floodplain rough compound channels as input to seek for energy slopes. It is obvious that it is impossible to find both bed roughness and bed slope (or equivalent energy slope) at once, one of them should always be known in advance.

Finally, the result of inverse solutions for non-uniform flows over all bed rough compound channel is presented by using 4 cm of bed roughness as input to the solver. The Table 5-14, Table 5-15, Figure 5-16 and Figure 5-17 are showing the details of this non-uniform flow over all bed rough compound channel.

Table 5-14 : Inverse solution details for all bed rough compound channel, Case 5

Case	5
Z (m)	0.222
S_0	0.004
S_f	0.005
$Q_{Experimental}$ (m^3/s)	0.0635
$Q_{Numerical}$(m^3/s)	0.0653
% Error in Q	2.99
Surface RMSE=	8.66

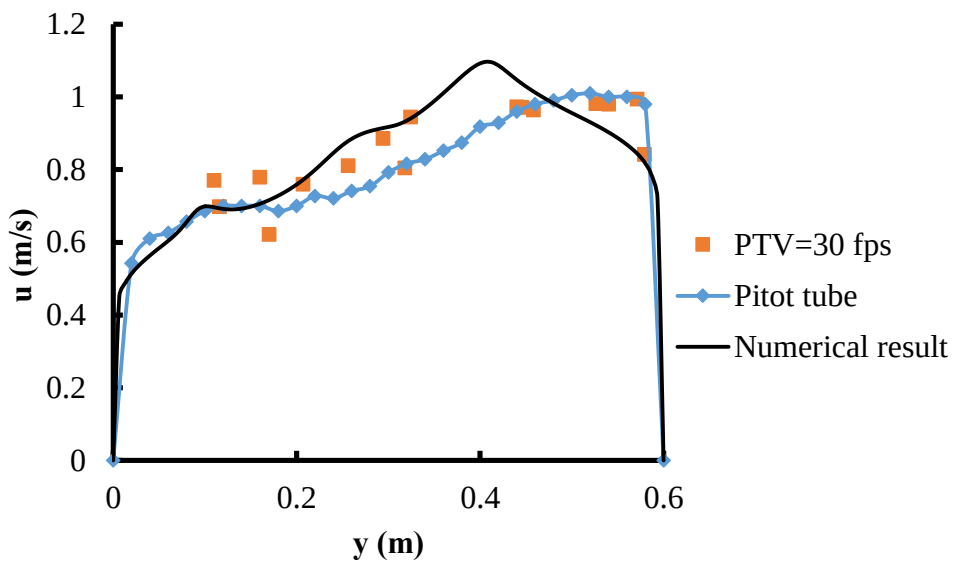

Figure 5-16 : Numerical and experimental Surface velocity for all bed rough compound channel for Case 5

Table 5-15 : Inverse solution details for all bed rough compound channel, Case 6

Case	6
Z (m)	0.209
S_0	0.001
S_f	0.004
$Q_{Experimental}$ (m^3/s)	0.0505
$Q_{Numerical}$(m^3/s)	0.0507
% Error in Q	0.41
Surface RMSE=	9.22

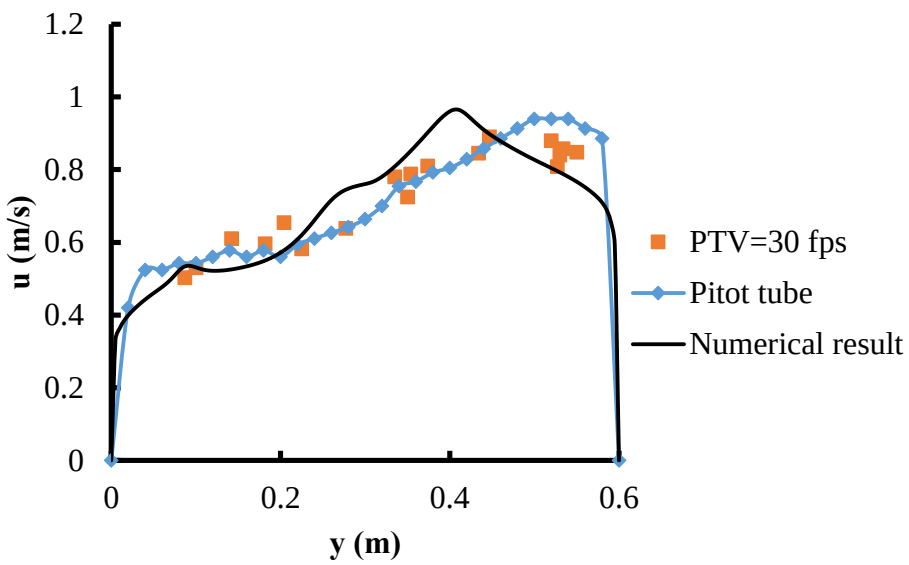

Figure 5-17 : Numerical and experimental Surface velocity for all bed rough compound channel for Case 5

The result of numerical and experimental flood plain discharge comparison for all bed rough compound channels is also demonstrated in Table 5-16.

Table 5-16 : Numerical and experimental flood plain discharge comparisons for all bed rough compound channels

Case	Numerical flood plain discharge (m^3/s)	Experimental flood plain discharge (m^3/s)	Error
1	0.0247	0.0218	-11.41
2	0.0228	0.0210	-7.58
3	0.0121	0.0110	-9.09
4	0.0095	0.0075	-20.80
5	0.0116	0.0119	3.36
6	0.0079	0.0072	-9.18

The velocity measurements in flood plain in all bed rough channels by Pitot tube are attached in Appendix N.

5.3 Inverse solutions in floodplain rough compound channels

As it was once defined, the floodplain rough compound channel is constructed by placing roughness elements (square ribs) on the flood plain. The flow condition on floodplain rough channels were seen to be very unstable. In none of the experiments, uniform flow was established. As already discussed, if flow is not uniform, it implies that bed slope of the channel is not useful anymore and it has to be replaced by energy slope. If energy slope and bed roughness are both unknown, it would be difficult to complete the inverse solution. It was decided then, that the roughness found in all bed rough channels (k_s=4 cm) be used as an input to the solver on the flood plain. Instead, energy slope and discharge will have to be computed. With all these in mind, known roughness was applied to the flood plain and energy slope was calculated in addition to discharge. The result of the invers solutions are given in Table 5-17 through Table 5-21.

Table 5-17 : Inverse solution details for floodplain rough compound channel, Case 1

Case	1
Z (m)	0.197
S_0	0.025
S_f	0.017
$Q_{Experimental}$ (m^3/s)	0.160
$Q_{Numerical}$(m^3/s)	0.171
% Error in Q	7.42
Surface RMSE=	24.55

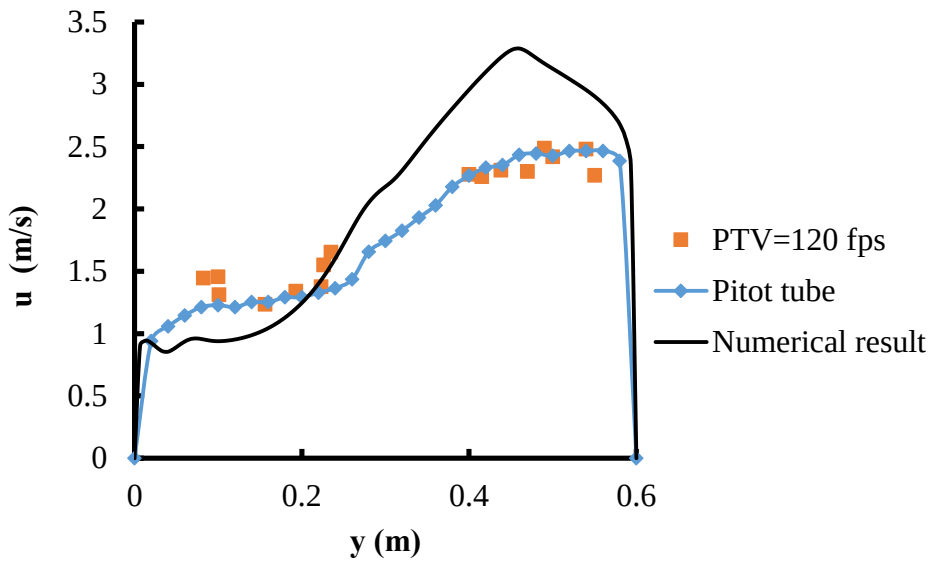

Figure 5-18 : Numerical and experimental Surface velocity for floodplain rough compound channel for Case 1

Table 5-18 : Inverse solution details for floodplain rough compound channel, Case 2

Case	2
Z (m)	0.204
S_0	0.02
S_f	0.0135
$Q_{Experimental}$ (m^3/s)	0.147
$Q_{Numerical}$ (m^3/s)	0.158
% Error in Q	7.74
Surface RMSE=	29.4

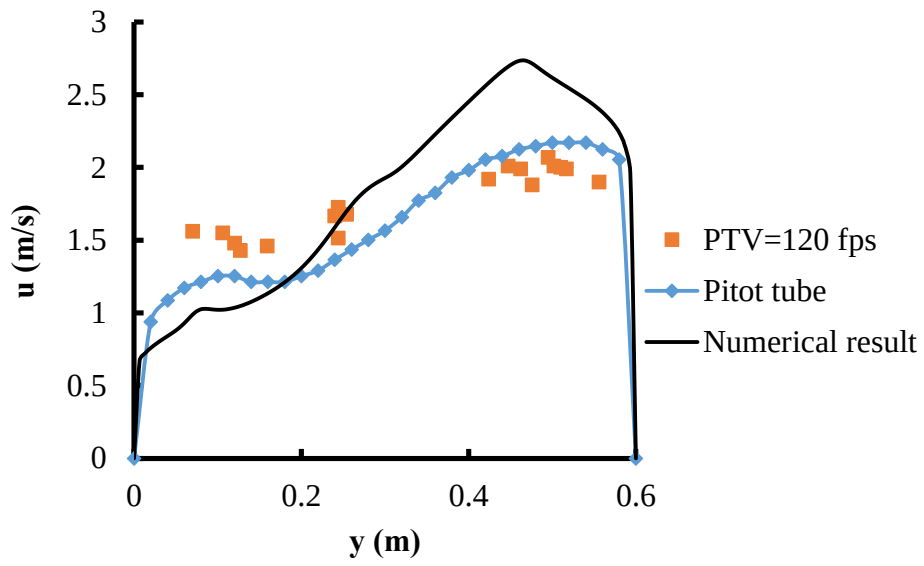

Figure 5-19 : Numerical and experimental Surface velocity for floodplain rough compound channel for Case 2

Table 5-19 : Inverse solution details for floodplain rough compound channel, Case 3

Case	3
Z (m)	0.206
S_0	0.008
S_f	0.0066
$Q_{Experimental}$ (m^3/s)	0.100
$Q_{Numerical}$ (m^3/s)	0.109
% Error in Q	9.92
Surface RMSE=	13.39

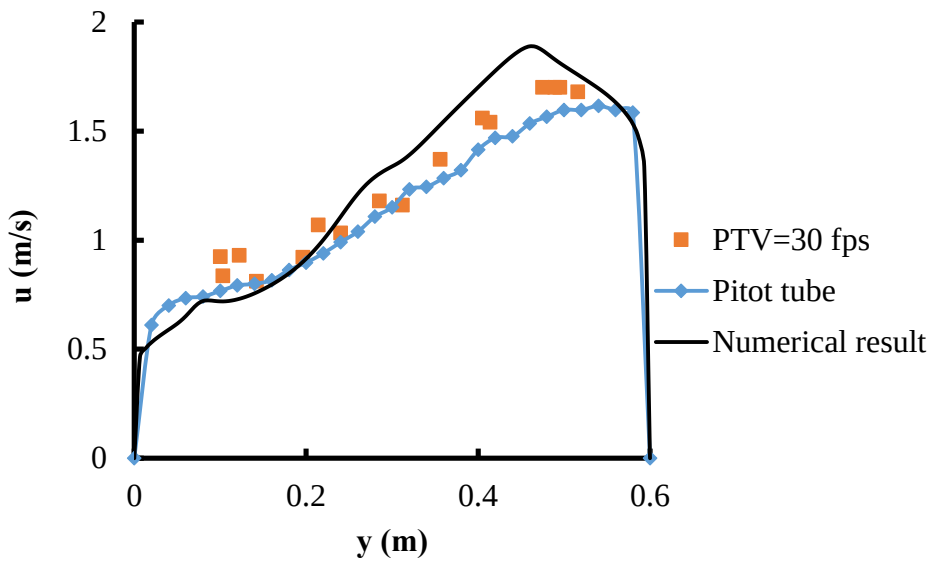

Figure 5-20 : Numerical and experimental Surface velocity for floodplain rough compound channel for Case 3

Table 5-20 : Inverse solution details for floodplain rough compound channel, Case 4

Case	4
Z (m)	0.235
S_0	0.004
S_f	0.00475
$Q_{Experimental}$ (m^3/s)	0.1
$Q_{Numerical}$ (m^3/s)	0.1115
% Error in Q	11.54
Surface RMSE=	11.58

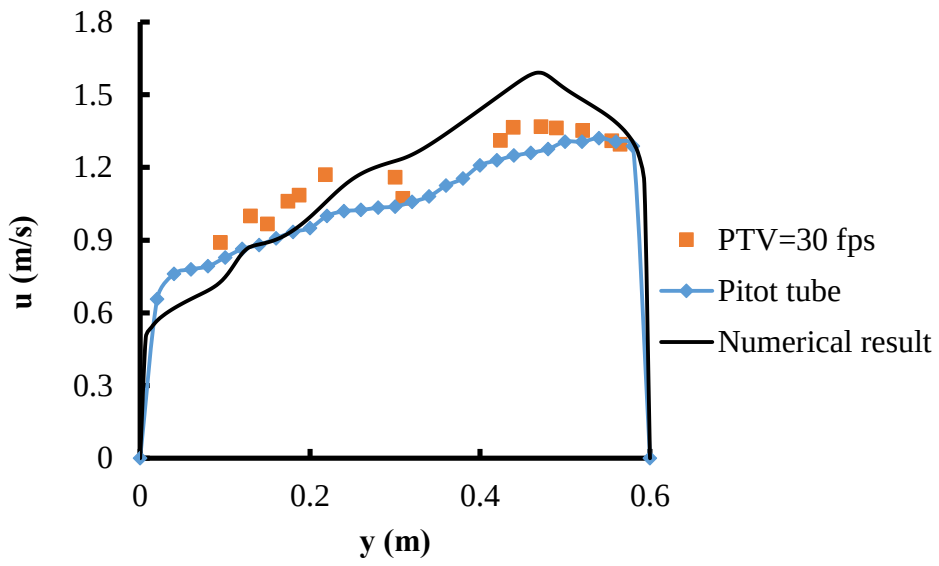

Figure 5-21 : Numerical and experimental Surface velocity for floodplain rough compound channel for Case 4

Table 5-21 : Inverse solution details for floodplain rough compound channel, Case 5

Case	5
Z (m)	0.245
S_0	0.002
S_f	0.0039
$Q_{Experimental}$ (m^3/s)	0.100
$Q_{Numerical}$(m^3/s)	0.105
% Error in Q	5.67
Surface RMSE=	11.41

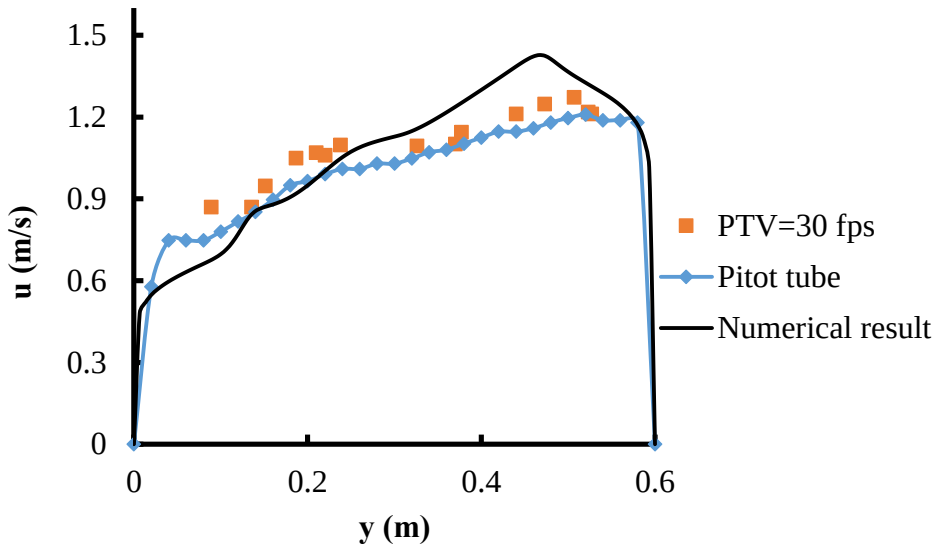

Figure 5-22 : Numerical and experimental Surface velocity for floodplain rough compound channel for Case 5

The result of numerical and experimental flood plain discharge comparison for floodplain rough compound channels is also demonstrated in Table 5-22.

Table 5-22 : Numerical and experimental flood plain discharge comparisons for all bed rough compound channels

Case	Numerical flood plain discharge (m^3/s)	Experimental flood plain discharge (m^3/s)	Error
1	0.0158	0.0138	-12.15
2	0.0173	0.0152	-13.13
3	0.0121	0.0104	-14.46
4	0.0179	0.0174	-2.45
5	0.0189	0.0200	0.58

The velocity measurements in flood plain of floodplain rough compound channels by Pitot tube are attached in Appendix O.

CHAPTER 6

CONCLUSIONS AND RECCOMENDATIONS

This chapter highlights the achievements of the research and presents recommendations for the future work on the subject. The conclusions are summarized results of experiments and numerical simulations. The numerous experiments carried out in the lab have contributed to the exploration of valuable remarks on PIV and PTV methods. Some portion of experimental data are utilized for repairing and calibrating the numerical model. On the other hand, a framework set of rules are established for water surface velocity measurement by the experimental observations and experiences. Therefore, the research is named as combined experimental and computational approach of discharge measurement in open channels. Lastly, recommendations are made for the future work.

6.1 Conclusions

Extensive laboratory experiments were carried out in a tilting channel of rectangular and compound cross section. The primary purpose of the experiments was to measure the velocity on the free surface of water for different flow conditions. Different flow conditions were provided by changing the stream discharge, channel bed slope, channel bed roughness and channel cross section. Pitot tube and Hot-film measurements were also conducted for comparison and verification purposes. However, the major measurement method to combine with the numerical analysis and CFD tool development is imagery method. The following conclusions are obtained from the experimental and numerical studies conducted.

a) Lens distortion effect removal was systematically observed to be not needed in conventional laboratory working conditions. By contrast, it is widely practiced in the field.
b) The recording from oblique angles was tried and image correction was applied. Analysis over rectified images was performed and PTV results were shown to be acceptable. This is an important step because in future work, image rectification and at the same time lens distortion effect elimination can be quite obligatory and the required knowledge for it has been attested and verified in the lab.
c) Uniform flow generation was always a challenge. The Manning resistance coefficient was calculated by recording water surface profiles and benefitting optimization technique in rectangular channels. Uniform depth was adjusted accordingly later. It was clearly shown that the Manning relation was not practical in compound channel.
d) Hot-film measurements were conducted to collect velocity field in the flow cross section and more importantly near the free surface. The measurements and experience with Hot-film device proved that device was giving good results in the water depth but not so accurate near the free surface. Thus, Pitot tube was substituted in place of Hot-film in near surface velocity measurement for validation of PIV and PTV data.
e) Depending on the state of flow, it was seen that Pitot tube measurement can be functional if the tube is submerged about 1 to 1.5 cm underneath the free surface. The Pitot tube measurement was used for comparing the velocities to PTV analysis and sometimes for verification of numerical model.
f) Surface velocity measurements by image analysis were used to introduce a set of useful hints and relations based on experimental experiences and observations. The hints often include a variety of tips related to particle tracer (size, material and travel distance), camera position, particle dispenser, lighting conditions and image distortion. The technical issue of relating recording speed with respect to flow condition was also addressed by setting up limits and formulating the problem using the parameter involved (Such as equation (4.6)) which is believed to be quite handy under laboratory working conditions.

g) Experimental free surface data base was required to look after the computational surface velocity calibration as it was incomplete in the first place. The task was accomplished by introducing the surface damping parameter into the numerical model.

h) Ultimately, channel boundary roughness determination was investigated. In natural streams, flow takes place over very rough surfaces and roughness value is often an unknown parameter. The flow rate was successfully estimated in addition to solid boundary roughness when surface velocity was a known quantity. For reaching this goal, a linear optimization model was installed inside the CFD solver that searches the best fitting computational and measured free surface velocities by shifting the boundary roughness.

i) Sometimes in compound channels uniform flow generation was impossible due to short length of the channel. Under such circumstances, no matter if the channel was smooth or rough, energy slope was inversely calculated instead of roughness. The result of inverse calculations are precise and reliable. Two type of roughness was examined on compound channels. The full bed rough and floodplain rough cases. In reality, floodplain is rougher than main channel. The flow was luckily uniform over fully rough bed compound channel and therefore discharge and roughness estimations were indeed impressive. For the floodplain rough compound channels, uniformity was never reached and absolute roughness value found from the previous case was used to search for energy slope instead. The discharge prediction for this case was poorer in quality compared to fully rough case.

6.2 Recommendations

The findings of the present research have signaled that future work in the same direction can have excellent extensions.

A major prospective extension of this work can be the application of the current technique to the field. If a nearly straight-reach stream is supposed to be investigated in the nature, the current version of the solver is expected to predict its boundary roughness and discharge acceptably. Many natural cross sections of rivers can be assumed rectangular, if flow can be

considered uniform then the current solver can be of great use. On the other hand, however, the image processing part of the work can suffer an assortment of new challenges. There are numerous reports in the literature to address those problems that are faced in the nature with regard to PIV analysis, for instance. Problems tied with PIV analysis can be ignited due to many sources. These can include the shades and light reflections on the water surface, muddy water, random objects floating around, changing weather conditions, daylight intensity, foams on the water surface and positioning the camera. More importantly, it requires interdisciplinary collaboration between different fields of science to carry out the task such as performing real time image analysis in field.

When the flow is GVF, the problem to solve would be to figure out a resolution to find both boundary roughness and energy slope at the same time.

Numerical improvement is another high priority task even as of now. The numerical shortcomings observed in failure to accurately predict the surface velocity in compound channels is a testimony for the issue. Although it was tried in several ways to correct the surface velocity in compound channels, it was seen that none of the parameters including the surface damping parameter can control the surface velocity and solve the problem. Therefore, a modification to the turbulence model maybe required or a new set of equations may have to be solved. On the numerical improvement, the solution domain is also a subject for future addressing which comes into picture when dealing with field work. In irregular cross section geometries, the current structured system of grid and its solution will have to be redesigned. Solving the flow governing equations on irregular flow domains requires that a new numerical approach be taken to tackle the problem. In non-uniform irregular flows, it can be necessary that a full three-dimensional modeling with transport equation(s) included be undergone. This will certainly complicate the problem to a large degree, but can be actualized as part of the future work on the continuity of the present study.

REFERENCES

Adam J., Bechle S.M., Chin H. Wu, M., Wen-Cheng L., Nobuaki K., (2012). "Development and Application of an Automated River-Estuary Discharge Imaging System." Journal of Hydraulic Engineering © ASCE / APRIL 1, Vol. 138, No. 4, 327- 339.

Adrian, R.J. (1991). "Particle-Imaging Techniques for Experimental Fluid Mechanics." Ann. Rev. Fluid Mech., 23, pp. 261-304.

Aya, S., I. Fujita, M. Yagyu (1995), "Field-observation of flood in a river by video image analysis." Proc. Hydraul. Eng., 39, 447– 452, 1995.

Aydin, I. (2003). "Uniform flow computations in natural open channels". Proc., Int. Symp. on Shallow Flows, Delft, Netherlands, June 2003, Vol.2, pp.245-250.

Aydin, I. (2009). "Nonlinear Mixing Length Model for Prediction of Secondary Currents in Uniform Channel Flows". J. Hydraul. Eng. 2009.135:146-153.

Baud, O., Hager, W.H., Minor, H.E. (2005). "Toward nonintrusive flood discharge measurement.", J. Hydraul. Eng., 131(12), 1031-1035.

Bradley, A. A., Kruger, A., Meselhe, E. A., Muste, M. V. (2002). "Flow measurement in streams using video imagery." Water Resour. Res., 38(12), 1315–1322.

Brevis W, Niño Y and Jirka GH (2011). "Integrating cross-correlation and relaxation algorithms for particle tracking velocimetry". Experiments in Fluids, 50 (1), pp 135-147.

Costa, J. E., Cheng, R. T., Haeni, F. P., Melcher, N., Spicer, K. R., Hayes, E., Plant, E., Hayes, K., Teague, C., and Barrick, D. (2006). “Use of radars to monitor stream discharge by noncontact methods.” Water Resour. Res., 42, W07422.

Costa, J. E., Spicer, K. R., Chenge, R. T., Haeni, R., Melcher, N. B., Thurman, M. E. (2000). “Measuring stream discharge by non-contact methods: A proof-of-concept experiment.” Geophys. Res. Lett., 27(4), 553–556.

Creutin, J. D., Muste, M., Bradley, A. A., Kim, S. C., Kruger, A. (2003). “River gauging using PIV techniques: A proof of concept experiment on the Iowa River.” J. Hydrol. (Amsterdam), 277(3/4), 182–194.

Dramais, G., Le Coz, J., Camenen, B., Hauet, A., (2011). “Advantages of a mobile LSPIV method for measuring flood discharges and improving stage- discharge curves.” Journal of Hydro-environment Research 5 (2011) 301-312.

D. Pokrajac, L.J. Campbell, V. Nikora, C. Manes, I. McEwan, (2007) "Quadrant analysis of persistent spatial velocity perturbations over square-bar roughness" , Exp. Fluids. 42; 413–423. doi:10.1007/s00348-006-0248-0.

Fujita, I., Aya, S., Deguchi, T. (1997). “Surface Velocity Measurement of River Flow Using Video Images of an Oblique Angle.” Proceedings XXVIIth IAHR Conference, Theme B, Vol. I, San Fransisco, CA, pp. 227-232.

Fujita, I., Hino, T. (2003). “Unseeded and seeded PIV measurements of river flows videotaped from a helicopter.” J. Visualization, 6(3), 245–252.

Fujita, I., Komura, S. (1994). “Application of Video Image Analysis for Measurements of River-Surface Flows.” Proc. of Hydraulic Engineering, JSCE, 38, 733-738 (in Japanese).

Fujita, I., Muste, M., Kruger, A. (1998). “Large-Scale particle image velocimetry for flow analysis in hydraulic engineering applications.” J. Hydraul. Res., 36 (3), 397–414.

Gerard, R. (1978). “Scondary flow in noncircular conducts”. Journal of the Hydraulics Division, 104 (HY5), 755-773.

Goodman, J.W. “Introduction to Fourier Optics.”, (1968)- McGraw-Hill, London, New York.

Grant, I (1997). “Particle image velocimety: a review.” Proceeding of the institution of mechanical engineering, Part C-Journal of mechanical engineering sciences, Volume: 211 Issue: 1 Pages: 55-76.

Hassan, Y. A. Canaan, R. E. (1991), “Full-field bubbly flow velocity measurements using a multi frame particle tracking technique.” Exp. Fluids., Vol. 12, pp. 49-60.

Hauet A, Jodeau M, Le Coz J, Marchand B, Moran AD, Le Boursicaud R and Dramais G. “Application of the LSPIV method for the measurement of velocity fields and flood discharges in reduced scale model and in rivers” Houille Blanche-Revue Internationale de Leau. 2014; 3: 16-22.

Hauet, A., Kruger, A., Krajewski,W., Bradley, A.,Muste,M., Creutin, J., Wilson, M. (2008). “Experimental system for real-time discharge estimation using an image-based method.” J. Hydrol. Eng., 13(2), 105–110.

Huang, H. T., Fiedler, H. E., Wang, J. J. (1993a), “Limitation of PIV-part 1: limitation of conventional techniques due to deformation of particle image patterns.” Exp. Fluids., Vol. 15, pp. 168-174.

Huang, H. T., Fiedler, H. E., Wang, J. J. (1993b), “Limitation of PIV-part 2: particle image distortion, a novel technique.” Exp. Fluids, Vol. 15, pp. 263-273.

Ishikawa, M., Yamamoto, F., Murai, Y., Iguchi, M., Wada, A. (1997), “A novel PIV algorithm using velocity gradient tensor.”, in Proc. Second International Workshop on PIV’ 97-Fukui, T. Kobayashi and F. Yamamoto (Eds.), Visualization Society of Japan, pp. 51-56.

Jodeau, M., Hauet, A., Paquier, A., Coz, Le. J., Dramais, G. (2008). “Application and evaluation of LS-PIV technique for the monitoring of river surface velocities in high flow conditions.” Flow Meas. Instrum., 19(2), 117–127.

Kim, Y., Muste, M., Hauet, A., Krajewski, F., Kruger, A., Bradley, A. (2008). “Stream discharge using mobile large-scale particle image velocimetry: A proof of concept.” Water Resour. Res., 44(9), W09502.

Kinsdvater, C. E. and Cater, R. W. (1957). “Discharge Characteristics of Rectangular Thin-Plate Weirs.” Journal of *Hydraulics Division*, Vol. 83, No. 6, December, 1-36.

Koblinsky, C. J., R. T. Clarke, A. C. Brenner, and H. Frey (1993). “Measurement of river level with satellite altimetry.” Water Resour. Res., 29(6), 1839– 1848.

Kobayashi, T., Saga, T., Segawa, S. (1989), “Multipoint velocity measurement for unsteady flow field by digital image processing.” in Flow Visualization V, R. Reznicek (Ed.), Hemisphere, New York, pp. 197-202.

Labonté, G. (1999), “A new neural network for particle-tracking velocimetry.” Exp. Fluids., Vol. 26, pp. 340-346.

Le Coz, J., Hauet, A., Pierrefeu, G., Dramais, G., Camenen, B. (2010). “Performance of image-based velocimetry (LSPIV) applied to flashflood discharge measurements in Mediterranean rivers.” J. Hydrol. (Amsterdam), 394(1,2), 42–52.

Melcher, N. B., Costa, J. E., Haeni, F. P., Cheng, R. T., Thurman, E. M., Buursink, M., Spicer, K. R., Hayes, E. (2002). “River discharge measurements by using helicopter-mounted radar.” Geophys. Res. Lett., 29(22) 2084–2087.

Muste, M., Fujita, I., Hauet, A., (2009). “Large-scale particle image velocimetry for measurements in riverine environments.” Water Resources Research 44, W00D19. doi:10.1029/2008WR006950.

Muste, M., Ho, H-C., Kim, D., (2011). “Consideration on direct stream flow measurements using video imagery: outlook and research needs.”, Journal of Hydro-environment Research 5 (4), 289-300.

Oberg, K. A., A. R. Schmidt (1994). “Measurement of leakage from Lake Michigan through three control structures near Chicago.”, Illinois, April – October 1993, U. S. Geol. Surv. Water Resour. Invest. Rep., 94- 4112.

Ohyama, R., Takagi, T., Tsukiji, T., Nakanishi, S., Kaneko, K. (1993), “Particle tracking technique and velocity measurement of visualized flow fields by means of genetic algorithm.” J. Visualization Soc. Japan, Vol. 13, pp. 35-38.

Okamoto, K., Hassan, Y.A., Schmidt, W.D. (1995), “New Tracking Algorithm for Particle Image Velocimetry.” Exp. Fluids., Vol. 19, pp. 342-347.

Plant, W. J., Keller, W. C., Hayes, K. (2005). “Measurement of river surface currents with coherent microwave systems.” IEEE Trans. Geosci. Remote Sensing, 43(6), 1242–1257.

Polatel C. “Large-scale roughness effect on free-surface and bulk flow characteristics in open channel flows” Ph.D. Thesis, Iowa Institute of Hydraulic Research, The Univ.of Iowa, Ames, Iowa, 2006.

Raffel M., Willert, C. E. & Kompenhans, J. (1998). Particle image velocitimetry, a practical guide. Springer, Berlin, Heidelberg, New York.

Ramesh, R., Datta, B., Bhallamudi, S.M. and Narayana, A. (2000). “Optimal estimation of roughness in open channel flows” J. Hydraulic Eng., 126, 299-303.

Rehbock, T. (1929). “Discussion of precise weir measurement by EW Schoder and KB Turner”. ASCE; Vol 93. pp. 1143-1162.

Roussinova V and Balachandar R. (2011). “Open channel flow past a train of rib roughness.” Journal of Turbulence; Vol. 12, No. 28, P: 1-17.

S. Gharahjeh, I. Aydin, A.B. Altan- Sakarya (2015). “Weir Velocity Formulation for Sharp-Crested Rectangular Weirs” Flow Measurement and Instrumentation- Vol. 41; pp. 50–56.

Stevans, C., Coates, M. (1994). “Applications of a Maximized Cross-Correlation Technique for Resolving Velocity Fields in Laboratory Experiments.” Journal of Hydraulic Research, 32(2), 195-212.

Tauro F, Pagano C, Phamduy P, Grimaldi S and Porfiri M. “Large scale particle image velocimetry from an unmanned aerial vehicle” IEEE/ASME Transactions on Mechatronics. 2015; 20: 3269-3275.

Uemura, T., Yamamoto, F., Ohmi, K. (1989), “A high speed algorithm of image analysis for real time measurement of two-dimensional velocity distribution.” in Flow Visualization, B.

Urquhart, W. J. (1975). Hydraulics: engineering field manual. U.S. Department of Agriculture, Soil Conservation Service, Washington, D.C.

Utami, T., Blackwelder, R.F., Ueno, T. (1991). “A Cross-Correlation Technique for Velocity Field Extraction from Paniculate Visualization.” Experiments in Fluids, 10, 213-223.

V. Weitbrecht ∗, G.Kühn, G.H. Jirka (2002). “Large scale PIV-measurements at the surface of shallow water flows”. In Flow Measurement and Instrumentation Vol. 13; pp.237–245.

Van Dyke, M. (1982), “An Album of Fluid Motion.” Parabolic Press, Stanford, California.

Vorosmarty, C. J., C. J. Willmott, B. J. Choudhury, A. L. Schloss, T. K. Stearns, S. M. Robeson, T. J. Dorman (1996). “Analyzing the discharge regime of a large tropical river through remote sensing.” Ground-based climatic data and modeling, Water Resour. Res., 32(10), 3137– 3150.

Willert, C. E. and Gharib, M. (1991), “Digital particle image velocimetry.” Exp. Fluids, Vol. 10, pp. 181-193.

Zhang Z, Wang X, Fan T and Xu L. “River surface target enhancement and background suppression for unseeded LSPIV” Flow Measurement and Instrumentation. 2013; 30: 99-111.

APPENDIX A

WATER SURFACE PROFILES FOR SMOOTH COMPOUND CHANNEL EXPERIMENTS

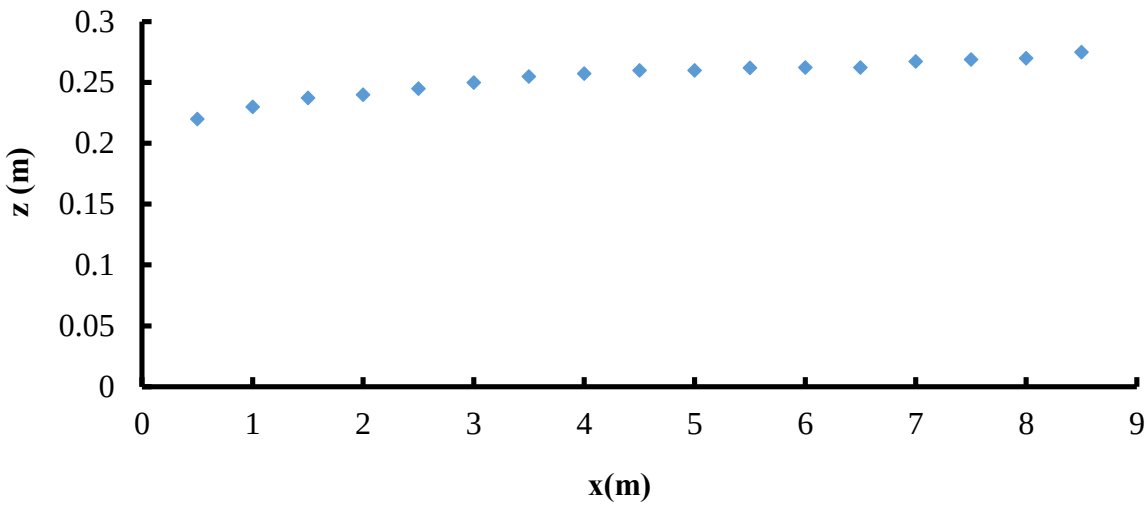

Figure A-1 : Water surface profile of smooth compound channel (S_0=0.0005 & Q=0.094 m^3/s)

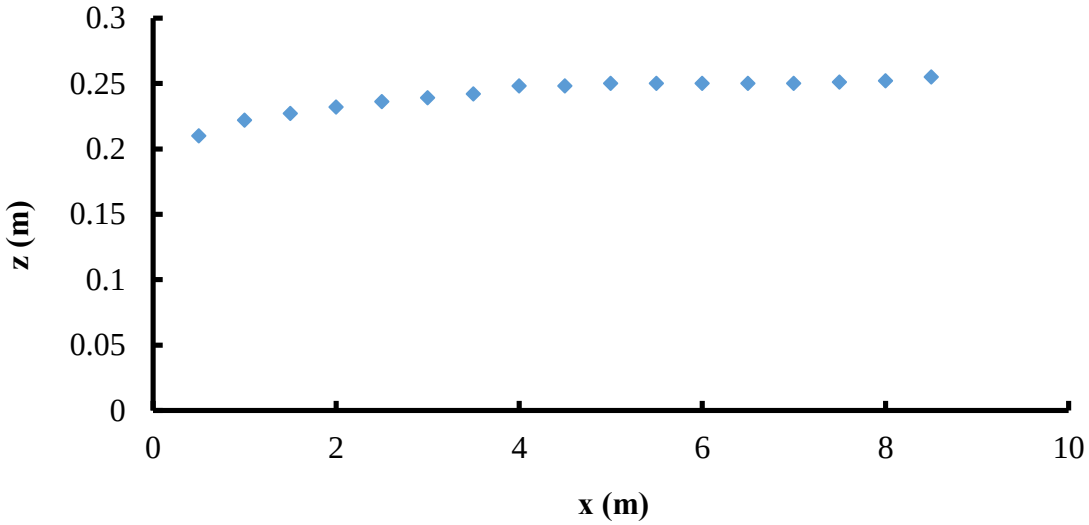

Figure A-2 :Water surface profile of smooth compound channel (S_0=0.001 & Q=0.102 m^3/s)

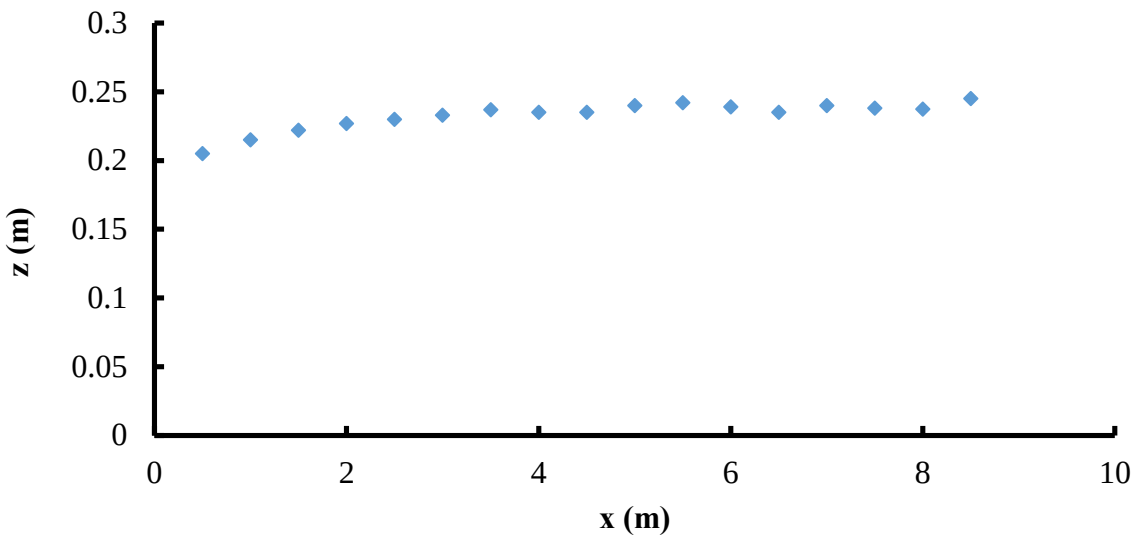

Figure A-3 :Water surface profile of smooth compound channel (S_0=0.002 & Q=0.102 m^3/s)

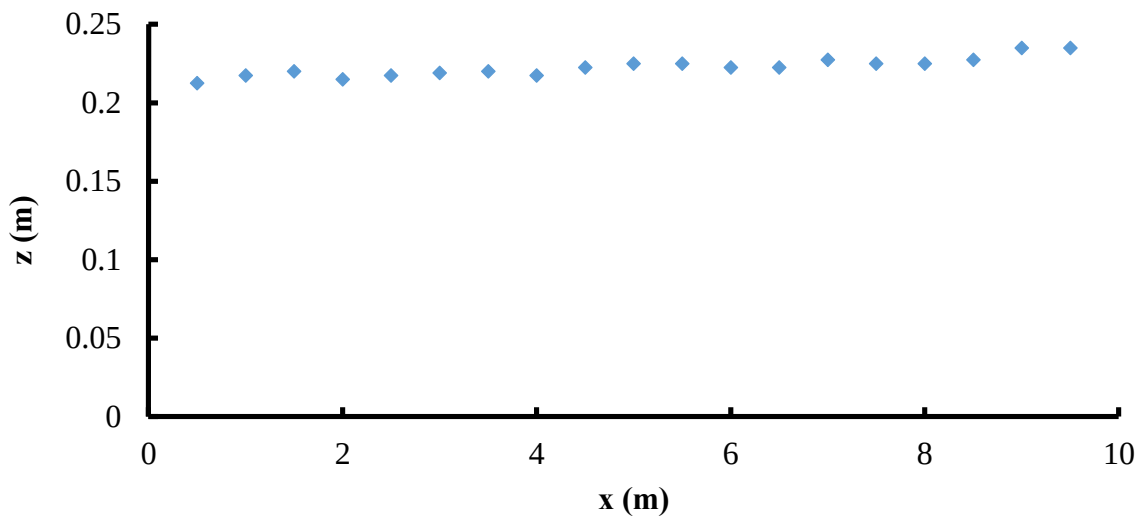

Figure A-4 : Water surface profile of smooth compound channel (S_0=0.01 & Q=0.166 m^3/s)

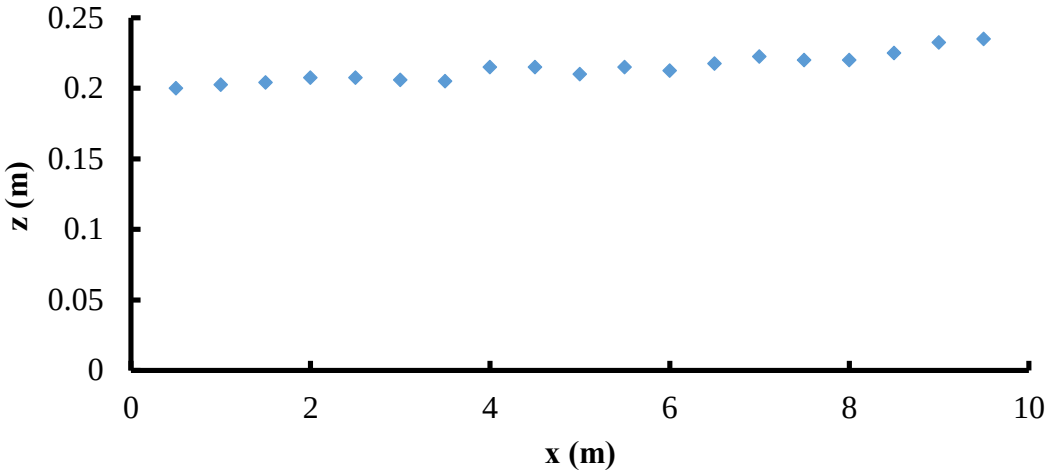

Figure A-5 :Water surface profile of smooth compound channel (S_0=0.015 & Q=0.166 m^3/s)

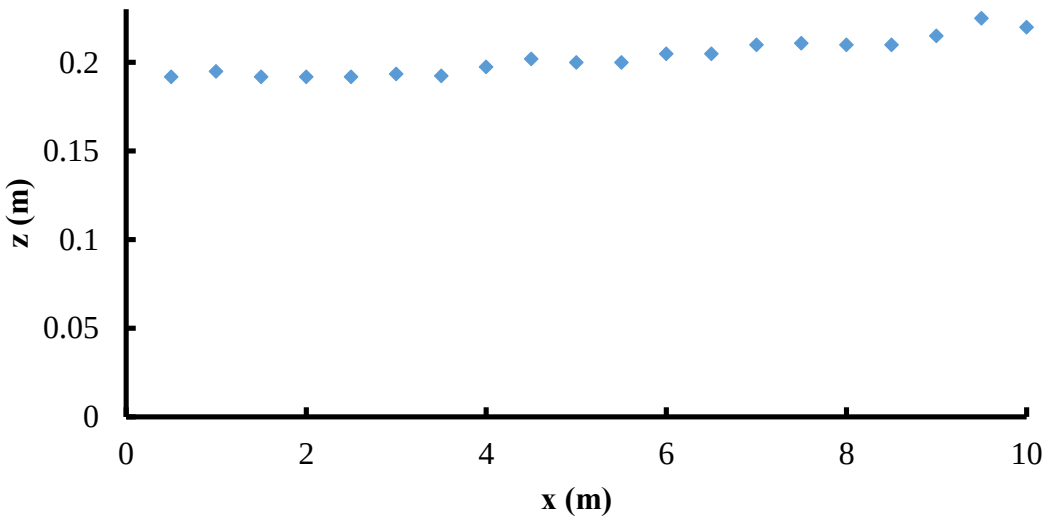

Figure A-6 :Water surface profile of smooth compound channel (S_0=0.02 & Q=0.166 m^3/s)

APPENDIX B

WATER SURFACE PROFILES FOR FLOODPLAIN ROUGH COMPOUND CHANNEL EXPERIMENTS

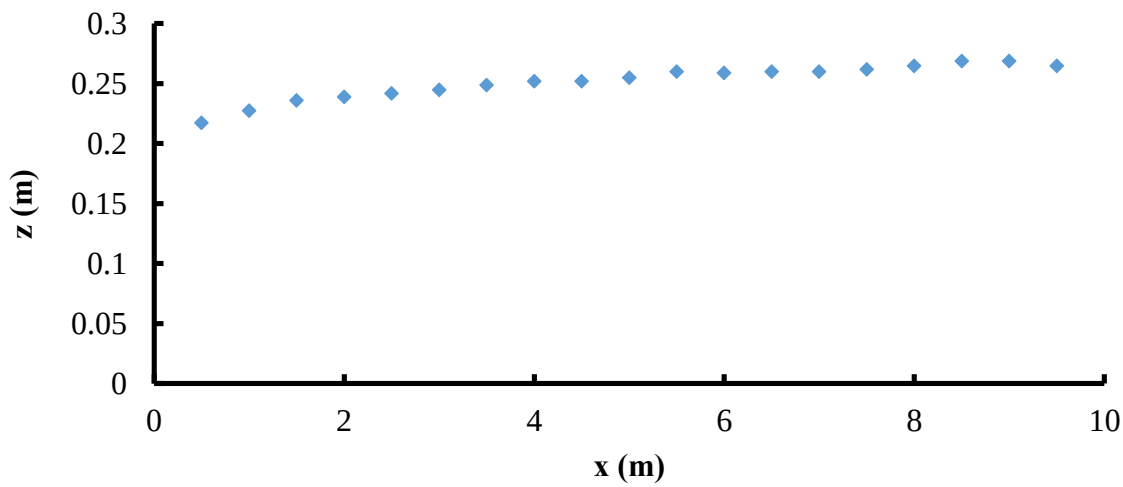

Figure B-1 : Water surface profile of smooth compound channel (S_0=0.002 & Q=0.1 m^3/s)

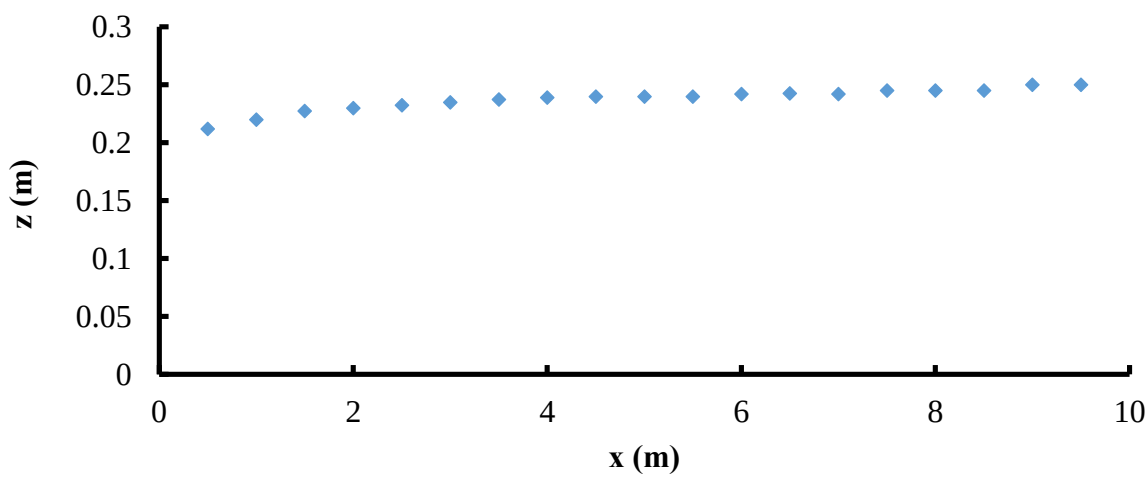

Figure B-2 : Water surface profile of smooth compound channel (S_0=0.004 & Q=0.1 m^3/s)

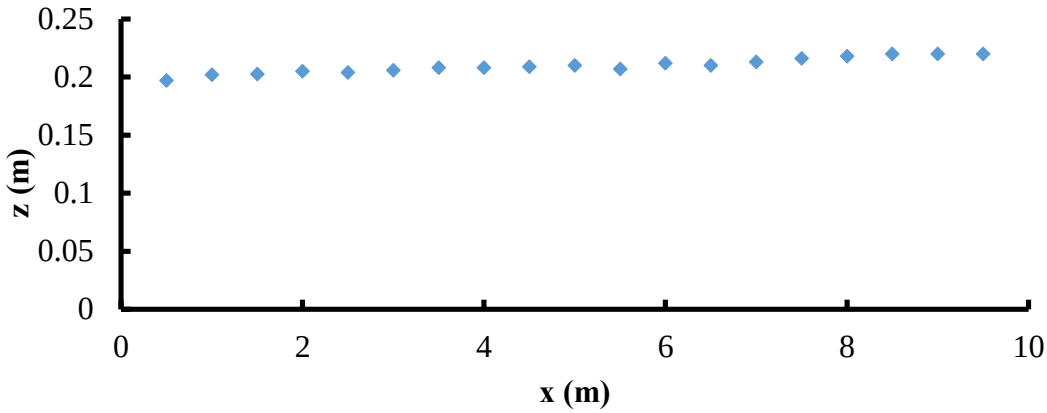

Figure B-3 : Water surface profile of smooth compound channel (S_0=0.008 & Q=0.1 m^3/s)

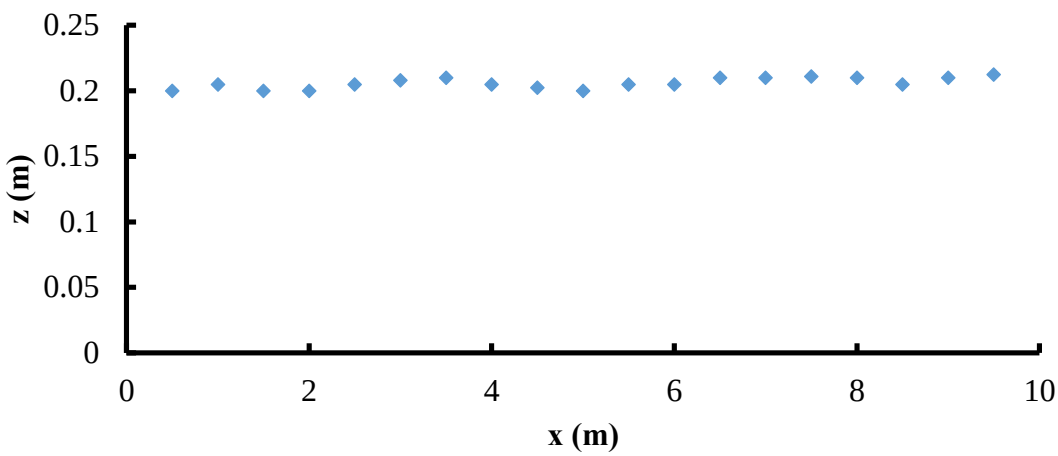

Figure B-4 : Water surface profile of smooth compound channel (S_0=0.02 & Q=0.147 m^3/s)

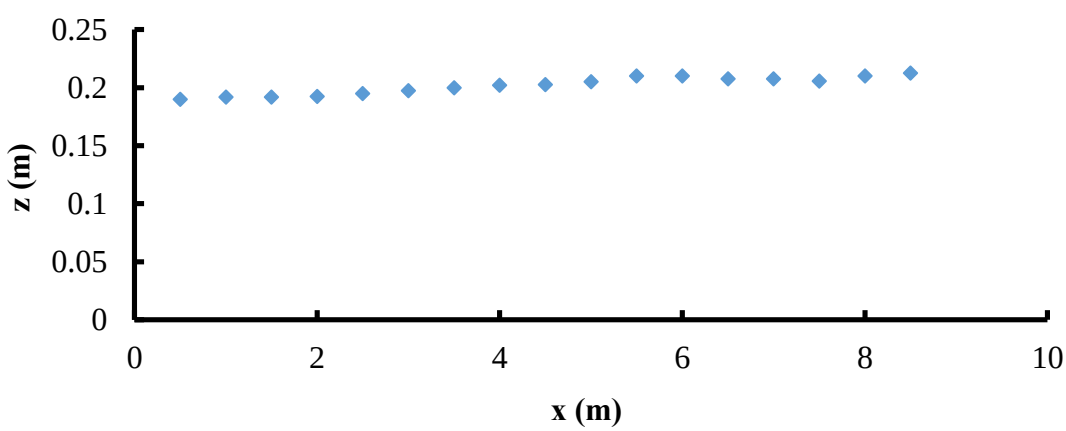

Figure B-5 : Water surface profile of smooth compound channel (S_0=0.025 & Q=0.16 m^3/s)

APPENDIX C

WATER SURFACE PROFILES FOR ROUGH COMPOUND CHANNEL EXPERIMENTS

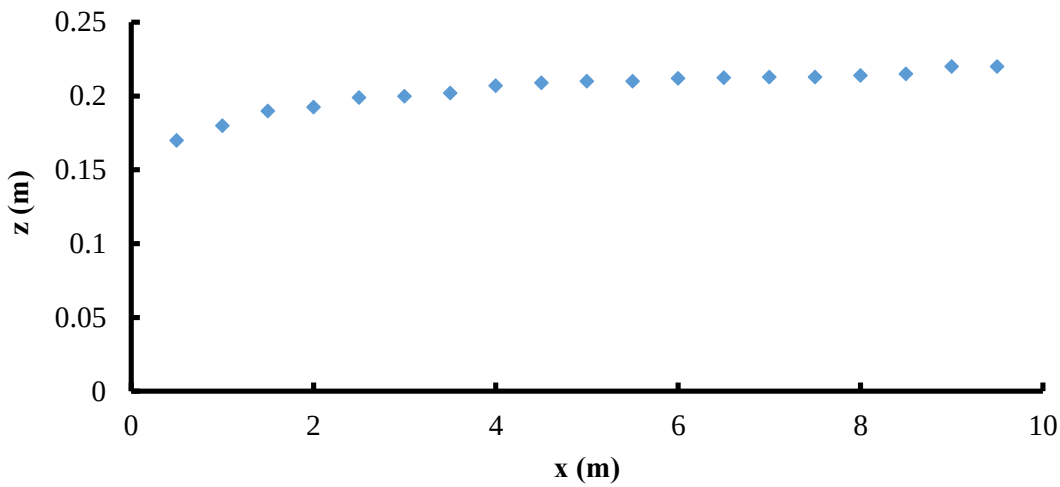

Figure C-1 : Water surface profile of smooth compound channel (S_0=0.002 & Q=0.0505 m^3/s)

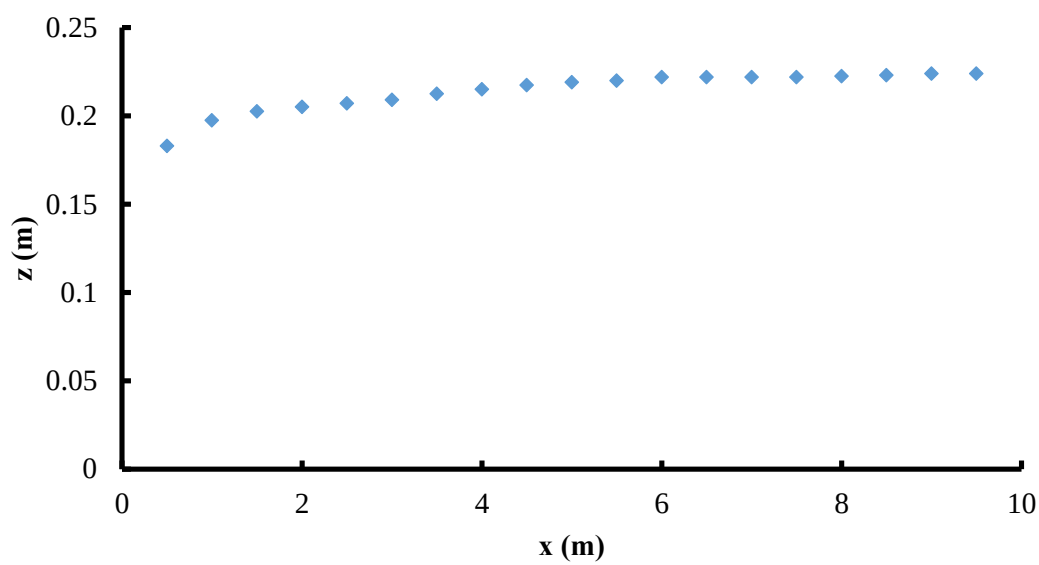

Figure C-2 : Water surface profile of smooth compound channel (S_0=0.004 & Q=0.0635 m^3/s)

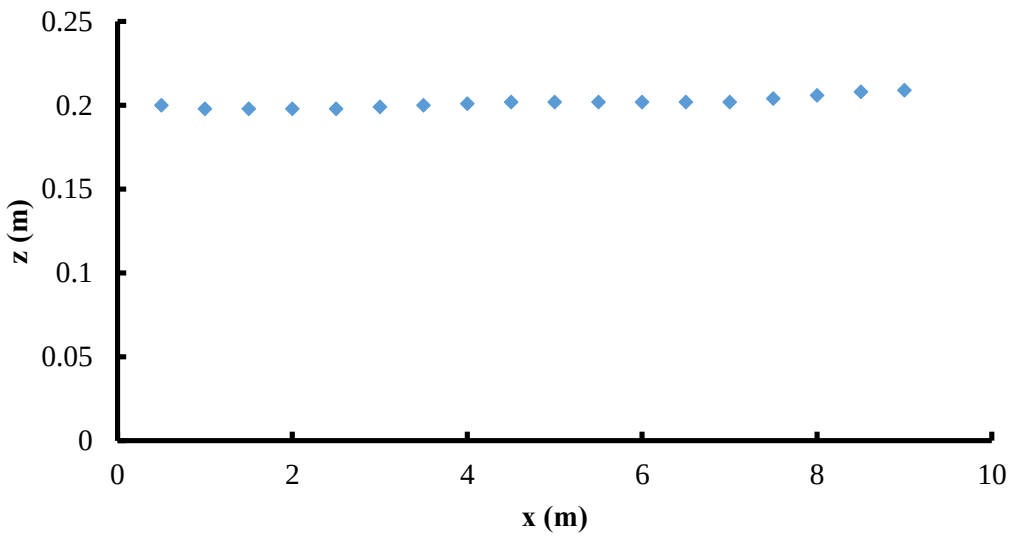

Figure C-3 : Water surface profile of smooth compound channel

(S_0=0.01 & Q=0.074 m^3/s, Z_n=0.199 m)

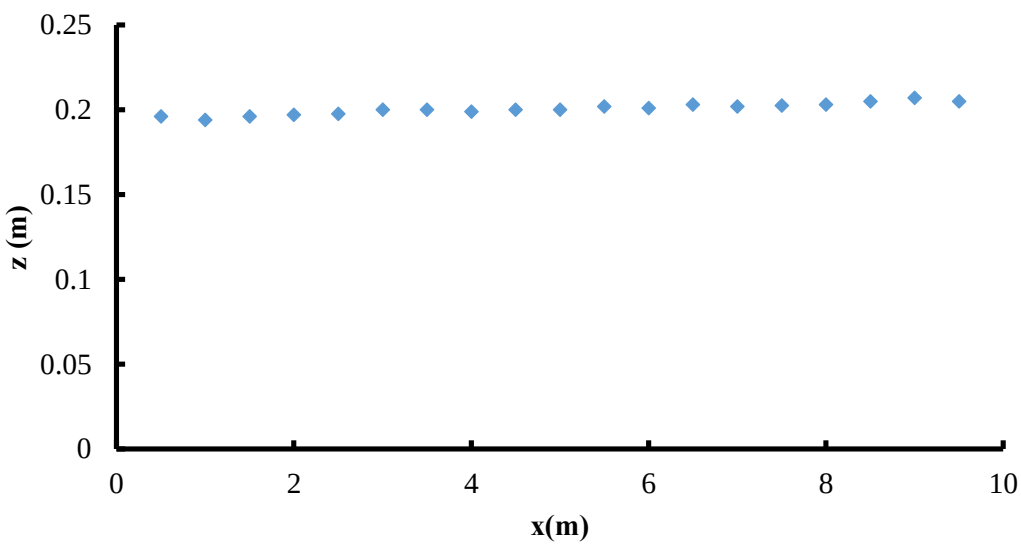

Figure C-4 : Water surface profile of smooth compound channel

(S_0=0.02 & Q=0.1 m^3/s, Z_n=0.2 m)

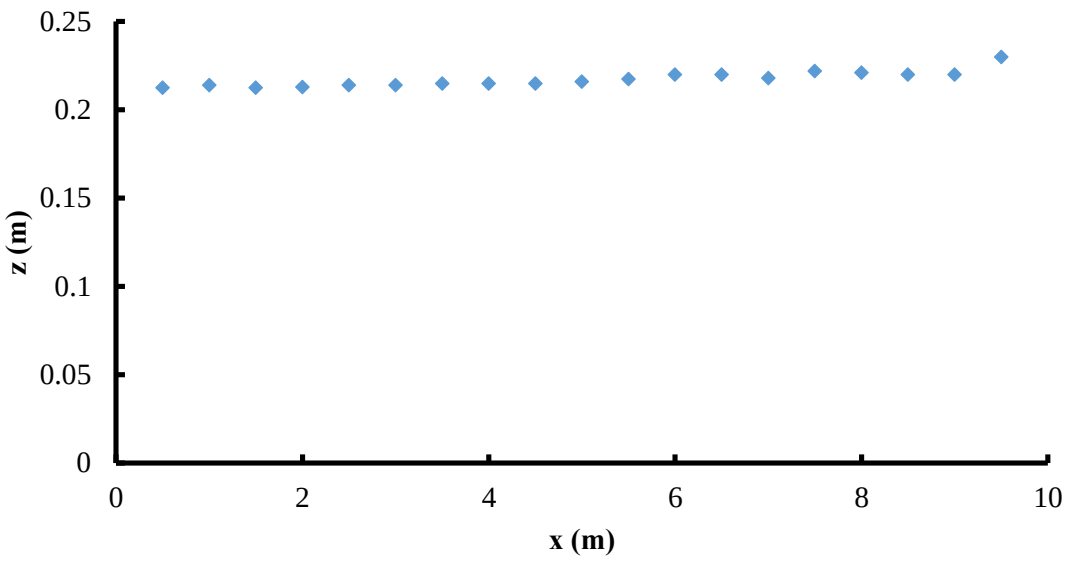

Figure C-5 : Water surface profile of smooth compound channel

(S_0=0.03 & Q=0.15 m^3/s, Z_n=0.214 m)

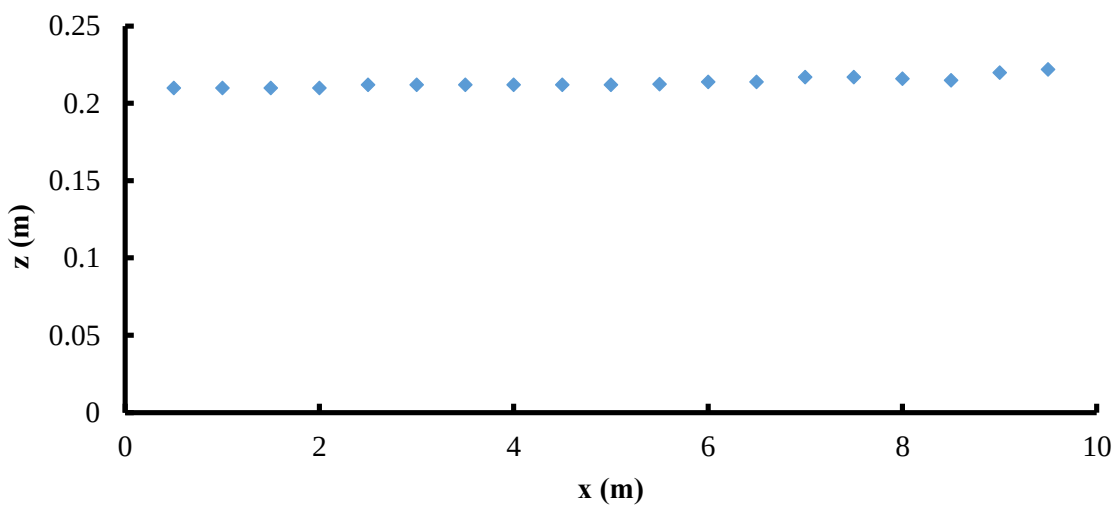

Figure C-6 : Water surface profile of smooth compound channel

(S_0=0.035 & Q=0.16 m^3/s, Z_n=0.212 m)

APPENDIX D

HOT-FILM MEASUREMENTS

The result of experiments for Hot-film measurement are shown for free surface and central water column cases. First 5 figures are for channel center line water column velocity measurements and the other 5 figures are for free surface velocity of the same first 5 experiments.

Since approaching the probe near surface is risky due to oscillating interface (especially in high flows), Hot-film can be exposed to air which then would yield wrong results. For this reason, for surface measurements the probe was submerged into water for at least a centimeter. Overall, the results show that measurements near surface are not very promising when compared to PIV and numerical computations. Some attempts were made to clarify the cause as in increasing the recording time and making sure of no temperature changes in test duration but no logical cause could be identified. That brings up this recommendation that perhaps Hot-film may not be practical option for surface velocity measurements. (More detailed information is provided in chapter 2).

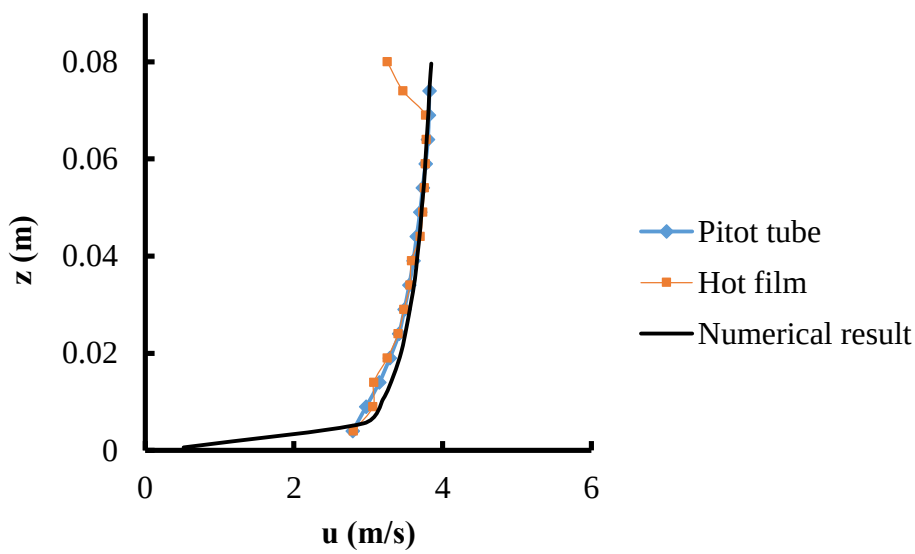

Figure D-1 : Vertical central line velocity distribution with S_0=0.055, Q=0.162 m^3/s and Z_n=0.8 m

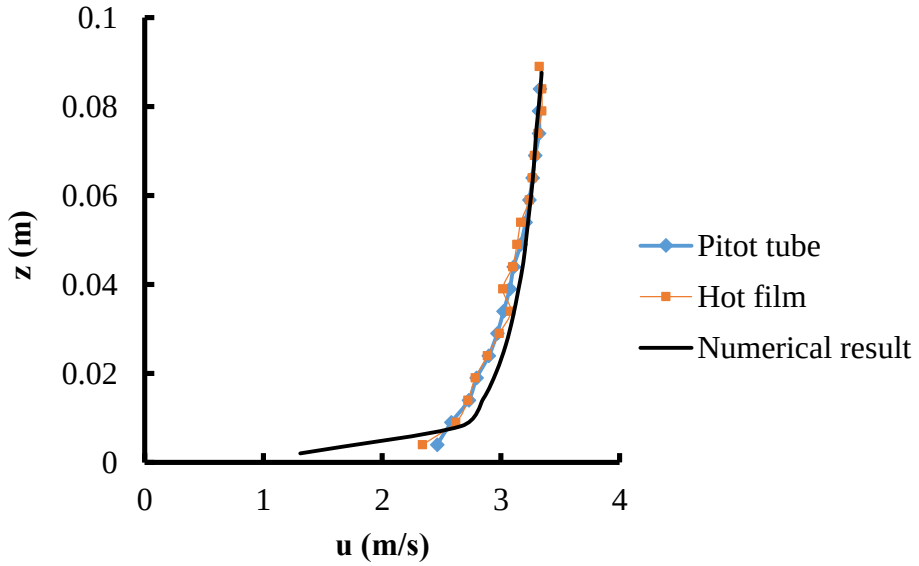

Figure D-2 : Vertical central line velocity distribution with S_0=0.035, Q=0.1588 m^3/s and Z_n=0.9 m

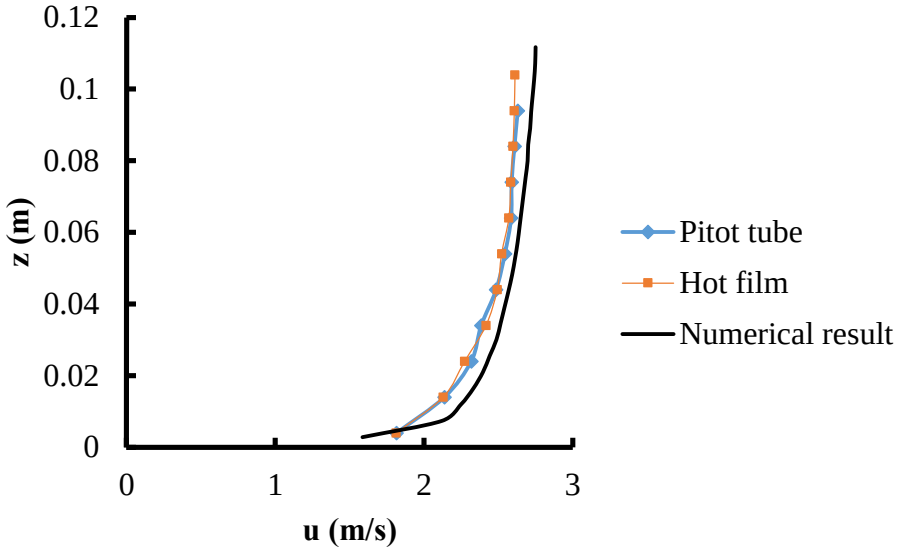

Figure D-3 : Vertical central line velocity distribution with S_0=0.015, Q=0.1675 m^3/s and Z_n=0.115 m

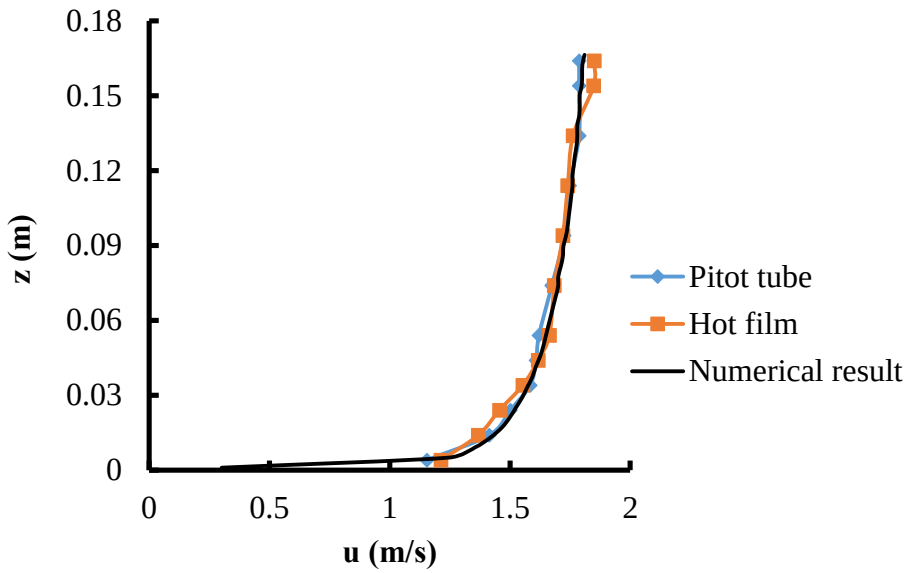

Figure D-4 : Vertical central line velocity distribution with S_0=0.004, Q=0.1632 m^3/s and Z_n=0.17 m

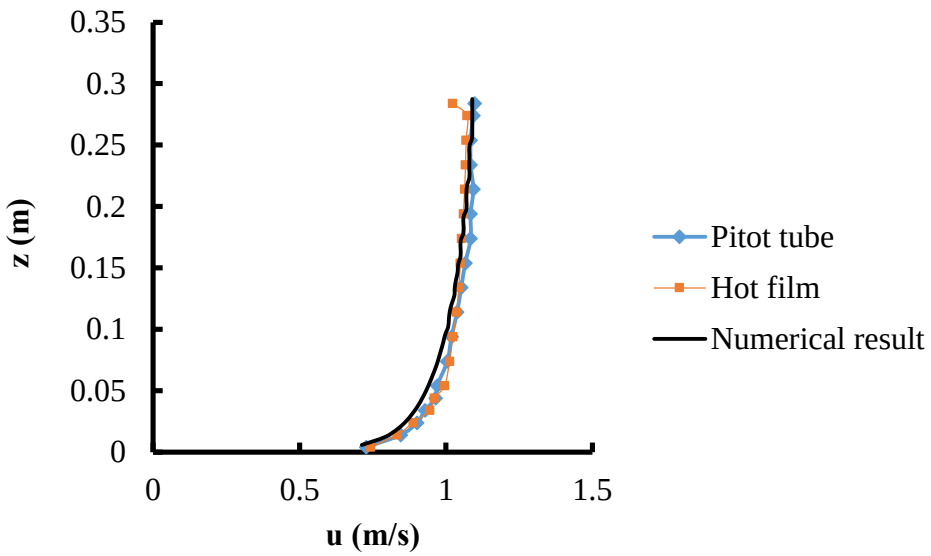

Figure D-5 : Vertical central line velocity distribution with S_0=0.001, Q=0.17065 m^3/s and Z_n=0.29 m

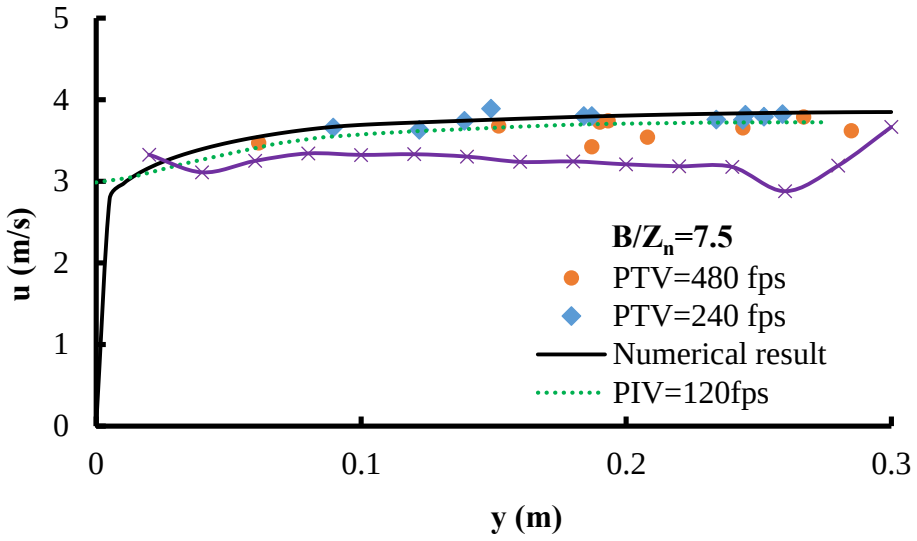

Figure D-6 : Surface velocity distribution with S_0=0.055, Q=0.1623 m^3/s and Z_n=0.08 m

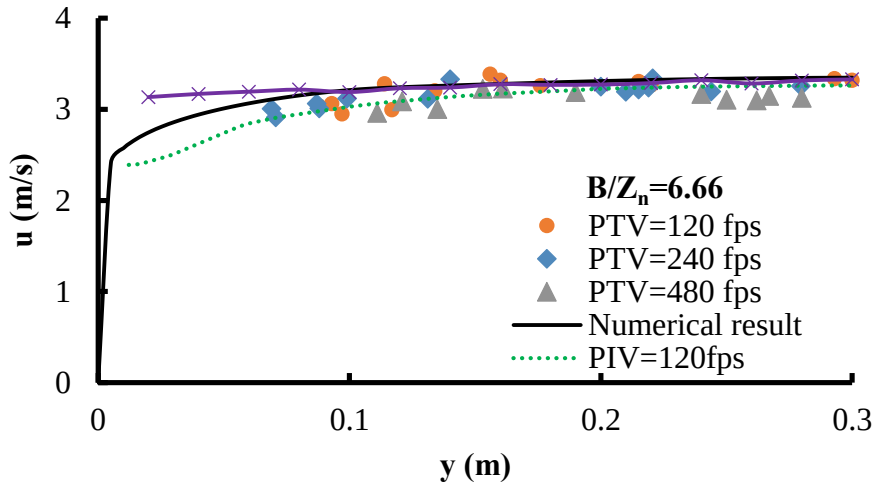

Figure D-7 : Surface velocity distribution with S_0=0.035, Q=0.1588 m^3/s and Z_n=0.09 m

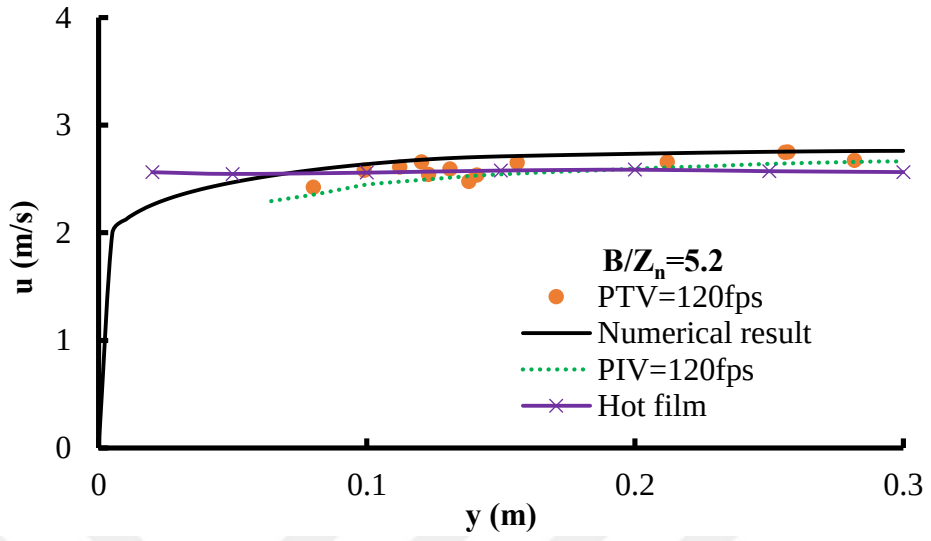

Figure D-8 : Surface velocity distribution with S_{0c}=0.015, Q=0.1675 m^3/s and Z_n=0.115 m

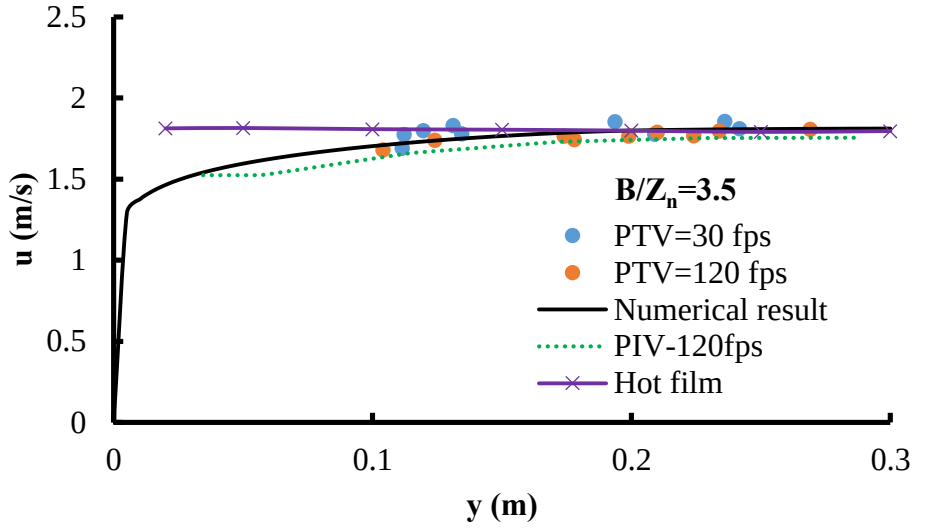

Figure D-9 : Surface velocity distribution with S_0=0.004, Q=0.1632 m^3/s and Z_n=0.17 m

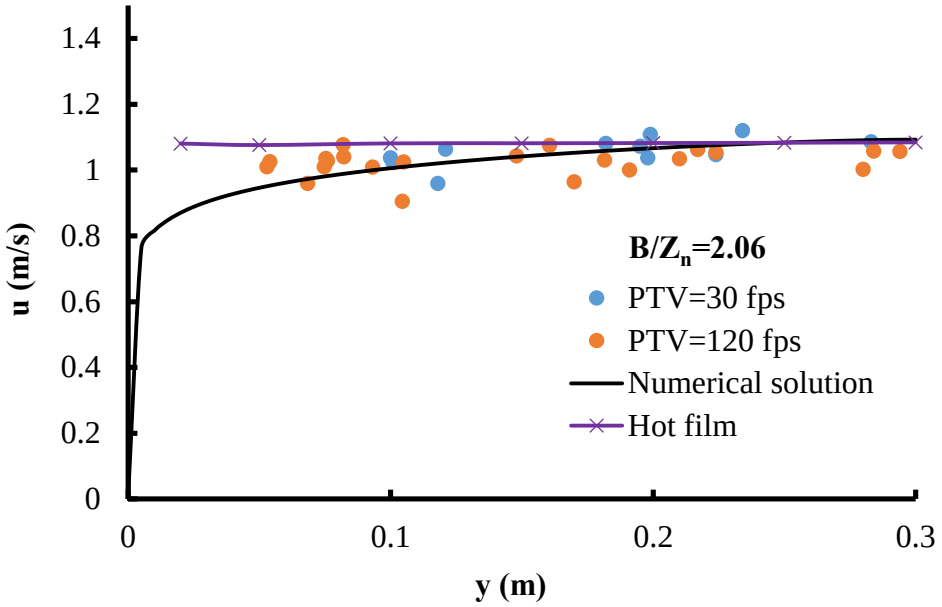

Figure D-10 : Surface velocity distribution with S_0=0.001, Q=0.17064 m^3/s and Z_n=0.29 m

APPENDIX E

COMPUTER PROGRAM THAT DOES THE PTV ANALYSIS AND IMAGE RECTIFICATION

```
%% Code for Object Tracking and computing its velocity +
calibrating image to real world distances
%Assumptions:
           % 1-Particle assumed to be moving along a stright
line.
                        % (if curved,no effect on analysis
though)
           % 2-One single particle maybe tracked at a time.
           % 3-Background should have enough contrast
intensity.
           % 4-The code will work in Matlab 2014 or any
version newer.
           % 5-Particle can be either white or black.
           % 6-The code is capable of rectifying oblique
images if and only if:
                              %regardless of world
dimensions, the ground control
                              %points fall on a horizontal
SQUARE
clc
clear all
close all
format long

Decision_on_video_or_frames=menu('Do you need to convert
video into frames?','Yes','No');
if(Decision_on_video_or_frames==1 )
    [filename, pathname] = uigetfile( ...
    {'*.avi;*.mpg;*.mpeg;*.MOV','Video Files
(*.avi,*.mpg,*.mpeg,*.MOV)';
     '*.*',  'All Files (*.*)'}, ...
     'Select a video file');
vid = VideoReader(fullfile(pathname,filename));  %video
loaded at this stage
t=vid.Duration % video duration
 numFrames = vid.NumberOfFrames
 n=numFrames;
 delT=t/n
% writing images to folder
if (n<100)
 for i =1:9
```

```
 cd(pathname);
 frames = read(vid,i);
 frames=rgb2gray(frames);
 imwrite(frames,[ '0',int2str(i), '.jpg']);
 im(i)=image(frames);
 end
 for i =10:n
 cd(pathname);
 frames = read(vid,i);
 frames=rgb2gray(frames);
 imwrite(frames,[ int2str(i), '.jpg']);
 im(i)=image(frames);
 end
end
if (n>100 & n<1000)
 for i =1:9
 cd(pathname);
 frames = read(vid,i);
 frames=rgb2gray(frames);
 imwrite(frames,[ '00',int2str(i), '.jpg']);
 im(i)=image(frames);
 end
 for i =10:99
 cd(pathname);
 frames = read(vid,i);
 frames=rgb2gray(frames);
 imwrite(frames,[ '0',int2str(i), '.jpg']);
 im(i)=image(frames);
 end
 for i =100:n
 cd(pathname);
 frames = read(vid,i);
 frames=rgb2gray(frames);
 imwrite(frames,[ int2str(i), '.jpg']);
 im(i)=image(frames);
 end
end
   if (n>1000)
 for i =1:9
 cd(pathname);
 frames = read(vid,i);
 frames=rgb2gray(frames);
 imwrite(frames,[ '000',int2str(i), '.jpg']);
 im(i)=image(frames);
 end
 for i =10:99
 cd(pathname);
```

```
 frames = read(vid,i);
 frames=rgb2gray(frames);
 imwrite(frames,[ '00',int2str(i), '.jpg']);
 im(i)=image(frames);
 end
 for i =100:999
 cd(pathname);
 frames = read(vid,i);
 frames=rgb2gray(frames);
 imwrite(frames,[ '0',int2str(i), '.jpg']);
 im(i)=image(frames);
 end
  for i =1000:n
 cd(pathname);
 frames = read(vid,i);
 frames=rgb2gray(frames);
 imwrite(frames,[ int2str(i), '.jpg']);
 im(i)=image(frames);
 end
 end

 close all
  %% this will be executed when no video is to be converted
else
    [filename, pathname] = uigetfile( ...
    {'*.jpg' ,  'All Files (*.*)'}, ...
     'Select any one image to start the analysis');
 delT=0.033366666666667; %distance b/w two frames in seconds
% calib_pic = imread(fullfile(pathname,filename));
 cd(pathname)
end
%% Reading frames
  a=dir(fullfile(pathname,'*.jpg'));
fileNames={a.name};
fileNames = dir(fullfile(pathname, '*.jpg'));
I = cell(length(fileNames), 1);
cd(pathname);
for k = 1:length(fileNames)
    filename = [fileNames(k).name];
    I{k} = imread(filename);
%     imshow(I{k})
%     drawnow
%     pause
%     k
end
```

```
%% Rectifying- it is valid if ground control points are edges
of a squre, otherwise modification is needed
    Test=menu('Do you like to rectify images?','No','Yes');
while(Test==2)
% display('Start from South West and turn clock-wise')
% at this time, an approximately rectangular region may be
handled only
[filename, pathname] = uigetfile( ...
    {'*.jpg' ,  'All Files (*.*)'}, ...
     'Select a photo for rectifying...');
calib_pic = imread(fullfile(pathname,filename));
 imshow(calib_pic);title('Click on Ground control points,
Start from South West and turn clock-wise'); hold on
impixelinfo
axis on
[xlocat(1),ylocat(1)] = ginput(1);
 plot(xlocat(1),ylocat(1),'r*', 'MarkerSize', 20)
 [xlocat(2),ylocat(2)] = ginput(1);

p1 = [xlocat(1),ylocat(1)];
p2 = [xlocat(2),ylocat(2)];
plot([p1(1,1),p2(1,1)],[p1(1,2),p2(1,2)],'Color','r','LineWid
th',2);hold on
% plot([x1 x2],[y1 y2])
[xlocat(3),ylocat(3)] = ginput(1);
p3 = [xlocat(3),ylocat(3)];
plot([p2(1,1),p3(1,1)],[p2(1,2),p3(1,2)],'Color','r','LineWid
th',2);hold on

 [xlocat(4),ylocat(4)] = ginput(1);
p4 = [xlocat(4),ylocat(4)];
plot([p3(1,1),p4(1,1)],[p3(1,2),p4(1,2)],'Color','r','LineWid
th',2);hold on
pause(0.3);
plot([p1(1,1),p4(1,1)],[p1(1,2),p4(1,2)],'Color','r','LineWid
th',2);hold on

c=[xlocat(1) xlocat(2) xlocat(3) xlocat(4)]'; %[x1 x2 x3 x4]
in terms of pixel
r=[ylocat(1) ylocat(2) ylocat(3) ylocat(4)]'; %[y1 y2 y3 y4]
in terms of pixel
 base=[-0.5  0.5; -0.5  -0.5; 0.5  -0.5; 0.5  0.5]; %[x1
tf=cp2tform([c r],base*200,'projective'); %200 is a scale of
enlargment, according to the area of square (Surrounding the
ground control points), this is the only parameter to be
modified.
close all
```

```
T=tf.tdata.T;
[xf1, XData, YData]=imtransform(calib_pic,tf);
% imagesc(xf1)
imshow(xf1)
impixelinfo
axis on
Test=menu('Is it OK?:','Yes','No');
 close all

 while(Test==1)

for k = 1:length(fileNames)
     [I{k}, XData, YData]=imtransform(I{k},tf);
%     imshow(I{k})
%     drawnow
%     pause
%     k
end
imwrite(I{floor(k/2)},['Rectified for calib.jpg']);
n=length(fileNames);
close all
Test2=menu('Do you like to save the rectified
images?','Yes','No');
while(Test2==1)
     cd(pathname);
     if (n<100)
 for i =1:9
 imwrite(I{i},[ '0',int2str(i), '.jpg']);
 end
 for i =10:n
 imwrite(I{i},[ int2str(i), '.jpg']);
 end
end
if (n>100 & n<1000)
 for i =1:9
 imwrite(I{i},[ '00',int2str(i), '.jpg']);
 end
 for i =10:99
 imwrite(I{i},[ '0',int2str(i), '.jpg']);
 end
 for i =100:n
 imwrite(I{i},[ int2str(i), '.jpg'])
 end
end
   if (n>1000)
 for i =1:9
 imwrite(I{i},[ '000',int2str(i), '.jpg']);
```

```
 end
 for i =10:99
 imwrite(I{i},[ '00',int2str(i), '.jpg']);
  end
 for i =100:999
 imwrite(I{i},[ '0',int2str(i), '.jpg']);
   for i =1000:n
 imwrite(I{i},[ int2str(i), '.jpg']);
  end
 end
   end
Test2=2;
end
 break
 end
close all
end

%% Setting time step, dt in seconds
Video_rate=menu('What is
fps?','30','120','240','480','1000');
if (Video_rate==1)
    delT;
elseif(Video_rate==2)
delT=delT/4;
elseif(Video_rate==3)
delT=delT/8;
elseif(Video_rate==4)
    delT=delT/16;
elseif(Video_rate==5)
    delT=delT/33.333;
end

%% overlapping a couple of images
% for checking the position of particles
Five_To_overlay=length(fileNames);
Calibration_image=I{floor(Five_To_overlay/2)}; %mid way image
selected for calibration
  h(1)=imshow( I{floor(Five_To_overlay/2)-5} );title('Click
to continue, Overlapping acouple of particles'); hold on;
 h(2)=imshow( I{floor(Five_To_overlay/2)-3} ); hold on;
 h(3)=imshow( I{floor(Five_To_overlay/2)+2} ); hold on;
 h(4)=imshow( I{floor(Five_To_overlay/2)+5} ); hold on;
 h(5)=imshow( I{floor(Five_To_overlay/2)} ); hold on;
 h(6)=imshow( I{floor(Five_To_overlay/2)-10} ); hold on;
 h(7)=imshow( I{floor(Five_To_overlay/2)+10} ); hold on;
```

```
 h=[h(1) h(2) h(3) h(4) h(5) h(6) h(7)];
  set( h, 'AlphaData', .30 ); % .5 transparency
 colormap gray
waitforbuttonpress
close all
Test=2;
while(Test==2)
display('Select an image to specify region of interest')
% at this time, an approximately rectangular region may be
handled only
[filename, pathname] = uigetfile( ...
    {'*.jpg' ,  'All Files (*.*)'}, ...
     'Select an image for specifying the region of
interest');
calib_pic = imread(fullfile(pathname,filename));
 imshow(calib_pic);title('Select a region of interest'); hold
on
impixelinfo
axis on
[xlocat(1),ylocat(1)] = ginput(1);
 plot(xlocat(1),ylocat(1),'r*', 'MarkerSize', 20)
 [xlocat(2),ylocat(2)] = ginput(1);

p1 = [xlocat(1),ylocat(1)];
p2 = [xlocat(2),ylocat(2)];
plot([p1(1,1),p2(1,1)],[p1(1,2),p2(1,2)],'Color','r','LineWid
th',2);hold on
% plot([x1 x2],[y1 y2])
[xlocat(3),ylocat(3)] = ginput(1);
p3 = [xlocat(3),ylocat(3)];
plot([p2(1,1),p3(1,1)],[p2(1,2),p3(1,2)],'Color','r','LineWid
th',2);hold on

 [xlocat(4),ylocat(4)] = ginput(1);
p4 = [xlocat(4),ylocat(4)];;
plot([p3(1,1),p4(1,1)],[p3(1,2),p4(1,2)],'Color','r','LineWid
th',2);hold on
pause(0.3);
plot([p1(1,1),p4(1,1)],[p1(1,2),p4(1,2)],'Color','r','LineWid
th',2);hold on


 Test=menu('Is it the right ROI?:','Yes','No');
 close all
end

%% Image cropping phase %learn oblique cropping
```

```
 for k = 1:length(fileNames)
    filename = [fileNames(k).name];
    I{k} = imread(filename);
  I{k}=imcrop(I{k},[min(xlocat) min(ylocat) abs(max(xlocat)-
min(xlocat))...
 abs(max(ylocat)-min(ylocat))]);% [xmin ymin width height]
 end
  %% Inverting colors according particle being black or white
particle_type=menu('What color are the
particles?','black','white')
if (particle_type==1)
for k = 1:length(fileNames)
 I{k} = imcomplement(I{k});
end
calib_pic=imcomplement(calib_pic);
end
 %% Determining the thresholding intensity
  Test=2;
while(Test==2)
    intensity=input('Select a thresholding intensity b/w 1
and 0. If in doubt put 0.25 :');
   calib_pic_t= im2bw(calib_pic,intensity);
     imshow(calib_pic_t);
     Test=menu('Is it the right intensity?:','Yes','No');
close all
end

 %% Detecting the particle to enter and record the number of
frame
  for k = 1:length(fileNames)
      %the density of thresholding should be automated
      I{k}=im2bw(I{k},intensity);%BW = im2bw(I, level)
I{k} = imfill(I{k},'holes');
stat = regionprops(I{k},'centroid');
if (sum(size(stat))==2)
    Starting=k;
    break
end
  end

  %% Detecting the particle to exit and record the number of
frame
      for k = length(fileNames):-1:1
      I{k}=im2bw(I{k},intensity);%BW = im2bw(I, level)
I{k} = imfill(I{k},'holes');
% Ilabel = bwlabel(I{k});
stat = regionprops(I{k},'centroid');
```

```
if (sum(size(stat))==2)
    Ending=k;
    break
end
  end
for k=Starting:Ending
    I{k}=im2bw(I{k},intensity);%BW = im2bw(I, level) level=[0
1]
end
close all
for show=Starting:Ending
    drawnow;
    pause (0.1)
    stat = regionprops(I{show},'centroid');
    %for the evaluating aim, please keep the green lines
below
imshow( I{show});title('Particles detected'); hold on;
  impixelinfo
axis on
  for x = 1: numel(stat)
    plot(stat(x).Centroid(1),stat(x).Centroid(2),'ro');
  end
end
pause(1)
close all
%% Image analysis manual range setting
% If automatic image start and ending detection fails,
% select a sarting and ending image number manually.
% This problem will not be faced in most of the cases under
lab conditions.
Manual_range_detection=menu('Do you like to set the number of
images for region of interest manually?','Yes','No');
if (Manual_range_detection==1)
for k=1:length(fileNames)
        drawnow;
    I{k}=im2bw(I{k},intensity);%BW = im2bw(I, level) level=[0
1]
    imshow( I{k});title(['Press click... Image
number=',num2str(k)]); hold on;
        waitforbuttonpress
end
close all
Starting=input('Enter the image number at which particle
enters the region of interest:');
Ending=input('Enter the image number at which particle exits
the region of interest:');
end
```

```
%% Calculation of DeltaX & velocities
k=0;
 for i=Starting:Ending-1
%1st image
image_1st=Starting+k;
stat = regionprops(I{image_1st},'centroid');
particles_no=struct2cell(stat); % new
particles_no=cell2mat(particles_no); %new
No_particle=sum(size(stat))-1; % new---number of particles
detected

area = regionprops(I{image_1st},'area');  %new, properties of
areas will be stored
area_info=struct2cell(area); %new
area_info=cell2mat(area_info); %new

Index_Biggest_particle = find(area_info == max(area_info),
1); %new
Picture_of_interest=2*Index_Biggest_particle-1 ; %new the
index of x coordinate
location1=[particles_no(Picture_of_interest)
particles_no(Picture_of_interest+1)]; %new
image_2nd=image_1st+1; %analysis of 2nd image pai
stat = regionprops(I{image_2nd},'centroid');
% Particle_control_2=sum(size(stat));%indication of existance
of particle in image2
particles_no=struct2cell(stat); % new
particles_no=cell2mat(particles_no); %new
No_particle=sum(size(stat))-1; % new---number of particle

area = regionprops(I{image_2nd},'area');  %new
area_info=struct2cell(area); %new
area_info=cell2mat(area_info) ;%new

Index_Biggest_particle = find(area_info == max(area_info),
1); %new
Picture_of_interest=2*Index_Biggest_particle-1;  %new the
index of x coordinate
location2=[particles_no(Picture_of_interest)
particles_no(Picture_of_interest+1)] ;%new
k=1+k;
 Oblique_Distance_btw_2particles=sqrt((abs(location2(1)-
location1(1)))^2+...
     (abs(location2(2)-location1(2)))^2)  ; %pixel wise
distance
PixelWise_velocity(k)=Oblique_Distance_btw_2particles/delT;
```

```
  end
 %% Calibration phase
display('Calibration phase')
real_length=input('Enter the real length for
calibration(channel width...)in meters:'); %channel width in
meters, may be considered as input
Test=2;
while(Test==2)
imshow(calib_pic);title('Select 2 points to calibrate its
length'); hold on
impixelinfo
axis on
[xlocat,ylocat] = ginput(1);
plot(xlocat(1),ylocat(1),'Marker','p','Color',[.88 .48
0],'MarkerSize',15) ;
% plot(xlocat(1),ylocat(1),'r*', 'MarkerSize', 20)
p1 = [xlocat(1),ylocat(1)];
[xlocat(2),ylocat(2)] = ginput(1);
p2 = [xlocat(2),ylocat(2)];
plot(xlocat(2),ylocat(2),'Marker','p','Color',[.88 .48
0],'MarkerSize',15) ;
plot([p1(1,1),p2(1,1)],[p1(1,2),p2(1,2)],'Color','r','LineWid
th',2);hold on
        Test=menu('Is it the right length?:','Yes','No');
end
close all
Channel_width_pixelwize=...
    sqrt(abs(xlocat(2)-xlocat(1))^2+abs(ylocat(2)-
ylocat(1))^2);
Calib_velocity=PixelWise_velocity*real_length/Channel_width_p
ixelwize;
Calib_velocity(length(Calib_velocity))=[];
Calib_velocity(1)=[];
plotyy(1:length(Calib_velocity),Calib_velocity,1:length(Calib
_velocity),Calib_velocity,'plot','stem')
xlabel('Number of velocity')
ylabel('Velocity (m/s)')
title('Velocity range')

point_wise_velocity=mean(Calib_velocity)% m/s
display('in m/s')
display('Click on the Figure to continue')
waitforbuttonpress
close all
%% Computing the distance of particle to the wall
Test=2;
while(Test==2)
```

```
imshow(calib_pic);title('Select 2 points to indicate the wall
& 1 point for particle:'); hold on
impixelinfo
axis on
[xlocat,ylocat] = ginput(1);
plot(xlocat(1),ylocat(1),'Marker','p','Color',[.88 .48
0],'MarkerSize',15) ;
% plot(xlocat(1),ylocat(1),'r*', 'MarkerSize', 20)
p1 = [xlocat(1),ylocat(1)];
[xlocat(2),ylocat(2)] = ginput(1);
p2 = [xlocat(2),ylocat(2)];
plot(xlocat(2),ylocat(2),'Marker','p','Color',[.88 .48
0],'MarkerSize',15) ;
plot([p1(1,1),p2(1,1)],[p1(1,2),p2(1,2)],'Color','r','LineWid
th',2);hold on

[xlocat,ylocat] = ginput(1);
pt=[xlocat(1),ylocat(1)];
plot(xlocat(1),ylocat(1),'Marker','p','Color',[.88 .48
0],'MarkerSize',15) ;

p1=[p1 0];
p2=[p2 0];
pt=[pt 0];
      a = abs(p1 - p2);
      b = abs(pt - p2);
    d = (norm(cross(a,b)) /
norm(a))*(real_length/Channel_width_pixelwize);
Test= menu( ['Distance to wall=', num2str(d),'(m)']
,'Yes','No');
end
close all
d
    display('in (m)')
```

APPENDIX F

COMPUTER PROGRAM FOR GRADUALLY VARIED SURFACE PROFILE CALCULATIONS

```
! surface profile calculations for M2-S2-H1
 parameter (Section_num=2000) ! number of sections for calculation (mesh quality)
dimension::y(Section_num),veloc(Section_num),Rh(Section_num),Dx(Section_num),xlocat
(Section_num)
   character(100)::fileNAME=''
   character(len=20)::typ=' '
   real::n,Length
   print*,'REC for rectangle'
    print*,'COMP for compound rectangular channel'
   print*,''
   print*,''
   print*,'Enter channel geometry:'
   !read(*,*)typ
   typ='rec'
   if(typ.ne.'rec') then
    print*,'Code works for REC channel only at this time'
       go to 20
   end if
   print*,'Enter Q(m3/s):'
   read(*,*)Q
   print*,'channel slope S0:'
   read(*,*)S0
   print*,'Enter manning coefficient n: (n=0.01 for glass)'
   !read(*,*)n
   n=0.009
   if (S0==0) then
   print*,'Enter channel length L(m) :'
   read(*,*)Length
   end if
   if (typ=="rec")then
      print*,'Enter channel width B(m):'
      !read(*,*)B
      B=0.6
      call rectangle(B,Q,s0,n,yn,yc)
   end if
      if (typ=="comp") then
      a=2 !testing
   end if
   if(s0==0) then
      print*,'Horizontal channel'
      print*,'Enter Brink depth (m) :'
```

```
        read(*,*)yc
        !print*,'Enter water depth at the upstream:'
        !read(*,*)yn
        yn=0.32 ! channel height, this should be modified
    end if
    if (yn>yc) then
        print*,''
        print*,'Flow is subcritical Fr<1'
        print*,''
    end if
     if ( (s0.eq.0) .and. (yn.lt. yc)  )then
        print*,'Fr>1 and S0=0 can not happen at once'
        go to 20
    end if
    if (yc>yn) then
        print*,''
        print*,'Flow is supercritical Fr>1'
        print*,''
        go to 10
    end if
     if (S0>0) then
print*,'M2 profile with Fr<1'
     else
         print*,'H1 profile calculated'
     end if
ybrink=0.714*yc   !or try to read it experimentally, it seems brink depth leads to wrong
profile sketch
ybrink=yc
 y_difference=0.99*yn-ybrink
 dely=y_difference/Section_num
 y(1)=ybrink;
do i=2,Section_num
    y(i)=y(1)+i*dely;
end do
  do i=1,Section_num
     veloc(i)=q/(b*y(i));
 end do
 do i=1,Section_num
     Rh(i)=(y(i)*b/(2*y(i)+b));
 end do
do i=1,Section_num-1
     Dx(i)=abs(y(i+1)+(1./(2*9.8))*veloc(i+1)*veloc(i+1)-y(i)-
(1./(2*9.8))*veloc(i)*veloc(i))/abs(s0-
0.5*n*n*(veloc(i+1)*veloc(i+1)/(Rh(i+1)**(4./3))+veloc(i)*veloc(i)/(Rh(i)**(4./3))));
 end do
     xlocat(1)=0;
```

```
    do i=2,Section_num
       xlocat(i)= xlocat(i-1)+Dx(i-1);
    end do
        Fr=(Q/(b*yn))/sqrt(9.8*yn)
     if (s0>0) then
        print*,''
           print*,'Yn=',yn,'Yc=',yc
           print*,''
      write(fileNAME,'(a,F10.3,a,a,F10.2,a,a ,a)')' Q=',q,'  ','Fr=',Fr,'  ','M2','.dat'
   open(unit=2,file=fileNAME)
   do i=1,Section_num
     write(2,*) xlocat(i),y(i)
  end do
      print*,'M2=',xlocat(Section_num)
   write(2,*) ,'Yn=',  yn,'Yc=',yc
     end if
      print*,'Fr=',Fr
   print*,'V=',q/(yn*b)
    if (s0==0) then
       write(fileNAME,'(a,F10.3,a,a,F10.2,a,a, a)')' Q=',q,'  ','Fr=',Fr,'  ','H1','.dat'
   open(unit=2,file=fileNAME)
  !write(2,*) ,'variables =',  '"x",','"y",'
  do i=1,Section_num
       if (xlocat(i)<Length) then
     write(2,*) xlocat(i),y(i)
    k=i
     end if
  end do
  print*,'Y_upstream=',y(k),'Y_downstream=',yc
       write(2,*) ,'Y_upstream=',  y(k),'Y_downstream=',yc
              print*,'Fr=',Fr
   print*,'V=',q/(y(k)*b)
      end if
  go to 20
10 continue
  print*,'S2 profile with Fr>1'
   y_difference=yc-1.01*yn
 dely=y_difference/Section_num
y(1)=yc
do i=2,Section_num
       y(i)=y(1)-i*dely;
end do
  do i=1,Section_num
    veloc(i)=q/(b*y(i));
 end do
do i=1,Section_num
```

```
    Rh(i)=(y(i)*b/(2*y(i)+b));
 end do
 do i=1,Section_num-1
    Dx(i)=abs(y(i+1)+(1./(2*9.8))*veloc(i+1)*veloc(i+1)-y(i)-
(1./(2*9.8))*veloc(i)*veloc(i))/abs(s0-
0.5*n*n*(veloc(i+1)*veloc(i+1)/(Rh(i+1)**(4./3))+veloc(i)*veloc(i)/(Rh(i)**(4./3))));
 end do
    xlocat(1)=0;
    do i=2,Section_num
       xlocat(i)= xlocat(i-1)+Dx(i-1);
    end do
            print*,''
           print*,'Yn=',yn,'Yc=',yc
           print*,''
    Fr=(Q/(b*yn))/sqrt(9.8*yn)
     write(fileNAME,'(a,F10.3,a,a,F10.2,a,a, a)')' Q=',q,'  ','Fr=',Fr,'  ','S2','.dat'
   print*,'Fr=',Fr
   print*,'V=',q/(yn*b)
   open(unit=2,file=fileNAME)
  do i=1,Section_num
     write(2,*) xlocat(i),y(i)
  end do
    write(2,*) ,'Yn=',  yn,'Yc=',yc
 print*,'S2=',xlocat(Section_num)
     20 continue
   pause
   end
 ! sub-program for calculation of yn and yc for rectangular channels
 subroutine rectangle(B,Q,S0,n,yn,yc)
 real::n
 if (S0.eq.0) then
    yn=0
    yc=0
    go to 5 !no yn or yc will be calculated
    end if
 YN=0
 do iter=1,20
   yn=((1./b)*(q*n/(b*s0**0.5))**1.5*(2*yn+b))**(2./5);
 end do
 yc=((Q*Q)/(9.8*b*b))**(1./3)
5 continue
 End
```

APPENDIX G

SURFACE PROFILES FOR THE MANNING ROUGHNESS DETERMINATION IN SMOOTH RECTANGULAR CHANNELS

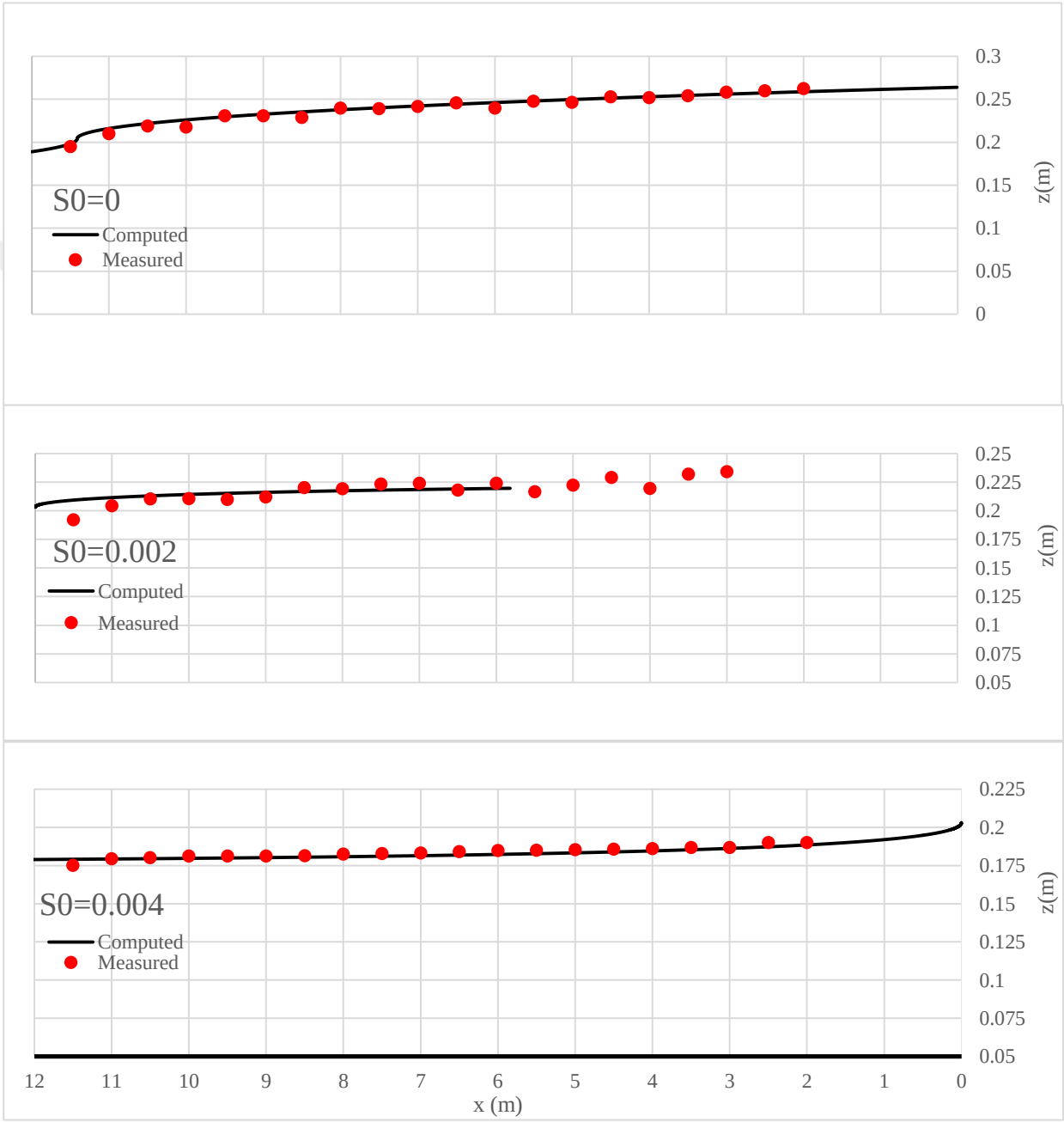

Figure G-1 : Surface profile for smooth rectangular channel with S0=0, 0.002 and 0.004

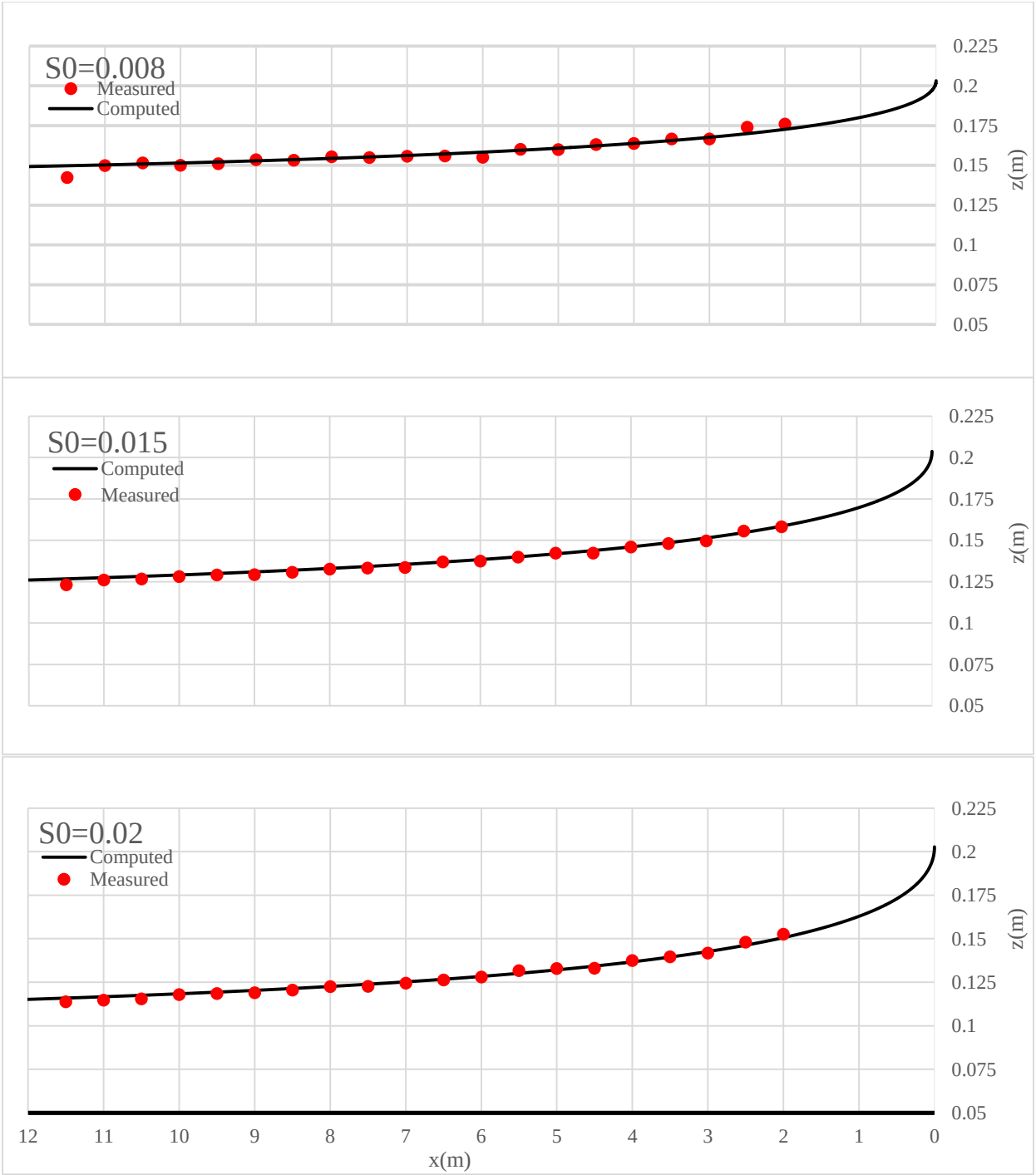

Figure G-2 : Surface profile for smooth rectangular channel with S0=0.008, 0.015 and 0.02

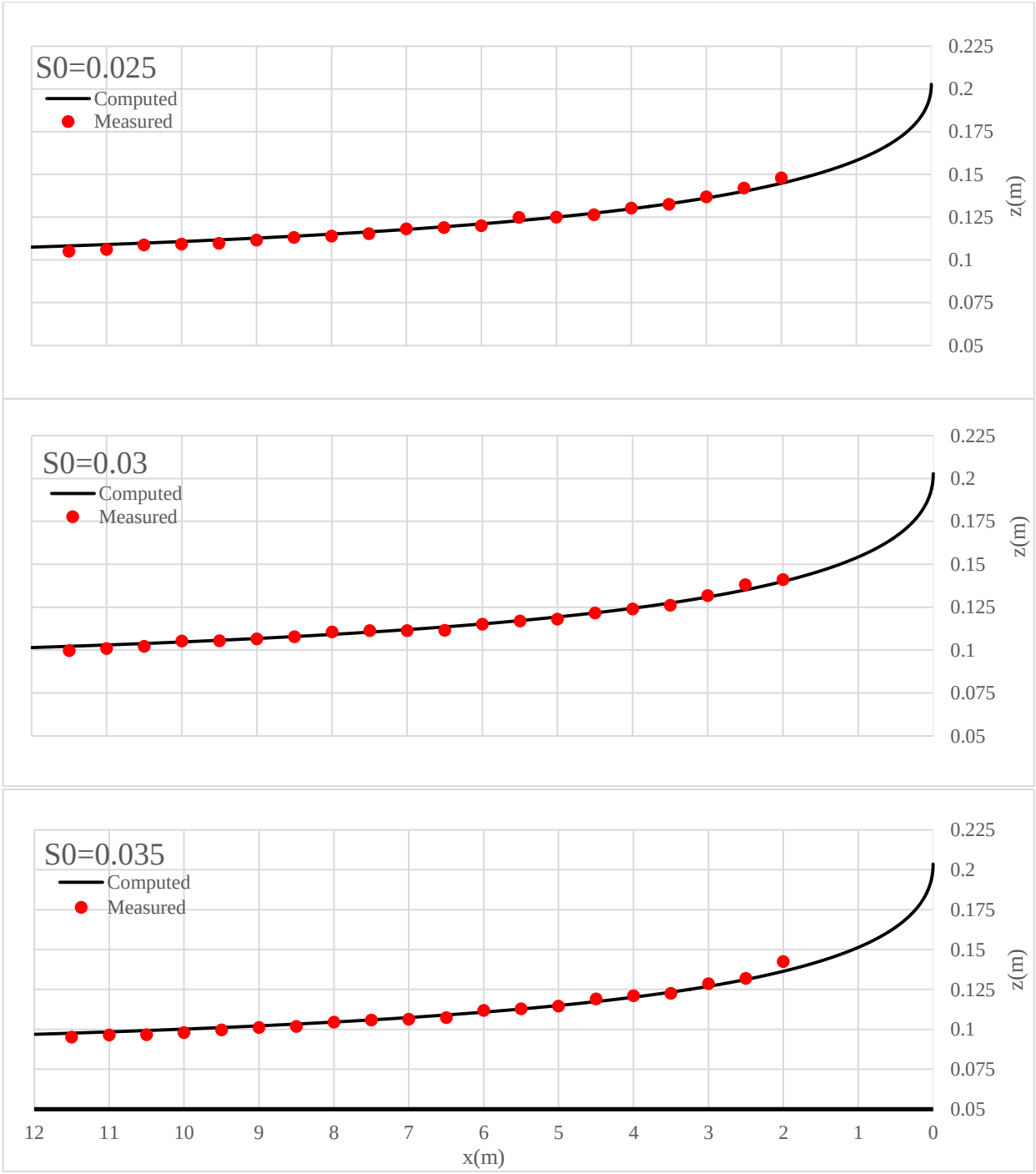

Figure G-3 : Surface profile for smooth rectangular channel with S0=0.025, 0.03 and 0.035

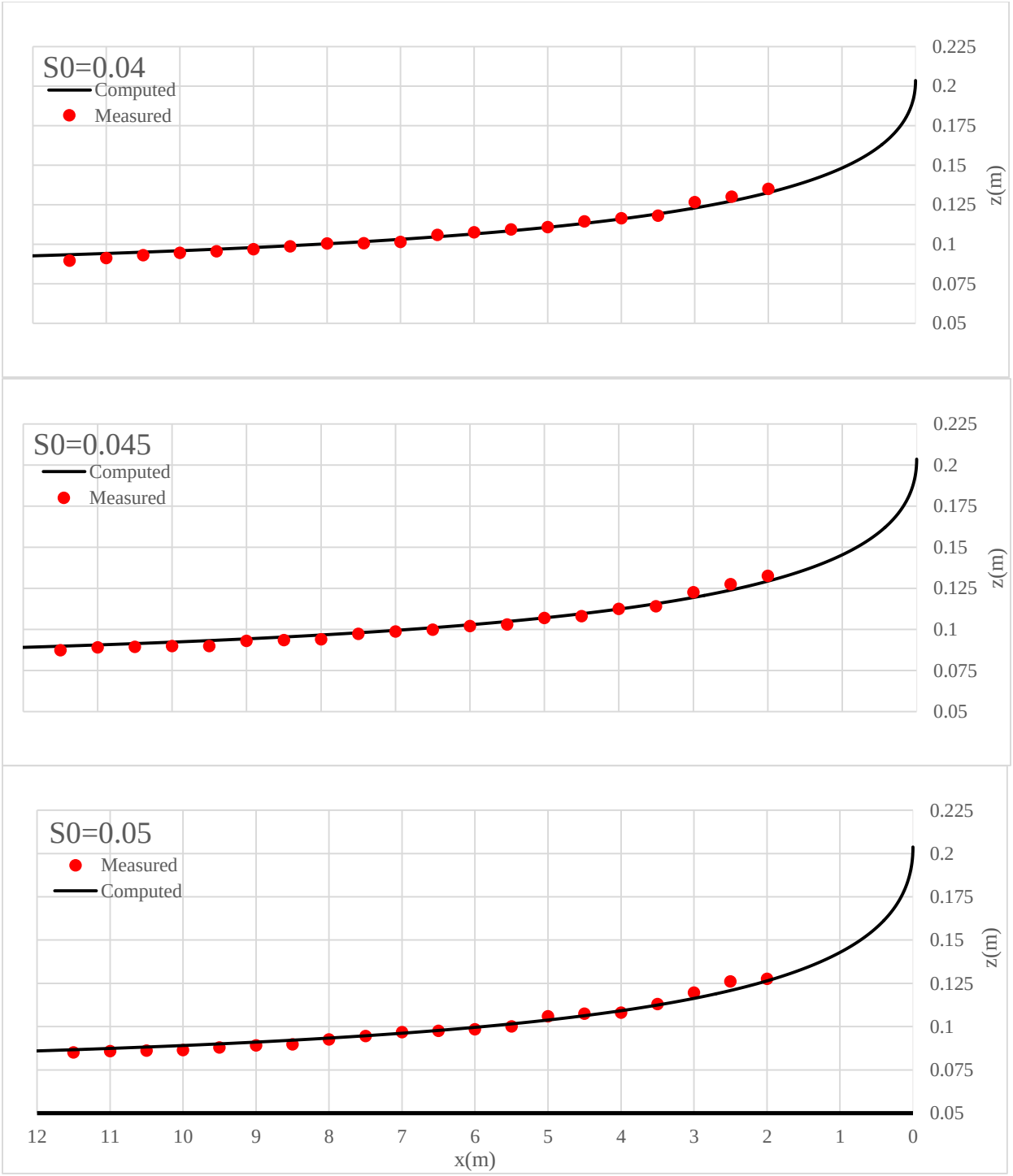

Figure G-4 : Surface profile for smooth rectangular channel with S0=0.04, 0.045 and 0.05

APPENDIX H

EXPERIMENTAL SURFACE VELOCITIES OBTAINED BY PTV FOR SMOOTH RECTANGULAR CHANNEL

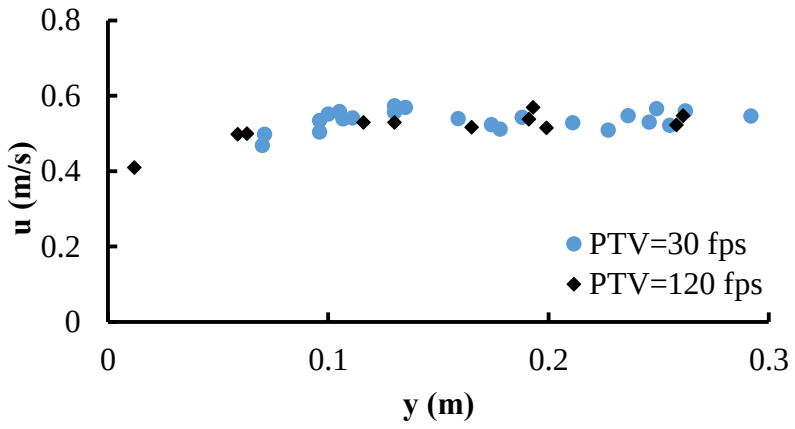

Figure H-1 : Surface velocity measured by PTV for S_0=0.001- Z_n=0.05 m- Q=12.9 l/s

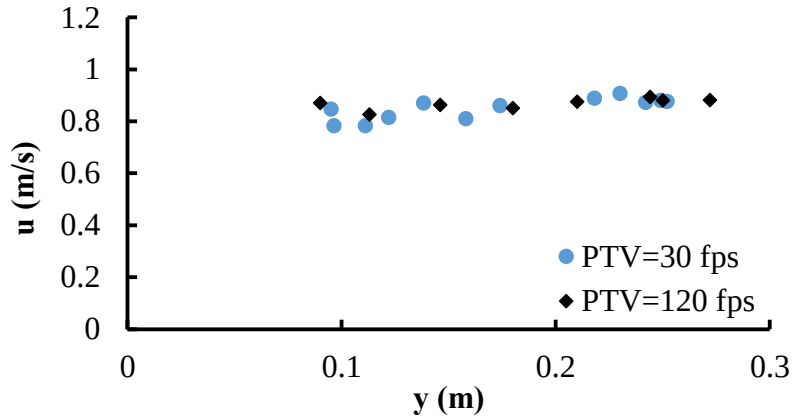

Figure H-2 : Surface velocity measured by PTV for S_0=0.001- Z_n=0.15 m- Q=68.13 l/s

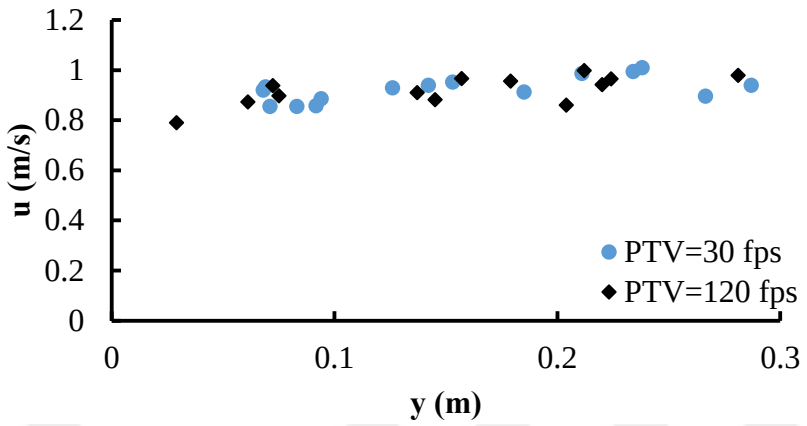

Figure H-3 : Surface velocity measured by PTV for S_0=0.001- Z_n=0.19 m- Q=95.45 l/s

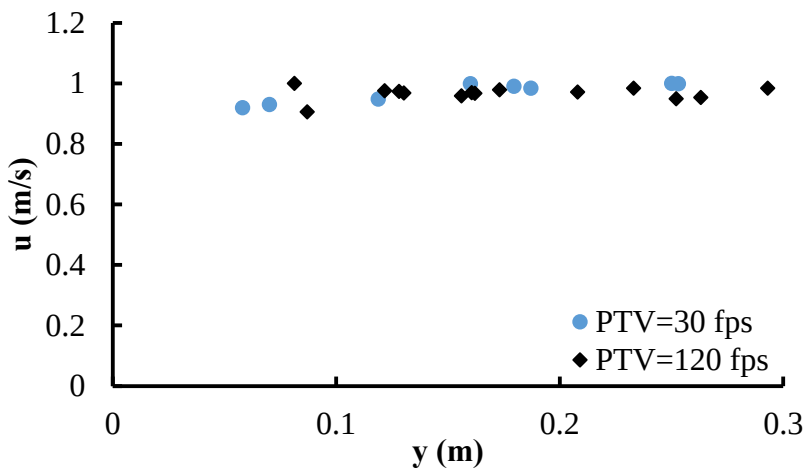

Figure H-4 : Surface velocity measured by PTV for S_0=0.001- Z_n=0.23 m- Q=124.55 l/s

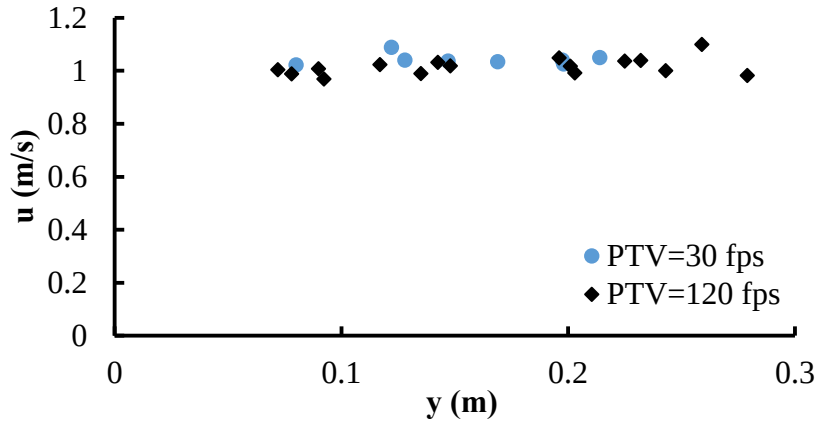

Figure H-5 : Surface velocity measured by PTV for S_0=0.001- Z_n=0.26 m- Q=147.28 l/s

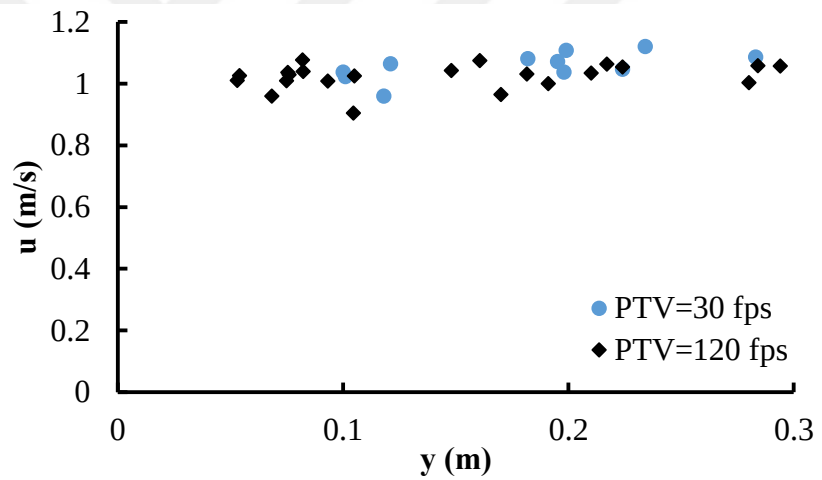

Figure H-6 : Surface velocity measured by PTV for S_0=0.001- Z_n=0.29 m- Q=170.64 l/s

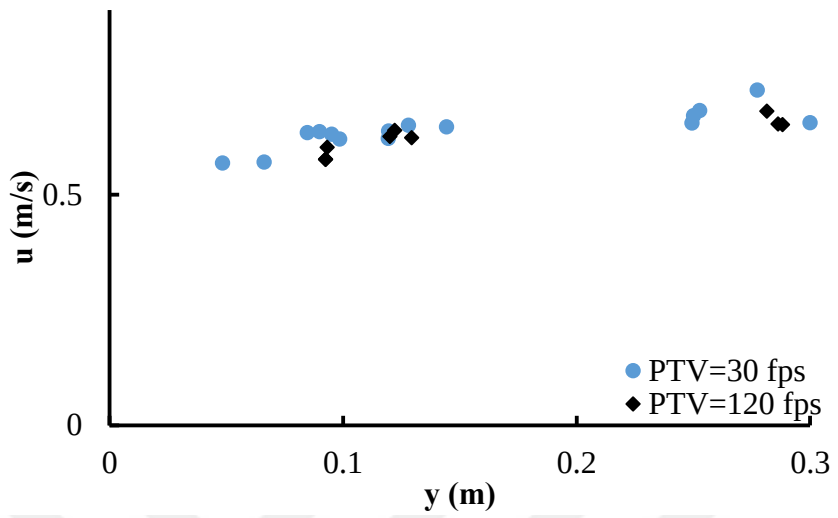

Figure H-7 : Surface velocity measured by PTV for S_0=0.002- Z_n=0.04 m- Q=12.9 l/s

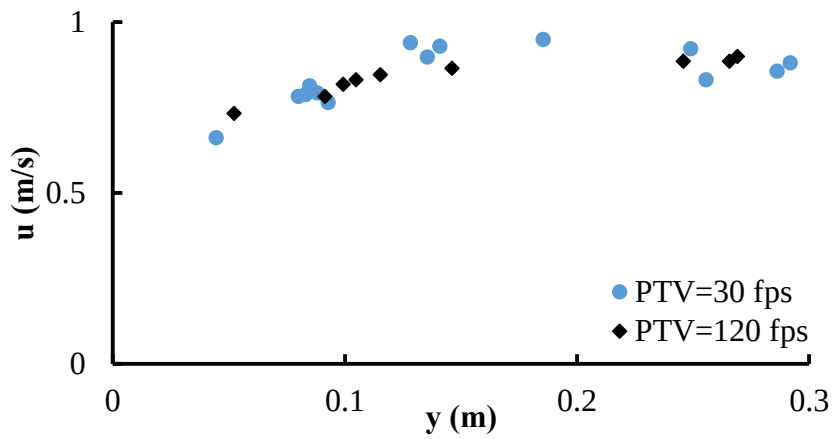

Figure H-8 : Surface velocity measured by PTV for S_0=0.002- Z_n=0.07 m- Q=30.85 l/s

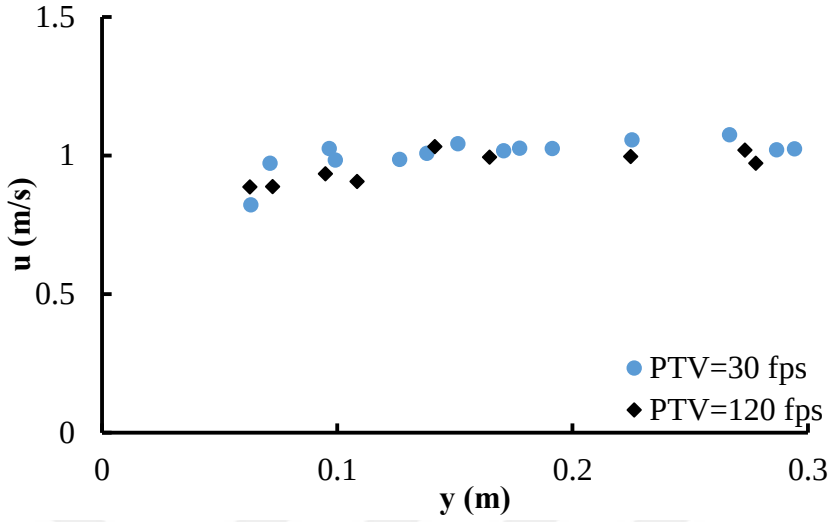

Figure H-9 : Surface velocity measured by PTV for S_0=0.002- Z_n=0.1 m- Q=53.05 l/s

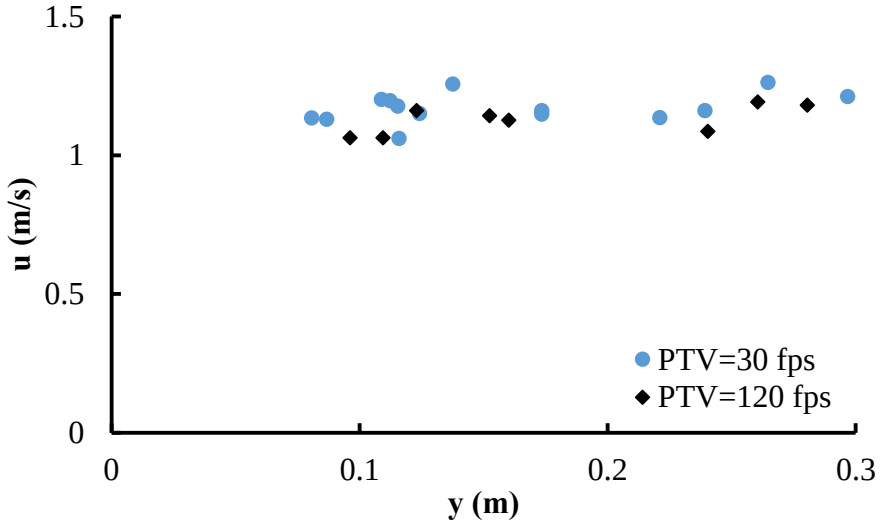

Figure H-10 : Surface velocity measured by PTV for S_0=0.002- Z_n=0.14 m- Q=87.2 l/s

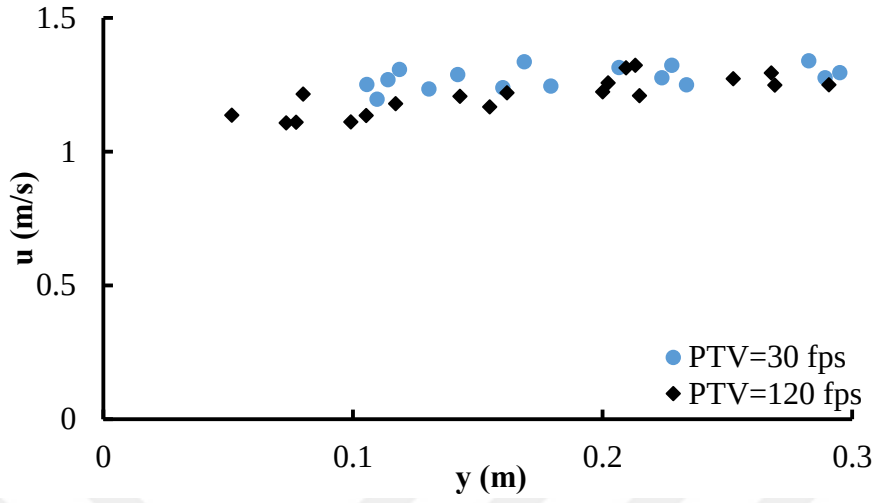

Figure H-11 : Surface velocity measured by PTV for S_0=0.002- Z_n=0.17 m- Q=115.3 l/s

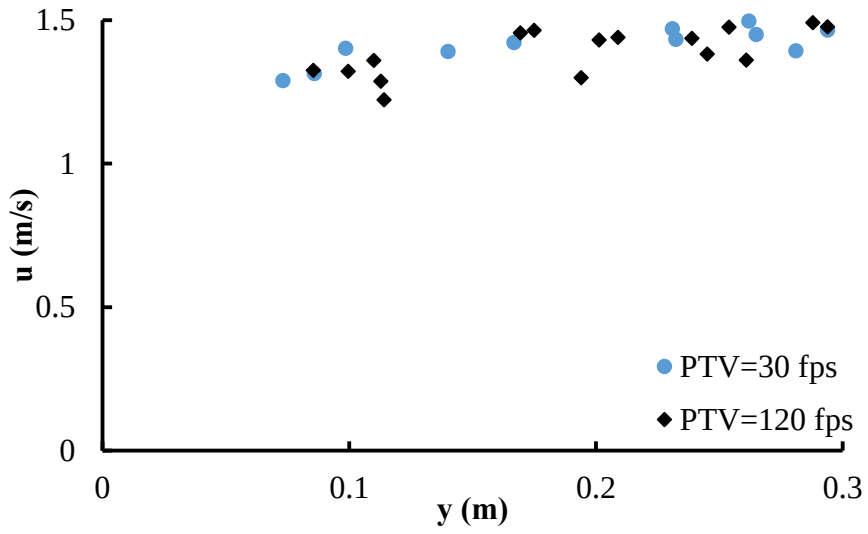

Figure H-12 : Surface velocity measured by PTV for S_0=0.002- Z_n=0.22 m- Q=165.7 l/s

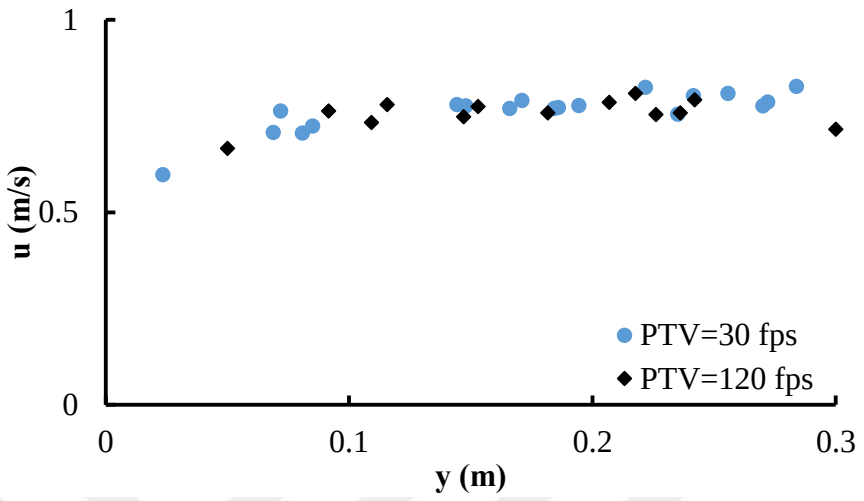

Figure H-13 : Surface velocity measured by PTV for S_0=0.004- Z_n=0.03 m- Q=11.5 l/s

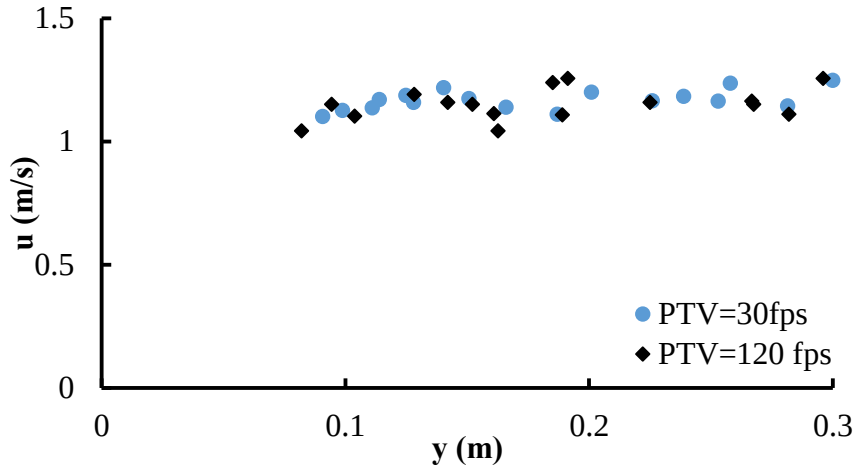

Figure H-14 : Surface velocity measured by PTV for S_0=0.004- Z_n=0.06 m- Q=34.4 l/s

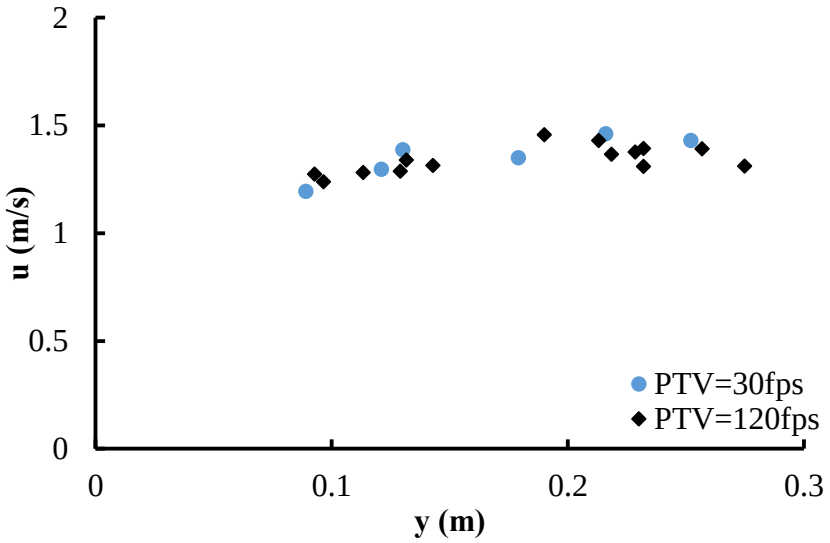

Figure H-15 : Surface velocity measured by PTV for S_0=0.004- Z_n=0.09 m- Q=64 l/s

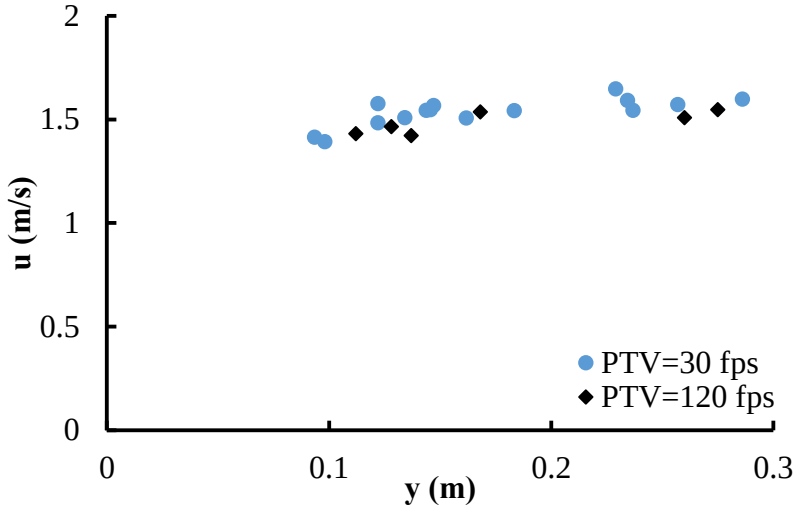

Figure H-16 : Surface velocity measured by PTV for S_0=0.004- Z_n=0.122 m- Q=98.4 l/s

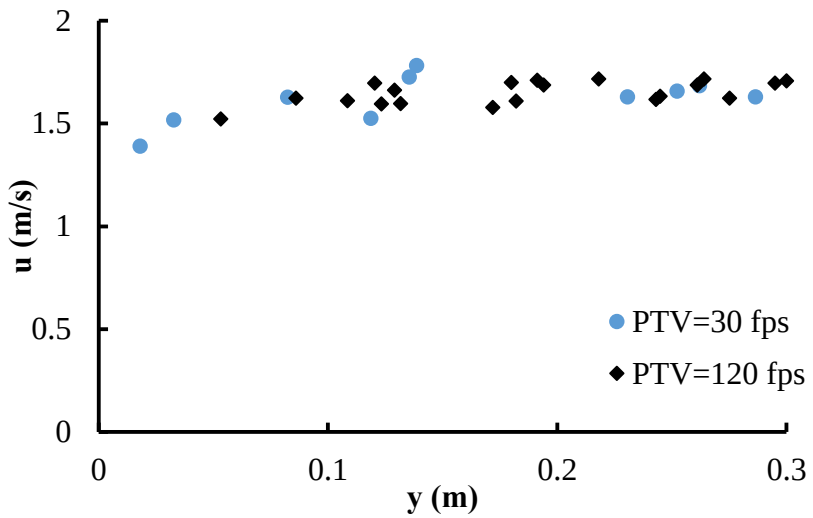

Figure H-17 : Surface velocity measured by PTV for S_0=0.004- Z_n=0.15 m- Q=136.3 l/s

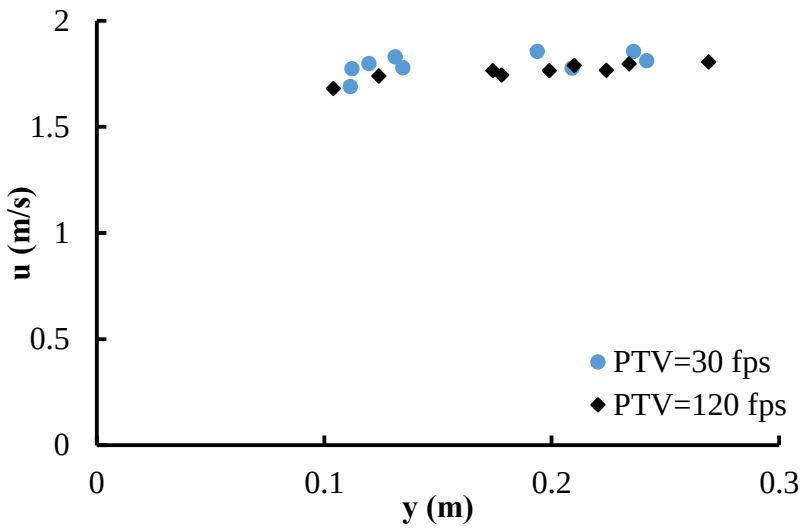

Figure H-18 : Surface velocity measured by PTV for S_0=0.004- Z_n=0.17 m- Q=163.2 l/s

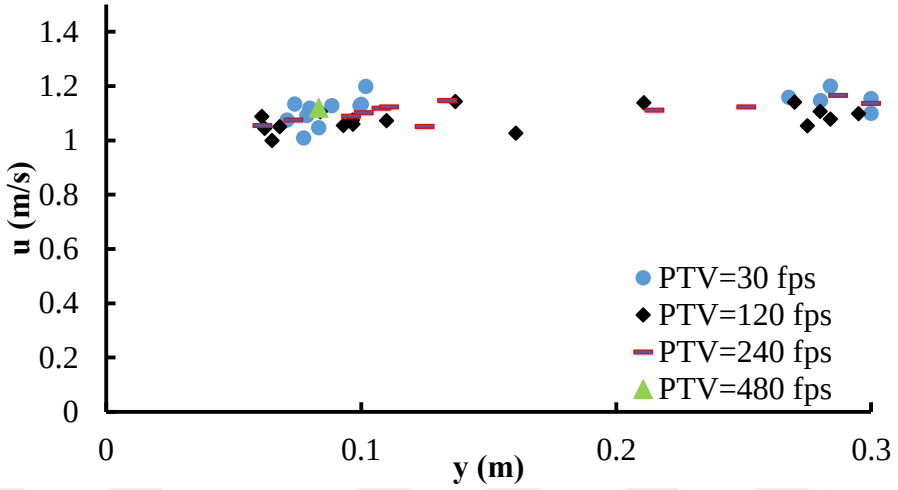

Figure H-19 : Surface velocity measured by PTV for S_0=0.008- Z_n=0.03 m- Q=16.5 l/s

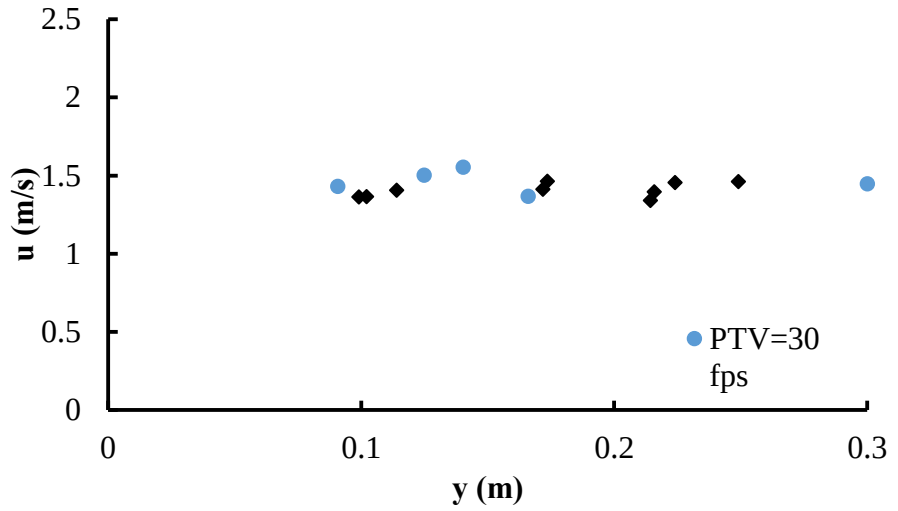

Figure H-20 : Surface velocity measured by PTV for S_0=0.008- Z_n=0.05 m- Q=36.6 l/s

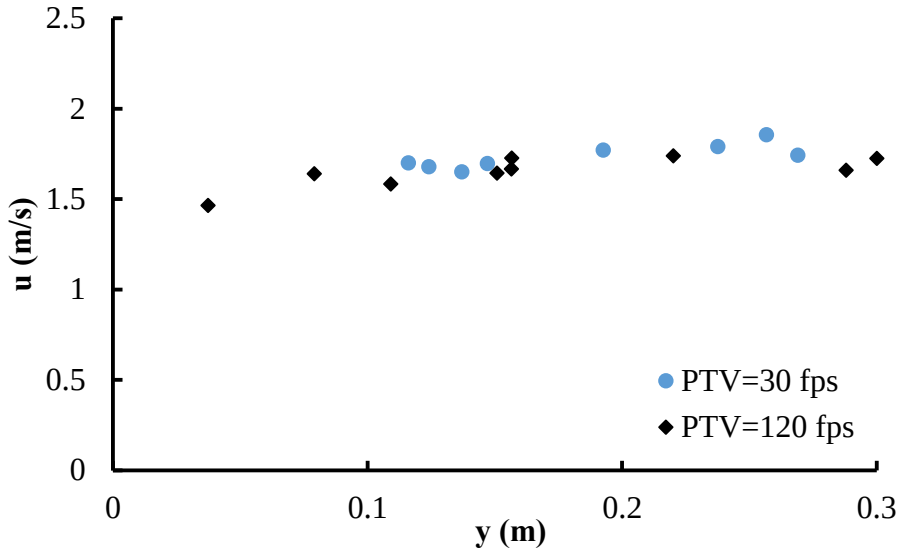

Figure H-21 : Surface velocity measured by PTV for S_0=0.008- Z_n=0.07 m- Q=61.75 l/s

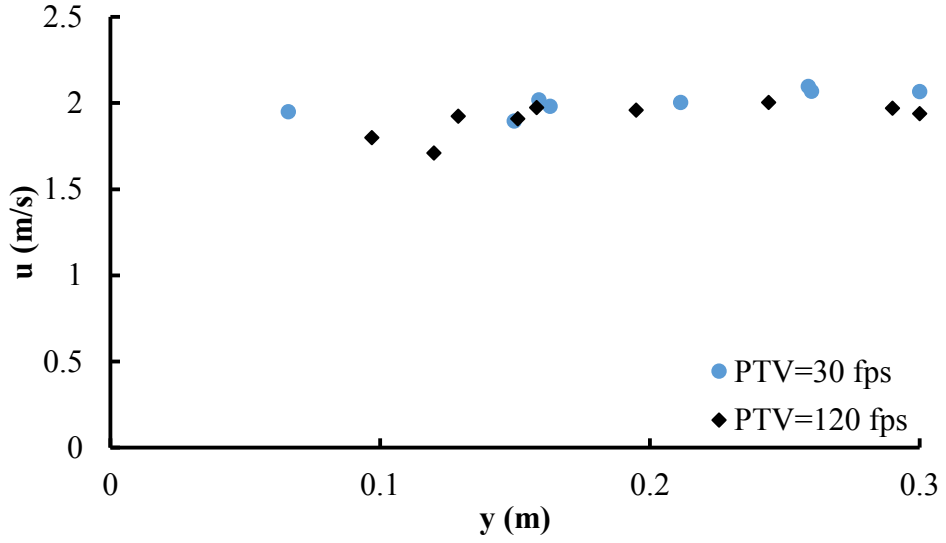

Figure H-22 : Surface velocity measured by PTV for S_0=0.008- Z_n=0.09 m- Q=90.5 l/s

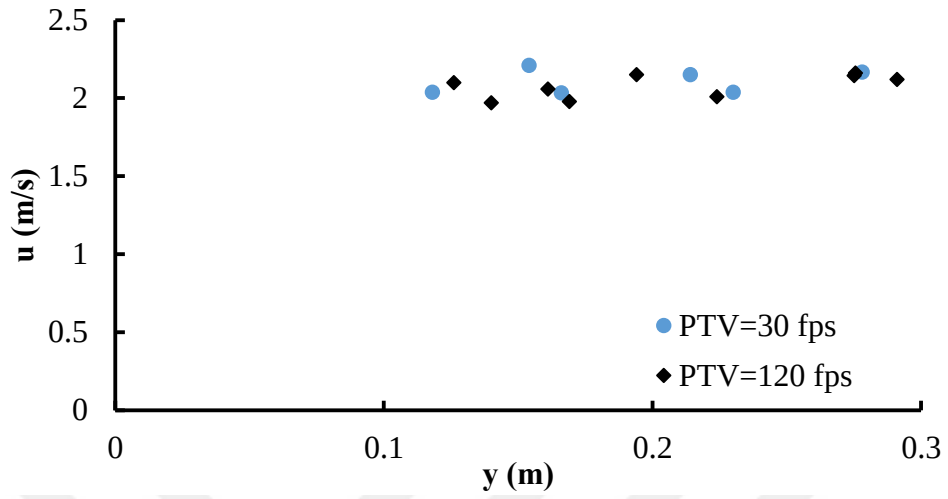

Figure H-23 : Surface velocity measured by PTV for S_0=0.008- Z_n=0.115 m- Q=130.65 l/s

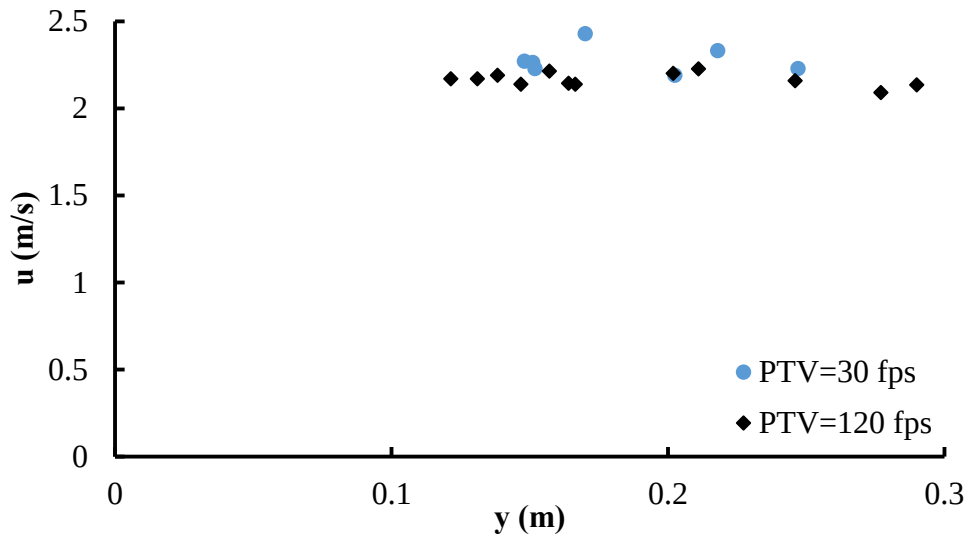

Figure H-24 : Surface velocity measured by PTV for S_0=0.008- Z_n=0.135 m- Q=165.4 l/s

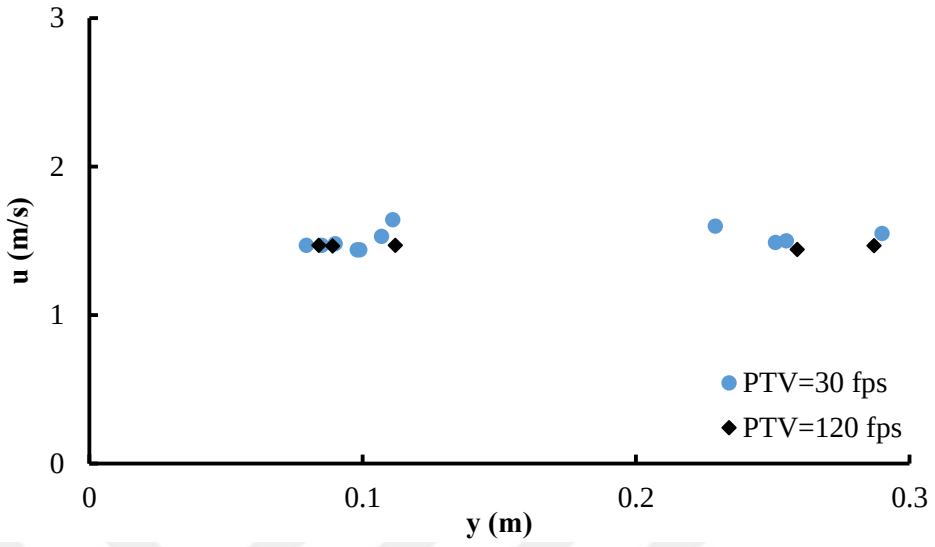

Figure H-25 : Surface velocity measured by PTV for S_0=0.015- Z_n=0.03 m- Q=22.2 l/s

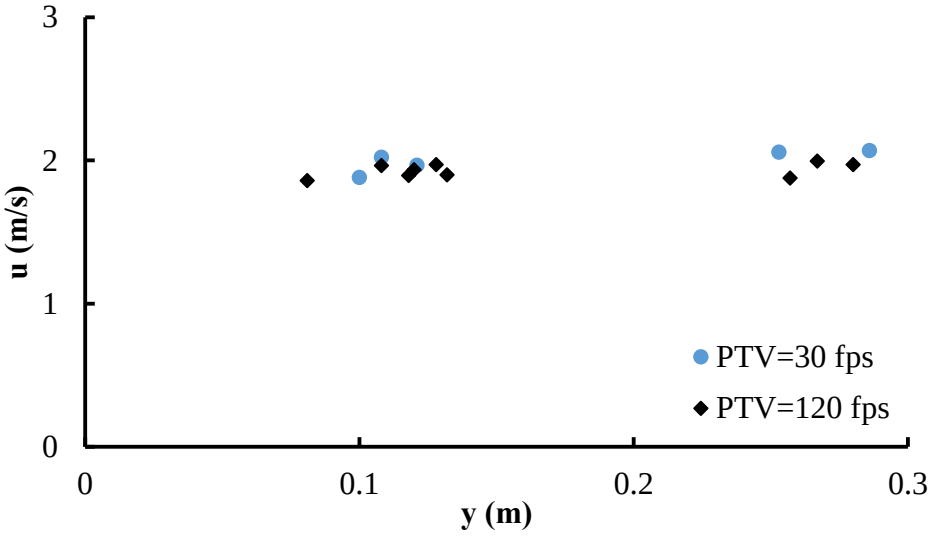

Figure H-26 : Surface velocity measured by PTV for S_0=0.015- Z_n=0.05 m- Q=50 l/s

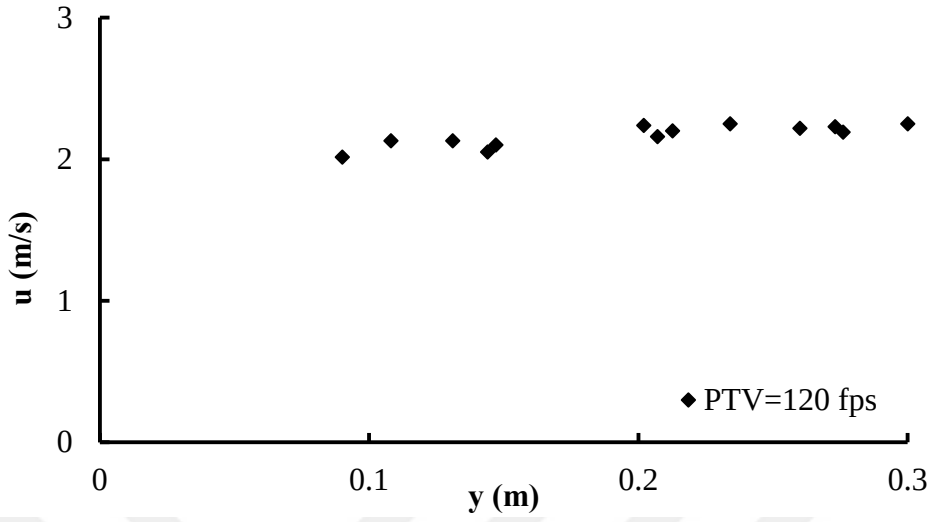

Figure H-27 : Surface velocity measured by PTV for S_0=0.015- Z_n=0.065 m- Q=75.3 l/s

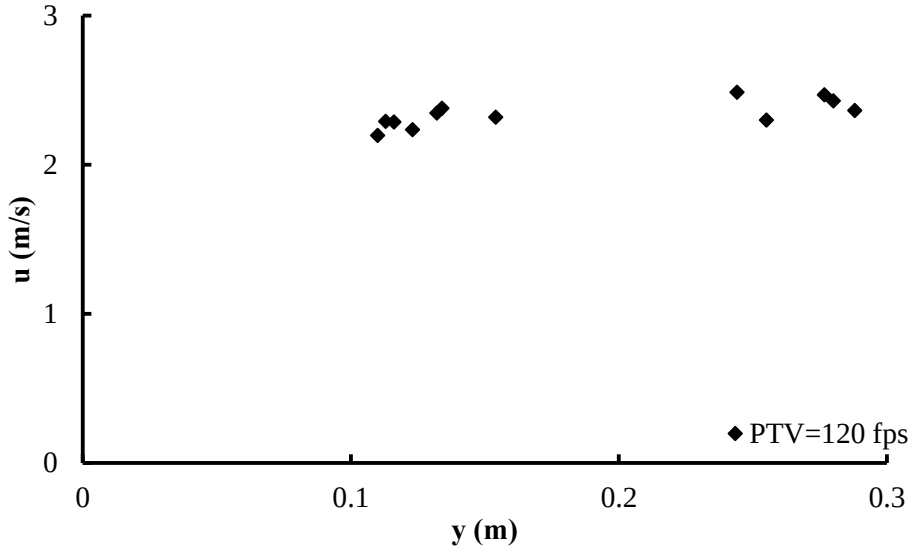

Figure H-28 : Surface velocity measured by PTV for S_0=0.015- Z_n=0.08 m- Q=103.7 l/s

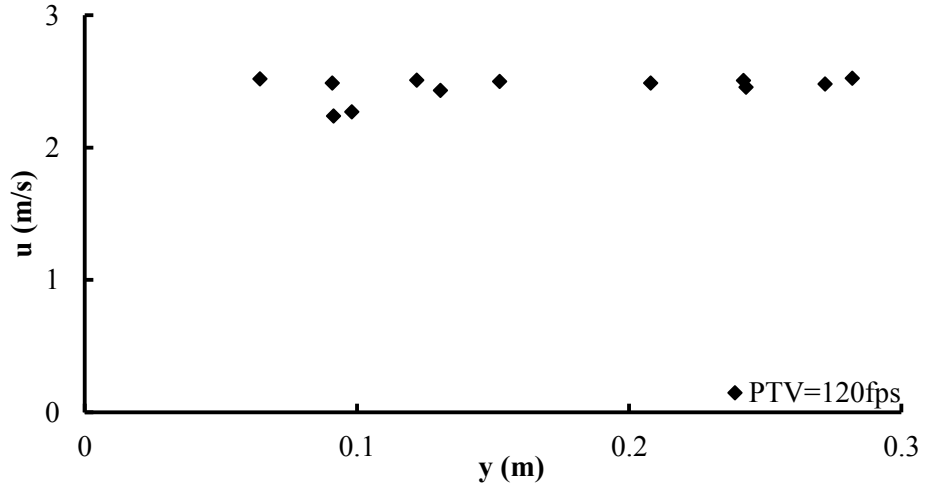

Figure H-28 : Surface velocity measured by PTV for S_0=0.015- Z_n=0.105 m- Q=146 l/s

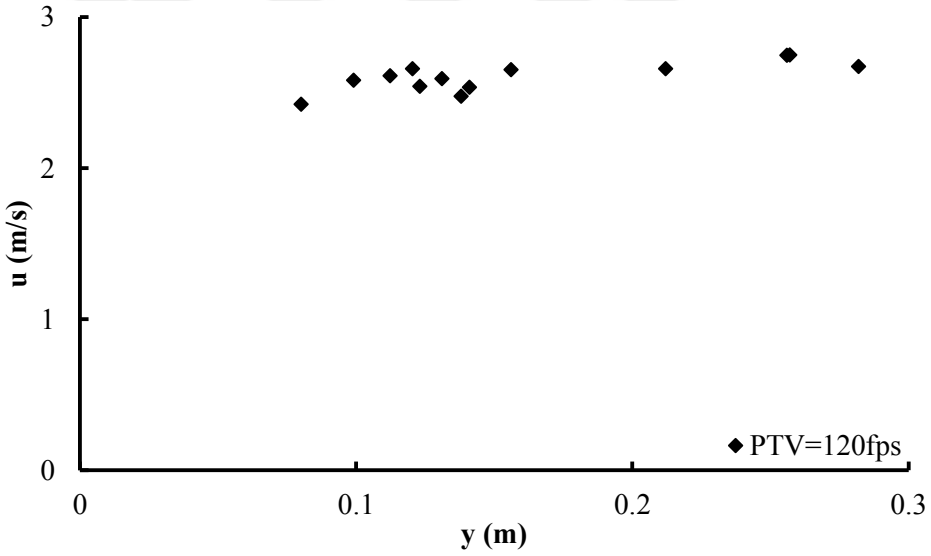

Figure H-29 : Surface velocity measured by PTV for S_f=0.0131- Z_n=0.115 m- Q=167.5 l/s

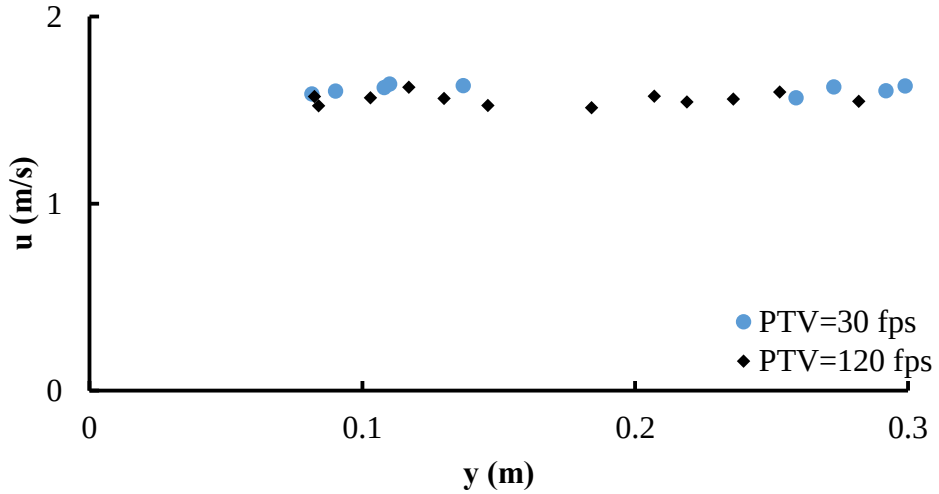

Figure H-30 : Surface velocity measured by PTV for S_0=0.025- Z_n=0.02 m- Q=15 l/s

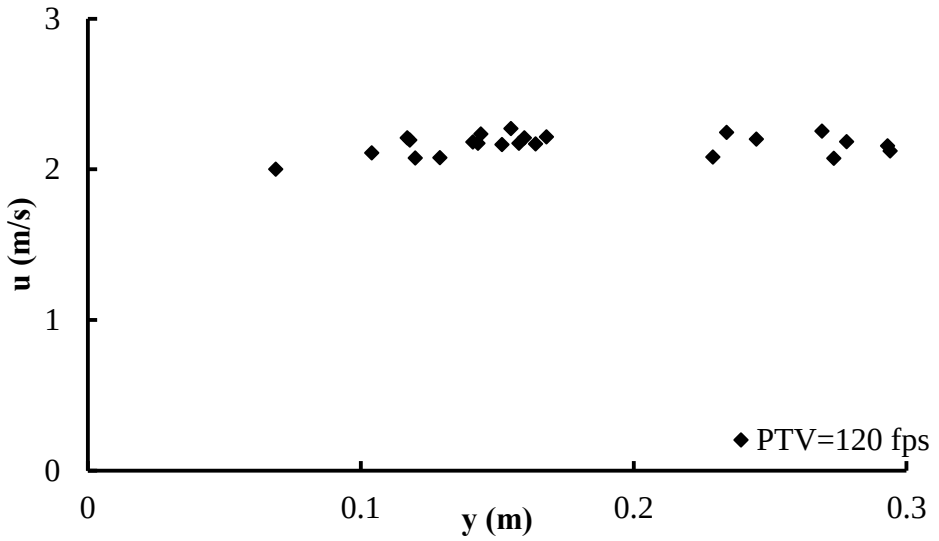

Figure H-31 : Surface velocity measured by PTV for S_0=0.025- Z_n=0.04 m- Q=45.5 l/s

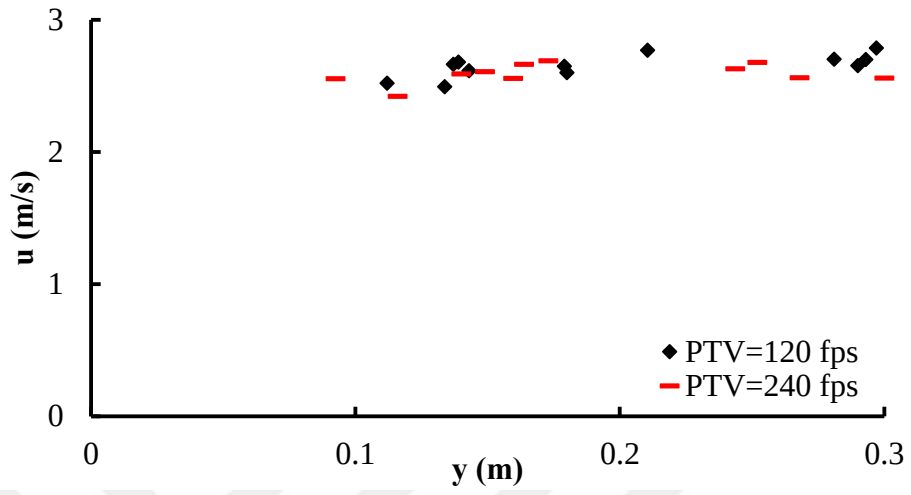

Figure H-32 : Surface velocity measured by PTV for S_0=0.025- Z_n=0.06 m- Q=86 l/s

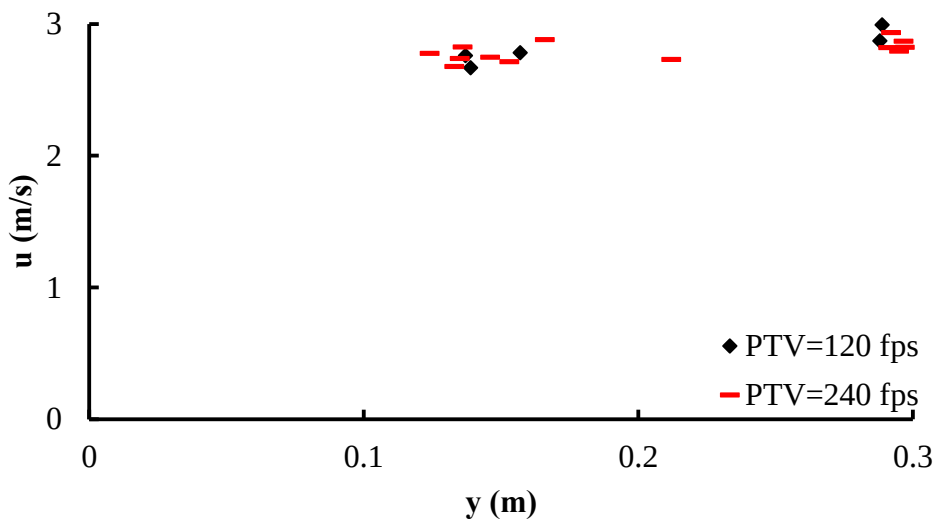

Figure H-33 : Surface velocity measured by PTV for S_f=0.02058- Z_n=0.08 m- Q=121.35 l/s

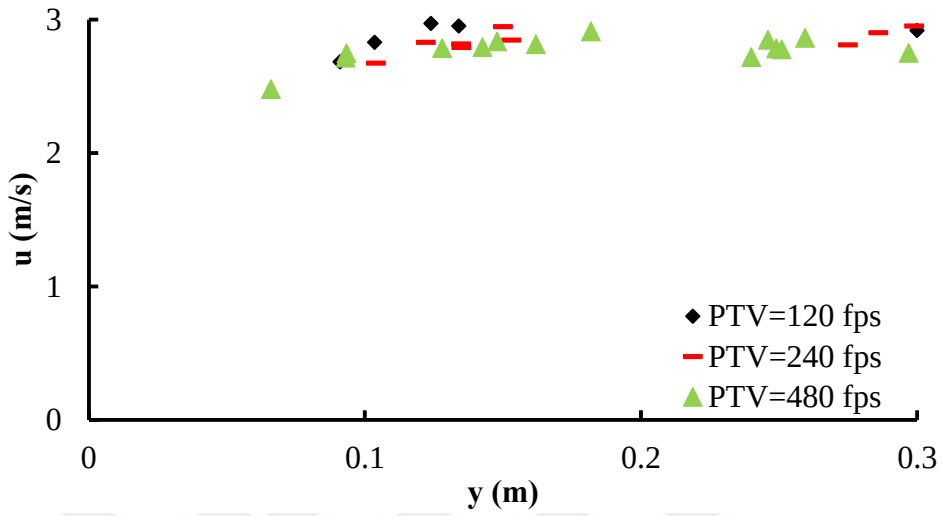

Figure H-34 : Surface velocity measured by PTV for S_f=0.01716- Z_n=0.102 m- Q=160 l/s

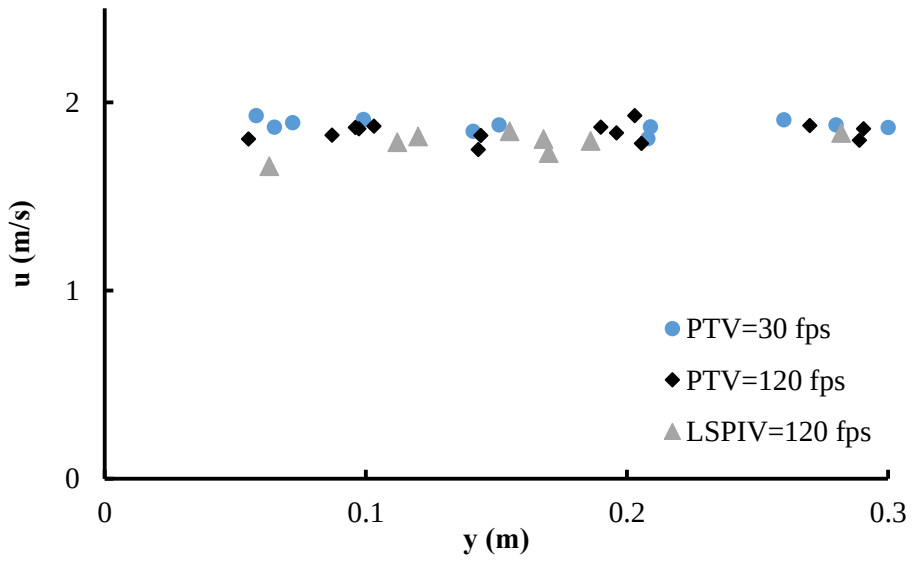

Figure H-35 : Surface velocity measured by PTV for S_0=0.035- Z_n=0.02 m- Q=17.7 l/s

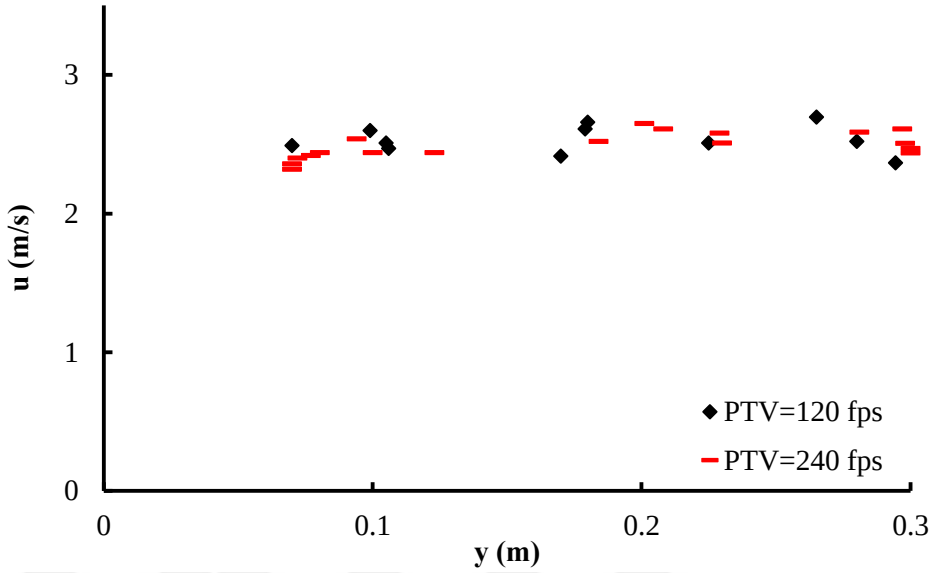

Figure H-36 : Surface velocity measured by PTV for S_0=0.035- Z_n=0.04 m- Q=53.7 l/s

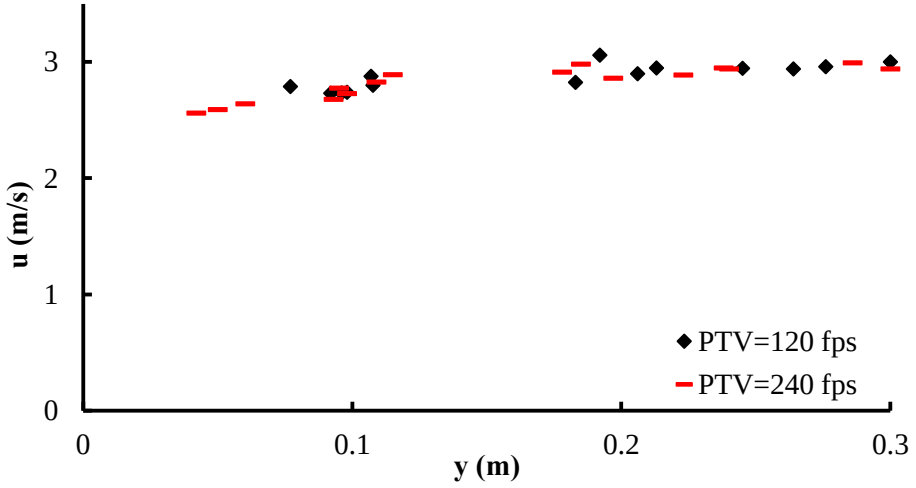

Figure H-37 : Surface velocity measured by PTV for S_f=0.02737- Z_n=0.065 m- Q=101.7 l/s

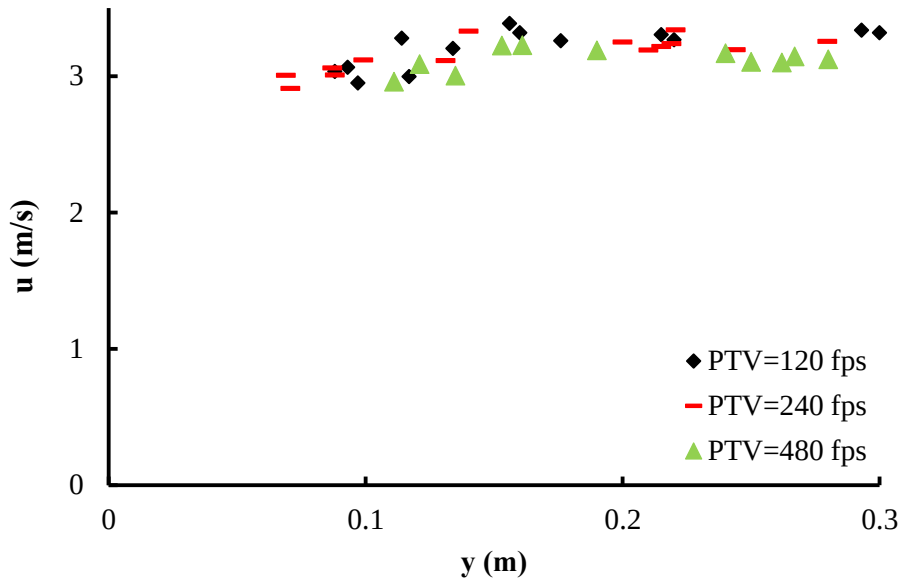

Figure H-38 : Surface velocity measured by PTV for S_f=0.0246- Z_n=0.09 m- Q=158.8 l/s

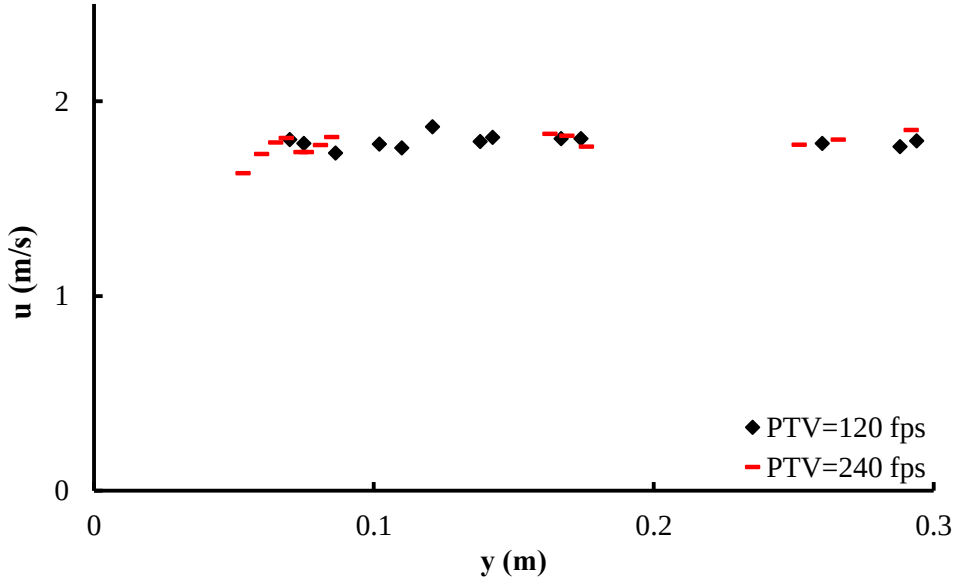

Figure H-39 : Surface velocity measured by PTV for S_0=0.045- Z_n=0.015 m- Q=12.5 l/s

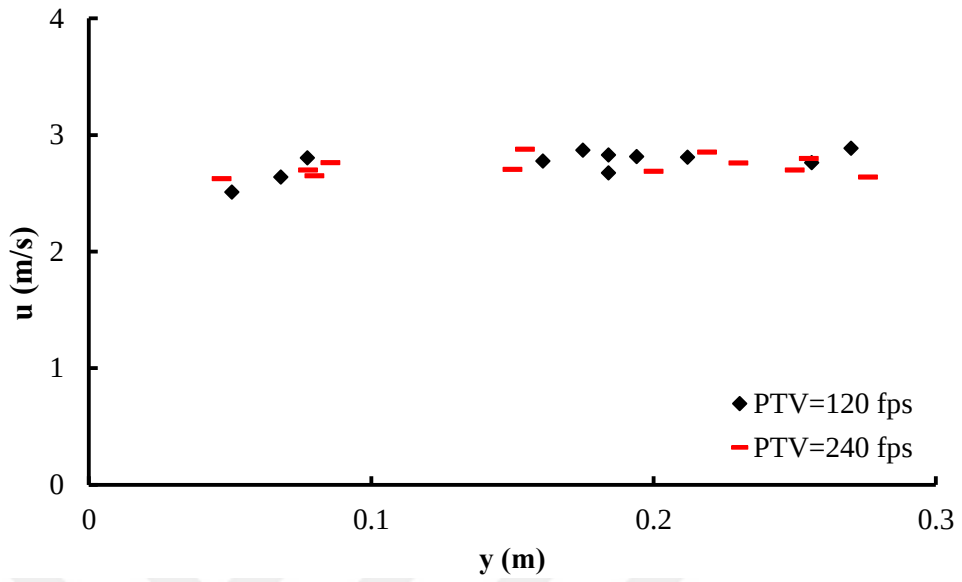

Figure H-40 : Surface velocity measured by PTV for S_0=0.045- Z_n=0.035 m- Q=49.25 l/s

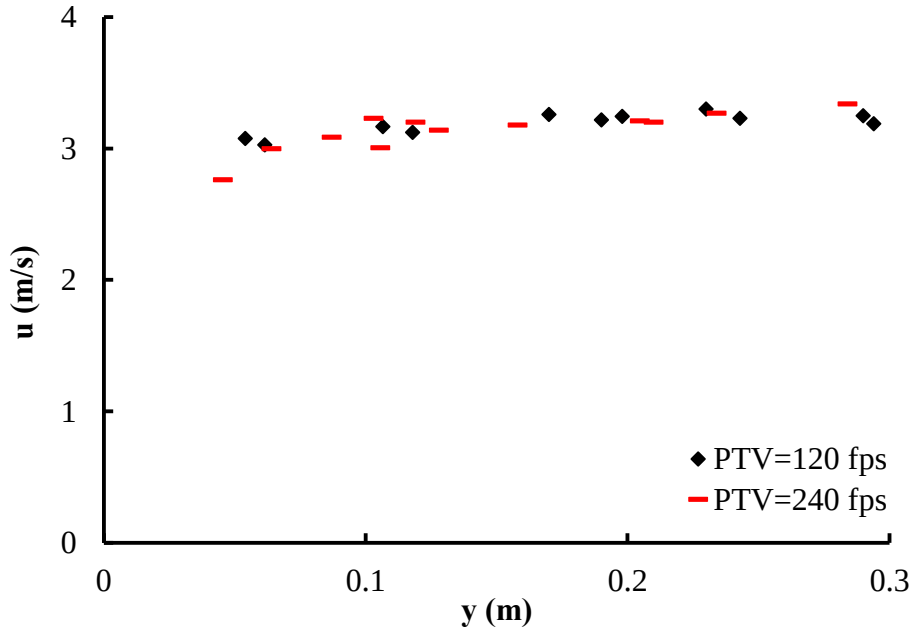

Figure H-41 : Surface velocity measured by PTV for S_f=0.03973- Z_n=0.0535 m- Q=87 l/s

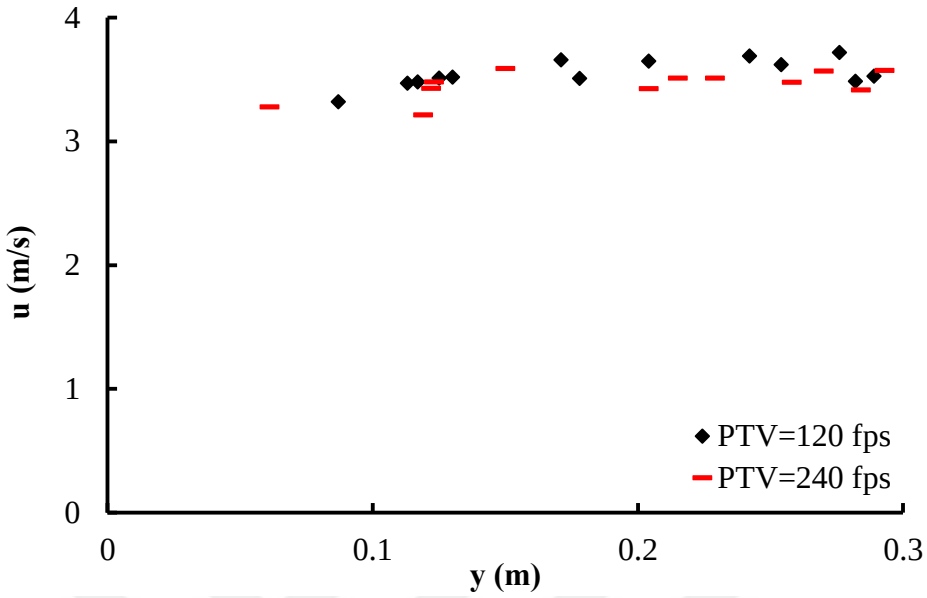

Figure H-42 : Surface velocity measured by PTV for S_f=0.02863- Z_n=0.087 m- Q=162.6 l/s

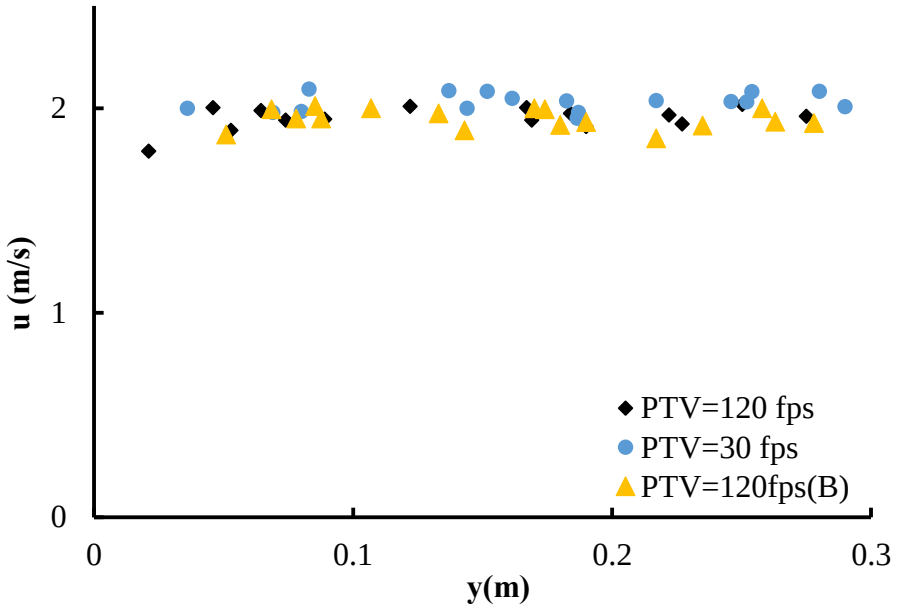

Figure H-43 : Surface velocity measured by PTV for S_0=0.055- Z_n=0.0145 m- Q=13.8 l/s

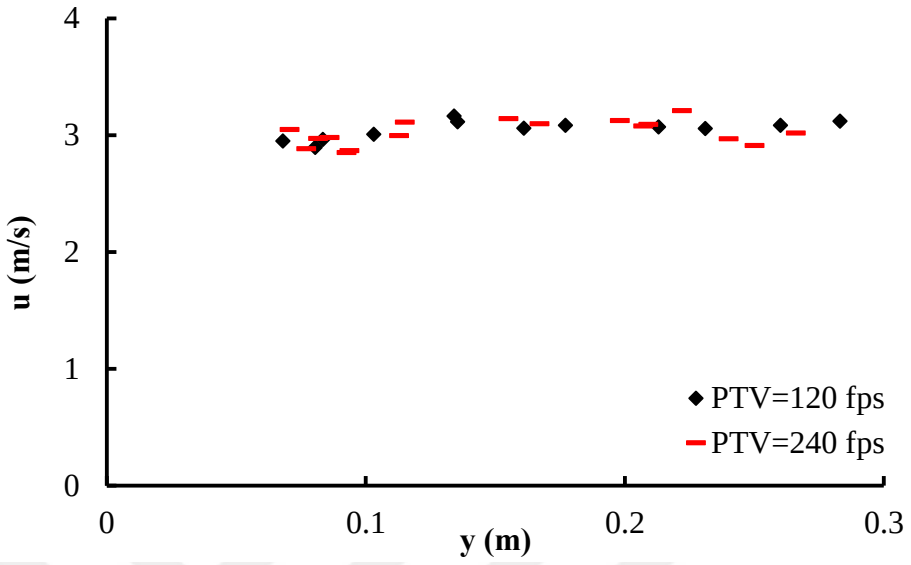

Figure H-44 : Surface velocity measured by PTV for S_0=0.055- Z_n=0.0345 m- Q=54.4 l/s

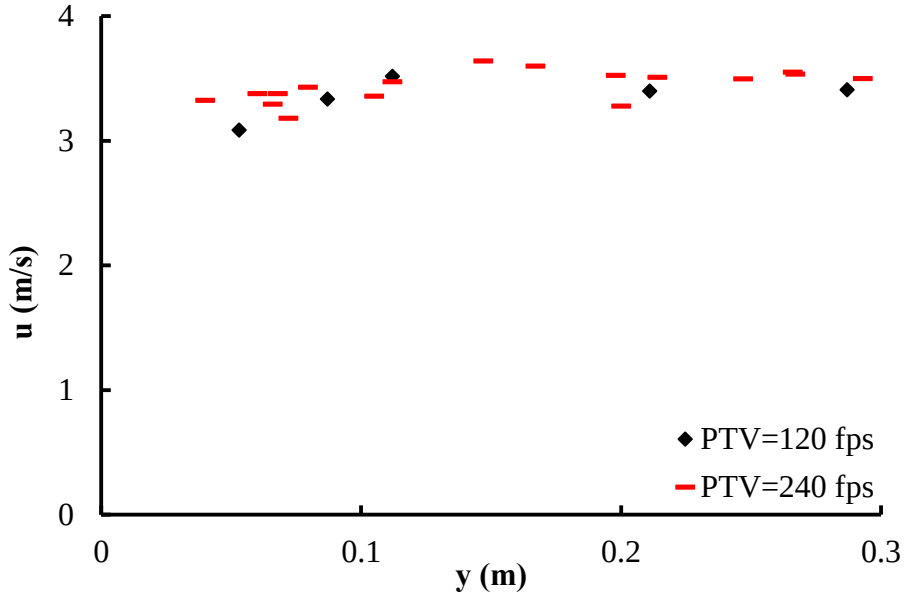

Figure H-45 : Surface velocity measured by PTV for S_f=0.04755- Z_n=0.0525 m- Q=96.1 l/s

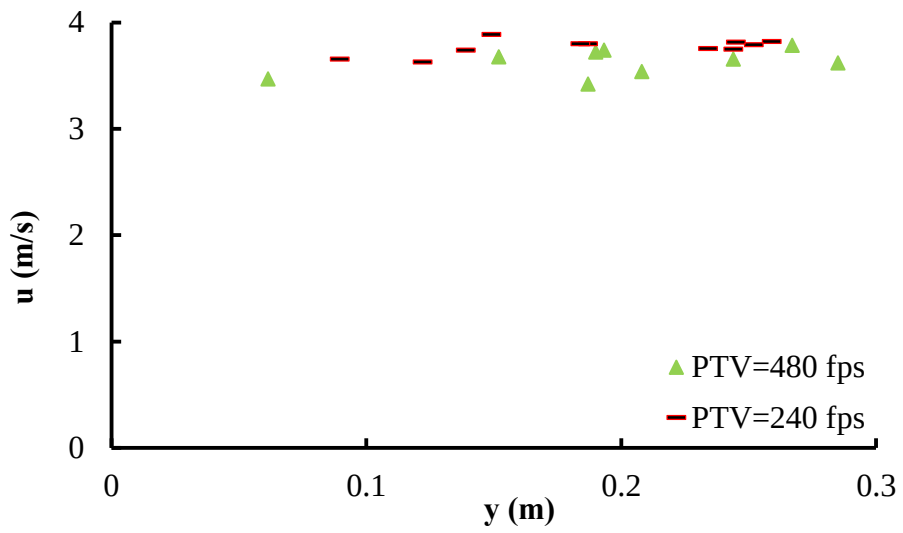

Figure H-46 : Surface velocity measured by PTV for S_f=0.0368- Z_n=0.08 m- Q=162.3 l/s

APPENDIX I

EXPERIMENTAL SURFACE VELOCITIES OBTAINED BY PIV FOR SMOOTH RECTANGULAR CHANNEL

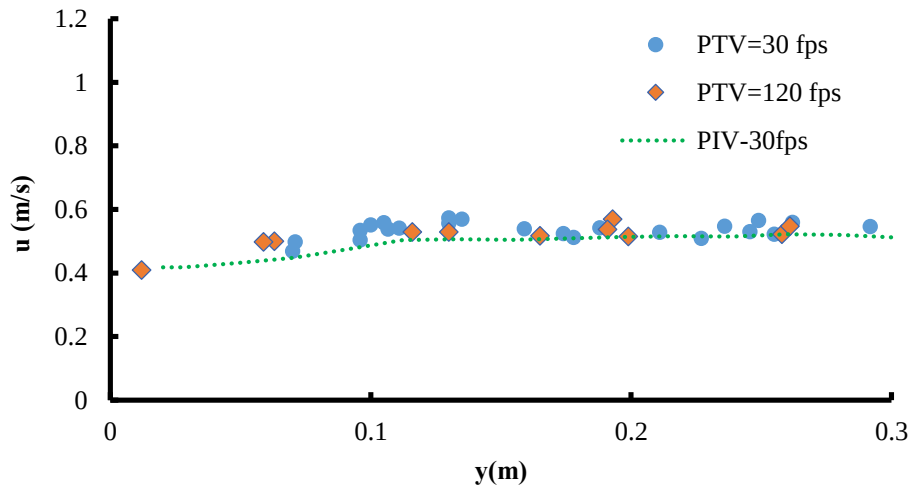

Figure I-1 : Surface velocity measured by PIV for S_0=0.001- Z_n=0.05 m- Q=12.9 l/s

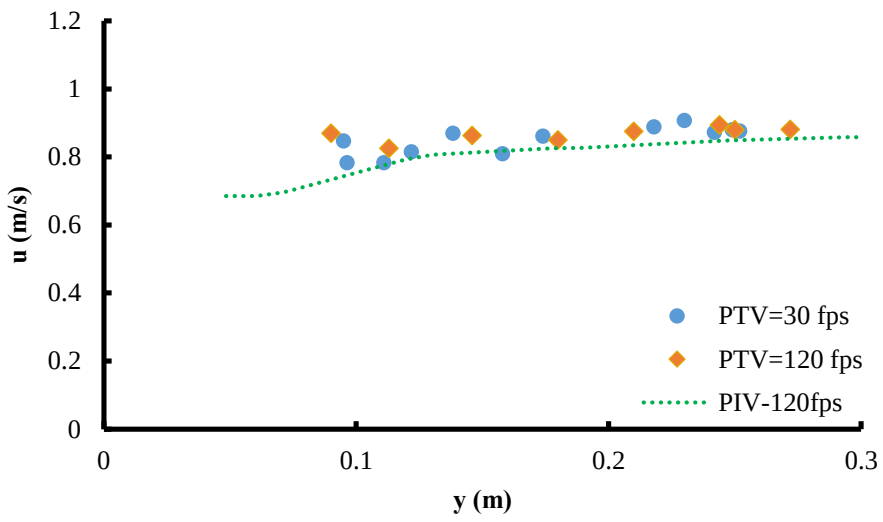

Figure I-2 : Surface velocity measured by PIV for S_0=0.001- Z_n=0.15 m- Q=68.13 l/s

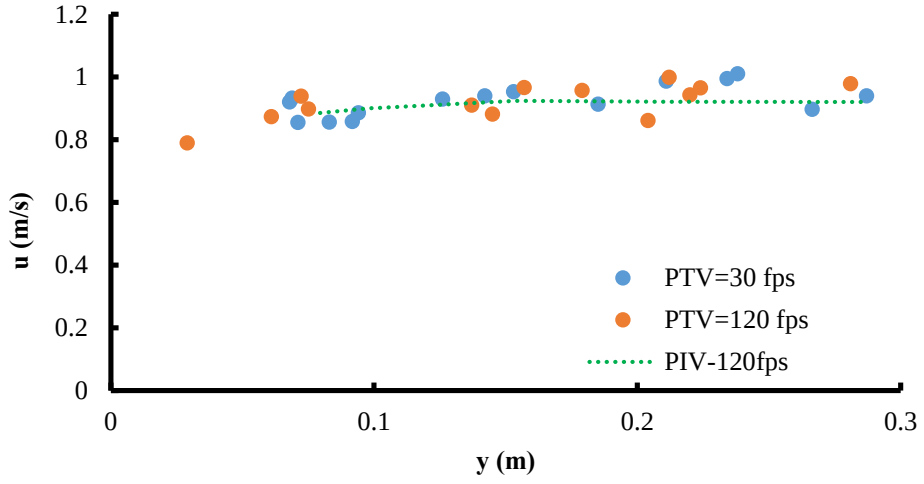

Figure I-3 : Surface velocity measured by PIV for S_0=0.001- Z_n=0.19 m- Q=95.45 l/s

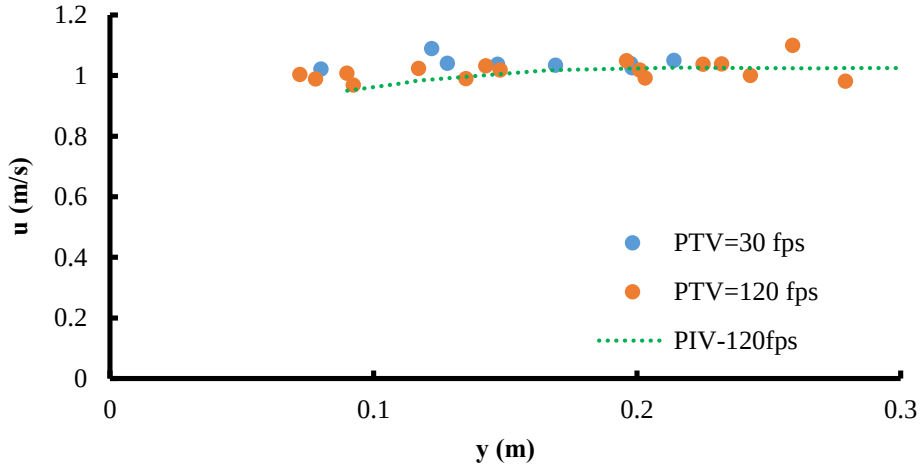

Figure I-4 : Surface velocity measured by PIV for S_0=0.001- Z_n=0.26 m- Q=147.28 l/s

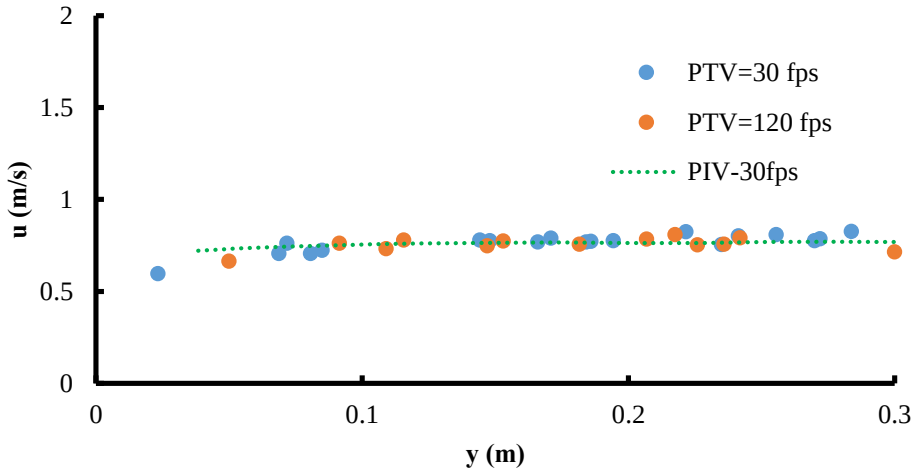

Figure I-5 : Surface velocity measured by PIV for S_0=0.004- Z_n=0.03 m- Q=11.5 l/s

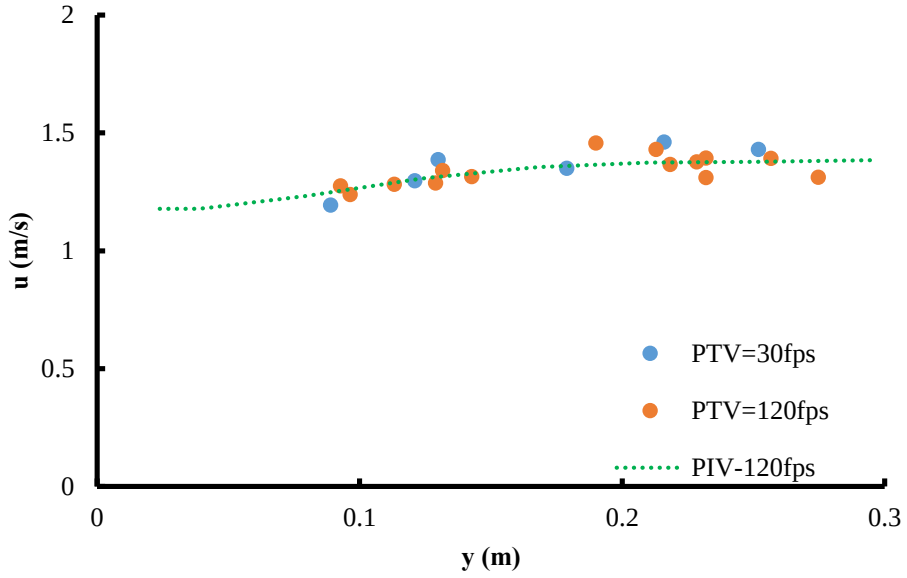

Figure I-6 : Surface velocity measured by PIV for S_0=0.004- Z_n=0.09 m- Q=64 l/s

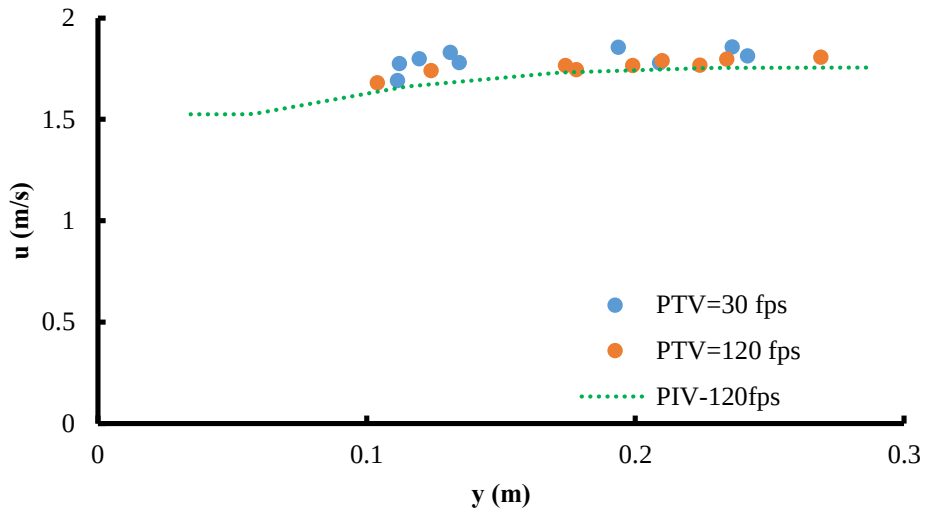

Figure I-7 : Surface velocity measured by PIV for S_0=0.004- Z_n=0.17 m- Q=163.2 l/s

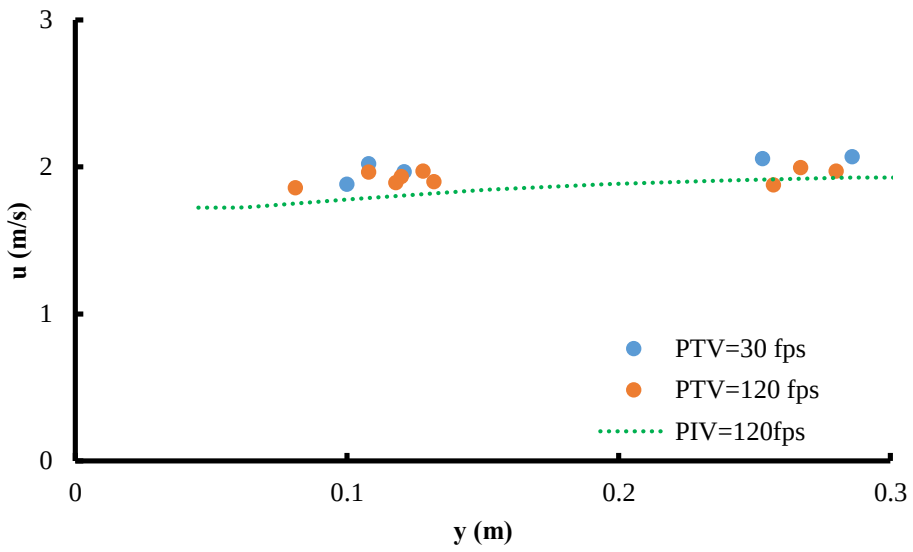

Figure I-8 : Surface velocity measured by PIV for S_0=0.015- Z_n=0.05 m- Q=50 l/s

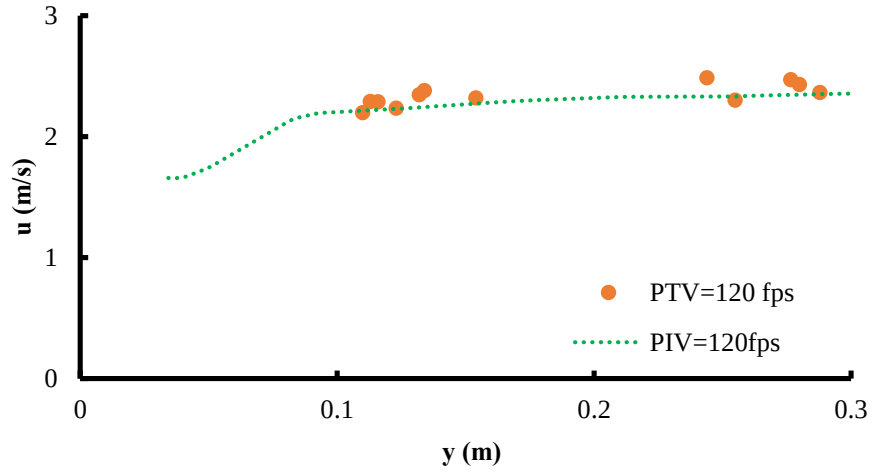

Figure I-9 : Surface velocity measured by PIV for S_0=0.015- Z_n=0.08 m- Q=103.7 l/s

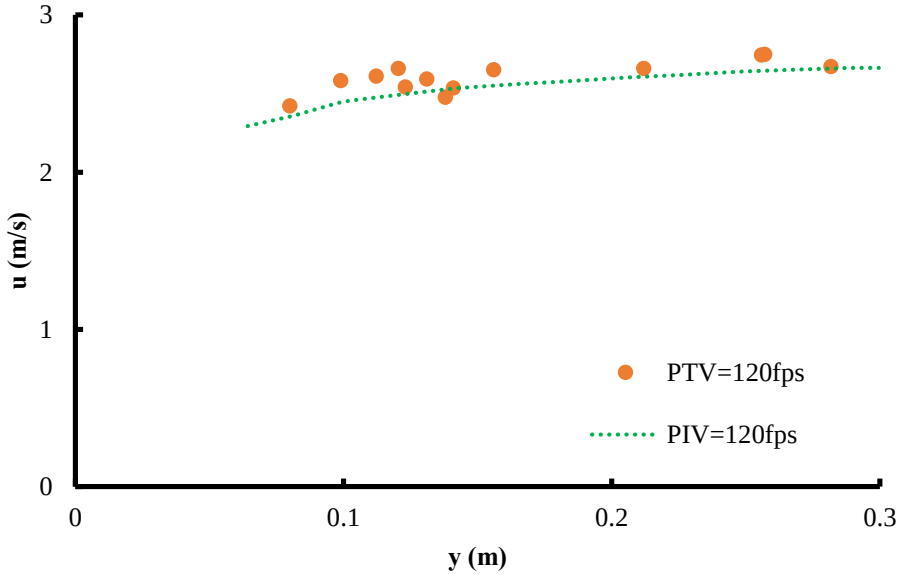

Figure I-10 : Surface velocity measured by PIV for S_f=0.0131- Z_n=0.115 m- Q=167.5 l/s

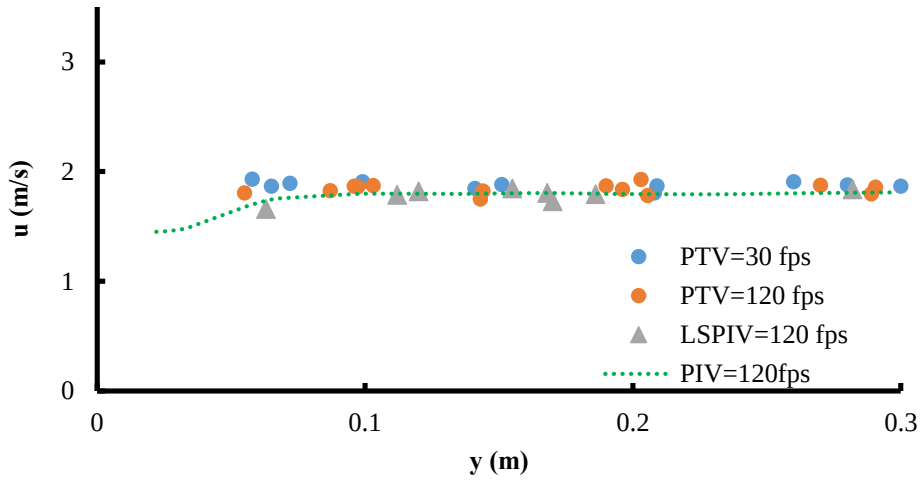

Figure I-11 : Surface velocity measured by PIV for S_0=0.035- Z_n=0.02 m- Q=17.7 l/s

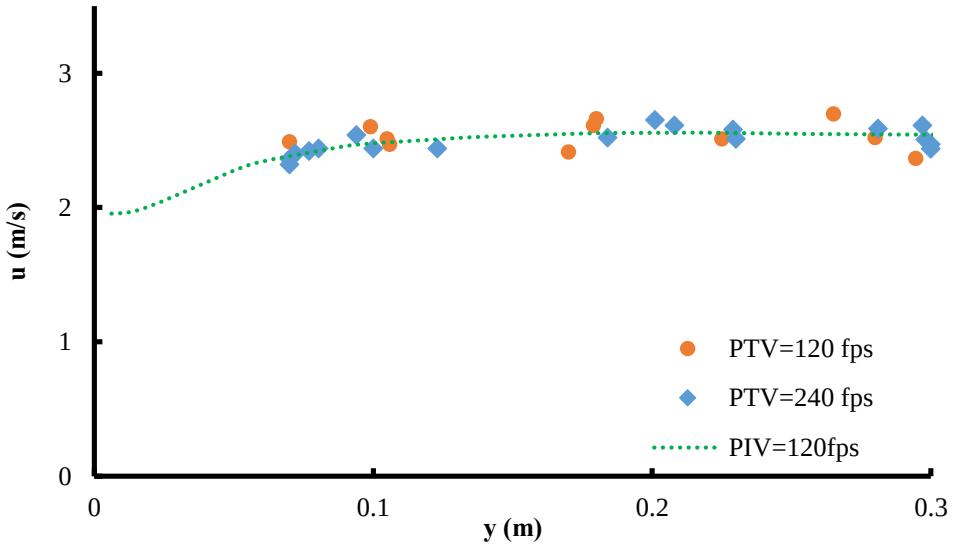

Figure I-12 : Surface velocity measured by PIV for S_0=0.035- Z_n=0.04 m- Q=53.7 l/s

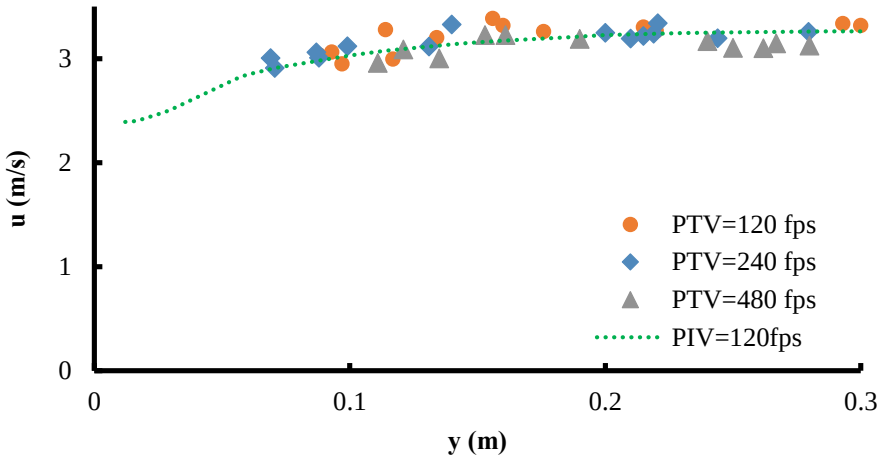

Figure I-13 : Surface velocity measured by PIV for S_f=0.0246- Z_n=0.09 m- Q=158.8 l/s

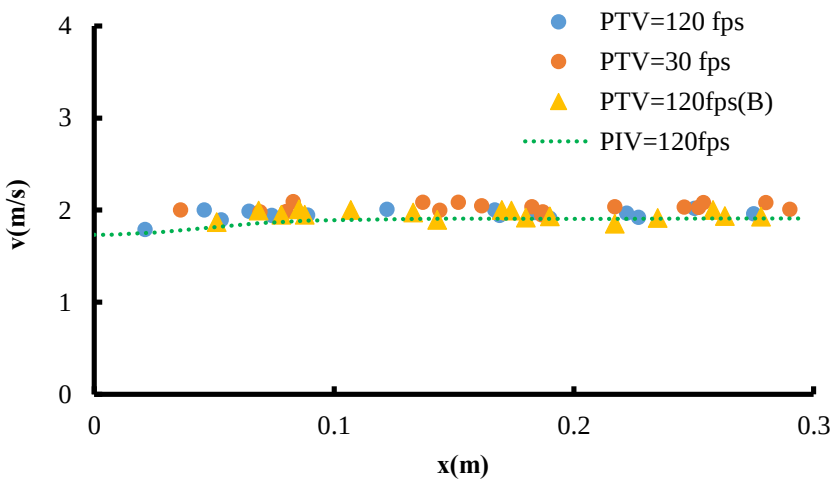

Figure I-14 : Surface velocity measured by PIV for S_0=0.055- Z_n=0.0145 m- Q=13.8 l/s

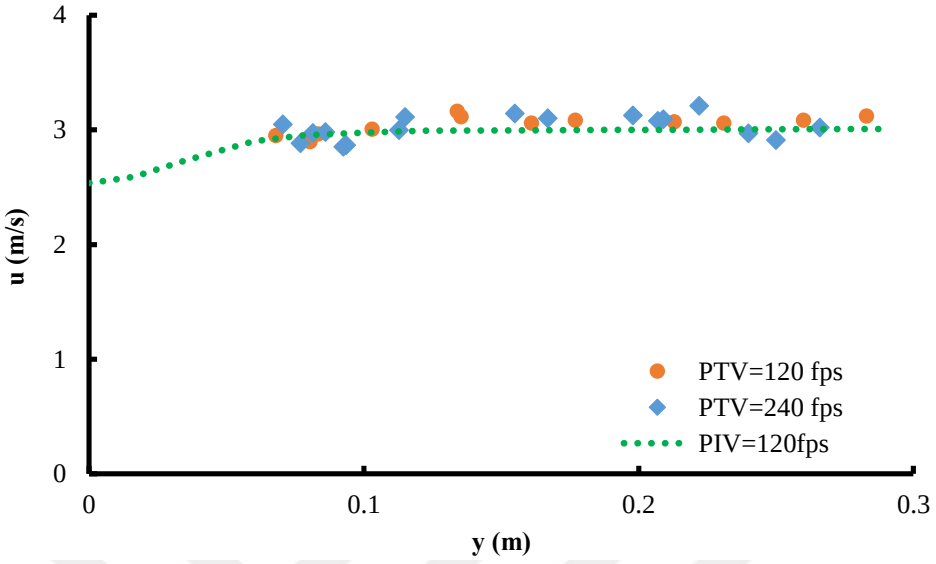

Figure I-15 : Surface velocity measured by PIV for S_0=0.055- Z_n=0.0345 m- Q=54.4 l/s

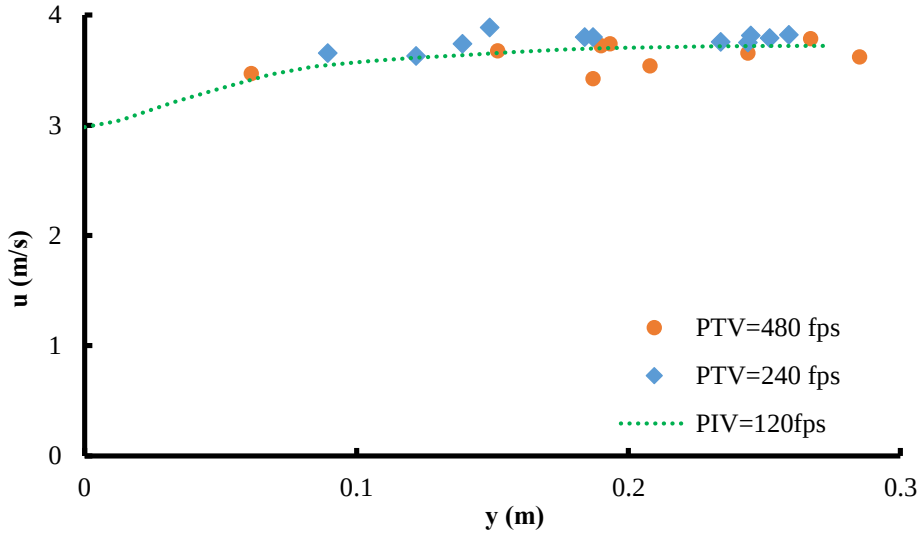

Figure I-16 : Surface velocity measured by PIV for S_f=0.0368- Z_n=0.08 m- Q=162.3 l/s

APPENDIX J

NUMERICAL AND EXPERIMENTAL SURFACE VELOCITIES IN SURFACE DAMPING FACTOR DETERMINATION PHASE IN SMOOTH RECTANGULAR CHANNELS

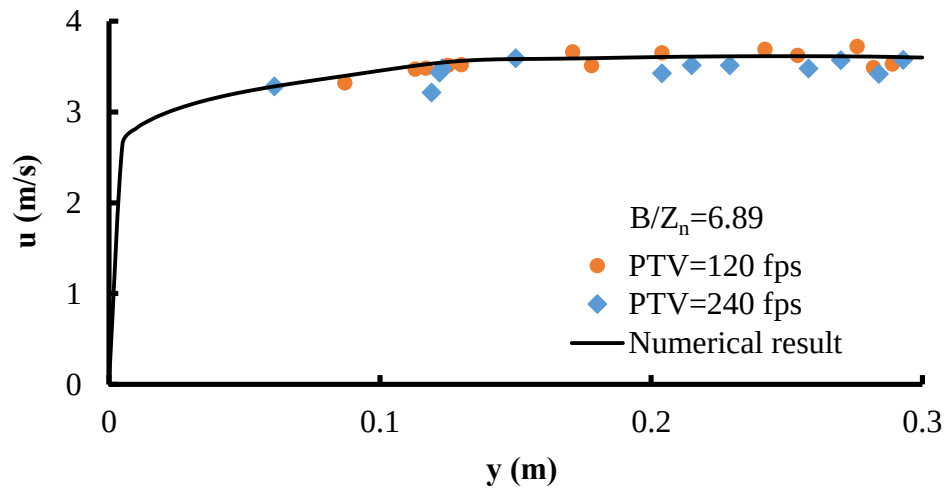

Figure J-1 : Numerical and experimental surface velocities for S_o=0.045 (Sf=0.0286)- Z_n=0.087 m- Q=162.61 l/s

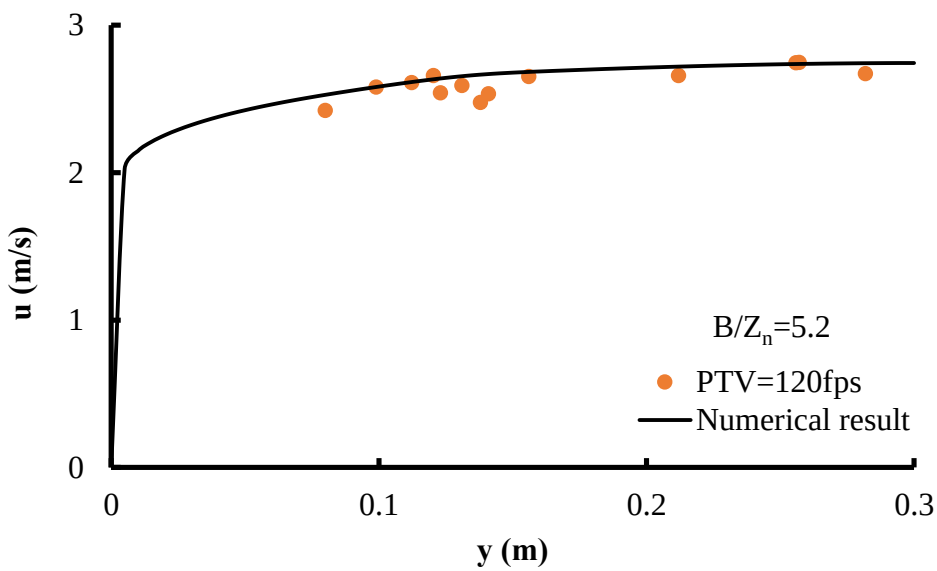

Figure J-2 : Numerical and experimental surface velocities for S_o=0.0131- Z_n=0.115 m- Q=167.5 l/s

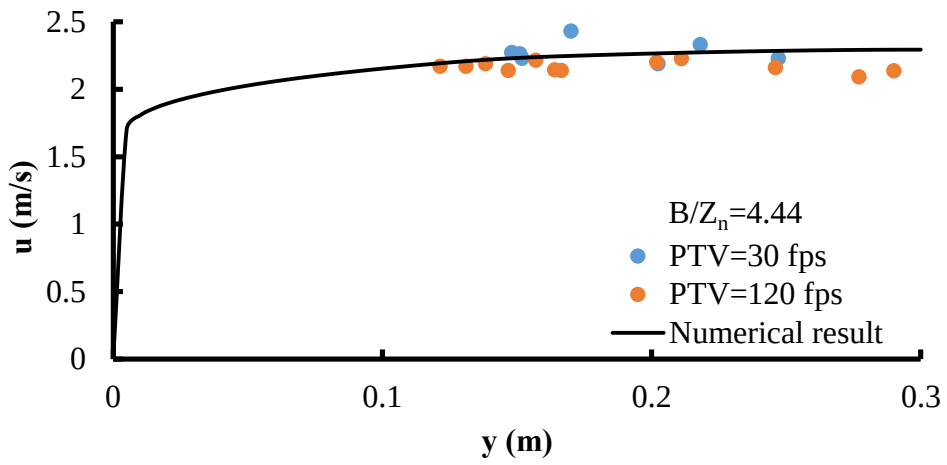

Figure J-3 : Numerical and experimental surface velocities for S_o=0.008- Z_n=0.135 m- Q=165.4 l/s

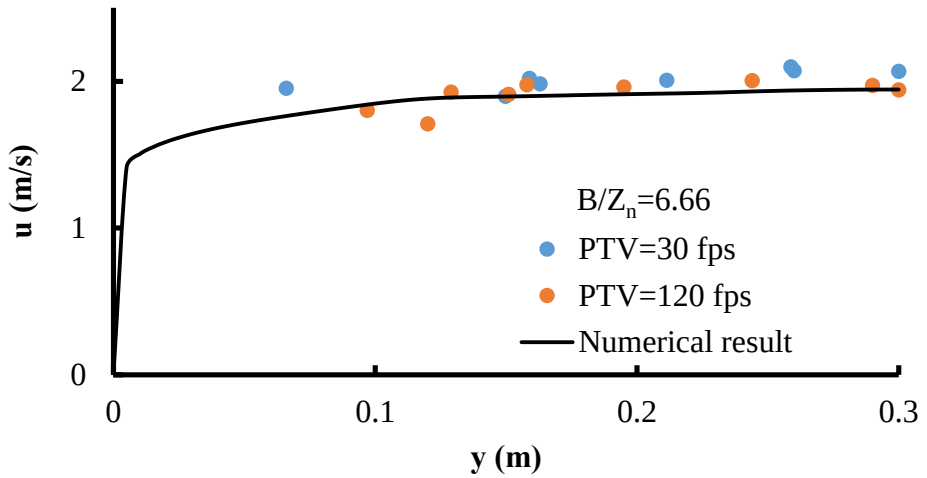

Figure J-4 : Numerical and experimental surface velocities for S_o=0.008- Z_n=0.09 m- Q=90.5 l/s

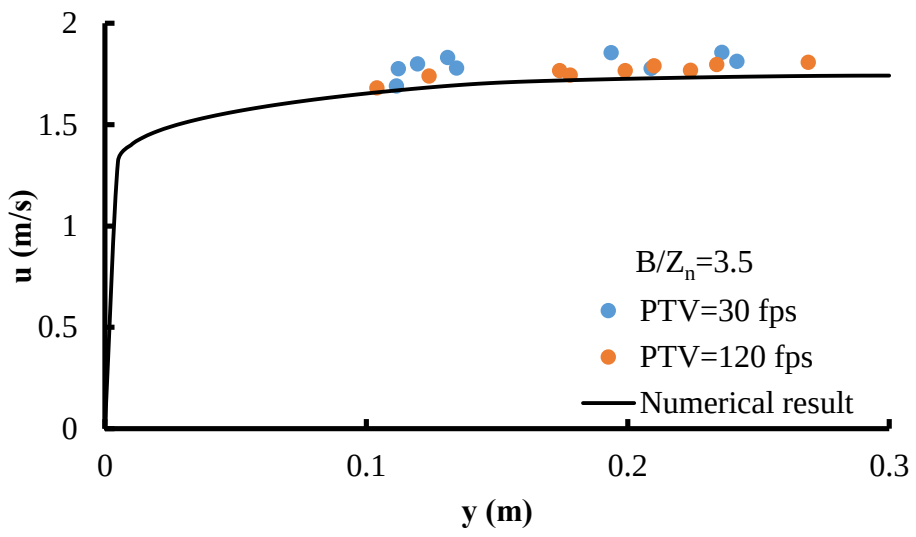

Figure J-5 : Numerical and experimental surface velocities for S_o=0.004- Z_n=0.17 m- Q=163.2 l/s

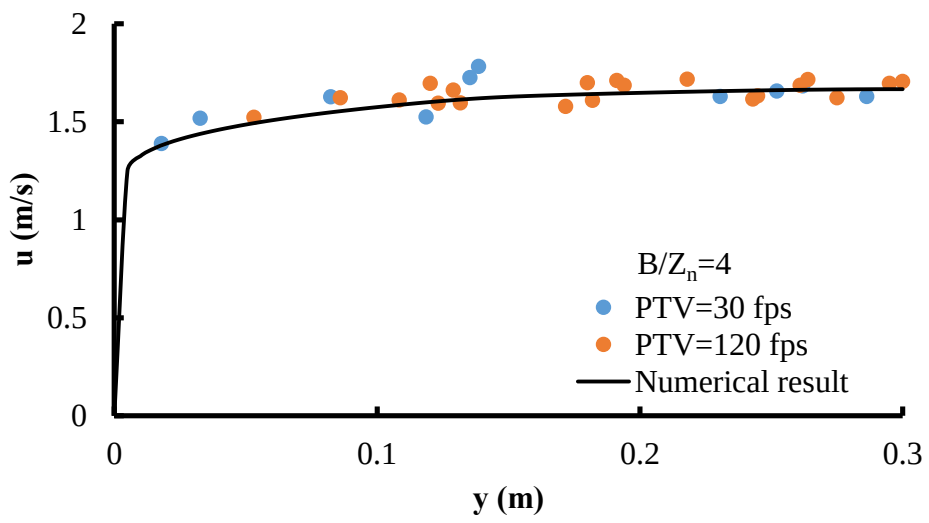

Figure J-6 : Numerical and experimental surface velocities for S_o=0.004- Z_n=0.15 m- Q=136.3 l/s

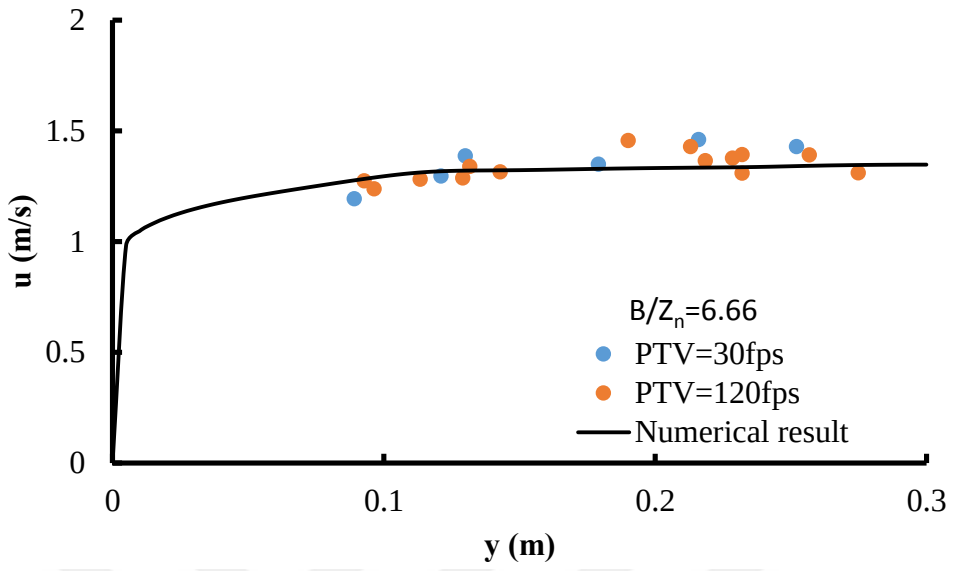

Figure J-7 : Numerical and experimental surface velocities for S_o=0.004- Z_n=0.09 m- Q=64 l/s

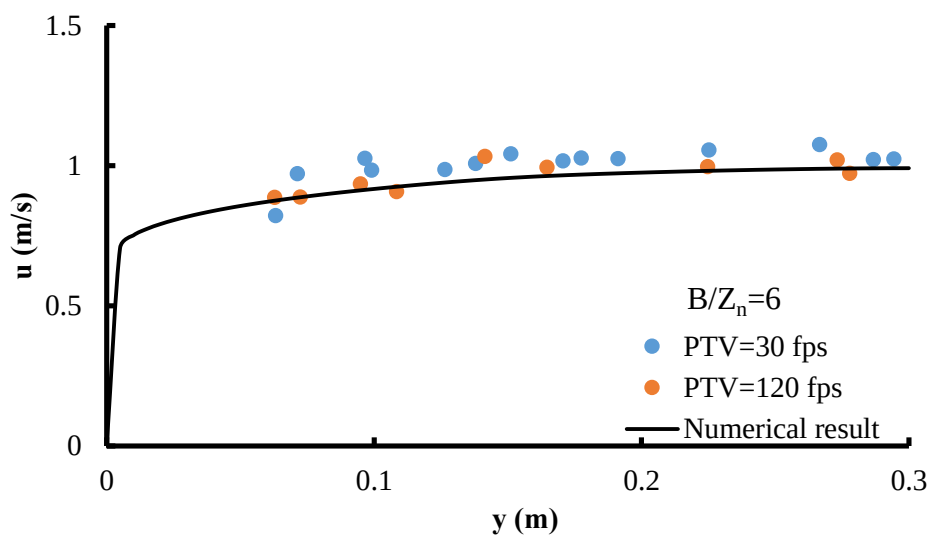

Figure J-8 : Numerical and experimental surface velocities for S_o=0.002- Z_n=0.1 m- Q=53.05 l/s

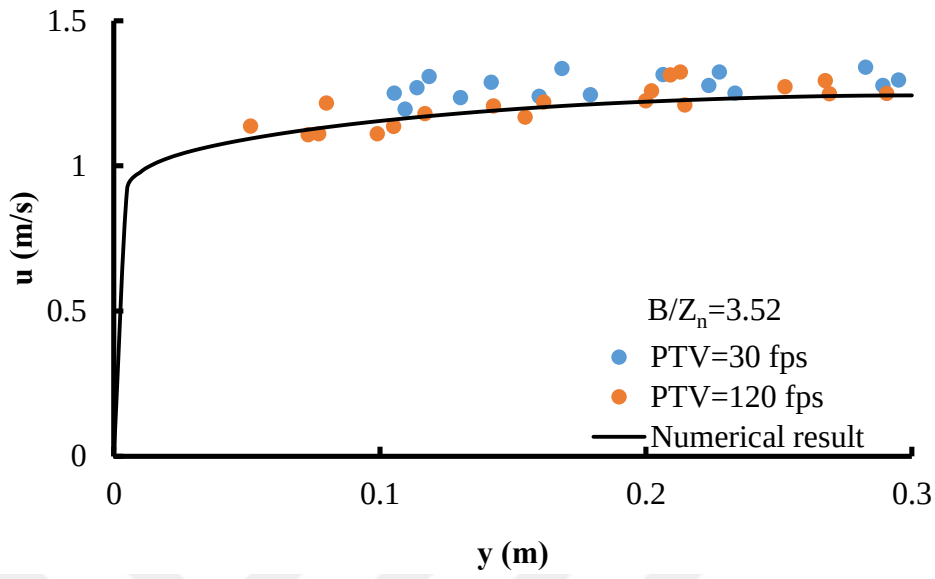

Figure J-9 : Numerical and experimental surface velocities for S_o=0.002- Z_n=0.17 m- Q=115.3 l/s

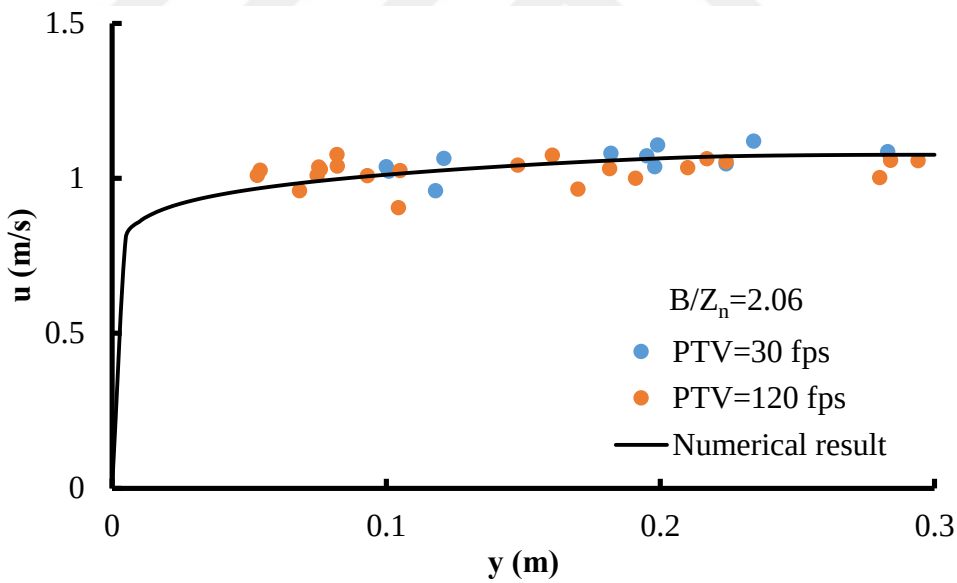

Figure J-10 : Numerical and experimental surface velocities for S_o=0.001- Z_n=0.29 m- Q=170.64 l/s

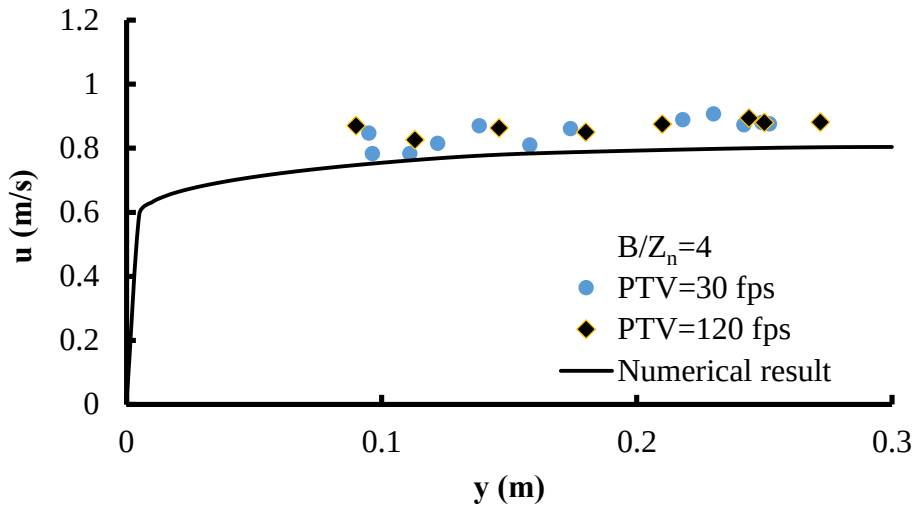

Figure J-11 : Numerical and experimental surface velocities for S_o=0.001- Z_n=0.15 m- Q=68.13 l/s

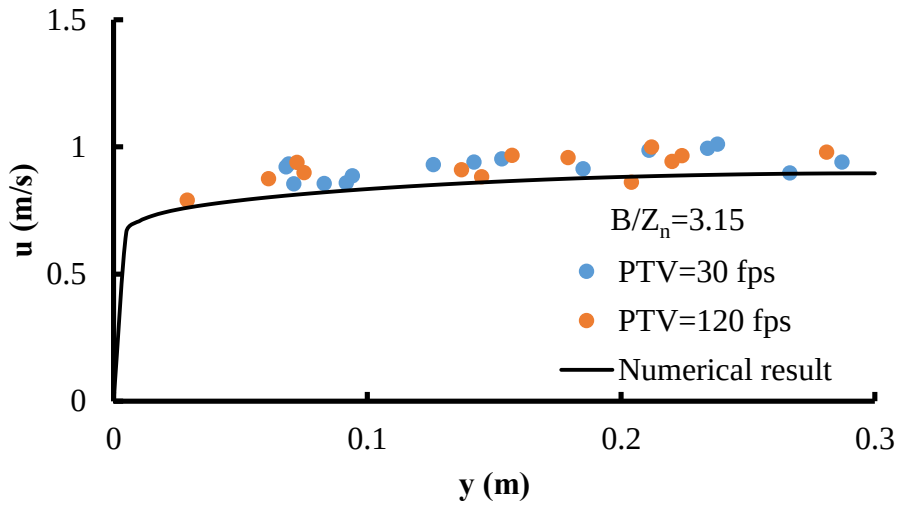

Figure J-12 : Numerical and experimental surface velocities for S_o=0.001- Z_n=0.19 m- Q=95.45 l/s

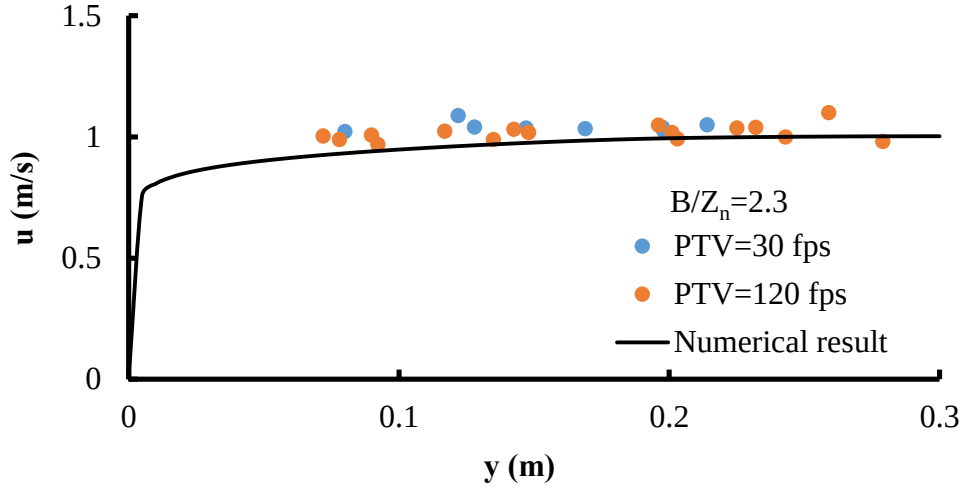

Figure J-13 : Numerical and experimental surface velocities for S_o=0.001- Z_n=0.26 m- Q=147.28 l/s

APPENDIX K

SURFACE VELOCITIES FOR INVERSE SOLUTIONS IN RECTANGULAR CHANNELS

Note: In some flow conditions Pitot tube velocity measurements are not presented. This is because of very small magnitudes of velocity which makes the device useless under such circumstances.

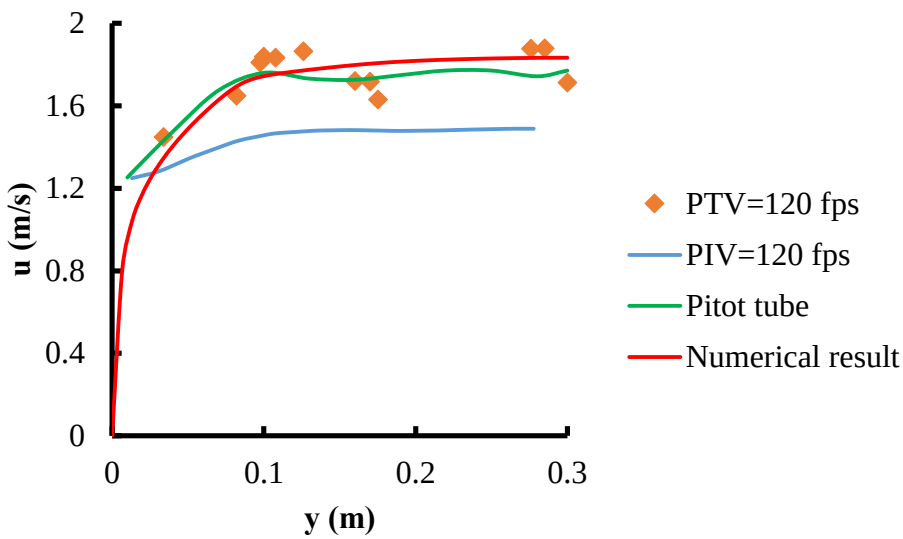

Figure K-1 : Measured and computed surface velocity with S_0=0.055, k_{s1}=3.9 cm, RMSE=6.24, Z_n=0.074 m, Q_{exp}=55 l/s

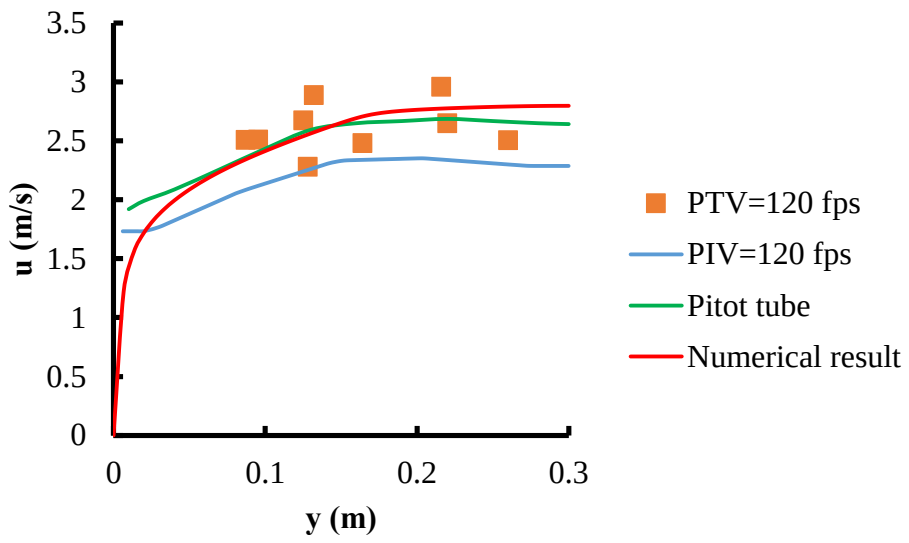

Figure K-2 : Measured and computed surface velocity with S_0=0.055, k_{s1}=2.9 cm, RMSE=8.23, Z_n=0.1325 m, Q_{exp}=162.4 l/s

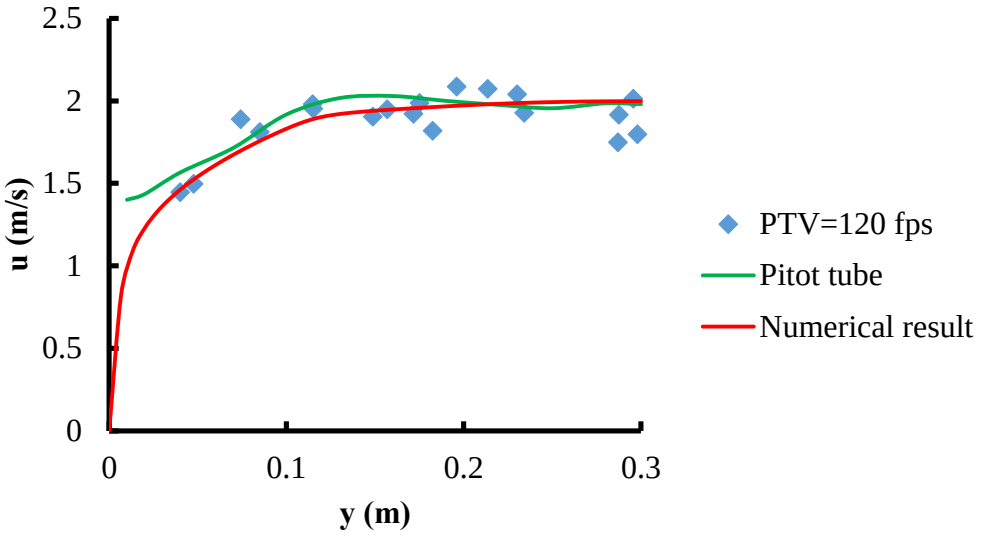

Figure K-3 : Measured and computed surface velocity with S_0=0.045, k_{s1}=3.6 cm, RMSE=5.53, Z_n=0.10031 m, Q_{exp}=87 l/s

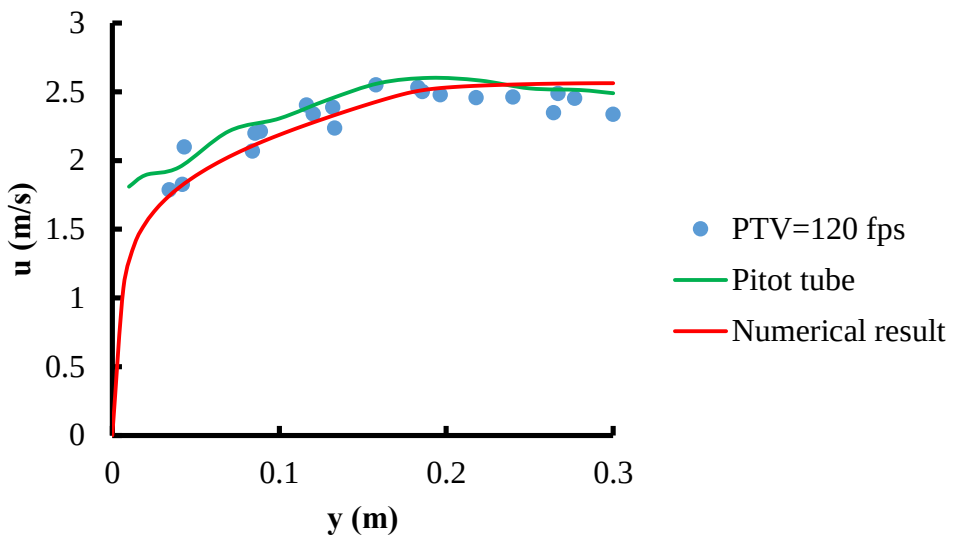

Figure K-4 : Measured and computed surface velocity with S_0=0.045, k_{s1}=3.1 cm, RMSE=5.95, Z_n=0.1426 m, Q $_{exp}$=87 l/s

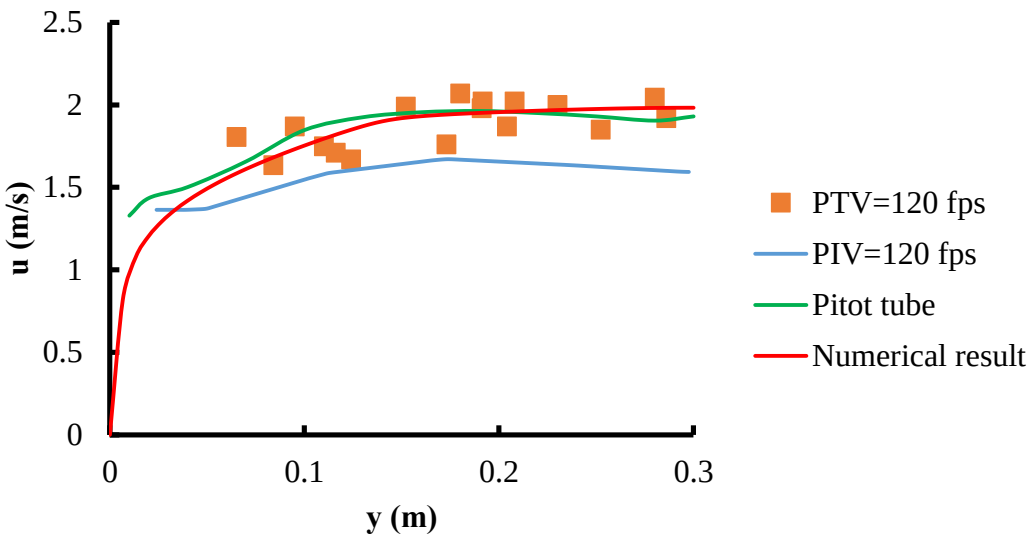

Figure K-5 : Measured and computed surface velocity with S_0=0.035, k_{s1}=3.35 cm, RMSE=5.95, Z_n=0.1173 m, Q $_{exp}$=101.8 l/s

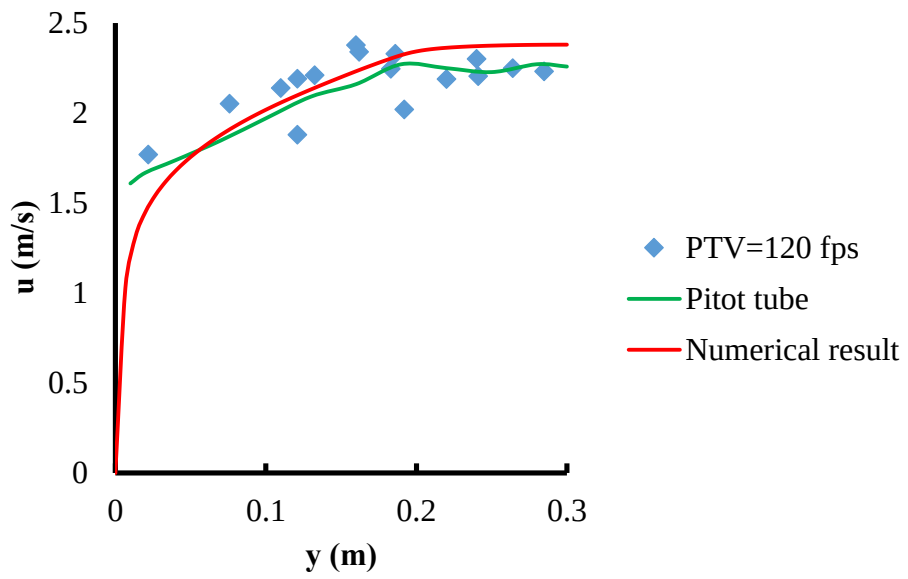

Figure K-6 : Measured and computed surface velocity with S_0=0.035, k_{s1}=2.85 cm, RMSE=7.98, Z_n=0.15 m, Q_{exp}=159.1 l/s

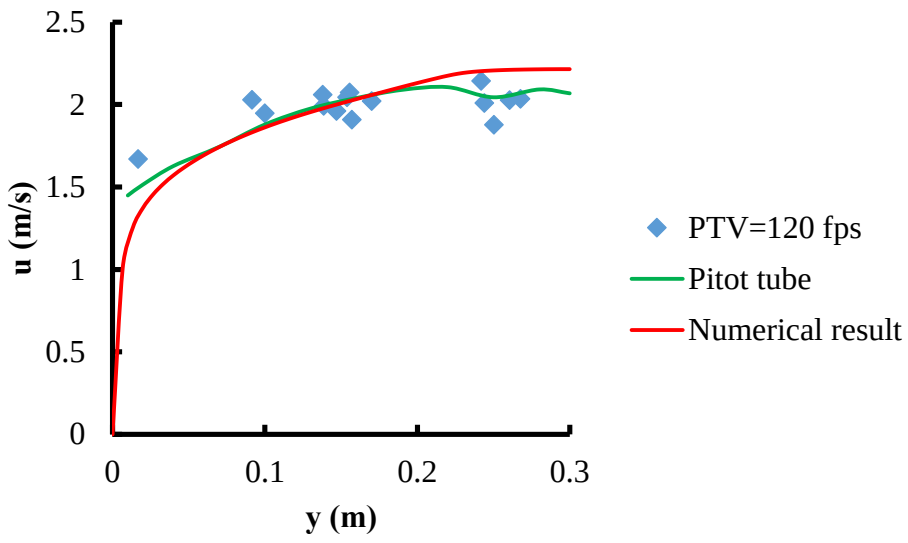

Figure K-7 : Measured and computed surface velocity with S_0=0.025, k_{s1}=3.15 cm, RMSE=7.1, Z_n=0.11561 m, Q_{exp}=86 l/s

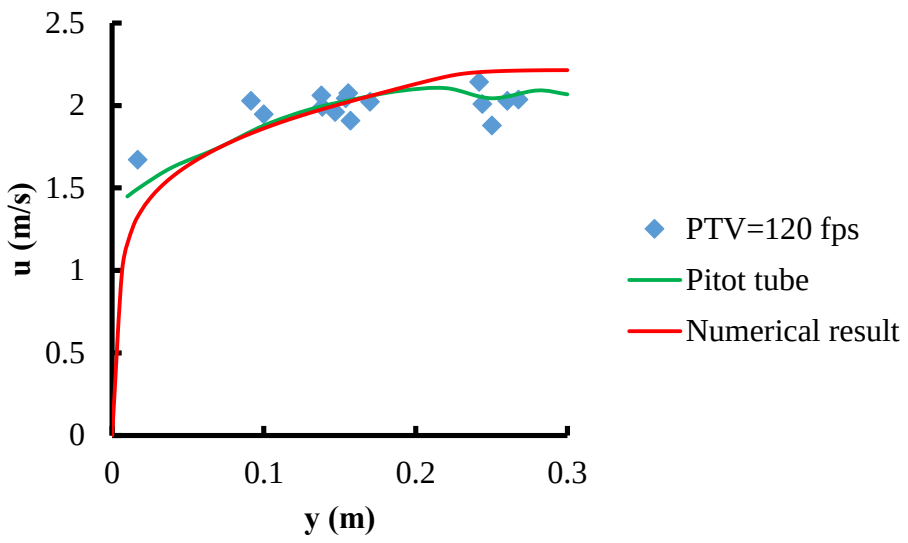

Figure K-8 : Measured and computed surface velocity with S_0=0.025, k_{s1}=2.75 cm, RMSE=9.55, Z_n=0.1678 m, Q $_{exp}$=160 l/s

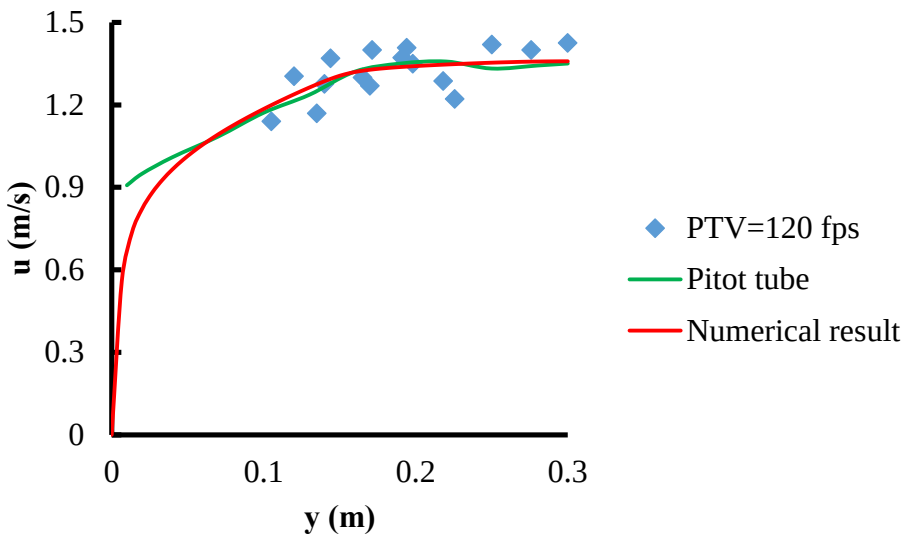

Figure K-9 : Measured and computed surface velocity with S_0=0.015, k_{s1}=3.4 cm, RMSE=4.88, Z_n=0.12618 m, Q $_{exp}$=75.3 l/s

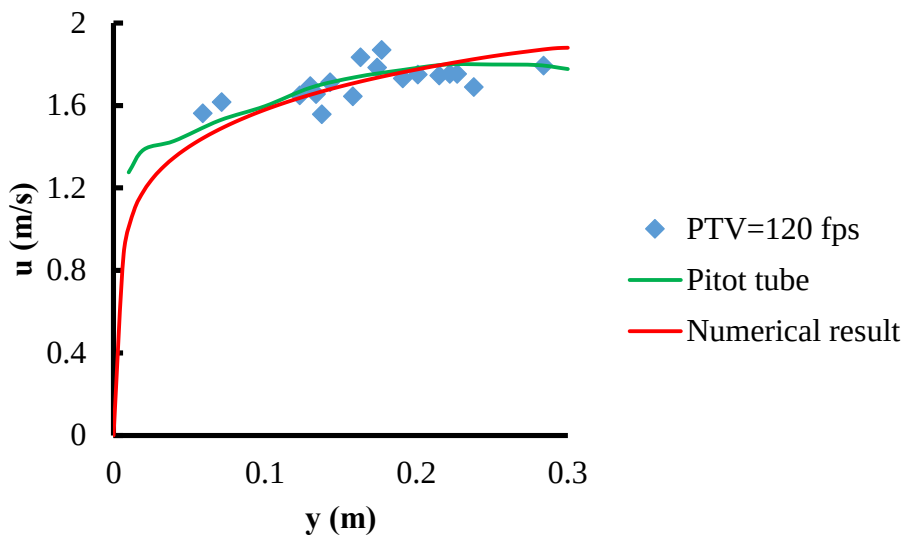

Figure K-10 : Measured and computed surface velocity with S_0=0.015, k_{s1}=2.32 cm, RMSE=4.86, Z_n=0.19825 m, Q $_{exp}$=167.7 l/s

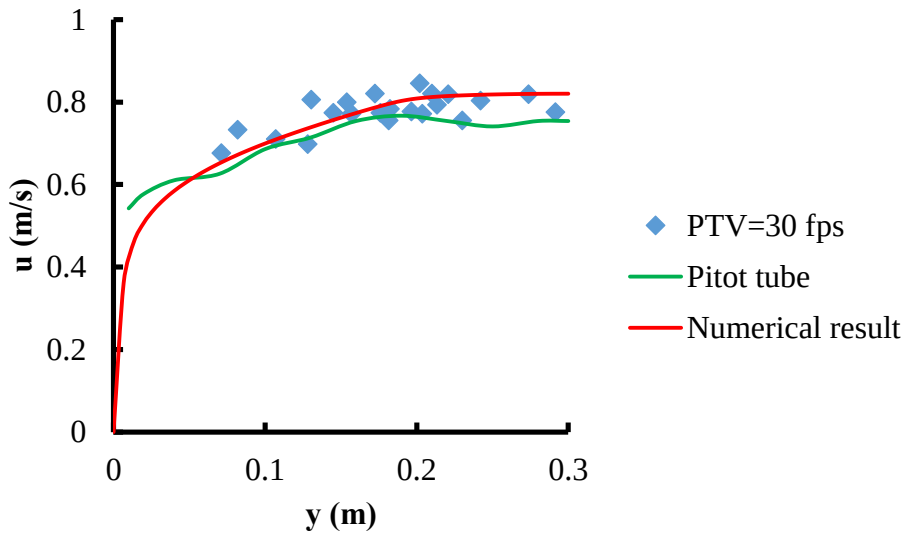

Figure K-11 : Measured and computed surface velocity with S_0=0.004, k_{s1}=3.5 cm, RMSE=7.7, Z_n=0.151 m, Q $_{exp}$=51 l/s

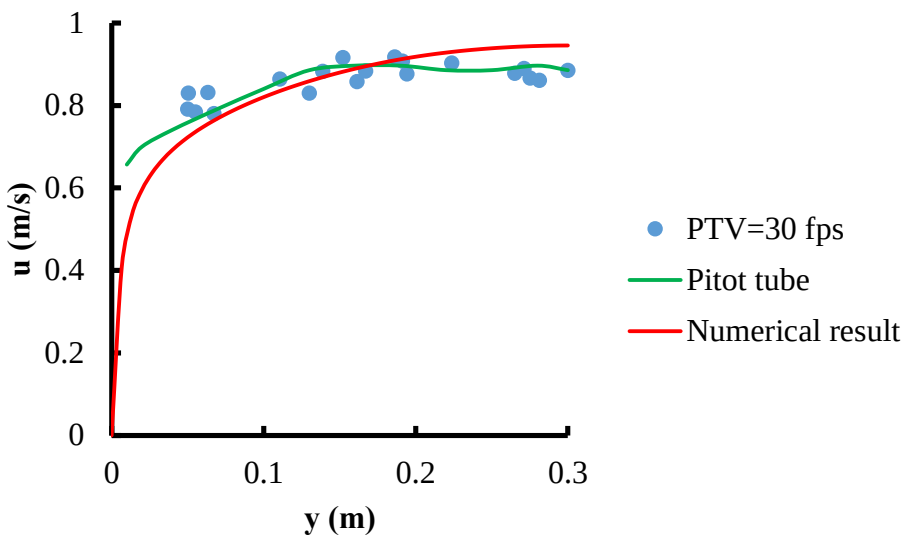

Figure K-12 : Measured and computed surface velocity with S_0=0.004, k_{s1}=4.3 cm, RMSE=6.6, Z_n=0.261 m, Q_{exp}=110 l/s

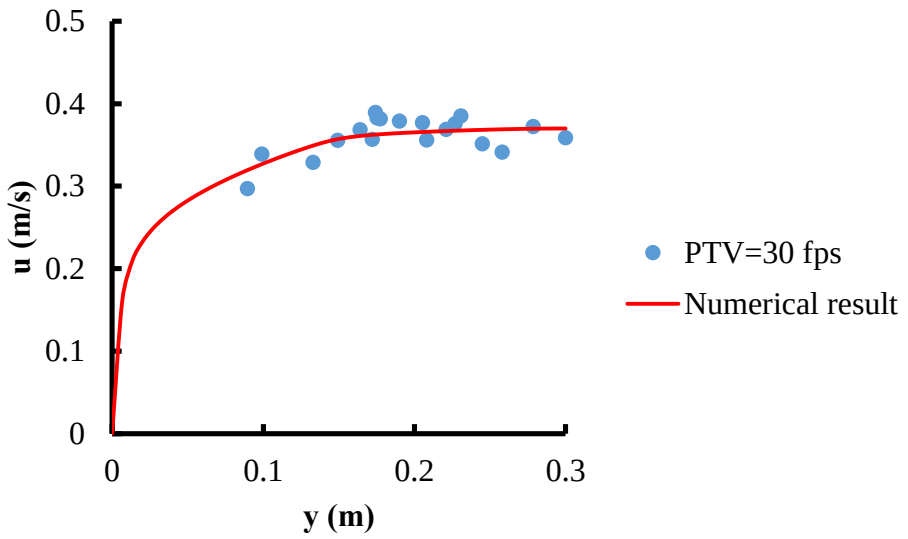

Figure K-13 : Measured and computed surface velocity with S_0=0.001, k_{s1}=3.3 cm, RMSE=4.65, Z_n=0.13 m, Q_{exp}=20.55 l/s

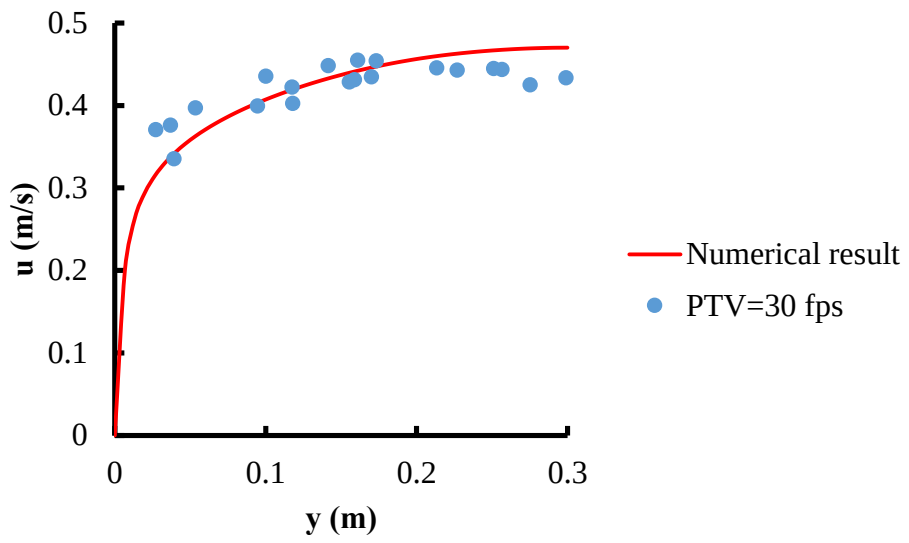

Figure K-14 : Measured and computed surface velocity with S_0=0.001, k_{s1}=4.25 cm, RMSE=6.43, Z_n=0.261 m, Q_{exp}=55 l/s

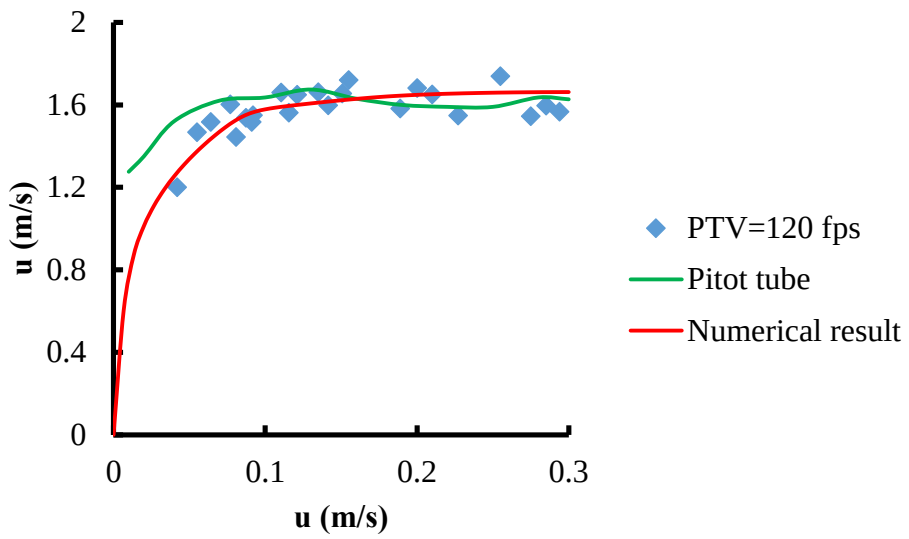

Figure K-15 : Measured and computed surface velocity with S_0=0.055, k_{s2}=5.4 cm, RMSE=9.52, Z_n=0.0784 m, Q_{exp}=55 l/s

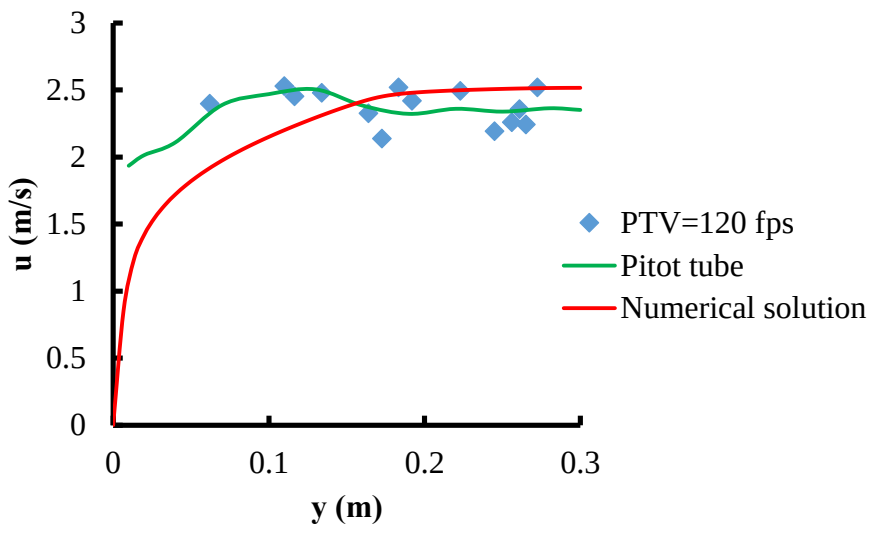

Figure K-16 : Measured and computed surface velocity with S_0=0.055, k_{s2}=4.4 cm, RMSE=10.66, Z_n=0.143 m, Q $_{exp}$=162.4 l/s

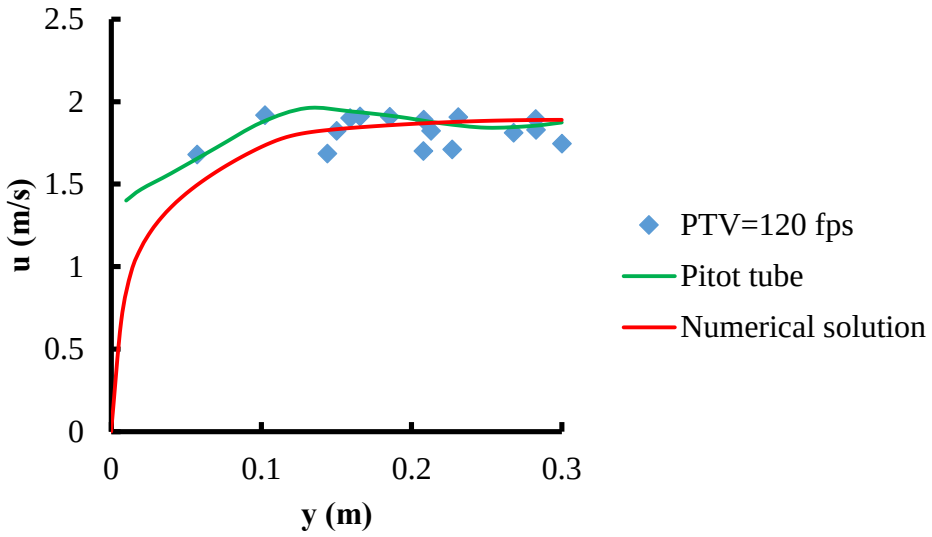

Figure K-17 : Measured and computed surface velocity with S_0=0.045, k_{s2}=4.8 cm, RMSE=11.1, Z_n=0.1062 m, Q $_{exp}$=87 l/s

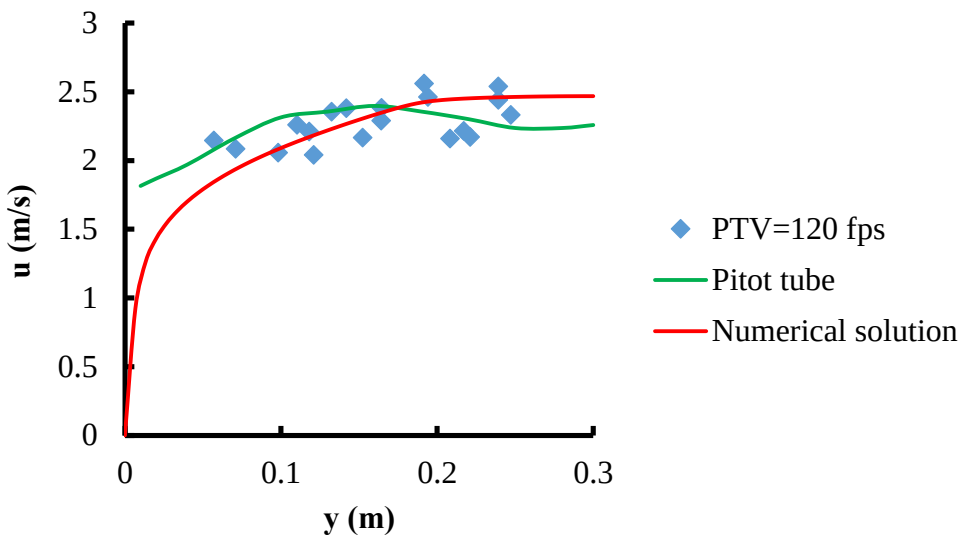

Figure K-18 : Measured and computed surface velocity with S_0=0.045, k_{s2}=4.2 cm, RMSE=10.4 , Z_n=0.1507 m, Q_{exp}=162.6 l/s

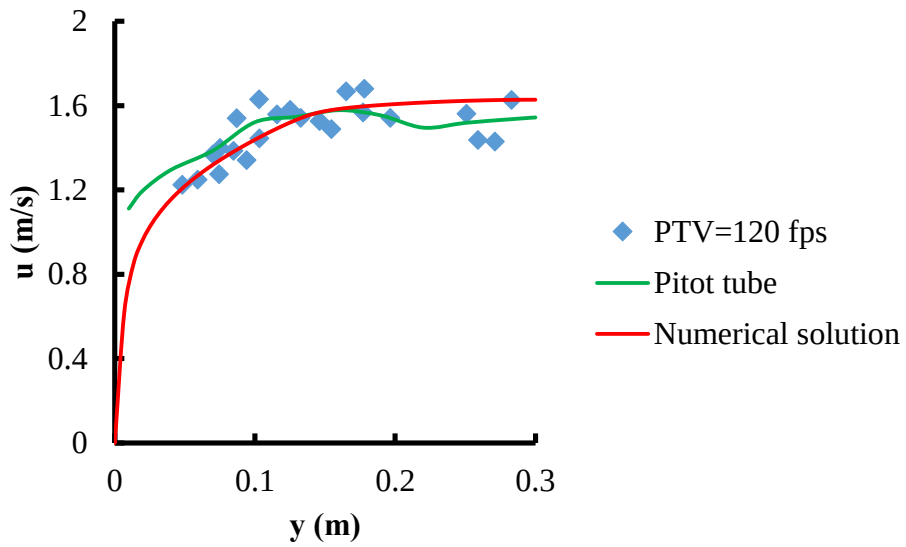

Figure K-19 : Measured and computed surface velocity with S_0=0.025, k_{s2}=4.55 cm, RMSE=7.75 , Z_n=0.1238 m, Q_{exp}=86 l/s

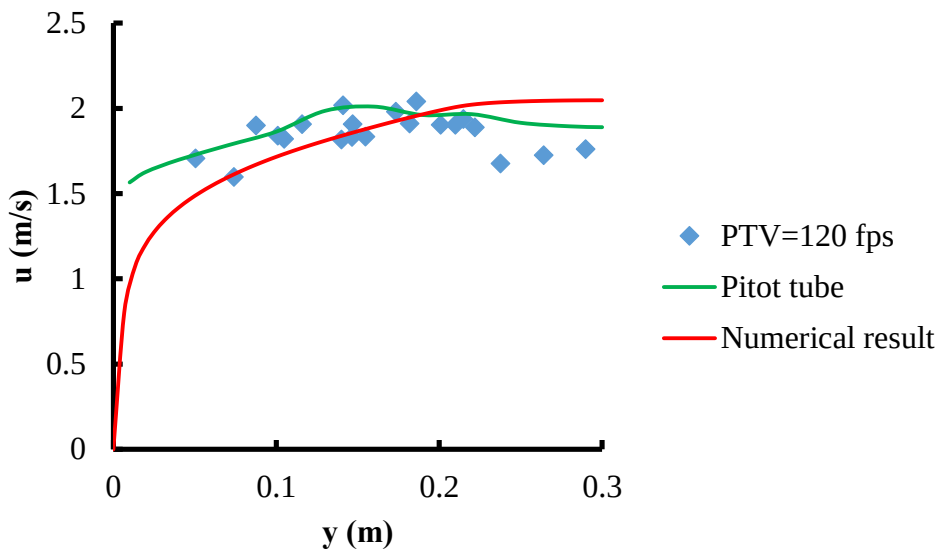

Figure K-20 : Measured and computed surface velocity with S_0=0.025, k_{s2}=3.6 cm, RMSE=9.2, Z_n=0.175 m, Q_{exp}=160 l/s

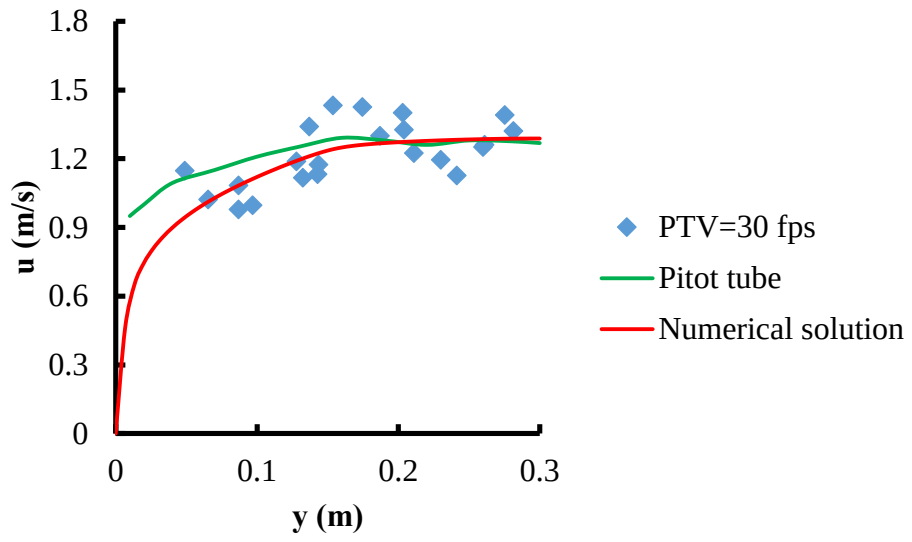

Figure K-21 : Measured and computed surface velocity with S_0=0.015, k_{s2}=4.6 cm, RMSE=11.01, Z_n=0.1336 m, Q_{exp}=75 l/s

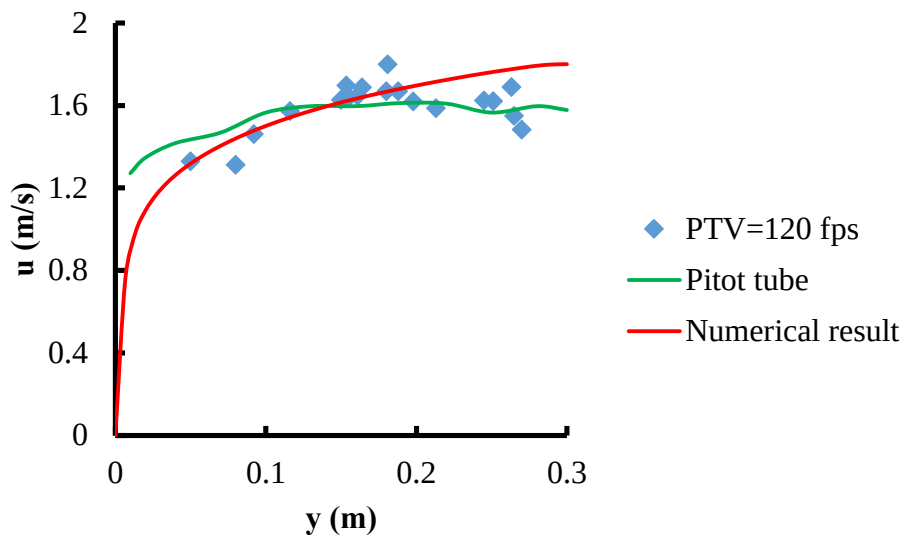

Figure K-22 : Measured and computed surface velocity with S_0=0.015, k_{s2}=3.3 cm, RMSE=8.74, Z_n=0.21 m, Q_{exp}=167.7 l/s

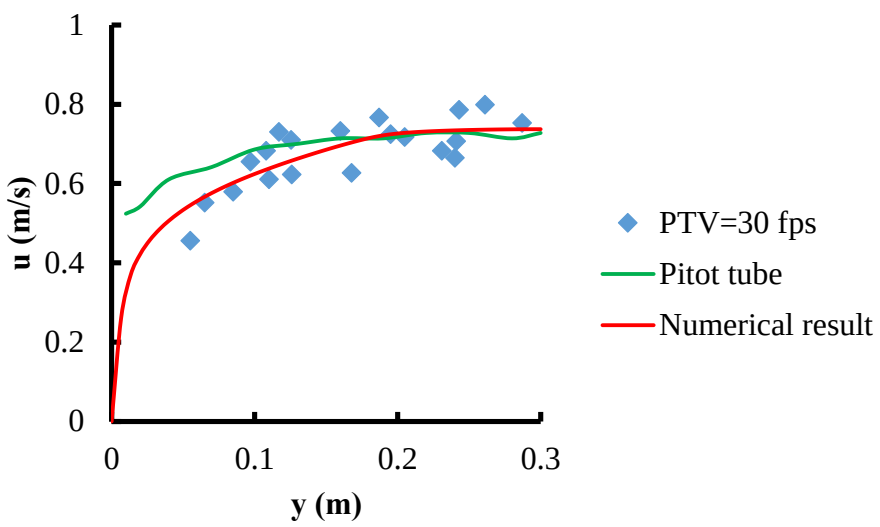

Figure K-23 : Measured and computed surface velocity with S_0=0.004, k_{s2}=4.65 cm, RMSE=8.5, Z_n=0.1586 m, Q_{exp}=51 l/s

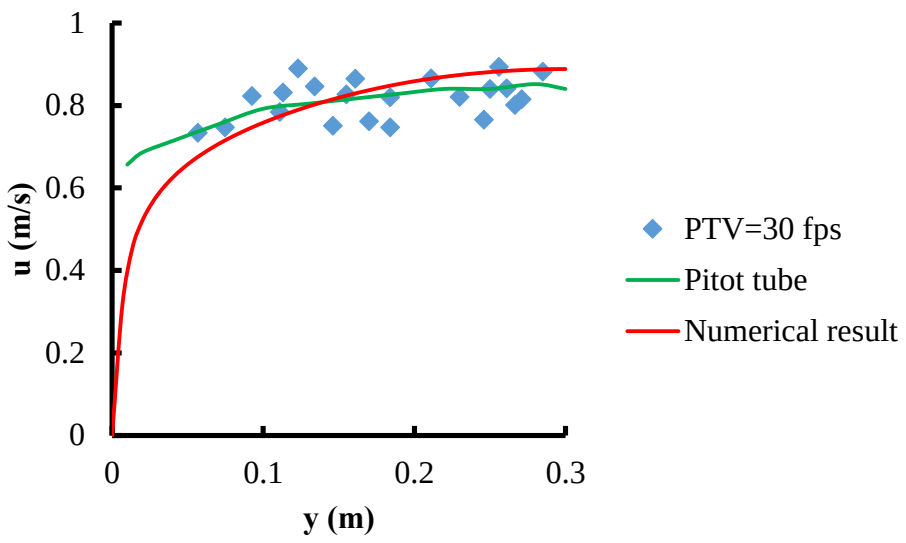

Figure K-24 : Measured and computed surface velocity with S_0=0.004, k_{s2}=5.8 cm, RMSE=11.13, Z_n=0.2763 m, Q $_{exp}$=110 l/s

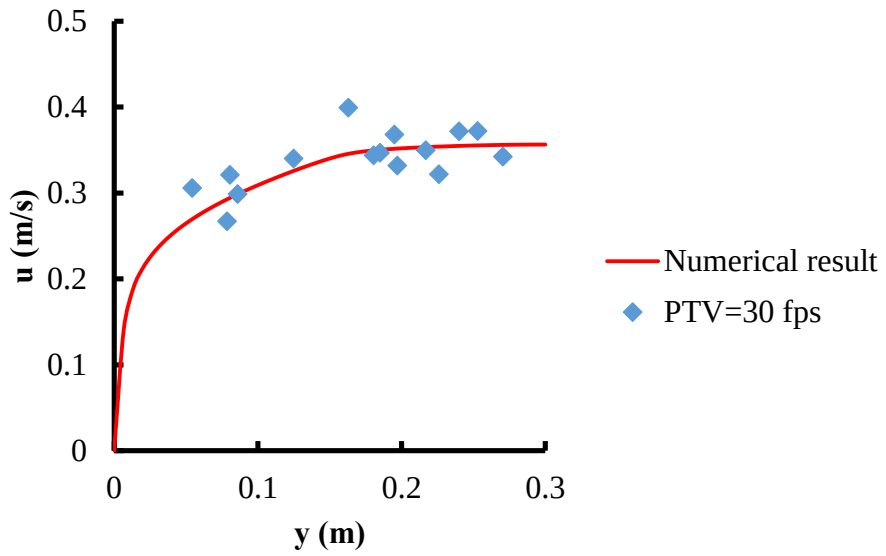

Figure K-25 : Measured and computed surface velocity with S_0=0.001, k_{s2}=4.3 cm, RMSE=10.83, Z_n=0.1365 m, Q $_{exp}$=20.55 l/s

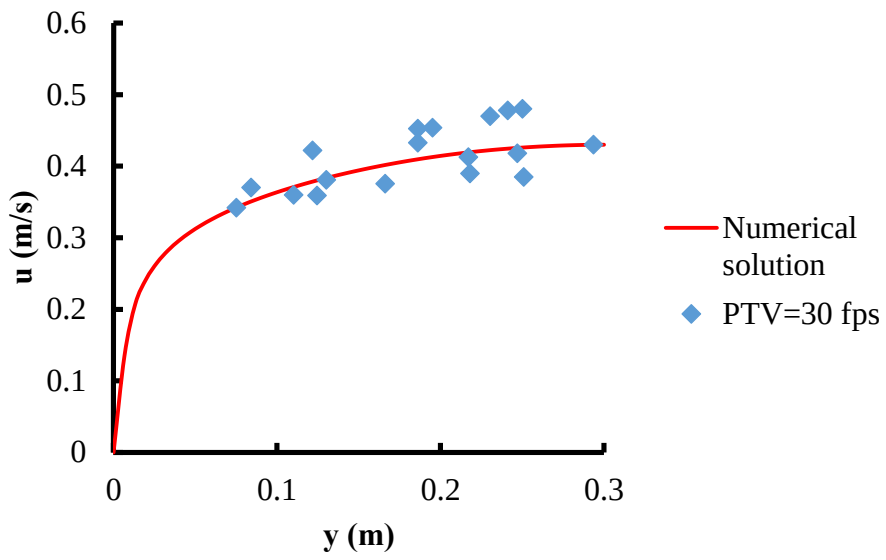

Figure K-26 : Measured and computed surface velocity with S_0=0.001, k_{s2}=5.8cm, RMSE=12.33, Z_n=0.2763 m, Q_{exp}=55 l/s

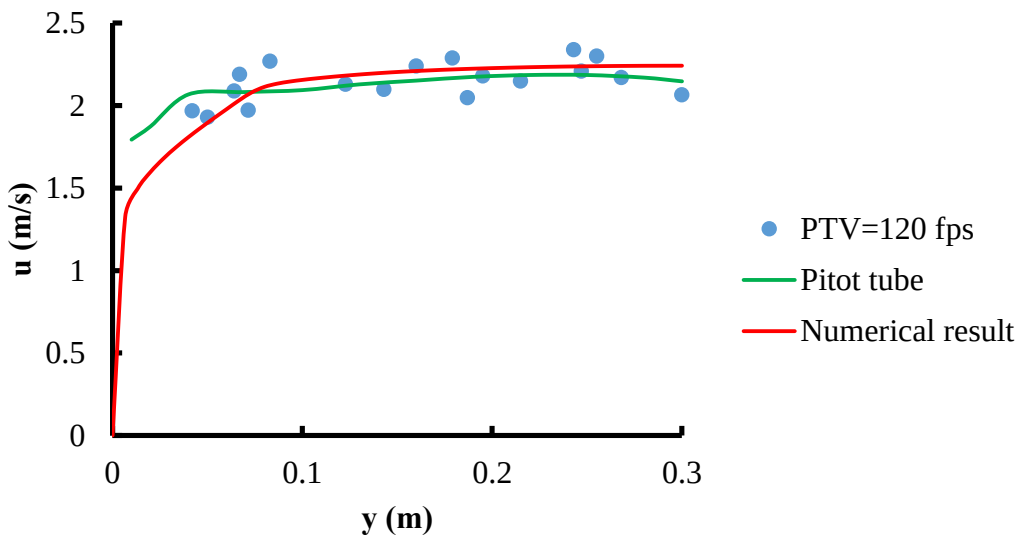

Figure K-27 : Measured and computed surface velocity with S_0=0.055, k_{s3}=0.44 cm, RMSE=5.15, Z_n=0.0516 m, Q_{exp}=55 l/s

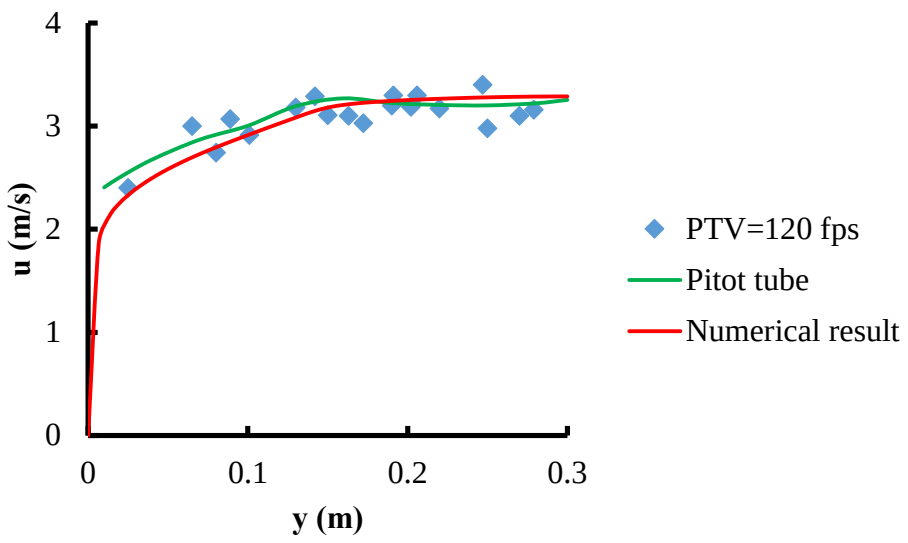

Figure K-28 : Measured and computed surface velocity with S_0=0.055, k_{s3}=0.53 cm, RMSE=4.85, Z_n=0.1031 m, Q_{exp}=162.4 l/s

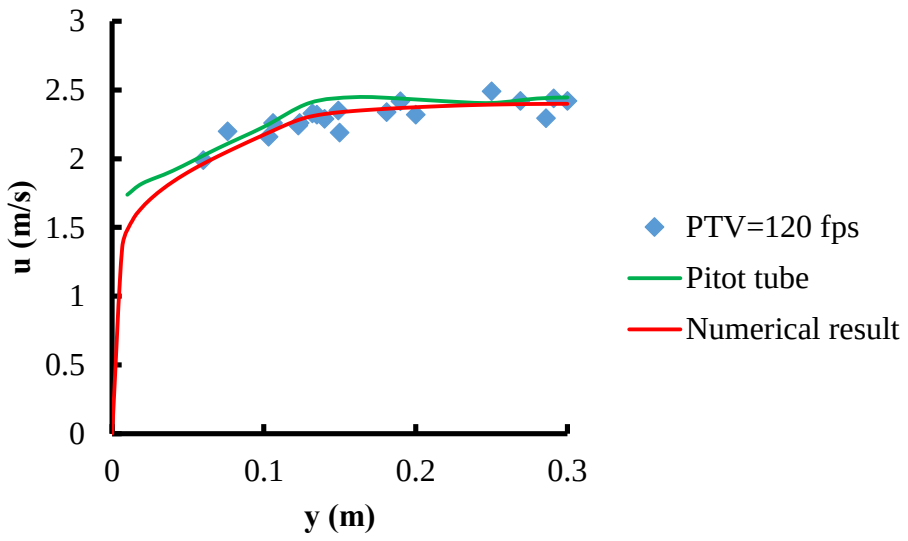

Figure K-29 : Measured and computed surface velocity with S_0=0.035, k_{s3}=0.56 cm, RMSE=2.92, Z_n=0.0891 m, Q_{exp}=101.8 l/s

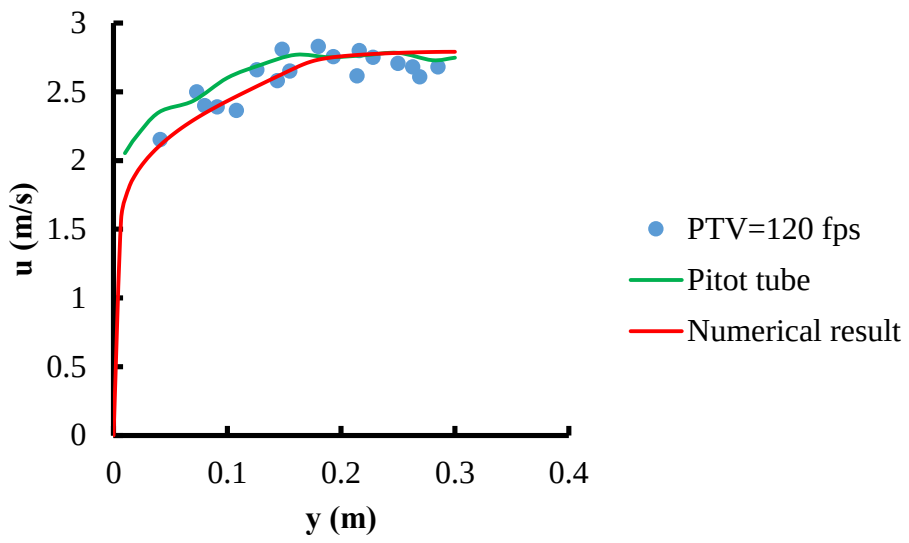

Figure K-30 : Measured and computed surface velocity with S_0=0.035, k_{s3}=0.55 cm, RMSE=4.02, Z_n=0.1185 m, Q $_{exp}$=159.1 l/s

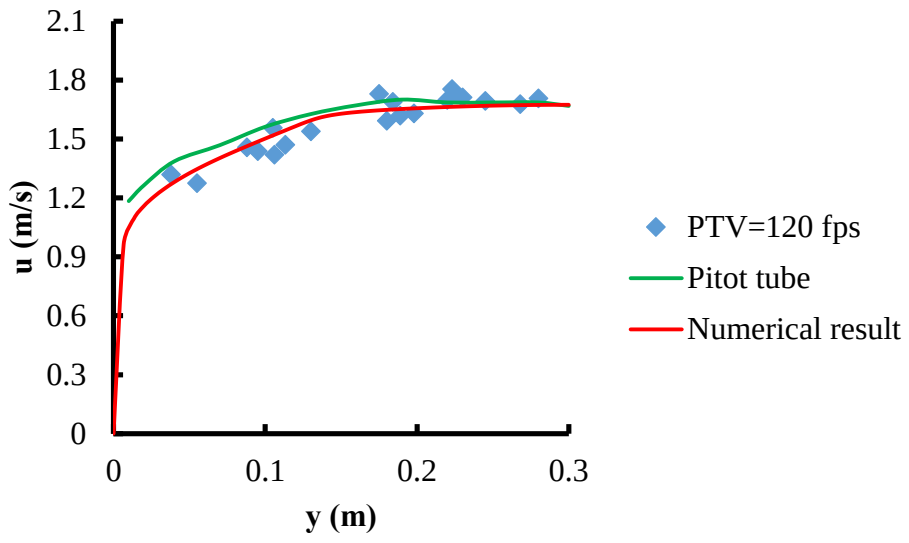

Figure K-31 : Measured and computed surface velocity with S_0=0.015, k_{s3}=0.48 cm, RMSE=3.532, Z_n=0.0944 m, Q $_{exp}$=75.3 l/s

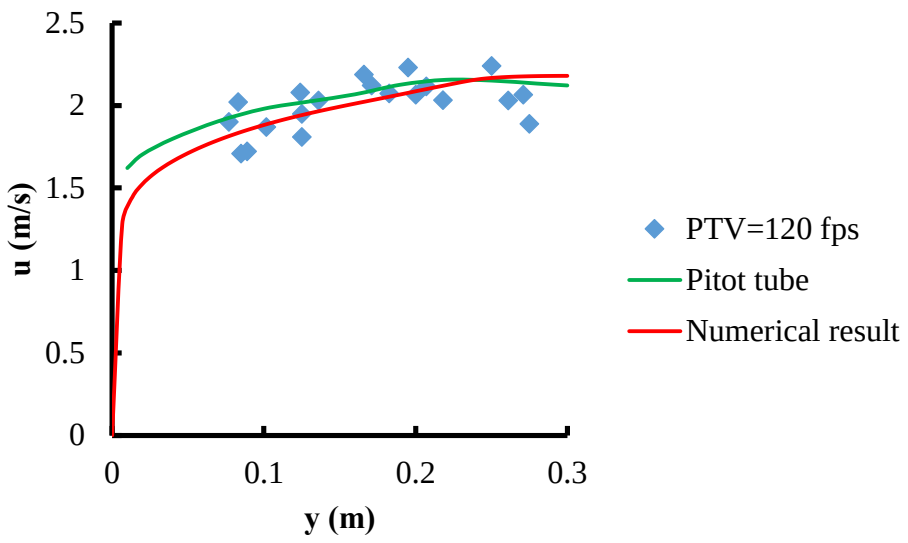

Figure K-32 : Measured and computed surface velocity with S_0=0.015, k_{s3}=0.4 cm, RMSE=6.12, Z_n=0.156 m, Q_{exp}=167.7 l/s

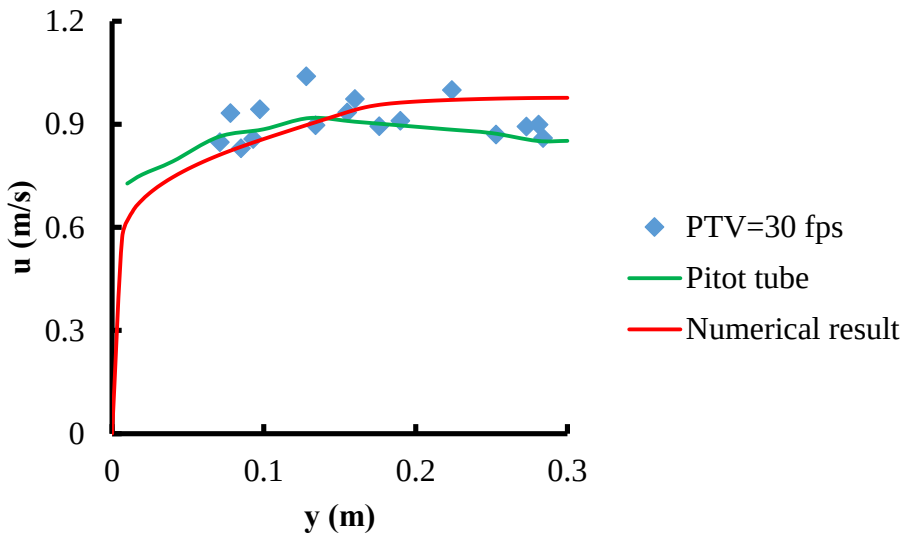

Figure K-33 : Measured and computed surface velocity with S_0=0.004, k_{s3}=0.5 cm, RMSE=8.1, Z_n=0.113 m, Q_{exp}=51 l/s

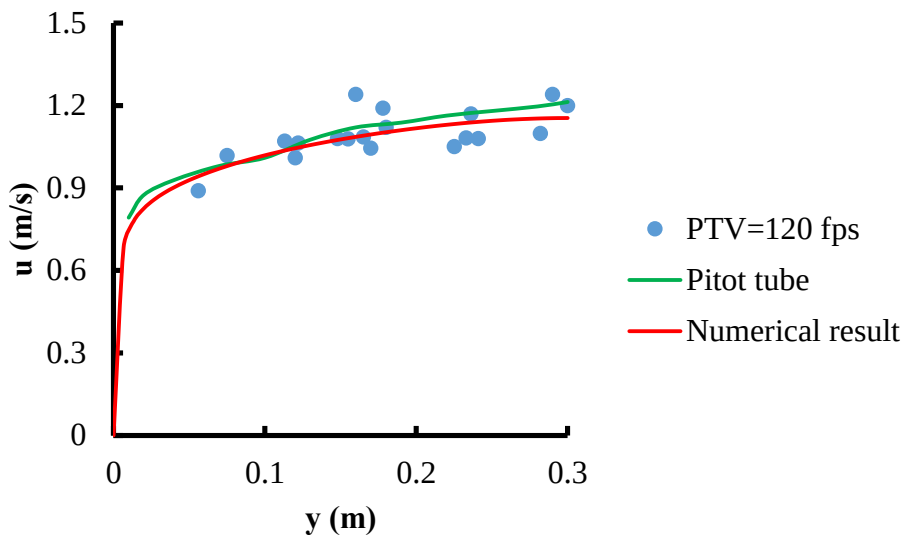

Figure K-34 : Measured and computed surface velocity with S_0=0.004, k_{s3}=0.57 cm, RMSE=5.54, Z_n=0.192 m, Q $_{exp}$=110 l/s

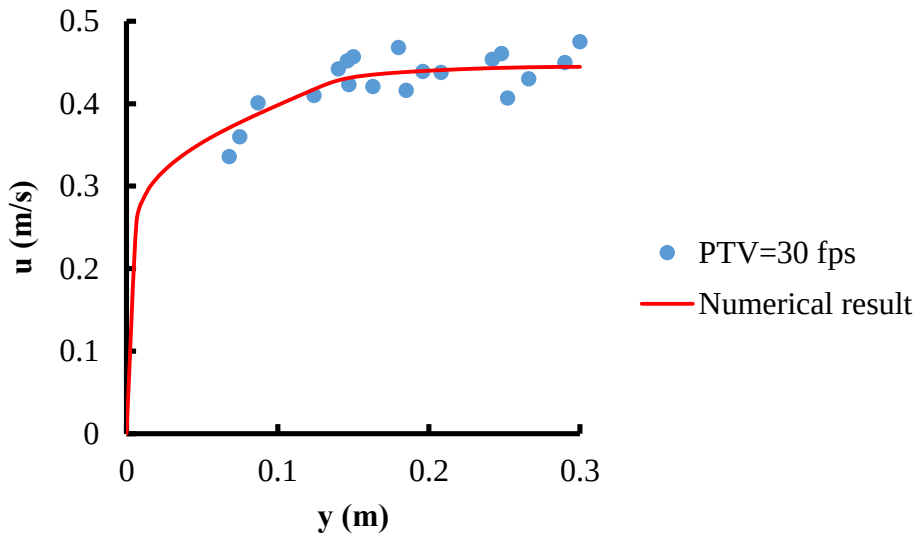

Figure K-35 : Measured and computed surface velocity with S_0=0.001, k_{s3}=0.49 cm, RMSE=4.68, Z_n=0.0977 m, Q $_{exp}$=20.55 l/s

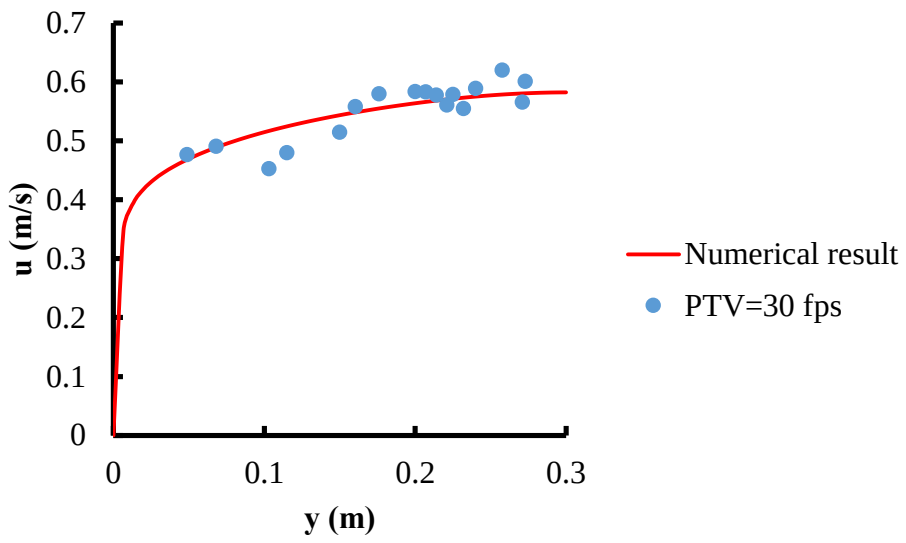

Figure K-36 : Measured and computed surface velocity with S_0=0.001, k_{s3}=0.5 cm, RMSE=4.81, Z_n=0.192 m, Q $_{exp}$=55 l/s

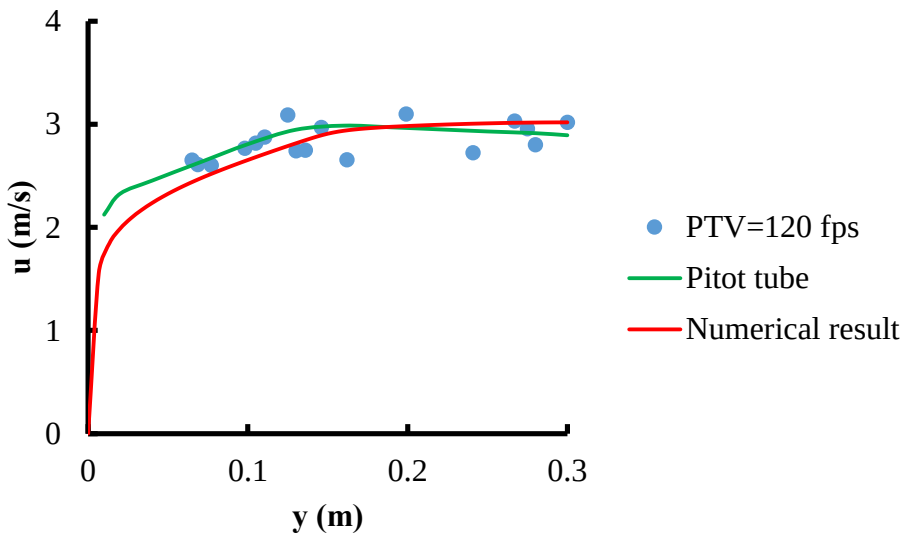

Figure K-37 : Measured and computed surface velocity with S_0=0.055, k_{s4}=1.07 cm, RMSE=7.31, Z_n=0.1133 m, Q $_{exp}$=162.4 l/s

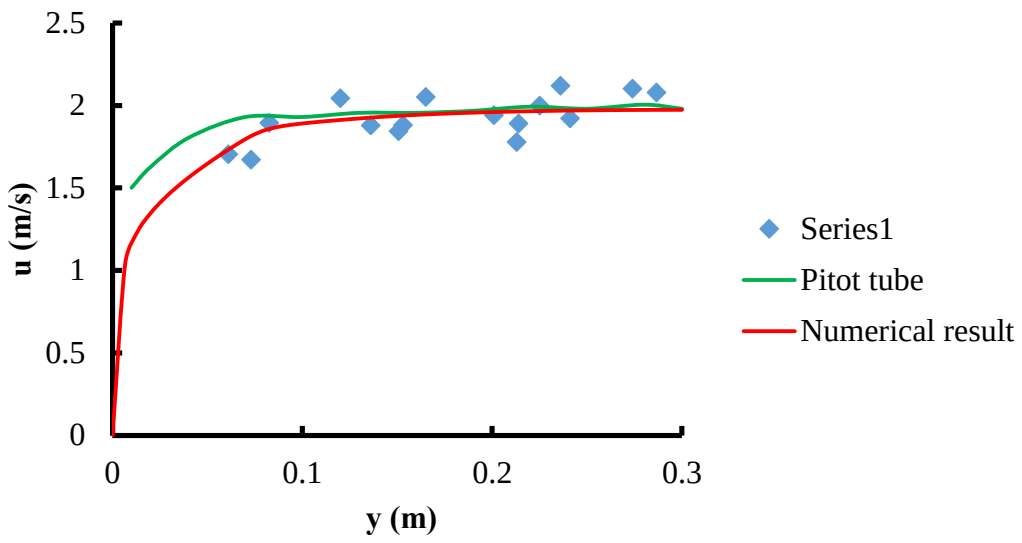

Figure K-38 : Measured and computed surface velocity with S_0=0.055, k_{s4}=1.25 cm, RMSE=5.166, Z_n=0.0599 m, Q_{exp}=55 l/s

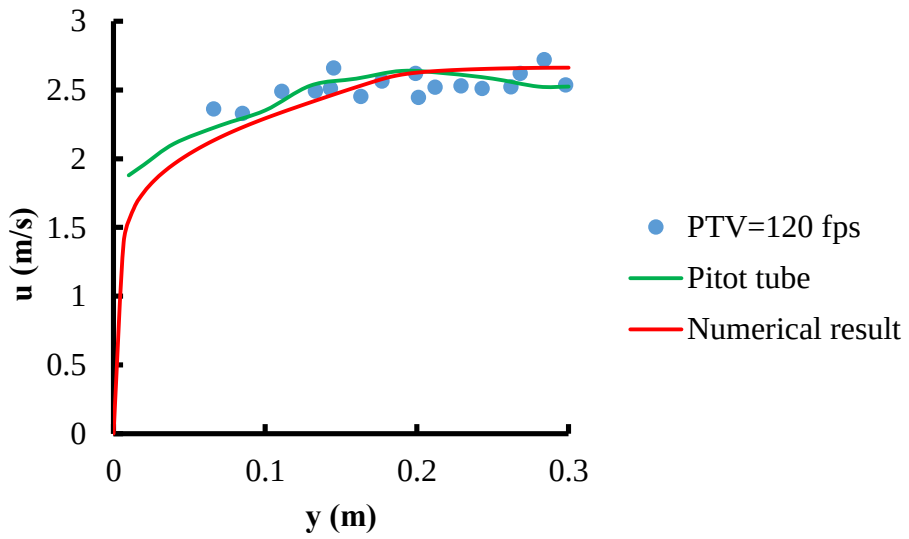

Figure K-39 : Measured and computed surface velocity with S_0=0.035, k_{s4}=1.25 cm, RMSE=5.056, Z_n=0.132 m, Q_{exp}=159.1 l/s

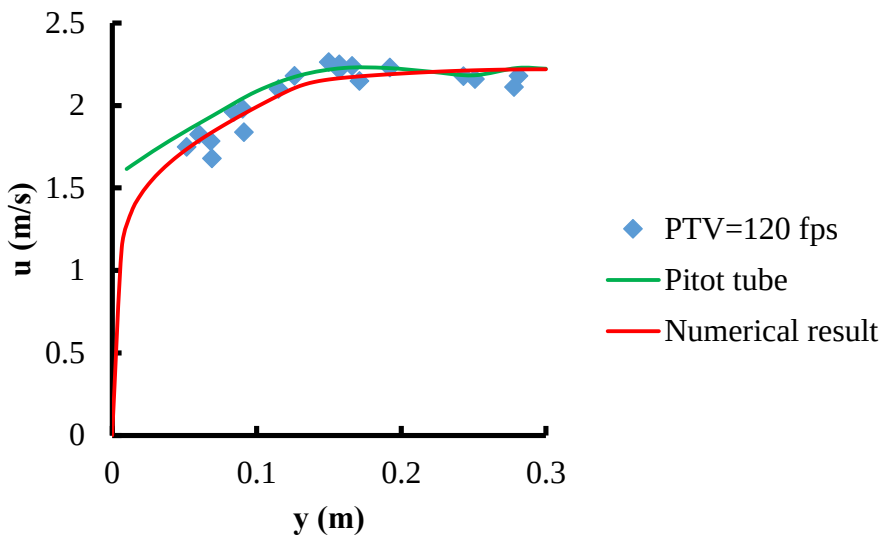

Figure K-40 : Measured and computed surface velocity with S_0=0.035, k_{s4}=1.32 cm, RMSE=3.53, Z_n=0.1003 m, Q_{exp}=101.8 l/s

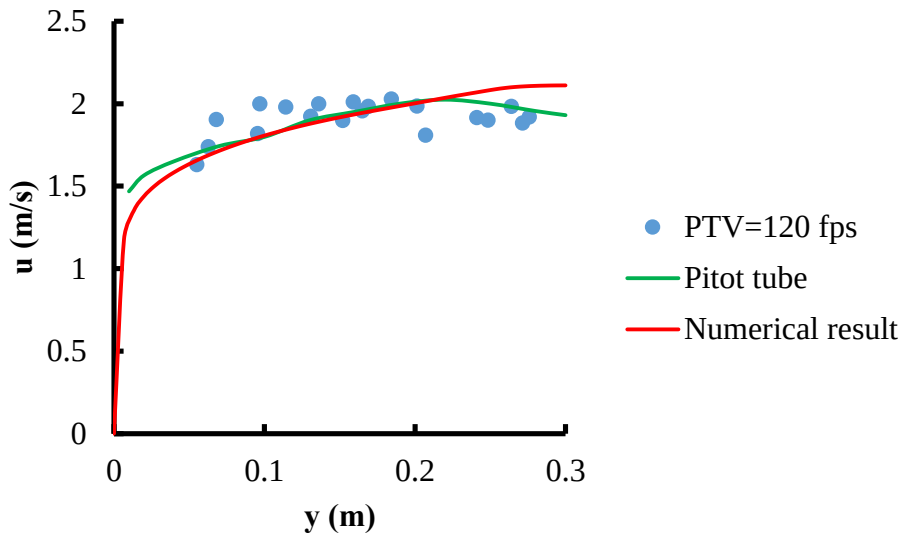

Figure K-41 : Measured and computed surface velocity with S_0=0.015, k_{s4}=0.9 cm, RMSE=6.51, Z_n=0.1723 m, Q_{exp}=167.7 l/s

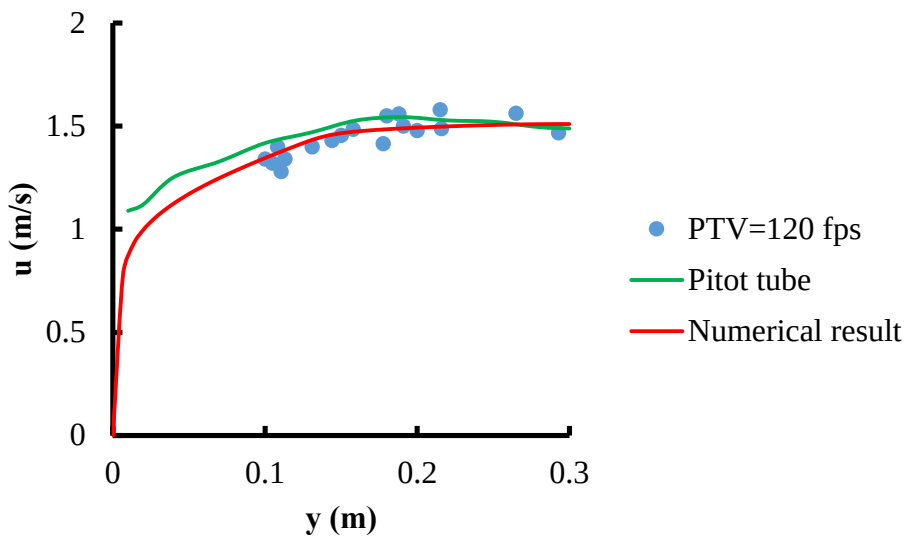

Figure K-42 : Measured and computed surface velocity with S_0=0.015, k_{s4}=1.1 cm, RMSE=3.33, Z_n=0.1054 m, Q $_{exp}$=75.3 l/s

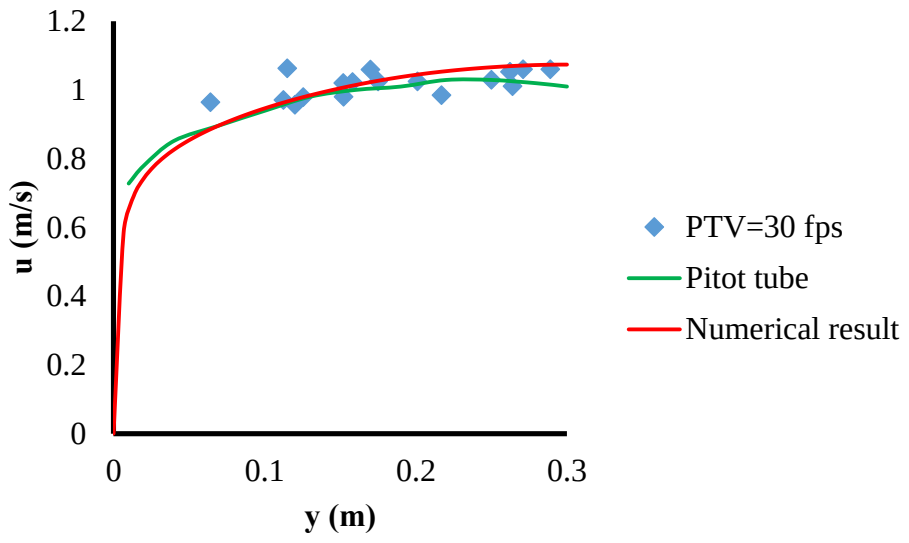

Figure K-43 : Measured and computed surface velocity with S_0=0.004, k_{s4}=1.5 cm, RMSE=4.17, Z_n=0.2194 m, Q $_{exp}$=110 l/s

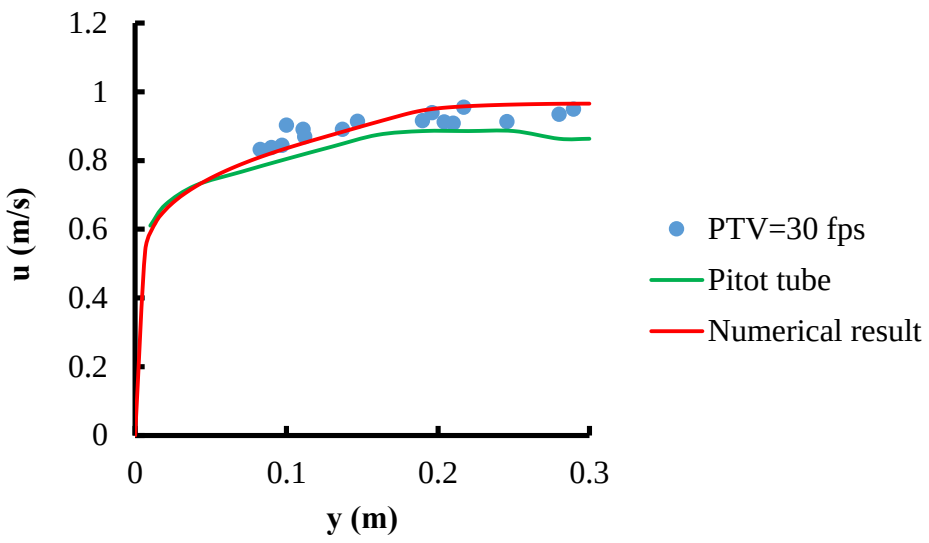

Figure K-44 : Measured and computed surface velocity with S_0=0.004, k_{s4}=1.25 cm, RMSE=3.55, Z_n=0.1281 m, Q $_{exp}$=51 l/s

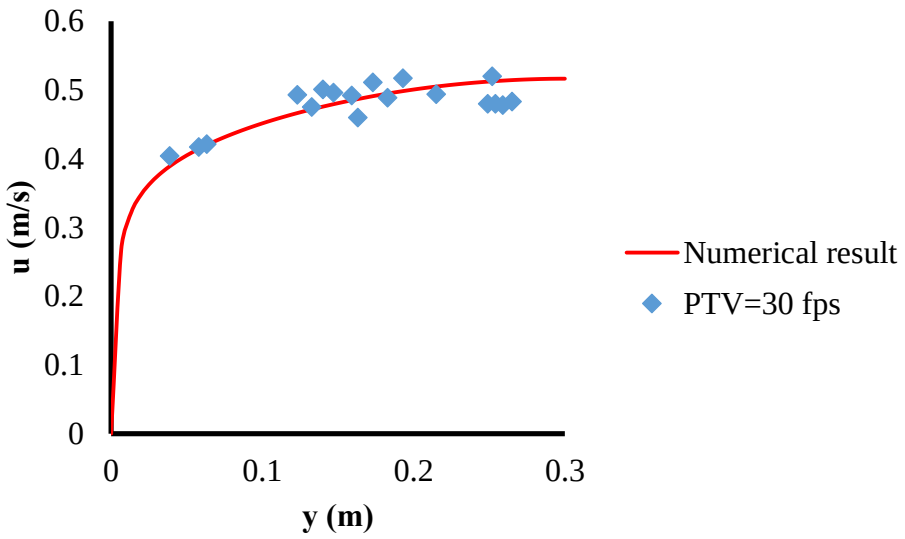

Figure K-45 : Measured and computed surface velocity with S_0=0.001, k_{s4}=1.55 cm, RMSE=4.25, Z_n=0.2194 m, Q $_{exp}$=55 l/s

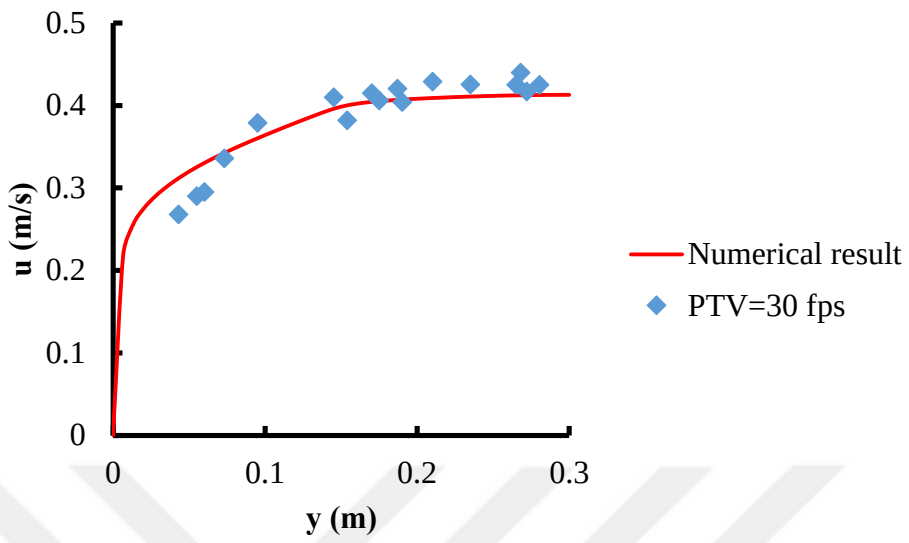

Figure K-46 : Measured and computed surface velocity with S_0=0.001, k_{s4}=1.2 cm, RMSE=5.99, Z_n=0.1107 m, Q_{exp}=20.55 l/s

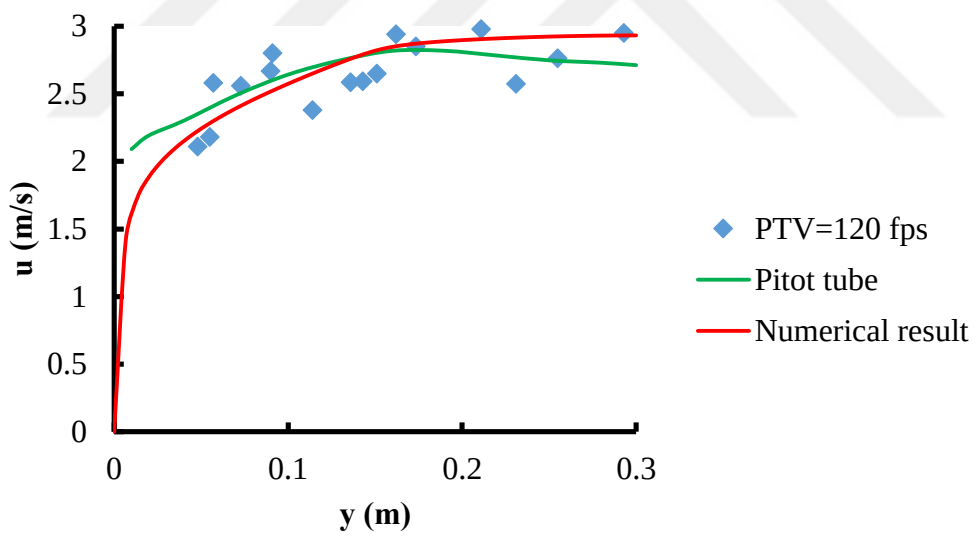

Figure K-47 : Measured and computed surface velocity with S_0=0.055, k_{s5}=2.1 cm, RMSE=6.7, Z_n=0.1254 m, Q_{exp}=162.4 l/s

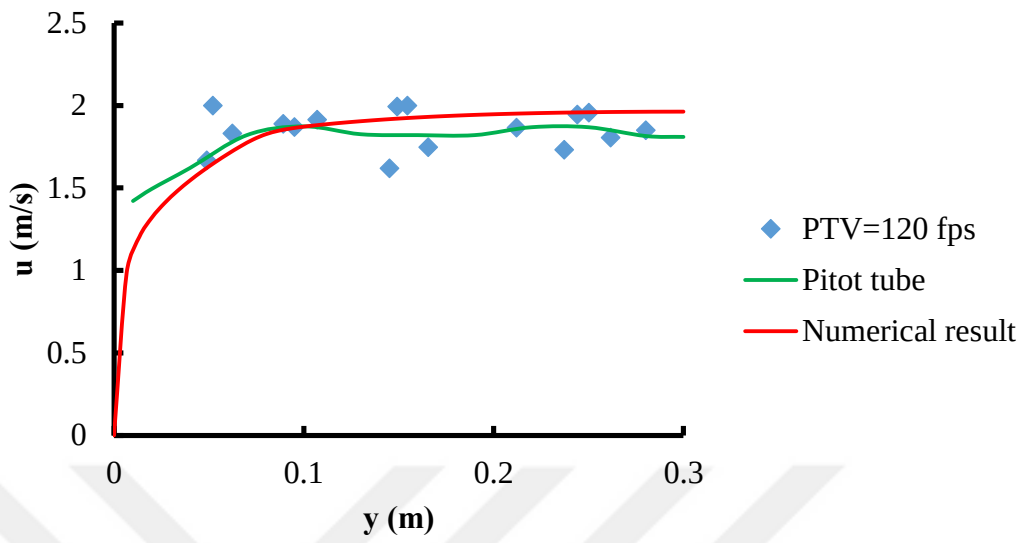

Figure K-48 : Measured and computed surface velocity with S_0=0.055, k_{s5}=2.7 cm, RMSE=6.7, Z_n=0.067 m, Q $_{exp}$=55 l/s

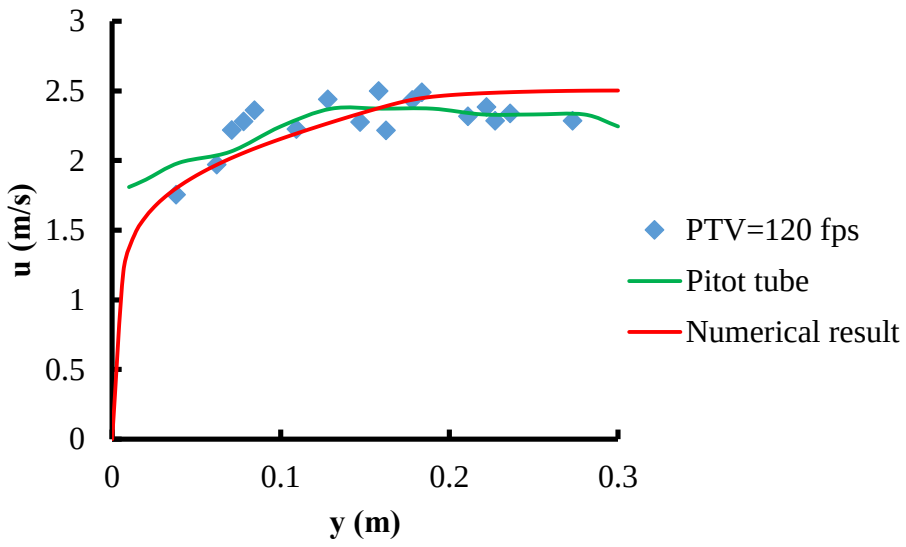

Figure K-49 : Measured and computed surface velocity with S_0=0.035, k_{s5}=2.4 cm, RMSE=8.2, Z_n=0.1416 m, Q $_{exp}$=159.1 l/s

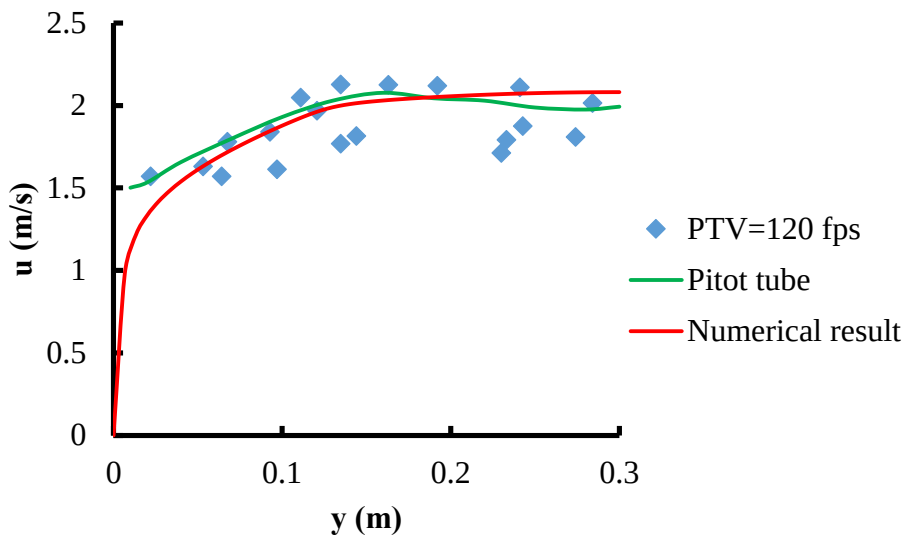

Figure K-50 : Measured and computed surface velocity with S_0=0.035, k_{s5}=2.15 cm, RMSE=10.25, Z_n=0.1082 m, Q $_{exp}$=101.8 l/s

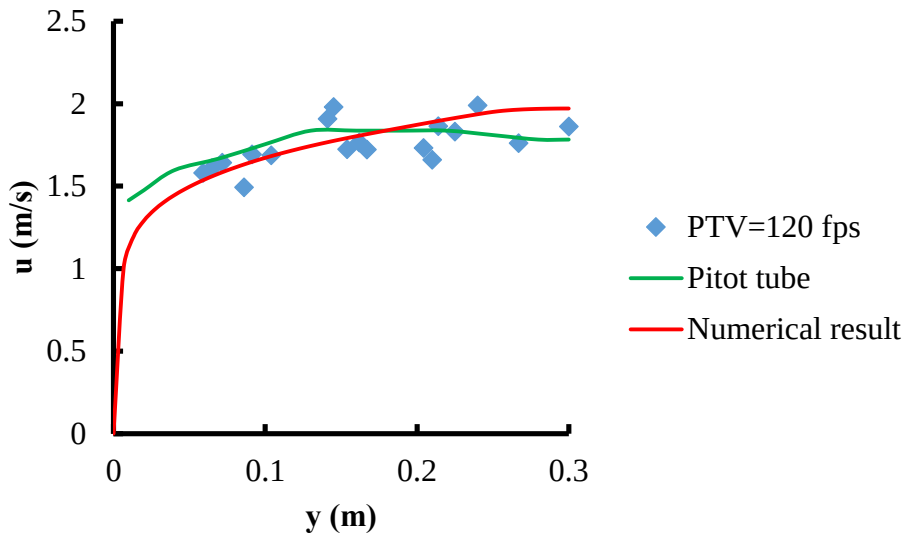

Figure K-51 : Measured and computed surface velocity with S_0=0.015, k_{s5}=1.5 cm, RMSE=7.55, Z_n=0.1861 m, Q $_{exp}$=167.7 l/s

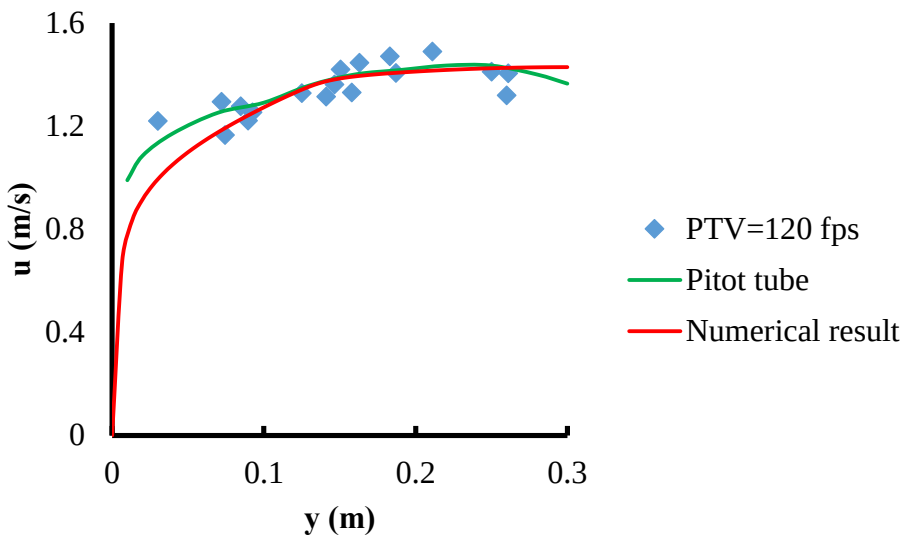

Figure K-52 : Measured and computed surface velocity with S_0=0.015, k_{s5}=2.2 cm, RMSE=7.55, Z_n=0.1151 m, Q $_{exp}$=75.3 l/s

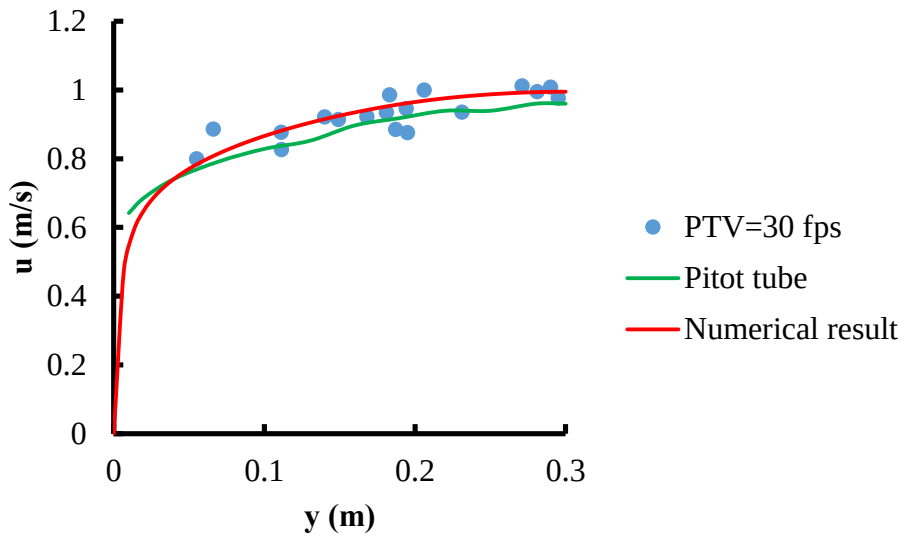

Figure K-53 : Measured and computed surface velocity with S_0=0.004, k_{s5}=2.8 cm, RMSE=3.55, Z_n=0.2421 m, Q $_{exp}$=110 l/s

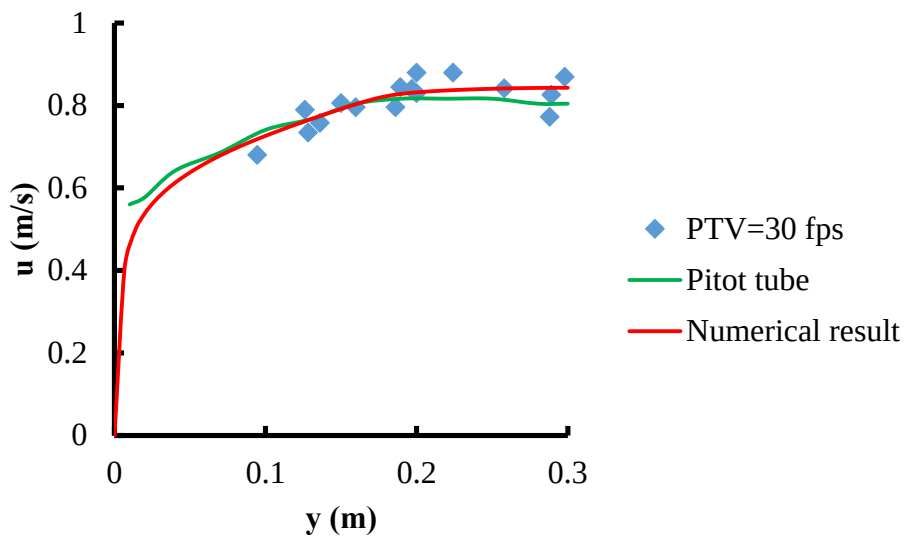

Figure K-54 : Measured and computed surface velocity with S_0=0.004, k_{s5}=2.4 cm, RMSE=4.6, Z_n=0.1405 m, Q $_{exp}$=51 l/s

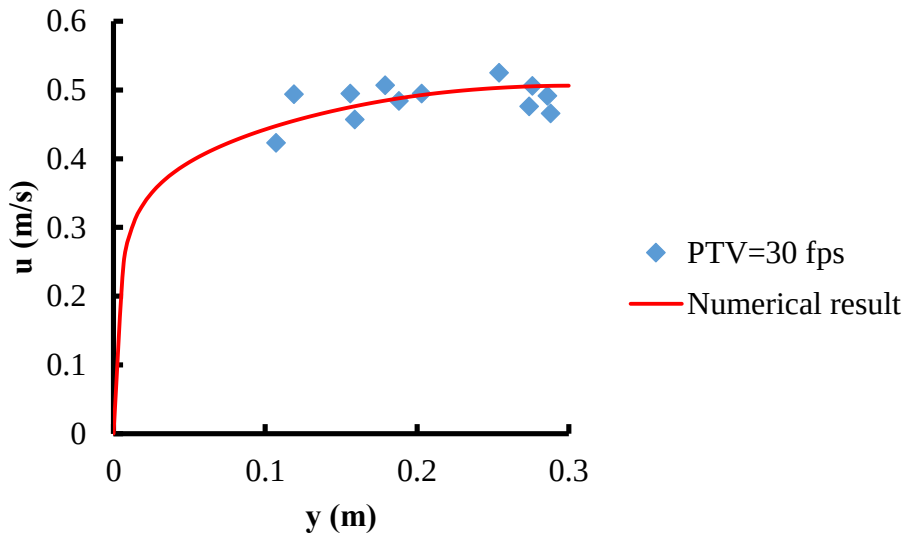

Figure K-55 : Measured and computed surface velocity with S_0=0.001, k_{s5}=2.9 cm, RMSE=5.5, Z_n=0.2421 m, Q $_{exp}$=55 l/s

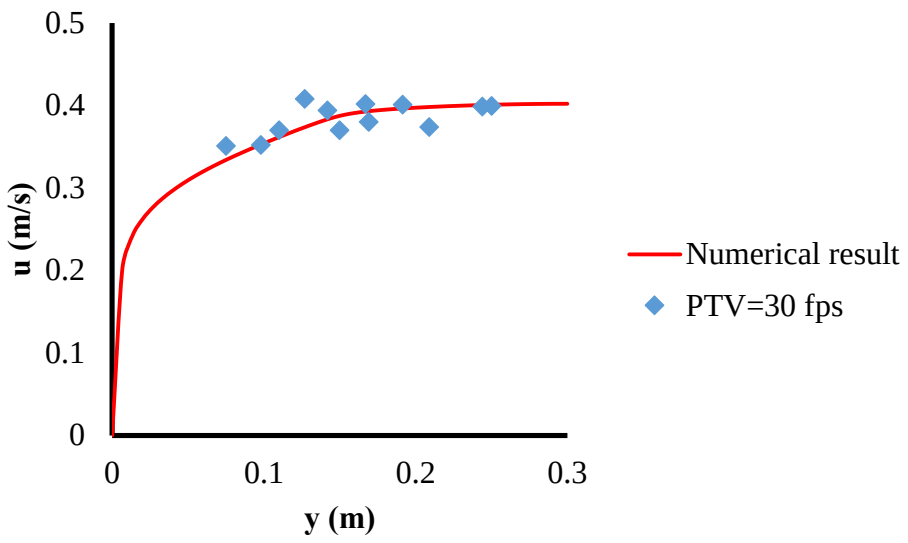

Figure K-56 : Measured and computed surface velocity with S_0=0.001, k_{s5}=2.2 cm, RMSE=2.1, Z_n=0.1212 m, Q_{exp}=20.55 l/s

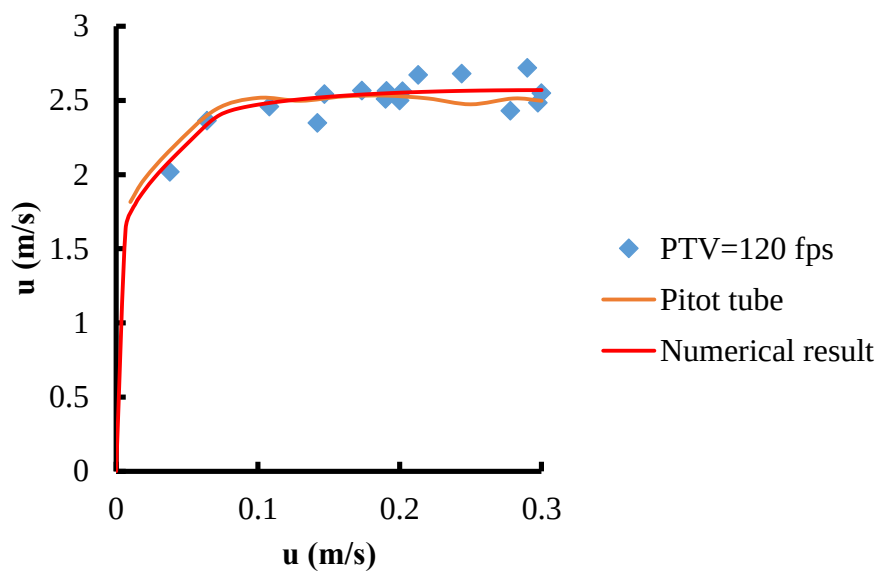

Figure K-57 : Measured and computed surface velocity with S_0=0.055, k_{s6}=0.2 cm, RMSE=3.45, Z_n=0.0476 m, Q_{exp}=55 l/s

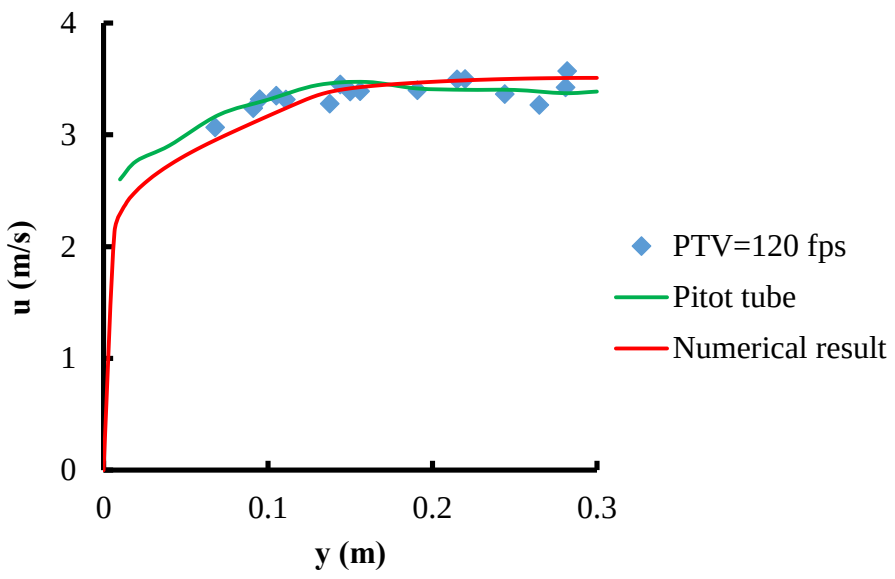

Figure K-58 : Measured and computed surface velocity with S_0=0.055, k_{s6}=0.3 cm, RMSE=2.25, Z_n=0.0943 m, Q_{exp}=162.4 l/s

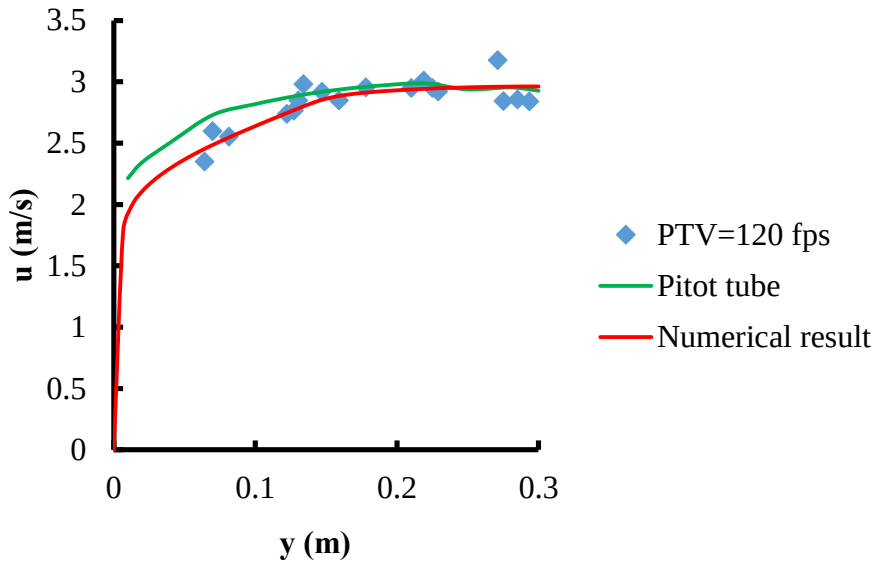

Figure K-59 : Measured and computed surface velocity with S_0=0.035, k_{s6}=0.34 cm, RMSE=3.75, Z_n=0.0943 m, Q_{exp}=162.4 l/s

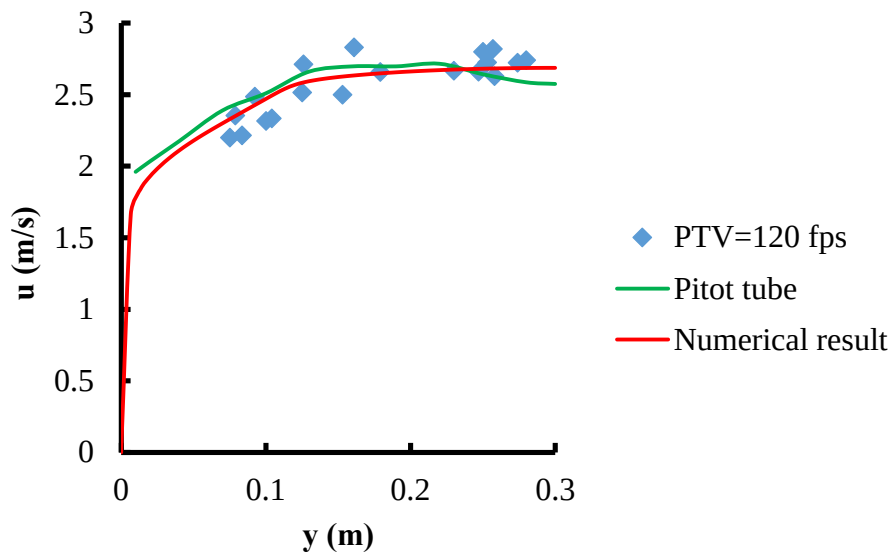

Figure K-60 : Measured and computed surface velocity with S_0=0.035, k_{s6}=0.23 cm, RMSE=4.1, Z_n=0.0805 m, Q_{exp}=101.8 l/s

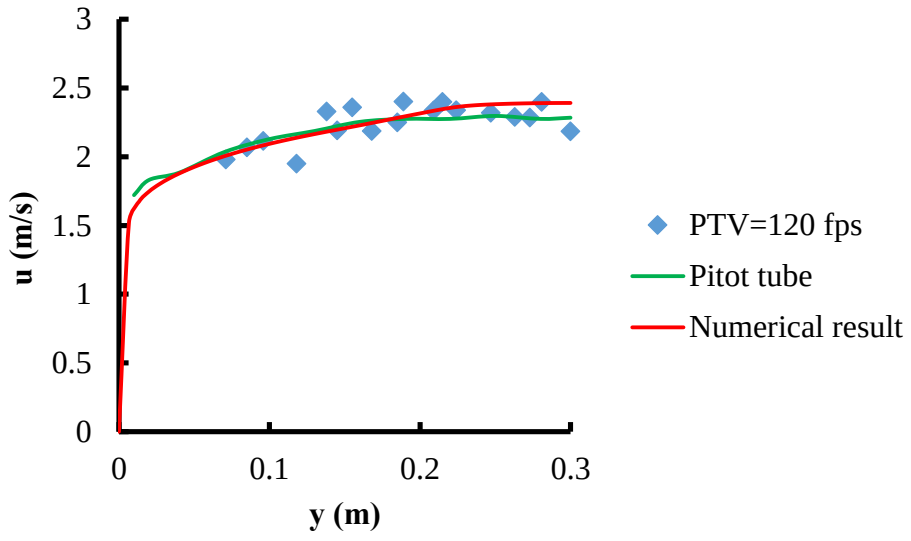

Figure K-61 : Measured and computed surface velocity with S_0=0.015, k_{s6}=0.19 cm, RMSE=3.68, Z_n=0.144 m, Q_{exp}=167.7 l/s

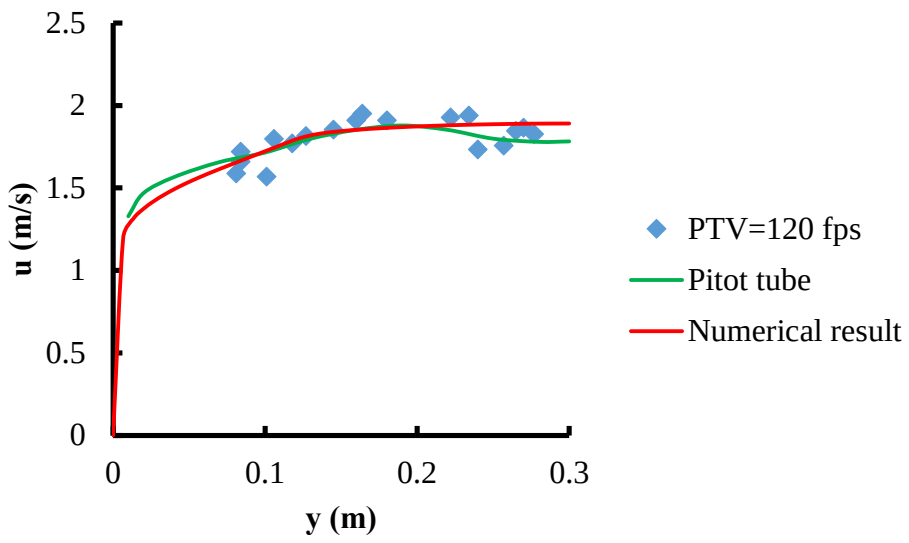

Figure K-62 : Measured and computed surface velocity with S_0=0.015, k_{s6}=0.16 cm, RMSE=2.5, Z_n=0.084 m, Q $_{exp}$=75.3 l/s

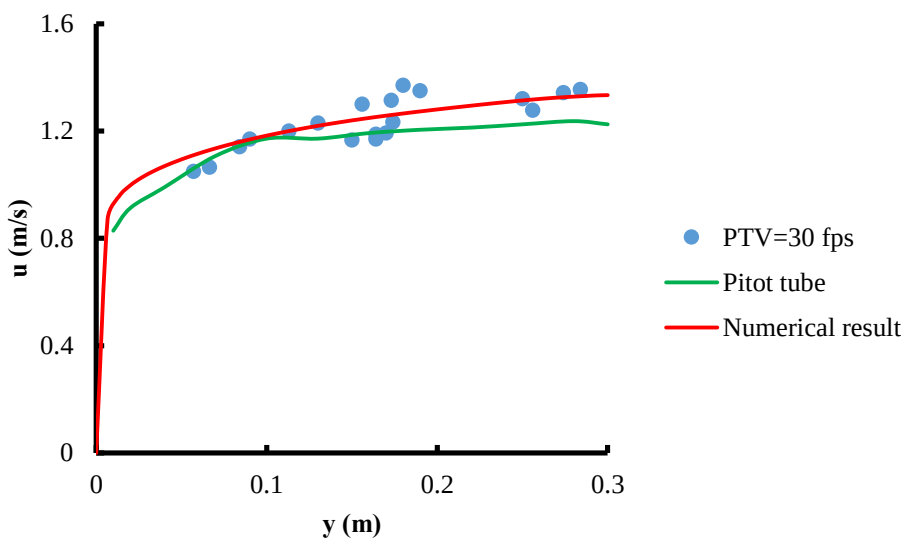

Figure K-63 : Measured and computed surface velocity with S_0=0.004, k_{s6}=0.18 cm, RMSE=3.3, Z_n=0.1756 m, Q $_{exp}$=110 l/s

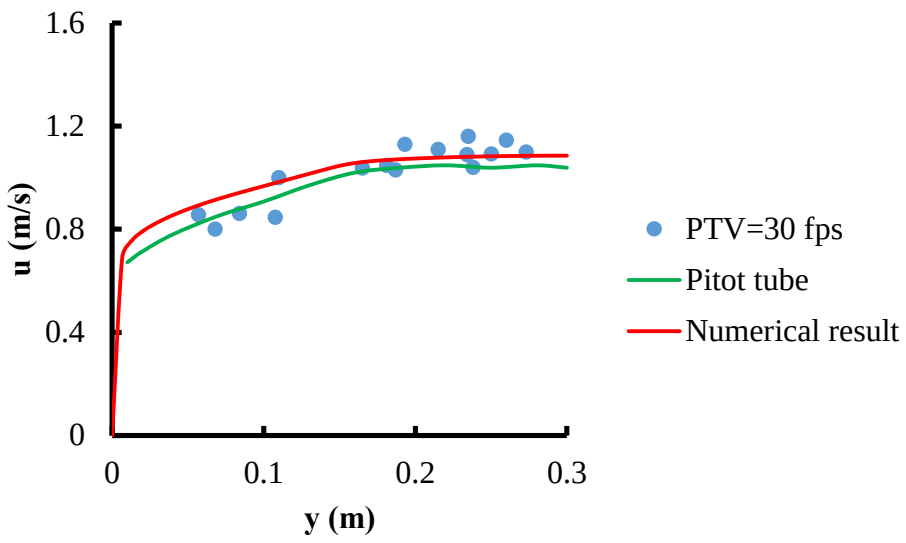

Figure K-64 : Measured and computed surface velocity with S_0=0.004, k_{s6}=0.16 cm, RMSE=5, Z_n=0.1037 m, Q_{exp}=51 l/s

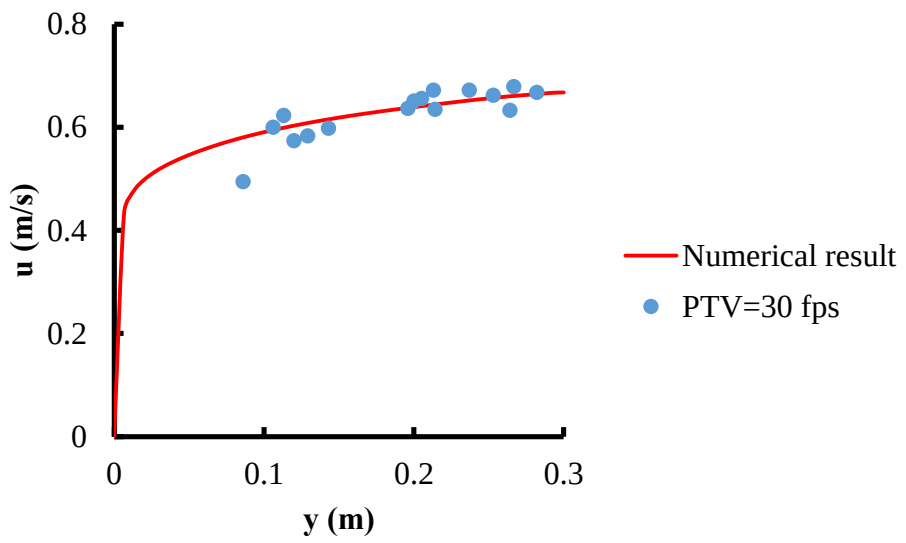

Figure K-65 : Measured and computed surface velocity with S_0=0.001, k_{s6}=0.18 cm, RMSE=2.75, Z_n=0.1755 m, Q_{exp}=55 l/s

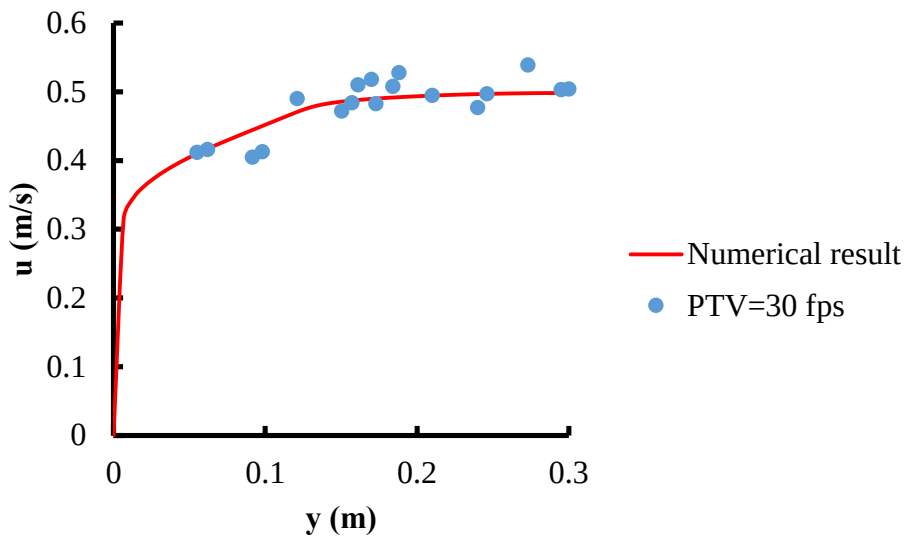

Figure K-66 : Measured and computed surface velocity with S_0=0.001, k_{s6}=0.18 cm, RMSE=3.9, Z_n=0.0898 m, Q_{exp}=20.55 l/s

APPENDIX L

CODE THAT INTEGRATES THE VELOCITY IN FLOOD PLAIN FOR DISCHARGE CALCULATION

```
clc
clear all
%!!!!!!!!!!!!!!!!!!!! CODE FOR INTEGRATING FLOOD PLAIN
DISCHARGE FROM
% PITOT TUBE MEASURMENTS
!!!!!!!!!!!!!!!!!!!!!!!!!!!!!!!!!!!!!!!!!!!!
Data=0; % u should select data from A to T
display('Insert the data from excel at this phase, from
column A to T.')
pause
Water_depth=25.1 ; %cm
Water_depth=10*Water_depth-150;
Horizon_distance=50; %mm
a=size(Data);
Depth=Data(:,2);
Depth=flipud(Depth);
Depth(a(1)+1)=0;
U(:,7)=Data(:,5);
U(:,6)=Data(:,8);
U(:,5)=Data(:,11);
U(:,4)=Data(:,14);
U(:,3)=Data(:,17);
U(:,2)=Data(:,20);
b=size(U);
U(2:b(1)+1,:)=U(1:b(1),:);
U(1,:)=0;
U=flipud(U);
surf(U);
U=1000*U; %change to mm
Depth=1000*Depth;
% Calculations of power determination for near wall velocity
profile
for i=2:b(2)
syms m
m=solve(U(b(1),i)== Depth(b(1))^m ,m>0);
power_y(i)=eval(m);
end
for i=1:b(1)
syms m
m=solve(U(i,2)== Horizon_distance^m ,m>0);
power_z(i)=eval(m);
```

```
end
% Internal discharge calculation loop
for j=1:(b(2)-2)
    for i=1:b(1)-1
        Dq(i,j)=[U(i,j+1)+U(i,j+2)+U(i+1,j+1)+U(i+1,j+2)]...
            *Horizon_distance*(Depth(i)-Depth(i+1))/4;
    end
end
Additional_depth=Water_depth-Depth(1);
Near_surface_Q=sum(Dq(1,:))*[Additional_depth/(Depth(1)-
Depth(2))];
power_y(1)=[];
power_z=transpose(power_z);
Dq=fliplr(Dq);
Dq(size(Dq,1)+1,size(Dq,2)+1)=0;
Dq=fliplr(Dq);
% Near Bottom Discharge Calculations
for i=1:size(U,2)-2
Power=[power_y(i)+power_y(i+1)]/2;
syms Hd
Aver_U=int(Hd^Power,0,Depth([length(Depth)-1]));
Aver_U=eval(Aver_U);
Aver_U=( (U(size(U,1)-1,i+1)+U(size(U,1)-
1,i+2))/2)*Horizon_distance*Depth([length(Depth)-1]) ...
    -Aver_U*Horizon_distance;
Dq(size(Dq,1),i+1)=Aver_U;
end
% Near Side Wall Discharge Calculations
for i=1:size(U,1)-2
Power=[power_z(i)+power_z(i+1)]/2;
syms Zd
Aver_U=int(Zd^Power,0,Horizon_distance);
Aver_U=eval(Aver_U);
Aver_U=( ((U(i,2)+U(i+1,2))/2)*Horizon_distance*[Depth(i)-
Depth(i+1)])  -...
    Aver_U*[Depth(i)-Depth(i+1)];
Dq(i,1)=Aver_U;
end
Dq(size(Dq,1),1)=[Dq(size(Dq,1)-1,1)+Dq(size(Dq,1),2)]/2;
T_Q=sum(sum(Dq))+Near_surface_Q;
T_Q=T_Q/1000000 ,display('l/s') % l/S
```

APPENDIX M

EXPERIMENTAL VELOCITY MEASUREMENTS BY PITOT TUBE IN FLOOD PLAIN IN SMOOTH COMPOUND CHANNELS

All Pitot tube measurements for smooth compound channels are presented here. The water depth in all figures are starting from the bed of the main channel. The distance from the side wall has been demonstrated by the symbol y.

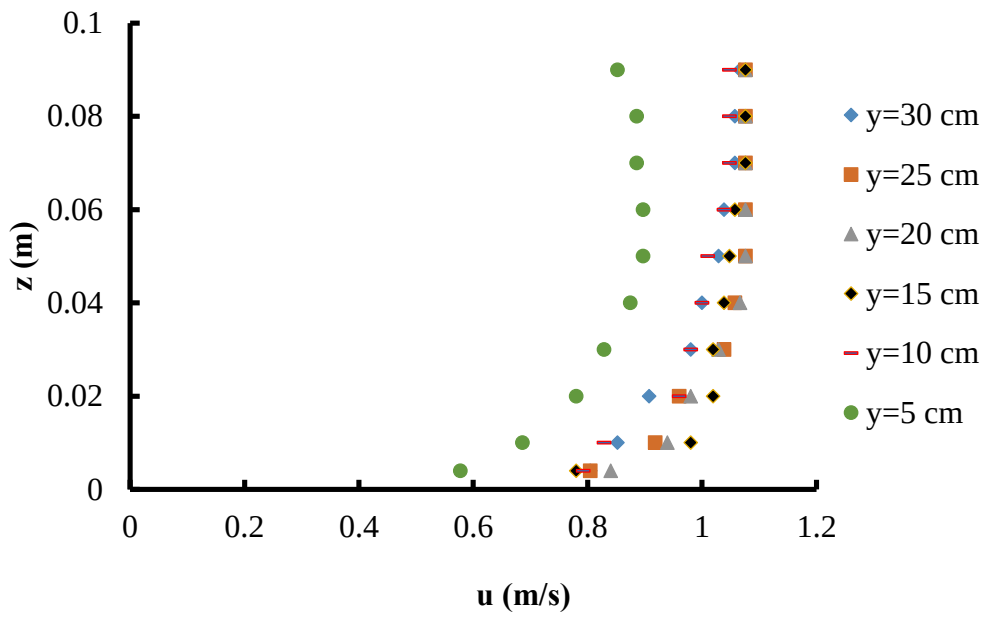

Figure M-1 : Flood plain Pitot tube measurements in smooth compound channels with Z=0.251m, Q=0.102 m^3/s and S_0=0.001

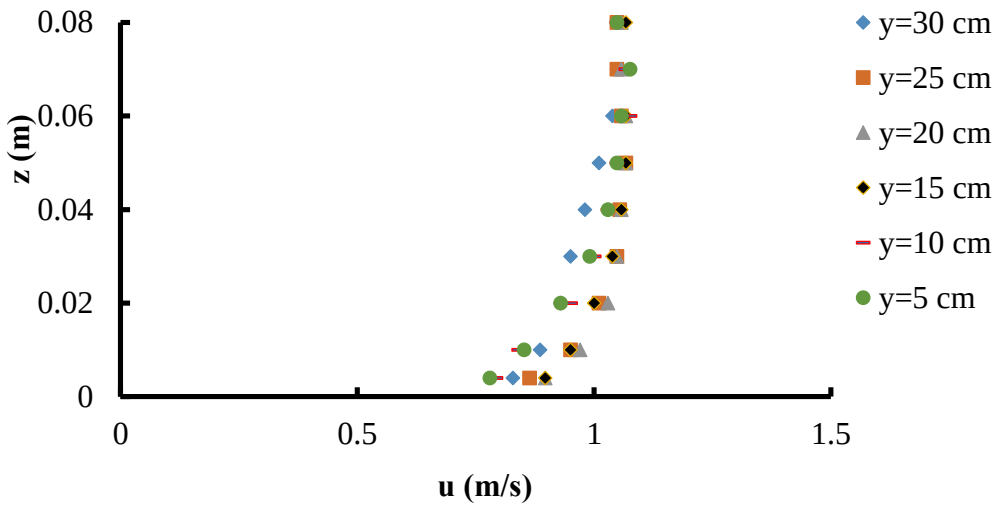

Figure M-2 : Flood plain Pitot tube measurements in smooth compound channels with Z=0.238 m, Q=0.102 m^3/s and S_0=0.002

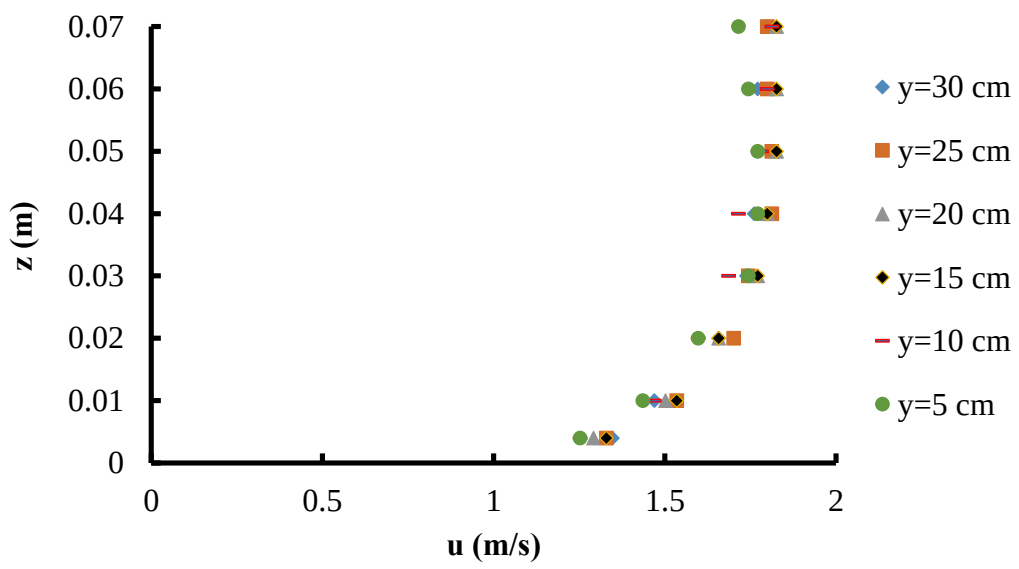

Figure M-3 : Flood plain Pitot tube measurements in smooth compound channels with Z=0.225 m, Q=0.166 m^3/s and S_0=0.01

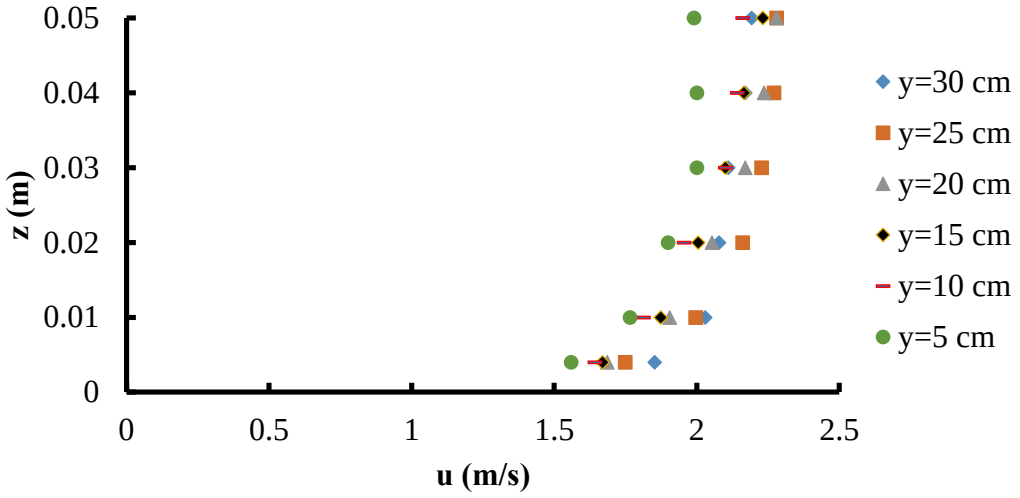

Figure M-4 : Flood plain Pitot tube measurements in smooth compound channels with Z=0.220 m, Q=0.166 m^3/s and S_0=0.015

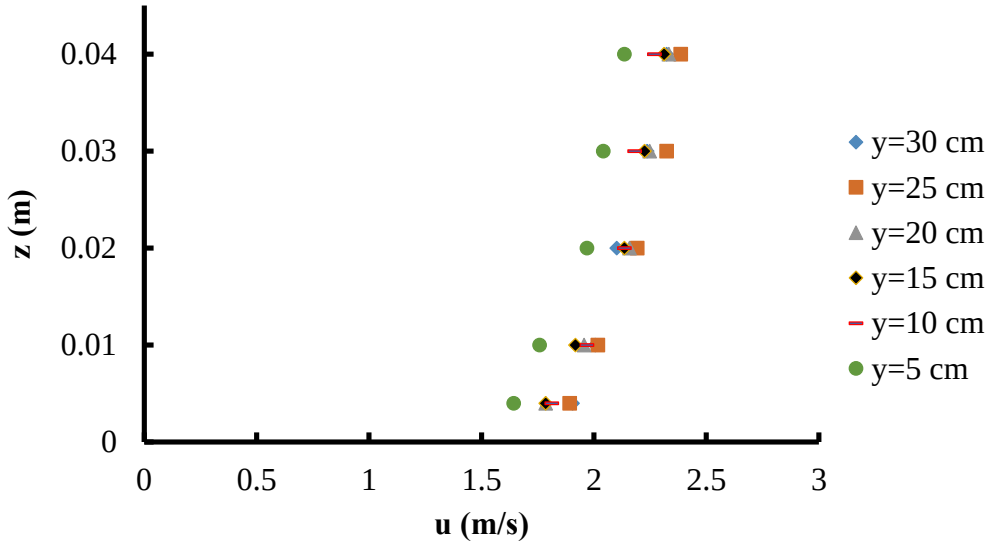

Figure M-5 : Flood plain Pitot tube measurements in smooth compound channels with Z=0.193 m, Q=0.166 m^3/s and S_0=0.02

APPENDIX N

EXPERIMENTAL VELOCITY MEASUREMENTS BY PITOT TUBE IN FLOOD PLAIN IN ALL BED ROUGH COMPOUND CHANNELS

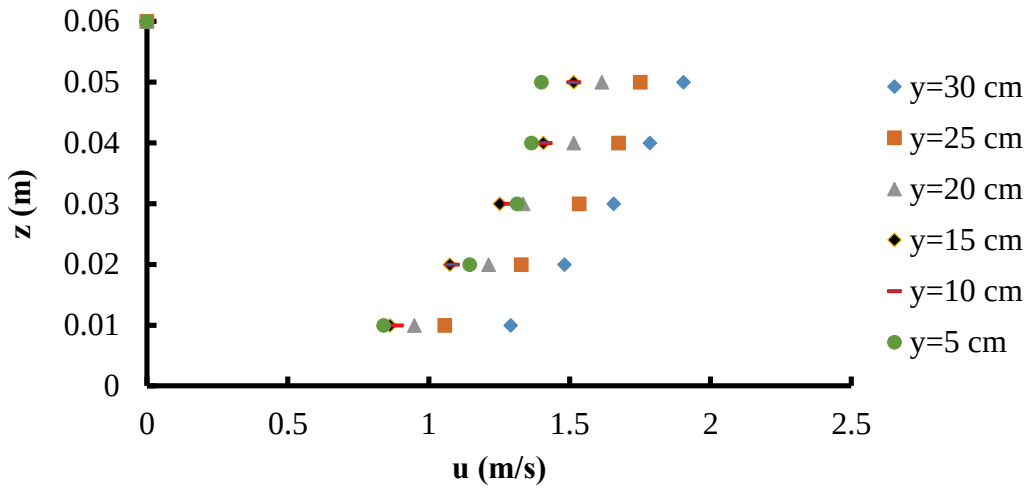

Figure **N**-1 : Flood plain Pitot tube measurements in all bed rough compound channels with Z_n=0.211 m, Q=0.16 m^3/s and S_0=0.035

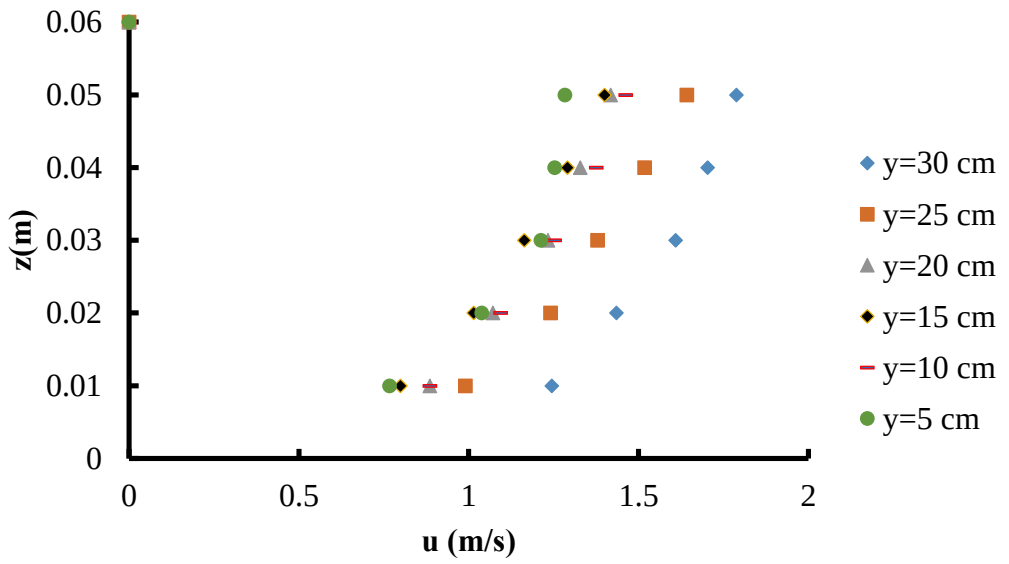

Figure **N**-2 : Flood plain Pitot tube measurements in all bed rough compound channels with Z_n=0.213 m, Q=0.15 m^3/s and S_0=0.03

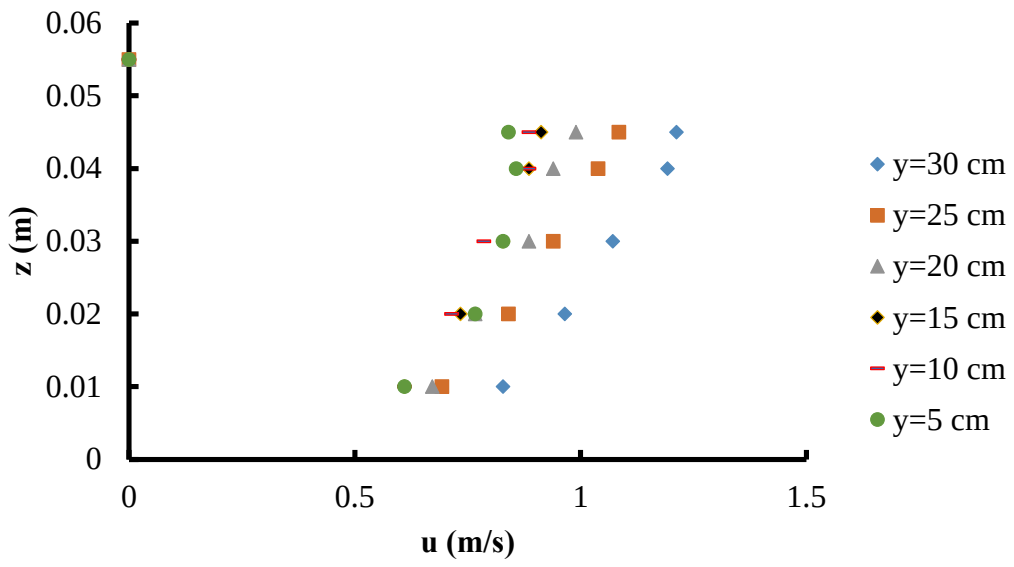

Figure **N**-3 : Flood plain Pitot tube measurements in all bed rough compound channels with Z_n=0.199 m, Q=0.1 m^3/s and S_0=0.02

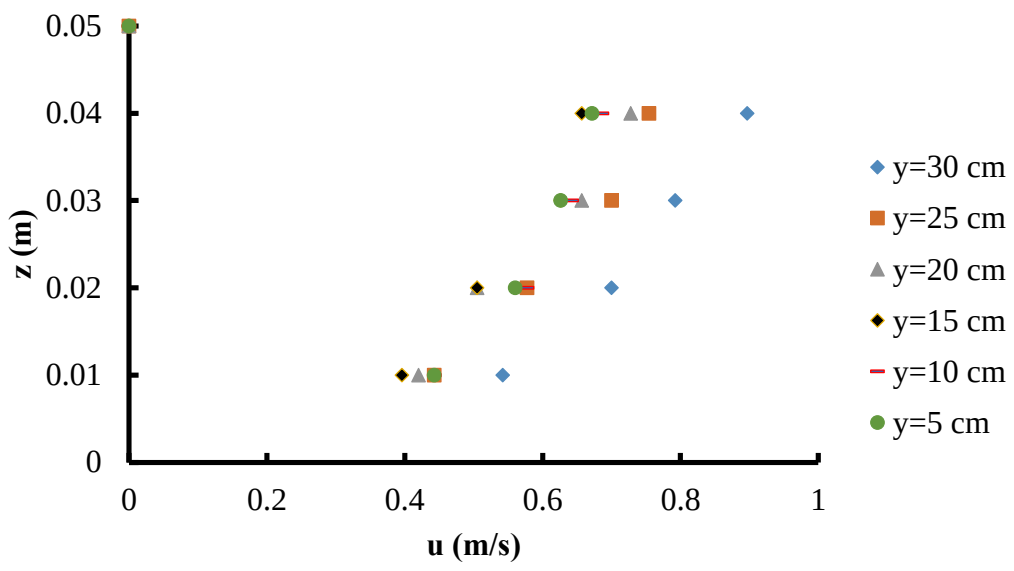

Figure **N**-4 : Flood plain Pitot tube measurements in all bed rough compound channels with Z_n=0.198 m, Q=0.074 m^3/s and S_0=0.01

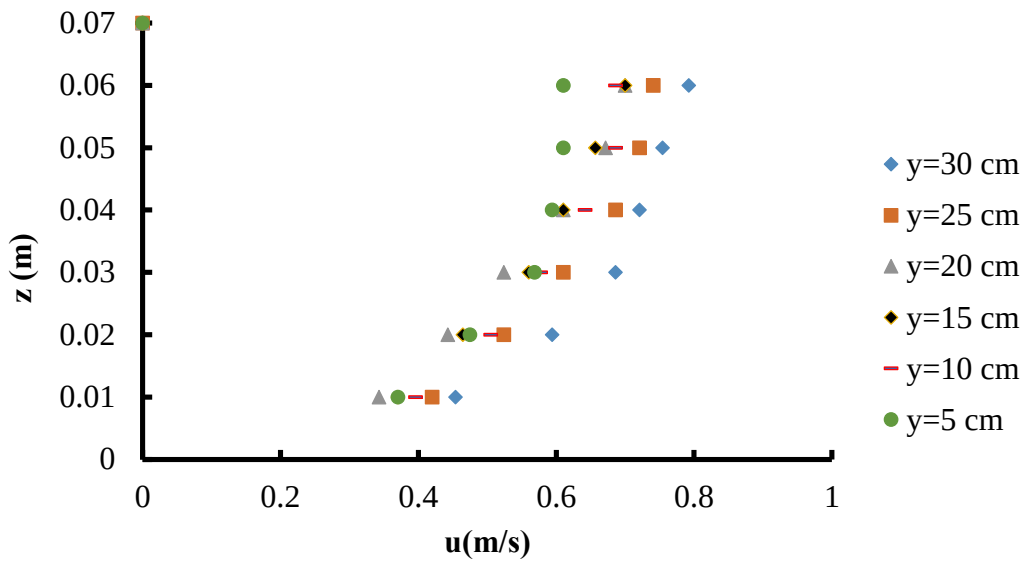

Figure **N**-5 : Flood plain Pitot tube measurements in all bed rough compound channels with Z=0.222 m, Q=0.0635 m^3/s and S_0=0.004

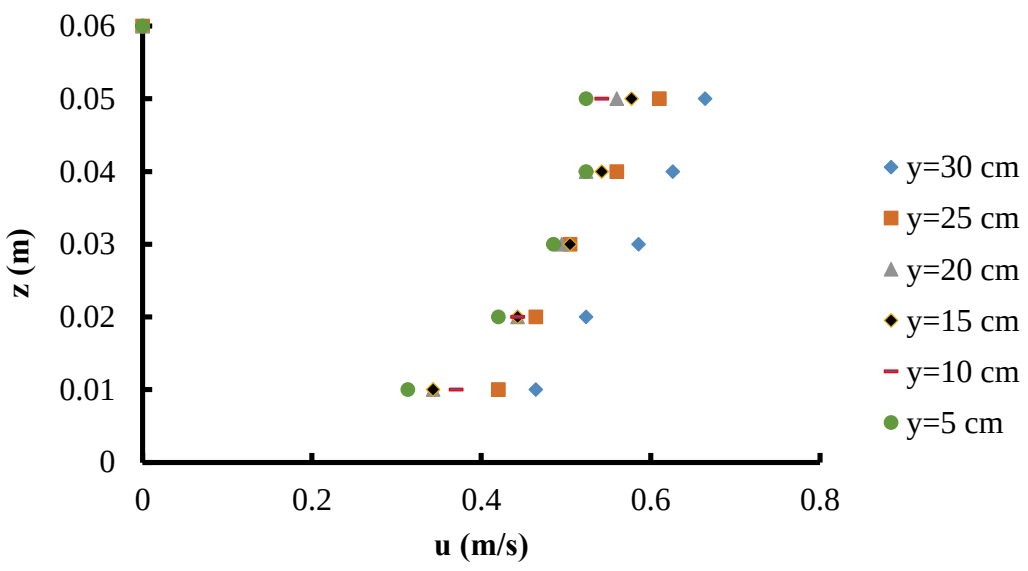

Figure **N**-6 : Flood plain Pitot tube measurements in all bed rough compound channels with Z=0.209 m, Q=0.0505 m^3/s and S_0=0.002

APPENDIX O

EXPERIMENTAL VELOCITY MEASUREMENTS BY PITOT TUBE IN FLOOD PLAIN IN FLOODPLAIN ROUGH COMPOUND CHANNELS

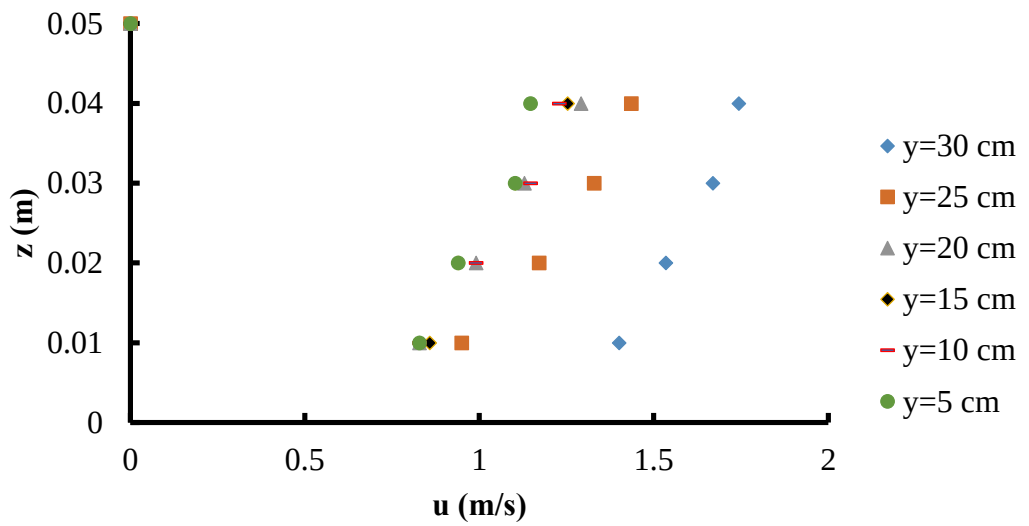

Figure O-1 : Flood plain Pitot tube measurements in all bed rough compound channels with Z=0.197 m, Q=0.16 m^3/s and S_0=0.025

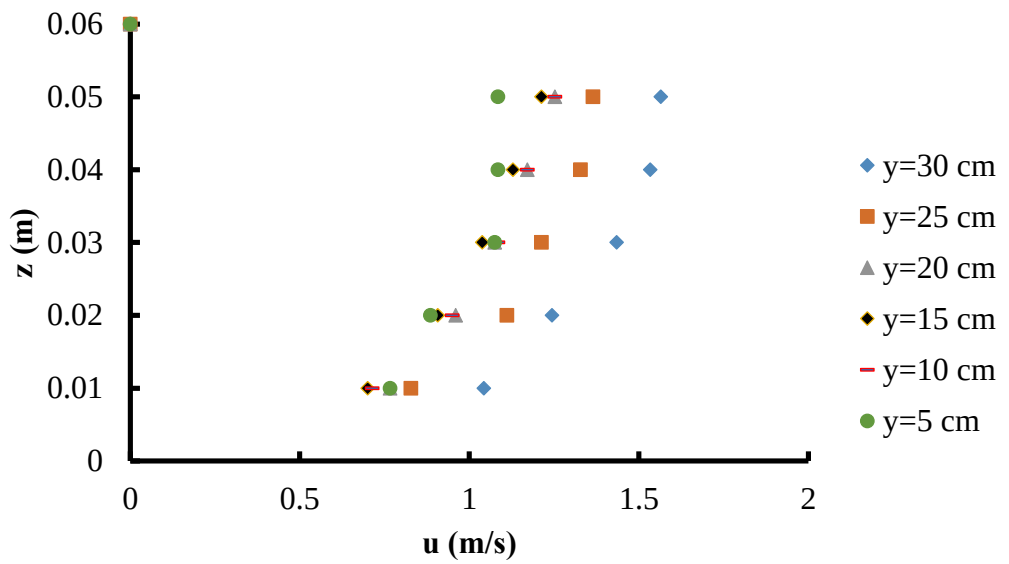

Figure O-2 : Flood plain Pitot tube measurements in all bed rough compound channels with Z=0.204 m, Q=0.147 m^3/s and S_0=0.02

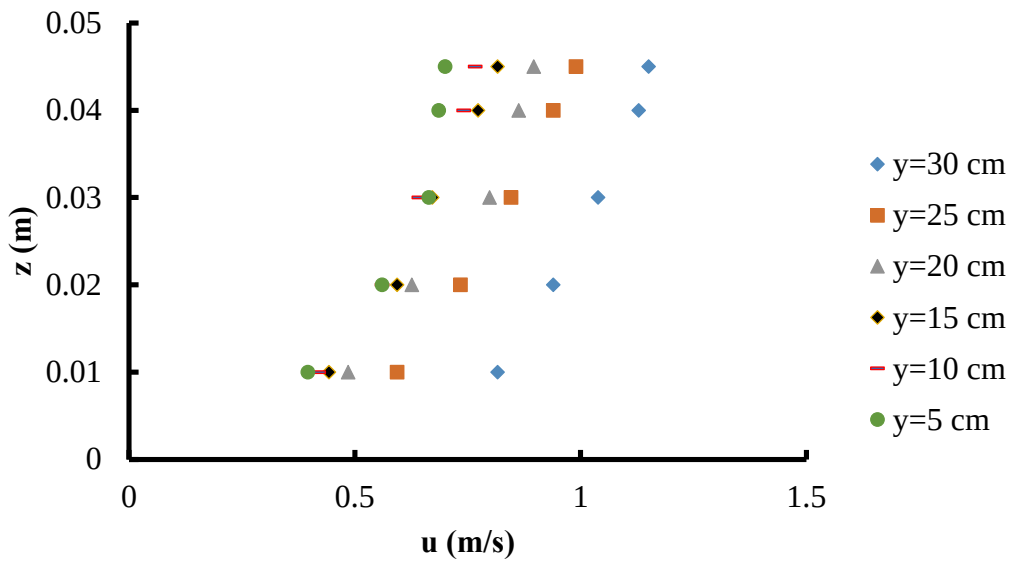

Figure O-3 : Flood plain Pitot tube measurements in all bed rough compound channels with Z=0.206 m, Q=0.1 m^3/s and S_0=0.008

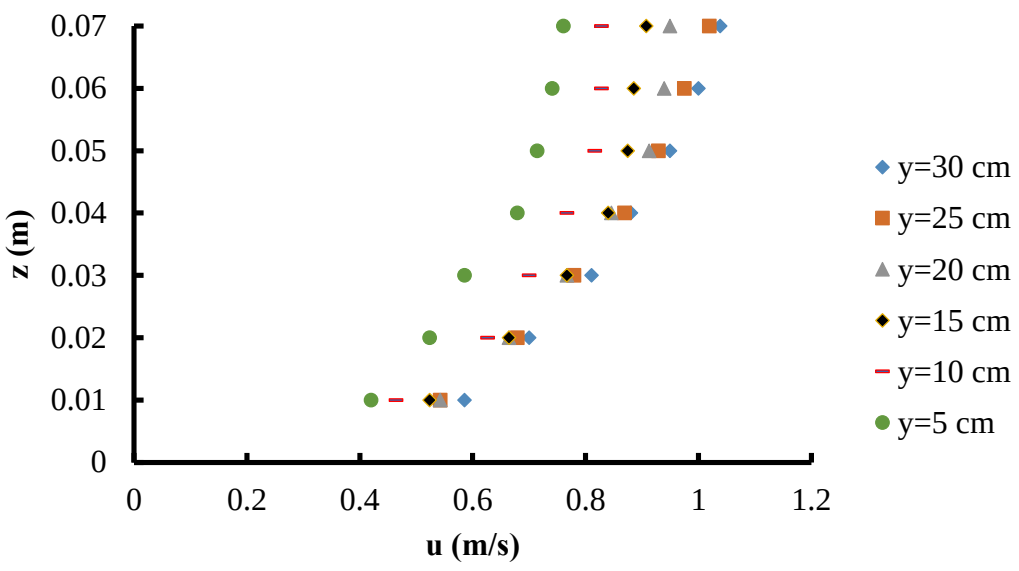

Figure O-4 : Flood plain Pitot tube measurements in all bed rough compound channels with Z=0.235 m, Q=0.1 m^3/s and S_0=0.004

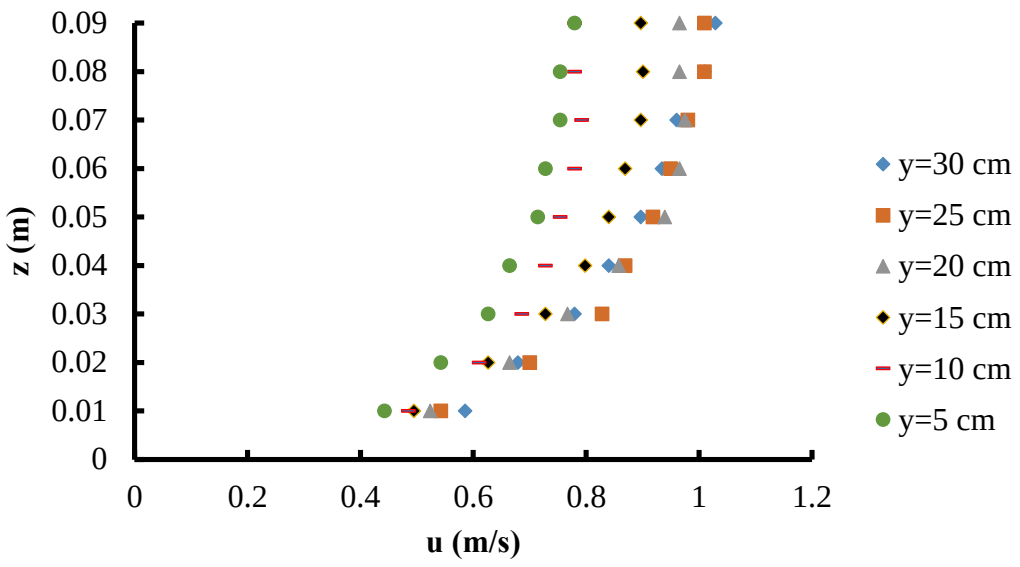

Figure O-5 : Flood plain Pitot tube measurements in all bed rough rough compound channels with Z=0.245 m, Q=0.1 m^3/s and S_0=0.002

CURRICULUM VITAE

PERSONAL INFORMATION

Surname, Name: Siamak Gharahjeh

Nationality: Iranian

Date and Birth Place: 3rd January 1987, Tabriz

Phone: +90 312 210 24 19

Email: siamak_ghh2000@yahoo.com

EDUCATION

2010-2012 Middle East Technical University (METU), Civil Engineering Department, MS.

2005-2009 Tabriz Azad University, Civil Engineering Department, BS.

WORK EXPERIENCE

2013- 2016 METU, Civil Engineering Department, RA.

PUBLICATIONS

I. Aydin, S. **Gharahjeh** "Roughness and discharge estimation in open channels by free surface velocity measurement". (To be Submitted).

S. **Gharahjeh**, I. Aydin "Application of video imagery techniques for low cost measurement of water free surface velocity in open channels". Submitted to Flow Measurement and Instrumentation, (under review).

S. **Gharahjeh**, A. Ashraf, G. Mahtabi Shirazi. "Numerical solution of 2-D steady incompressible lid-driven cavity flow with three different numerical schemes" Submitted to International Journal for Numerical Methods in Fluids. (under review).

S. **Gharahjeh**, I. Aydin, A.B. Altan- Sakarya "Weir Velocity Formulation for Sharp-Crested Rectangular Weirs" Flow Measurement and Instrumentation- 41(2015)50–56.

S. **Gharahjeh**, I. Aydin, A.B. Altan- Sakarya "Discharge Formula for Sharp-Crested Rectangular Weirs", ACE, 10th International Congress on Advances in Civil Engineering held in Ankara in October 2012.

Gh. Mahtabi, A. Hosseinzadeh Dalir, D. Farsadizadeh, S. **Gharahjeh** "Application of Current Deflecting Wall-Sill on Sediment Control at lateral Intake ", ACE, 10th International Congress on Advances in Civil Engineering held in Ankara in October 2012.

P. Lotfi, G. Mahtabi, H. Arvanaghi, S. **Gharahjeh**. "Investigation of flow properties over semi-cylindrical weir using Flow3D software". 13th Iranian Hydraulic Association in November 2014.

S. **Gharahjeh**, I. Aydin "Stream gauging by combined use of surface PTV and CFD techniques in channel flows ", IAHR. 2015, Hague, Netherlands in June 2015.

I. Aydin & S. **Gharahjeh**. "Determination of boundary roughness in channel flows ", Advances in Civil Engineering, Istanbul, Turkey, 2016.